

THE NEARBY ENVIRONMENT OF SEYFERT
GALAXIES: A COMPARATIVE STUDY

Marcel L. VanDalfsen

A thesis submitted to the Faculty of Graduate Studies
in partial fulfillment of the requirements
for the degree of

MASTER OF SCIENCE

Graduate Program in Physics and Astronomy
York University
North York, Ontario

September 1997



National Library
of Canada

Acquisitions and
Bibliographic Services

395 Wellington Street
Ottawa ON K1A 0N4
Canada

Bibliothèque nationale
du Canada

Acquisitions et
services bibliographiques

395, rue Wellington
Ottawa ON K1A 0N4
Canada

Your file *Votre référence*

Our file *Notre référence*

The author has granted a non-exclusive licence allowing the National Library of Canada to reproduce, loan, distribute or sell copies of this thesis in microform, paper or electronic formats.

The author retains ownership of the copyright in this thesis. Neither the thesis nor substantial extracts from it may be printed or otherwise reproduced without the author's permission.

L'auteur a accordé une licence non exclusive permettant à la Bibliothèque nationale du Canada de reproduire, prêter, distribuer ou vendre des copies de cette thèse sous la forme de microfiche/film, de reproduction sur papier ou sur format électronique.

L'auteur conserve la propriété du droit d'auteur qui protège cette thèse. Ni la thèse ni des extraits substantiels de celle-ci ne doivent être imprimés ou autrement reproduits sans son autorisation.

0-612-22881-9

The Nearby Environment of Seyfert Galaxies:
A Comparative Study

by

Marcel L. VanDalfsen

a thesis submitted to the Faculty of Graduate Studies of York
University in partial fulfillment of the requirements for the degree
of

Master of Science

© 1997

Permission has been granted to the LIBRARY OF YORK
UNIVERSITY to lend or sell copies of this thesis, to the
NATIONAL LIBRARY OF CANADA to microfilm this thesis and to
lend or sell copies of the film, and to **UNIVERSITY
MICROFILMS** to publish an abstract of this thesis.
The author reserves other publication rights, and neither the
thesis nor extensive extracts from it may be printed or otherwise
reproduced without the author's written permission.

Abstract

The question of whether active galactic nuclei (AGN) have more nearby companion galaxies than “normal” galaxies is important in providing evidence for the origin of activity in galactic nuclei, e.g., by tidal triggering. The “interaction hypothesis” suggests that Seyfert galaxies should have an excess of companions which may tidally trigger nuclear activity. By examining the host galaxy properties and nearby environments ($\lesssim 200$ kpc) of both Seyfert galaxies and a control set of non-active galaxies, the large-scale differences between Seyferts and non-active galaxies can be determined and the interaction hypothesis can be tested.

The two datasets were chosen from the Center for Astrophysics (CfA) spectroscopic sample, and were carefully matched in morphological type, absolute magnitude and redshift. Upon analyzing the properties of the 32 Seyfert galaxies and 49 control galaxies, there was indication that a fair comparison was in fact being made between the two samples. Counts of optical companion galaxies around the hosts and their magnitudes reveal that the Seyfert hosts occupy environments similar to the control hosts. There are also a similar number of disturbed morphologies and light asymmetries in both samples. These results indicate that interactions may not be the sole mechanism for initiating activity in Seyfert galaxies. Results which show the similarity of the environments of the Seyfert galaxies and the control galaxies will be presented in the body of the thesis, along with the techniques used to acquire these results.

Contents

Abstract	iv
Acknowledgments	v
List of Tables	ix
List of Figures	x
1 Introduction	1
1.1 Overview	1
1.2 Galaxies	2
1.2.1 Spiral Galaxies	3
1.2.2 Active Galaxies	4
1.2.2.1 Active Galactic Nuclei	5
1.3 Seyfert Galaxies	6
1.3.1 Properties and Types	6
1.3.1.1 Seyfert 1	7
1.3.1.2 Seyfert 2	8
1.3.1.3 Fractional Types	8
1.3.2 Unified Model	8
1.3.3 Interaction/Merger Hypothesis	11
1.3.4 Objective	12
1.4 Thesis Objective	12
1.4.1 Previous Work	13

2	Observations and Reduction Techniques	15
2.1	Introduction	15
2.2	Observations	15
2.2.1	Selection of Seyfert Galaxies and Control Galaxies	16
2.2.2	CCDs	16
2.2.3	Data Acquisition	17
2.3	Preliminary Reduction	18
2.3.1	CCD Pre-Processing in IRAF	19
2.3.2	Photometric Calibration	20
2.3.3	Host-Galaxy Magnitudes	21
2.4	Image Analysis	22
2.4.1	Image Statistics and Editing	22
2.4.2	Elliptical Isophotal Analysis	23
2.4.3	Surface Brightness Profile Fitting	27
2.4.4	Companion Galaxy Searching	29
2.4.5	Unsharp Masking and Morphology	29
2.4.6	Galaxy Parameters and Statistics	31
3	Discussion of Seyfert Galaxies	34
3.1	Introduction	34
3.2	Analysis	34
3.2.1	The Galaxies	35
3.3	Summary of Seyfert Galaxy Properties	58
4	Discussion of Control Galaxies	66
4.1	Introduction	66
4.2	Analysis	66
4.2.1	The Galaxies	66
4.3	Summary of Control Galaxy Properties	100
5	Comparison Between Seyfert and Control Galaxies	112
5.1	Introduction	112
5.2	Distribution of Host Galaxy Properties	113
5.2.1	Host Galaxies	113

5.2.2	Distribution of Fitted Parameters	117
5.3	Distribution of Environmental Properties	121
5.3.1	Properties Derived from Companion Galaxy Data	121
5.3.2	Host Galaxy Morphological Disturbances	129
5.4	Summary	132
6	Conclusions	133
	Bibliography	138
A	Programs Used for Analysis	141
A.1	IRAF Packages	141
A.1.1	Imexamine	141
A.1.2	STSDAS/Isophote/Ellipse	142
A.1.3	Imedit	143
A.1.4	Imarith	144
A.1.5	Gauss	144
A.2	User-Supplied Programs	144
A.2.1	galprof and splitprof	145
A.2.2	raddist	146
B	Ellipticity and Position Angle Plots	148
B.1	Seyfert Data Set	148
B.2	Control Data Set	148

List of Tables

1.1	Luminosities of various objects	5
2.1	Apparent magnitude transformation coefficients	21
3.1	Basic properties of Seyfert galaxy dataset	60
3.2	Seyfert galaxy image statistics	61
3.3	Ellipse parameters for the Seyfert galaxies	62
3.4	surface-brightness profile parameters for the Seyfert galaxies	63
3.5	surface-brightness profile parameters for the Seyfert galaxies, method II	64
3.6	Distance/luminosity parameters for the Seyfert galaxies	65
4.1	Basic properties of control galaxy dataset	102
4.1	continued	103
4.2	Control galaxy image statistics	104
4.2	continued	105
4.3	Ellipse parameters for the control galaxies	106
4.3	continued	107
4.4	surface-brightness profile parameters for the control galaxies	108
4.4	continued	109
4.5	Distance/luminosity parameters for the control galaxies	110
4.5	continued	111
5.1	Seyfert hosts: bars, rings and distortions	130
5.2	Control hosts: bars, rings and distortions	131
5.3	Frequency of bars, rings and distortions	131

List of Figures

1.1	An Elliptical galaxy	2
1.2	A Spiral galaxy	2
1.3	A Seyfert galaxy	2
1.4	Sample Seyfert spectra	7
1.5	AGN illustration	9
1.6	Seyfert orientation	10
2.1	Detector Quantum Efficiency (DQE) plot for Tek2048	18
2.2	Sample deblending of NGC 5541, I	26
2.3	Sample deblending of NGC 5541, B_1	26
2.4	Sample deblending of NGC 5541, A_1	26
2.5	Sample deblending of NGC 5541, A_2	26
2.6	1-D example of unsharp-masking	30
2.7	Sample unsharp-masked image of NGC 5289	32
2.8	Sample unsharp-masked image of NGC 3968	32
2.9	Sample unsharp-masked image of NGC 4172	32
2.10	Sample unsharp-masked image of NGC 6111	32
3.1	Intensity contour map of Mrk 0231	36
3.2	Radial profile and fit of Mrk 0231	36
3.3	Intensity contour map of Mrk 0461	36
3.4	Radial profile and fit of Mrk 0461	36
3.5	Intensity contour map of Mrk 0471	37
3.6	Radial profile and fit of Mrk 0471	37
3.7	Intensity contour map of Mrk 0789	38
3.8	Radial profile and fit of Mrk 0789	38
3.9	Intensity contour map of Mrk 0817	38

3.10	Radial profile and fit of Mrk 0817	38
3.11	Intensity contour map of Mrk 0841	39
3.12	Radial profile and fit of Mrk 0841	39
3.13	Intensity contour map of UGC 06100	40
3.14	Radial profile and fit of UGC 06100	40
3.15	Intensity contour map of UGC 08621	40
3.16	Radial profile and fit of UGC 08621	40
3.17	Intensity contour map of NGC 3080	41
3.18	Radial profile and fit of NGC 3080	41
3.19	Intensity contour map of NGC 3227	42
3.20	Radial profile and fit of NGC 3227	42
3.21	Intensity contour map of NGC 3362	42
3.22	Radial profile and fit of NGC 3362	42
3.23	Intensity contour map of NGC 3516	43
3.24	Radial profile and fit of NGC 3516	43
3.25	Intensity contour map of NGC 3718	44
3.26	Radial profile and fit of NGC 3718	44
3.27	Intensity contour map of NGC 3786	45
3.28	Radial profile and fit of NGC 3786	45
3.29	Intensity contour map of NGC 3982	45
3.30	Radial profile and fit of NGC 3982	45
3.31	Intensity contour map of NGC 4051	46
3.32	Radial profile and fit of NGC 4051	46
3.33	Intensity contour map of NGC 4151	47
3.34	Radial profile and fit of NGC 4151	47
3.35	Intensity contour map of NGC 4235	48
3.36	Radial profile and fit of NGC 4235	48
3.37	Intensity contour map of NGC 4253	48
3.38	Radial profile and fit of NGC 4253	48
3.39	Intensity contour map of NGC 4388	49
3.40	Radial profile and fit of NGC 4388	49
3.41	Intensity contour map of NGC 5252	50

3.42	Radial profile and fit of NGC 5252	50
3.43	Intensity contour map of NGC 5256	51
3.44	Intensity contour map of NGC 5273	51
3.45	Radial profile and fit of NGC 5273	51
3.46	Intensity contour map of NGC 5283	52
3.47	Radial profile and fit of NGC 5283	52
3.48	Intensity contour map of NGC 5347	53
3.49	Radial profile and fit of NGC 5347	53
3.50	Intensity contour map of NGC 5548	54
3.51	Radial profile and fit of NGC 5548	54
3.52	Intensity contour map of NGC 5674	54
3.53	Radial profile and fit of NGC 5674	54
3.54	Intensity contour map of NGC 5695	55
3.55	Radial profile and fit of NGC 5695	55
3.56	Intensity contour map of NGC 5929	56
3.57	Radial profile and fit of NGC 5929	56
3.58	Intensity contour map of NGC 5940	57
3.59	Radial profile and fit of NGC 5940	57
3.60	Intensity contour map of NGC 6104	57
3.61	Intensity contour map of NGC 6814	58
3.62	Radial profile and fit of NGC 6814	58
4.1	Intensity contour map of UGC 05734	67
4.2	Radial profile and fit of UGC 05734	67
4.3	Intensity contour map of UGC 07064	68
4.4	Radial profile and fit of UGC 07064	68
4.5	Intensity contour map of UGC 09295	68
4.6	Radial profile and fit of UGC 09295	68
4.7	Intensity contour map of UGC 10097	69
4.8	Radial profile and fit of UGC 10097	69
4.9	Intensity contour map of UGC 10407	70
4.10	Intensity contour map of UGC 11865	70
4.11	Radial profile and fit of UGC 11865	70

4.12	Intensity contour map of IC 875	71
4.13	Radial profile and fit of IC 875	71
4.14	Intensity contour map of IC 1141	72
4.15	Radial profile and fit of IC 1141	72
4.16	Intensity contour map of NGC 3169	73
4.17	Radial profile and fit of NGC 3169	73
4.18	Intensity contour map of NGC 3492	73
4.19	Radial profile and fit of NGC 3492	73
4.20	Intensity contour map of NGC 3756	74
4.21	Radial profile and fit of NGC 3756	74
4.22	Intensity contour map of NGC 3825	75
4.23	Radial profile and fit of NGC 3825	75
4.24	Intensity contour map of NGC 3938	76
4.25	Radial profile and fit of NGC 3938	76
4.26	Intensity contour map of NGC 3968	76
4.27	Radial profile and fit of NGC 3968	76
4.28	Intensity contour map of NGC 4045	77
4.29	Radial profile and fit of NGC 4045	77
4.30	Intensity contour map of NGC 4048	78
4.31	Radial profile and fit of NGC 4048	78
4.32	Intensity contour map of NGC 4088	78
4.33	Radial profile and fit of NGC 4088	78
4.34	Intensity contour map of NGC 4172	79
4.35	Radial profile and fit of NGC 4172	79
4.36	Intensity contour map of NGC 4224	80
4.37	Radial profile and fit of NGC 4224	80
4.38	Intensity contour map of NGC 4352	81
4.39	Radial profile and fit of NGC 4352	81
4.40	Intensity contour map of NGC 4375	81
4.41	Radial profile and fit of NGC 4375	81
4.42	Intensity contour map of NGC 4477	82
4.43	Radial profile and fit of NGC 4477	82

4.44	Intensity contour map of NGC 4799	83
4.45	Radial profile and fit of NGC 4799	83
4.46	Intensity contour map of NGC 4944	83
4.47	Radial profile and fit of NGC 4944	83
4.48	Intensity contour map of NGC 4954	84
4.49	Radial profile and fit of NGC 4954	84
4.50	Intensity contour map of NGC 5289	85
4.51	Radial profile and fit of NGC 5289	85
4.52	Intensity contour map of NGC 5375	85
4.53	Radial profile and fit of NGC 5375	85
4.54	Intensity contour map of NGC 5505	86
4.55	Radial profile and fit of NGC 5505	86
4.56	Intensity contour map of NGC 5515	87
4.57	Radial profile and fit of NGC 5515	87
4.58	Intensity contour map of NGC 5541	87
4.59	Radial profile and fit of NGC 5541	87
4.60	Intensity contour map of NGC 5603	88
4.61	Radial profile and fit of NGC 5603	88
4.62	Intensity contour map of NGC 5644	89
4.63	Radial profile and fit of NGC 5644	89
4.64	Intensity contour map of NGC 5690	90
4.65	Radial profile and fit of NGC 5690	90
4.66	Intensity contour map of NGC 5772	90
4.67	Radial profile and fit of NGC 5772	90
4.68	Intensity contour map of NGC 5806	91
4.69	Radial profile and fit of NGC 5806	91
4.70	Intensity contour map of NGC 5876	92
4.71	Radial profile and fit of NGC 5876	92
4.72	Intensity contour map of NGC 5908	92
4.73	Radial profile and fit of NGC 5908	92
4.74	Intensity contour map of NGC 5957	93
4.75	Radial profile and fit of NGC 5957	93

4.76	Intensity contour map of NGC 5980	94
4.77	Radial profile and fit of NGC 5980	94
4.78	Intensity contour map of NGC 6001	94
4.79	Radial profile and fit of NGC 6001	94
4.80	Intensity contour map of NGC 6014	95
4.81	Radial profile and fit of NGC 6014	95
4.82	Intensity contour map of NGC 6030	96
4.83	Radial profile and fit of NGC 6030	96
4.84	Intensity contour map of NGC 6085	96
4.85	Radial profile and fit of NGC 6085	96
4.86	Intensity contour map of NGC 6111	97
4.87	Radial profile and fit of NGC 6111	97
4.88	Intensity contour map of NGC 6126	98
4.89	Radial profile and fit of NGC 6126	98
4.90	Intensity contour map of NGC 6143	98
4.91	Radial profile and fit of NGC 6143	98
4.92	Intensity contour map of NGC 6155	99
4.93	Radial profile and fit of NGC 6155	99
4.94	Intensity contour map of NGC 6196	100
4.95	Radial profile and fit of NGC 6196	100
4.96	Intensity contour map of NGC 6764	101
4.97	Radial profile and fit of NGC 6764	101
5.1	Distribution of host redshift	114
5.2	Distribution of host distances	115
5.3	Distribution of host apparent magnitudes	115
5.4	Distribution of host absolute magnitudes	116
5.5	Distribution of host ellipticities	116
5.6	Distribution of disk scale radii	117
5.7	Distribution of bulge effective radii	118
5.8	Distribution of disk surface brightness	119
5.9	Distribution of bulge surface brightness	120
5.10	Number of companions around host	122

5.11	Distribution of companion separation distances	123
5.12	Distribution of companion position angles	124
5.13	Distribution of companion apparent magnitudes	125
5.14	Δmag between host and companion	126
5.15	Distribution of companion absolute magnitudes	126
5.16	Companion galaxy luminosities	127
5.17	Companion galaxy tidal parameters	127
5.18	Host galaxy tidal parameters	128
B.1	Ellipticity (Eps) and position angles (PA) of Mrk 0461, Mrk 0817 and NGC 3080	149
B.2	Eps and PA of Mrk 0471, UGC 06100 and NGC 3516	150
B.3	Eps and PA of Mrk 0231, NGC 3362, NGC 5548 and NGC 6814 . .	151
B.4	Eps and PA of Mrk 0789, NGC 3786, NGC 5252 and NGC 5347 . .	152
B.5	Eps and PA of NGC 3982, NGC 4151, NGC 4253 and NGC 5695 . .	153
B.6	Eps and PA of NGC 3227, NGC 5674, NGC 5929 and NGC 5940 . .	154
B.7	Eps and PA of NGC 3718, NGC 4051, NGC 4235 and NGC 4388 . .	155
B.8	Eps and PA of Mrk 0841, UGC 08621, NGC 5273 and NGC 5283 . .	156
B.9	Eps and PA of IC 875, NGC 3492, NGC 6155 and NGC 6196	157
B.10	Eps and PA of NGC 4172, NGC 4375, NGC 4477 and NGC 6014 . .	158
B.11	Eps and PA of UGC 09295, IC 1141, NGC 3169 and NGC 6030 . . .	159
B.12	Eps and PA of UGC 07064, UGC 10097 and NGC 3938	160
B.13	Eps and PA of NGC 4045, NGC 6001 and NGC 6085	161
B.14	Eps and PA of NGC 4352, NGC 5515, NGC 5806 and NGC 6111 . .	162
B.15	Eps and PA of NGC 4954, NGC 5772, NGC 5876 and NGC 5980 . .	163
B.16	Eps and PA of NGC 3756, NGC 5375, NGC 5541 and NGC 6143 . .	164
B.17	Eps and PA of NGC 3825, NGC 3968, NGC 4224 and NGC 5957 . .	165
B.18	Eps and PA of NGC 4088, NGC 4799, NGC 4944 and NGC 5289 . .	166
B.19	Eps and PA of NGC 4048, NGC 5505, NGC 5690 and NGC 5908 . .	167
B.20	Eps and PA of UGC 05734, NGC 4472 and NGC 6764	168
B.21	Eps and PA of UGC 11865, NGC 5603, NGC 5644 and NGC 6126 .	169

Chapter 1

Introduction

1.1 Overview

This thesis will compare the environmental and host-galaxy properties of a sample of Seyfert galaxies with a control sample of non-active spiral galaxies. In order to introduce this study, I will provide general background information on galaxies in Section 1.2, discussing relevant properties of both spiral galaxies and active galaxies along with their “central engines”. Section 1.3 will then provide detailed information about Seyfert galaxies and their properties. The Seyfert discussion will then lead into a description of the Unified Model of active galaxies (of which Seyfert galaxies are a member) in Section 1.3.2 followed by Section 1.3.3 which describes the triggering mechanism via the interaction/merger hypothesis. Finally, Section 1.4 will describe the objective of this thesis including a discussion of previous work in this field. Following this introductory chapter, Chapter 2 will describe the reduction and analysis techniques used in this study. Chapters 3 and 4 will present the results for both the Seyfert and control samples respectively. Chapter 5 will then discuss the comparison of the Seyfert and control-sample environments, followed by conclusions in Chapter 6.

1.2 Galaxies

Galaxies are the largest individual assemblages of stars, gas, and dust in the universe and have been recognized as such only since the 1920s. During this period, Edwin Hubble devised a classification scheme consisting of elliptical, spiral, and irregular galaxies. Since then other (sub)types of galaxies have been discovered such as lenticulars, dwarfs, and active galaxies, and more detailed classification schemes have been devised (e.g., de Vaucouleurs 1959). The following presents an example of an elliptical, spiral, and active galaxy: Figure 1.1 shows a fairly typical elliptical galaxy, M84, which is a member galaxy of the Virgo cluster; note the lack of structure in the galaxy. Figure 1.2 shows a face-on normal spiral galaxy, M74, found in Pisces; note the nucleus and the spiral arms that wind out from the core. Figure 1.3 presents a well studied active galaxy, the Seyfert galaxy NGC 4151, which is a spiral galaxy that also contains a very bright star-like nucleus. In the following sections, spiral galaxies and active galaxies (with an emphasis on Seyfert galaxies) will be discussed.

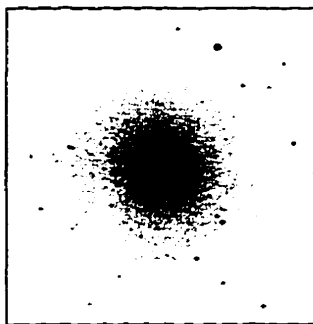


Figure 1.1: Elliptical galaxy M84

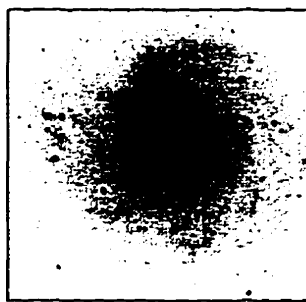


Figure 1.2: Spiral galaxy M74

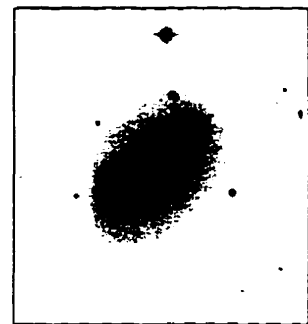


Figure 1.3: Seyfert Galaxy NGC 4151

1.2.1 Spiral Galaxies

Typical spiral galaxies consist of several components. The most notable components are a spheroidal bulge of stars and an exponential disk of stars (as well as gas and dust). A halo of old stars and globular clusters also surrounds a spiral galaxy (the halo may be an extension of the bulge). A large spiral galaxy has a diameter of 30 kpc and a thickness 2-5 kpc perpendicular to the plane of the disk. The bulge is made primarily of older, red stars which formed early in the galaxy's history. Spheroidal bulges of spiral galaxies are very similar to elliptical galaxies, in which the intensity or surface-brightness profile has been modeled by a number of functional forms including those devised by Hubble (1930), King (1966), and de Vaucouleurs (1948). Surface Brightness is a measure of brightness (intensity) per unit area. In general, a de Vaucouleurs's $r^{1/4}$ law is the most commonly used form for bulges (see Section 2.4.3 for the mathematical form of this law). The disk component of a spiral galaxy contains young stars, and material in the form of gas and dust. The intensity profile of the disk has been modeled well as an exponential by Freeman (1970) (see Section 2.4.3 for the equation), though there can be significant deviations from this law due to the presence of spiral arms, bars, rings, discrete star formation regions, and so on. One of the more spectacular features of a spiral galaxy is its spiral arms which contain enhanced star-formation regions and young, luminous O and B type stars.

Bars and rings are common "azimuthal asymmetries" which may also occur within a spiral galaxy. A bar is an elongated region of stellar and interstellar material centered on the nucleus with a nearly constant intensity profile along its major axis. Bars will be mentioned further in Section 1.3. A ring is often a region of increased star-formation at approximately a constant radius from the nucleus, and can occur in the

form of inner or outer rings. Both bars and rings can occasionally be manifestations of a recent galaxy-galaxy interaction, and so will be further discussed in Section 1.3.

1.2.2 Active Galaxies

The radiation of AGNs is primarily non-thermal in nature, which means it cannot be explained solely by stellar processes, including supernovae. Since much of the total luminosity in active galaxies comes from their nuclei they are referred-to as active galactic nuclei (AGN); these nuclei can be more luminous than the galaxy itself. Table 1.1 presents some sample order-of-magnitude luminosities of various objects. There are several classes of AGNs, ranging from QSOs to radio galaxies, Blazars, Seyferts, and LINERs (Low Ionization Nuclear Emission-line Region galaxies). QSOs are very luminous compact objects found at relatively high redshifts (large distances) and were originally observed to be very point-like, similarly to a star (hence the name: Quasi Stellar Object, or QSO for short). Radio galaxies and Blazars (a name coined for both BL Lac objects and Optically Violently Variable Quasars (OVVs)) are another type of active galaxy found predominantly as elliptical galaxies. Radio galaxies are perhaps not quite as luminous as QSOs, but they can have very radio-loud nuclei and often large radio lobes found well outside the optical galaxy which are fueled by jets of material emanating from the nucleus. Seyfert galaxies have moderate luminosities for AGNs but have spatial densities $\sim 10^2$ times greater than QSOs making them much easier to study in detail. Seyfert galaxies are found almost exclusively as spiral galaxies. At the low-luminosity end of the activity class are LINERs which have occasionally been called mini-Seyferts (Robson 1996), since they also occur primarily within spiral galaxies.

Table 1.1: Luminosities of various objects

Object	Total Luminosity	
Sun	$1 L_{\odot}$	10^{26} W
typical galaxy	$10^{10} L_{\odot}$	10^{36} W
LINER	$\lesssim 10^{10} L_{\odot}$	10^{36} W
Seyfert	$10^{11} L_{\odot}$	10^{37} W
QSO	$\gtrsim 10^{12} L_{\odot}$	10^{38} W

1.2.2.1 Active Galactic Nuclei

A question that comes to mind then is, “where is this extra luminosity coming from in AGN?” or “what powers an active galaxy?”. In general AGNs show some or all of the following properties:

1. Very high luminosity from an unresolved nucleus.
2. Non-thermal radiation which cannot be explained solely by stellar processes.
3. Significant variability on relatively short time-scales of days to weeks, indicating that the emission is originating from a region smaller than a light-week.
4. High ionization emission lines from material moving at high velocities within this small region.
5. Jets, lobes, and other explosive material being emitted from this region (found only in some AGNs).

The current leading theory to explain the power source of AGNs involves the accretion of gas onto a supermassive black hole (SBH) at their galactic centers. The mass of such an object is estimated to be $10^7\text{--}9 M_{\odot}$, and so the SBH has a Schwarzschild radius of $0.1 - 10 \text{ AU}$. This SBH is fed by a surrounding accretion disk, and in order to support the luminosity of an active galaxy, the SBH must sustain an accretion rate of approximately $0.1 - 1 M_{\odot} \text{ yr}^{-1}$. A key problem in AGN research involves the origin

of this gaseous material and how it fuels the accretion disk, as well as determining the length of time for which such activity lasts.

In summary, there are several classes of active galaxies, all of which are powered by an accreting supermassive black hole. I will now focus on one class of active galaxy: Seyfert galaxies.

1.3 Seyfert Galaxies

Seyfert galaxies are a class of active galaxy discovered by Carl Seyfert in the 1940s. Galaxies which exhibited broad emission lines were selected for his study (emission lines are absent in normal galaxies). These galaxies are also predominantly spiral galaxies, and contain a very bright and star-like core (Seyfert 1943; Seyfert 1947).

1.3.1 Properties and Types

As mentioned earlier, Seyfert galaxies are a separate class of AGN with moderate luminosity, appearing almost exclusively as spiral galaxies. They are noted for an unusually bright nucleus which appears star-like, as well as containing high-ionization emission lines (this is not the case for normal galaxies). Optical spectra of a Seyfert galaxy contain permitted emission lines from hydrogen as well as He I, He II (neutral and singly ionized helium), and Fe II; there is also the presence of forbidden lines from species such as [O I], [O II], [O III], [N II], [S II], [Fe VII], and [Fe X].

Based on their optical spectra, Seyfert galaxies are classified as Type 1 or Type 2. Figure 1.4 shows some sample spectra for both types of Seyferts in their observed frames with their major features labeled. The Seyfert 1 spectrum is presented in the top panel (NGC 7469), and the Seyfert 2 spectrum is in the middle panel (NGC 1388). In both cases, the lower curve represents the entire spectrum, while the upper curve is

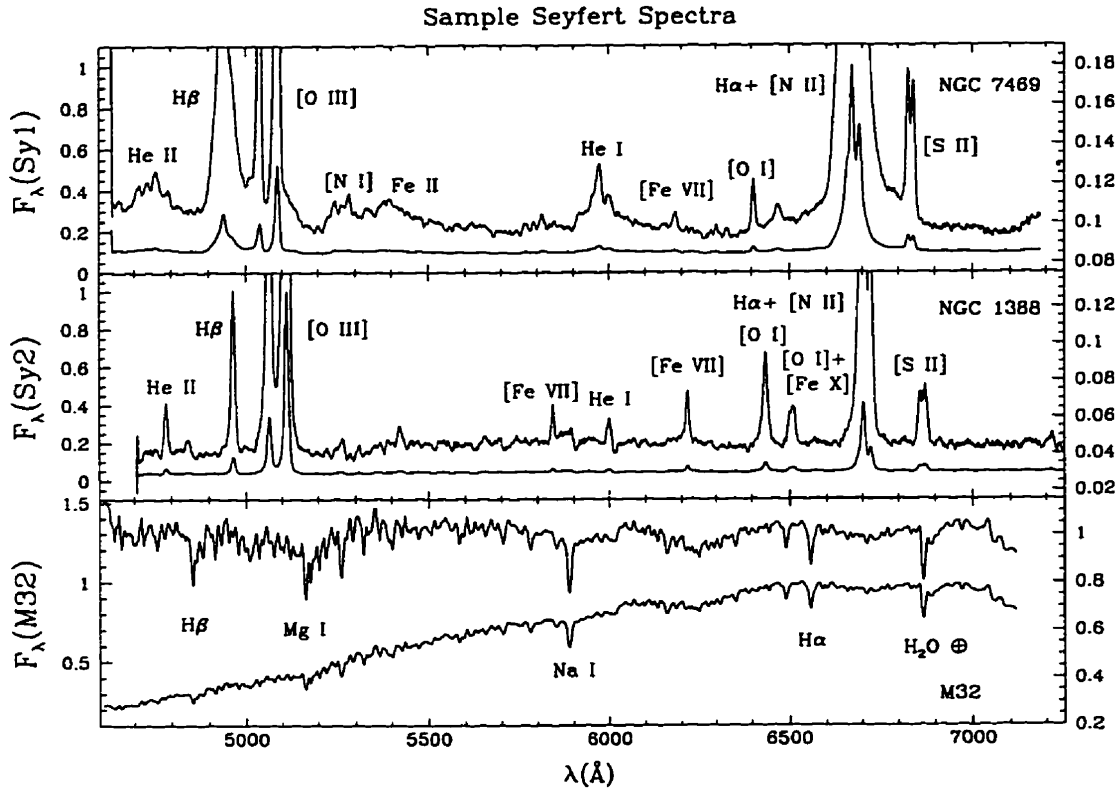


Figure 1.4: Sample spectra of Type 1 and 2 Seyfert galaxies and a normal galaxy

an expanded view to enhance the lower-intensity features. The bottom panel displays a normal galaxy (M32) for comparison. In this panel the lower curve is the galaxy's spectrum and the upper curve is the spectrum with a smooth continuum level divided out. These differences will be discussed further in Sections 1.3.1.1 and 1.3.1.2.

1.3.1.1 Seyfert 1

Type 1 Seyferts are characterized by having very broad permitted lines, with velocity widths in the range $1,000 - 10,000 \text{ km s}^{-1}$. The forbidden lines are narrower, with velocities $\lesssim 1,000 \text{ km s}^{-1}$. The broad lines are believed to come from a region of the

AGN which is located $\lesssim 1$ pc from the SBH. The narrow lines are thought to originate in a region surrounding the central “engine” at a distance of 10–100 pc.

1.3.1.2 Seyfert 2

In Type 2 Seyferts, both the permitted lines and the forbidden lines have similar widths, corresponding to velocities $\lesssim 1,000$ km s⁻¹. It is thought in this case that both lines originate in the region of the AGN, 10–100 pc distant from the SBH (depending on the intrinsic luminosity of the source).

1.3.1.3 Fractional Types

There are also sub-classes of Seyfert galaxies based on their spectra. The categories now recognized are types 1, 1.5, 1.8, 1.9, and 2. Type 1.5’s are galaxies in which the permitted lines contain both a broad component and a narrow component. Types 1.8 and 1.9 have mainly narrow permitted lines with a weaker broad component in the H α and H β lines. For the remainder of this thesis, I will refer to Seyfert 1s as consisting of types 1 and 1.5, and Seyfert 2s as consisting of types 1.8, 1.9, and 2.

1.3.2 Unified Model

In the past decade the so-called Unified Model has emerged which attempts to describe both broad-lined and narrow-lined AGN using a single model. Figure 1.5 shows the Unified-Model view of a hypothetical AGN at various scales, which I will now describe. (This Figure was adapted from Robson (1996), which was in turn adapted from Blandford, Netzer, and Woltjer 1990). At the very center of the AGN (10^{-4} pc or 20 AU) is a rotating SBH, which is surrounded by a thin, radiating accretion disk. The accretion-disk region is surrounded by fast-moving broad-line emission clouds (called the Broad-Line Region (BLR)), which extend from 10^{-3} pc out to 1 pc. The

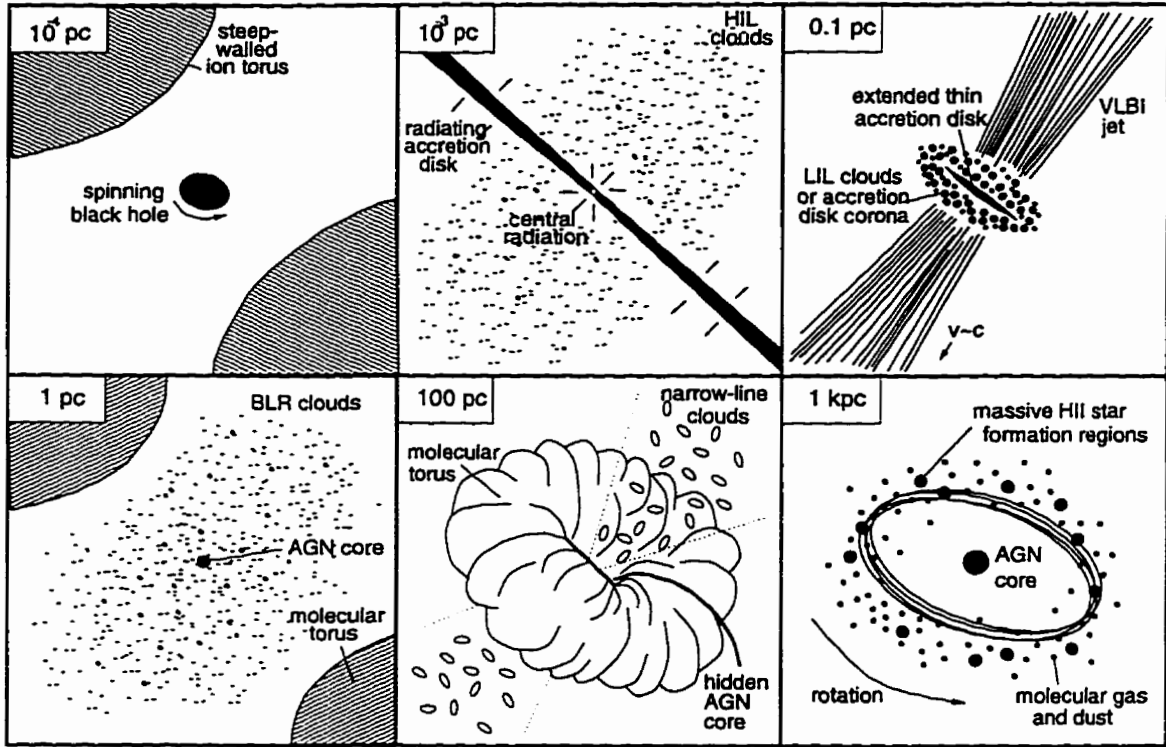


Figure 1.5: An illustration of AGN at various scales

BLR has typical velocity widths of 5000 km s^{-1} , as mentioned earlier. Closest to the SBH, the BLR is ionized by the central radiation, producing High-Ionization Line (HIL) clouds, which change into a Low-Ionization Line (LIL) region that is radiated by the extended accretion disk at the 0.1 pc scale. Moving outwards to 100 pc, we find that the BLR is surrounded by a torus of molecular gas and “low” velocity narrow-line clouds (called the Narrow-Line Region (NLR)), with a typical velocity of 500 km s^{-1} . The molecular torus is an obscuring cloud of material which can effectively hide the AGN core and BLR from sight under certain viewing angles. Beyond the molecular torus at the 1 kpc distance scale is a disk of molecular gas and dust which contains massive H II star-formation regions. These star-formation regions may be “fed” by a bar just outside this zone.

According to the Unified theories, the main distinction between Seyfert 1s and 2s arises from the viewing angle (i.e. the inclination of the torus to the line of sight), and depends on the opening angle created by the molecular torus (Figure 1.6 contains a schematic representation of this). In Seyfert 1s, the line-of-sight is perpendicular to the torus and thus the BLR can be seen; but in Seyfert 2s, the molecular torus obscures the BLR, so only the NLR is visible (Osterbrock 1989; Osterbrock 1993; Kukula et al. 1994; Robson 1996; Antonucci 1993). Lending support to the Unified theory is the observation that some Seyfert 2s can appear to possess a BLR (type 1 spectra) when observed in polarized light (Antonucci and Miller 1985); the BLR emission is reflected (and thus polarized) by material between the NLR clouds. With the Hubble Space Telescope (HST), it is hoped that images of the molecular torus in nearby AGNs will be acquired (Ward 1996), lending further support to the Unified Model.

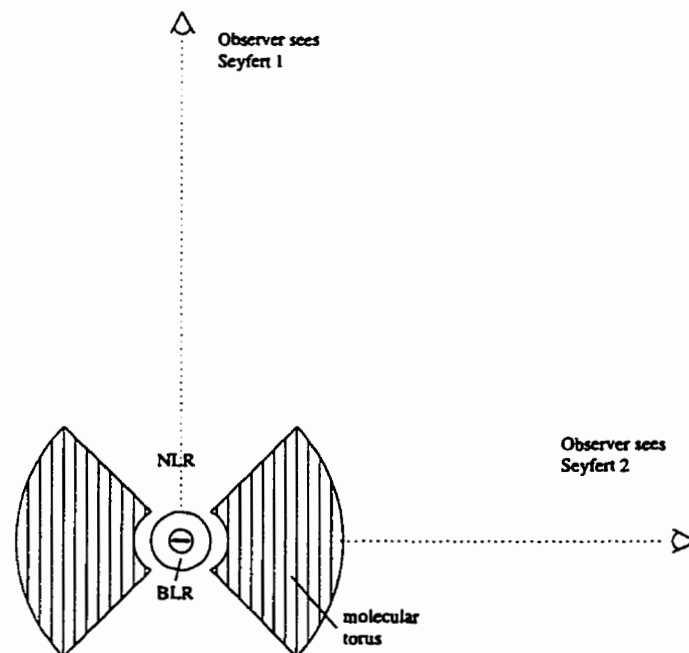


Figure 1.6: Seyfert orientation

1.3.3 Interaction/Merger Hypothesis

As noted in Section 1.2.2.1, fueling the AGN “monster” presents one of the greatest outstanding challenges to extragalactic astronomy. As seen in the Unified Model, gas falling into the SBH radiates gravitational potential energy, producing the required luminosity. What must be addressed is the mechanism by which the fuel is brought to the central region. An attractive theory which explains this involves gas losing angular momentum within a non-axisymmetric gravitational potential (Barnes and Hernquist 1991), though the question still remains of where this gas comes from. The “interaction/merger hypothesis” indicates that either directly (Bekki and Noguchi 1994) or indirectly (Barnes and Hernquist 1991), initiation of activity is caused by a perturbation by an interaction or merger with a companion galaxy. In the direct case, an actual merger may take place, in which material is transferred or tidally stripped from a companion object; this method would be required for a host without a sufficient gas supply of its own. In the indirect case, it is sufficient to simply perturb the host galaxy so that its own supply of gas will initiate activity. Bars in galaxies are an efficient way of transporting gas to central regions, and these can be produced from a perturbing interaction. In either case, the current theory suggests that the triggering of Seyfert activity is caused by galaxy-galaxy interactions involving two galaxies of comparable mass. This would suggest that the environment of Seyfert galaxies should be richer than the environment of the control sample.

There have been a variety of studies that have examined the triggering mechanism in AGNs. The theoretical groundwork was established by Toomre and Toomre (1972) and an environmental relation was first suggested by Adams (1977) using observational evidence for the case of Seyfert galaxies. Since this pioneering work, there have

been a number of analyses in more recent times that continue to probe this question. For example, Nesci (1986) examined the frequency of Seyfert galaxies in galaxy clusters and determined that they are found in open to medium clusters but not in compact clusters, and similarly that they are more commonly found in the outskirts of the cluster rather than the inner regions. McLeod and Rieke (1995) investigated the frequency of bars and rings in Seyfert galaxies in order to study the triggering mechanism. AGN triggering has also been examined by observing the orbital and kinematic clues of Seyfert galaxies and their companions by Keel (1996).

1.3.4 Objective

This thesis will attempt to test the interaction hypothesis. To accomplish this, the environments of Seyfert galaxies and a control set of normal galaxies will be examined for recent interactions or perturbations. This environmental examination involves searching for companion galaxies around the hosts and light asymmetries of the hosts which may be indicative of a recent interaction.

1.4 Thesis Objective

The nearby environments of Seyfert galaxies as well as a control sample of normal galaxies will be examined in order to test the interaction hypothesis. Many studies have been undertaken to address this question, though most of these were based on the Palomar Observatory Sky Survey (POSS), which possesses inherent problems for analysis. To accomplish this, and avoid the problems with the POSS, CCD data were acquired for a sample of 32 Seyfert galaxies and a control sample of 49 normal galaxies. In order to minimize possible selection effects, the two sample sets have been well matched in redshift, luminosity, and morphological type. This thesis will

accomplish two tasks: determine whether the control sample can in fact be fairly compared with the Seyfert sample and then examine and compare the environments of the two samples in order to test the interaction model. Testing the interaction model with these data involves a variety of tasks: finding optical companion galaxies to the host galaxies, examining the hosts' surface-brightness profiles as well as their ellipticity and position-angle profiles, and determining the frequency of morphological features such as bars, rings, and tidal tails. Before describing these analysis techniques in detail (Chapter 2), I will discuss previous studies which have attempted to test the interaction model.

1.4.1 Previous Work

Several others have compared Seyfert galaxies and non-active galaxies and studied their environments. These studies often involve determining the frequency of companion galaxies around the host galaxies.

Dahari (1984, 1985) used the POSS to examine the frequency of companion galaxies around Seyfert galaxies using a sample of 93 Seyfert galaxies and a control sample of 279 galaxies. The selection of his control sample was without regard to morphological type or redshift, but was based on large galaxies that were nearby on the same POSS plate. Dahari used galaxy counts from Shane (1975) to account for contamination by background galaxies and thus statistically derive the number of physical companions. Using this technique, he detected a significant excess of close physical companions around Seyfert galaxies compared to his control sample.

Fuentes-Williams and Stocke (1988) (FWS) also undertook a similar analysis using the POSS but chose a control sample that matched the morphology and luminosity of the Seyfert sample. They measured and counted the number of companion galaxies within a specified angular distance of each of the 53 Seyfert galaxies and 30 control

galaxies. They determined that there is only a marginal excess of bright companions around Seyfert galaxies, but that there is an excess of faint companions (though not as large as the excess found by Dahari).

Rafanelli, Violato, and Baruffolo (1995) repeated Dahari's type of analysis using 99 Seyfert 1 and 98 Seyfert 2 galaxies and a control sample of 197 galaxies. Their control sample was chosen by using a spiral galaxy near each Seyfert. Their findings were similar to Dahari's in that the Seyfert galaxies had a statistical excess of physical companions.

A detailed and extensive study using the POSS was undertaken by Laurikainen and Salo (1995). Their sample consisted of 104 Seyfert galaxies and 138 control galaxies. They paid careful attention to the selection of the control sample and attempted to understand the biases that would be introduced depending on the selection criteria. They repeated Dahari-type tests and FWS-type tests with their data, and in both cases found an excess of companions around Seyfert galaxies. However, their own analysis revealed only a marginal excess of companions which were concentrated around the Seyfert 2s, implying that Seyfert 1s and 2s are in different environments.

Other similar surveys have been performed by MacKenty (1989, 1990) and Keel et al. (1985) for example, who find an excess of companions around Seyfert galaxies. As noted above, there are a few who do not find an excess of companions, and so no consensus has yet been reached regarding the interaction hypothesis as it relates to Seyfert galaxies.

Chapter 2

Observations and Reduction Techniques

2.1 Introduction

This chapter will describe the acquisition of the data, as well as the reduction, processing, and analysis techniques that were used to extract information about the galaxies. This discussion is split into three parts. Section 2.2 will discuss the acquisition of the data. Section 2.3 will describe the pre-processing of the images. The analysis techniques used to analyze the data are described in Section 2.4.

2.2 Observations

Images were obtained of the Seyfert galaxies and the control galaxies in the Johnson B-band and R-band using the 0.9-m telescope at Kitt Peak National Observatory (KPNO). The telescope consists of a 0.9 meter primary mirror with a focal ratio of $f/7.5$. The data were taken on May 16-24, 1991 UT by M.M. DeRobertis and were transferred to 8mm Exabyte tapes for transport and analysis.

2.2.1 Selection of Seyfert Galaxies and Control Galaxies

For this survey, 32 Seyfert galaxies and a sample of 49 control galaxies were chosen. All galaxies were selected from the Center for Astrophysics (CfA) Redshift Survey (Huchra and Burg 1992), which is spectroscopically complete to magnitude 14.5 in the appropriate sky regions. Laurikainen et al. (1994) note that biases which are not easily understood could be introduced into the analysis if the Seyfert sample and the control sample are not well matched in redshift, morphological type, and luminosity. To minimize the selection effects of our data, for each Seyfert galaxy one or two control galaxies were selected from the CfA survey and were well matched to the Seyfert in terms of redshift, morphology, and absolute magnitude. By minimizing the differences between the two samples, it was hoped that a meaningful comparison of their environments would be possible.

2.2.2 Charge-Coupled Devices

A charge-coupled device (CCD) was used for acquiring the data. A CCD is a photoelectric device that is made of silicon (or other similar semiconducting material) and is divided into a 2-dimensional array of pixels. When a photon is absorbed in a pixel, an electron is freed and accumulates in a potential well created by an applied voltage on the front side of the chip during the exposure. An image is formed by collecting the electrons stored in each pixel at read-out. CCDs typically contain millions of square pixels. Each pixel subtends a solid angle on the sky which depends on the optics of the telescope. One of the most important aspects of CCDs is that their response to light is linear (i.e. 1 photon \leftrightarrow 1 electron), with Quantum Efficiencies (QE) typically $\sim 50-90\%$ over visible wavelengths.

CCDs are not perfect detectors. The data can be corrected for some of the inherent

imperfections, however. In the read-out process, noise is introduced while measuring the total charge in each pixel (this is called “read-noise”). Also added to the data is the bias, which is the instantaneous DC level of the chip’s electronics, as well as the dark current which arises from the thermal noise (although because these detectors are cryogenically cooled, the dark current is insignificant). There are also pixel-to-pixel QE variations across the chip which need to be corrected for, as well as trivial light variations caused by the opening and closing of the shutter. CCDs also have “cosmetic” defects (blocked columns) as well as “hot” pixels (which accumulate an excess charge) and “cold” pixels (which have a charge deficit). One of the most important limitations of CCDs is their limited dynamic range which can lead to saturated pixels (which can subsequently lead to “bleeding” of charge along columns below the saturated pixels). This limitation arises from the fact that most CCDs use a 15-bit Analog-to-Digital Converter (ADC), resulting in a dynamic range of $2^{15} \approx 32,000$ Analog-to-Digital Units (ADU). The translation of electrons into digital units is controlled by the “gain” of the chip, and so the full-well capacity of the detector is typically of order $10^5 e^-$. Thus an object brighter than this will result in saturation and bleeding (this is why care is taken in determining exposure times for observations).

2.2.3 Data Acquisition

Our data were acquired with a Tek2048 CCD. This device has a read-noise level of $13 e^-$ and a gain of $8.2 e^-/\text{ADU}$. The size of the chip is 2048×2048 pixels², but the unvignetted portion is 1700×2048 pixels², with a pixel size of $27 \mu\text{m}$; the image scale at the Cassegrain focus is $0.77 \text{ arcsec/pixel}$, yielding a field of view of $21 \times 26 \text{ arcmin}^2$. The detector is coated with Metachrome-2 to improve its blue sensitivity. See Figure 2.1 for a plot of the sensitivity of the detector as a function of wavelength

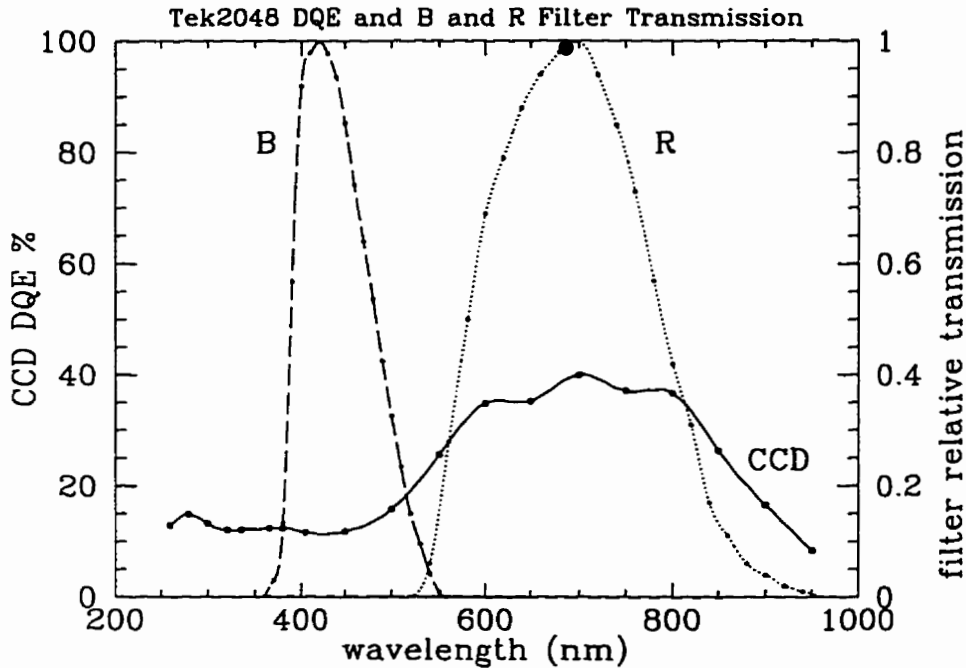


Figure 2.1: Detector Quantum Efficiency (DQE) plot for Tek2048

(solid curve).

The exposures relevant to this work were taken through the Johnson R-band filter, which is a “red” filter peaked at 700 nm with a full-width-half-max (FWHM) of 210 nm. Some images were also taken in B-band, a “blue” filter peaked at 420 nm with FWHM of 90 nm. Figure 2.1 shows the relative transmission curves of the R and B filters (dotted and long-dashed curves respectively).

2.3 Preliminary Reduction

Much of the preliminary reduction of the data was performed by K. Hayhoe and M.M. DeRobertis. The preprocessing, photometric calibration using standard stars, and measurement of the apparent magnitudes of the host galaxies were completed using a combination of Image Reduction and Analysis Facility (IRAF) and Picture

Processing Package (PPP) developed by Yee (1991).

2.3.1 CCD Pre-Processing in IRAF

CCD images require a certain amount of manipulation to correct for the detector's imperfections. These include removing the DC level of the exposure (bias frames), dark current due to thermal noise (dark frames), and high and low spatial frequency QE variations (flat frames). The bias level is determined by averaging a series of zero-second exposures. Dark current is accounted for by appropriately scaling a long exposure taken with the shutter closed. Pixel-to-pixel and large-scale QE variations across the chip can be removed with a flat field, which is a high-signal exposure of a uniformly illuminated reflective screen or the twilight sky (both of which were used in these reductions).

Taking these into account, the data were processed in the following manner. Each raw image was overscan-corrected by using a 5th order polynomial fit to the overscan region, thereby removing the DC level. An overscan region is a series of ~ 20 extra columns which are read out after the image buffer has been flushed, and thus contain the instantaneous DC level for that exposure. The actual bias images showed no 2-dimensional structure (they were flat) and so it was not necessary to subtract the bias frames. Based on a series of dark images taken throughout the night, the dark current was negligible for the relevant exposure times, and so was ignored. A series of dome flats and sky flats were also taken periodically during the observing run. These dome flats were averaged together and illumination-corrected using the sky flats. Quantum efficiency variations were corrected by dividing the data by the resulting flat-fields. This procedure is also described by DeRobertis, Hayhoe, and Yee (1997), and can be summed up in the following equation:

$$\text{Final Image} = \frac{\text{Raw Image} - \text{DC level}}{\text{Flat}(\text{dome, sky}) - \text{DC level}} \quad (2.1)$$

Since this thesis deals with the nearby environments of the program objects, the images were typically cropped to a size of 512×512 pixel² (or larger if necessary), with the host galaxy in the center of the frame. DeRobertis, Hayhoe, and Yee (1997), paper I, and DeRobertis, Yee, and Hayhoe (1997), paper II, utilized the uncropped images in order to study the large-scale environments of the galaxies.

2.3.2 Photometric Calibration

Once the program images have been pre-processed, they can be calibrated. This involves determining the transformation coefficients so that raw intensity counts can be converted to apparent magnitude or energy units as if the objects were observed above the atmosphere. The calibration was accomplished using Landolt (1992) standard stars. Images of 10–15 of these stars were taken throughout each night. The transformation coefficients were then calculated from the standard stars' instrumental magnitude using IRAF's `photcal` routines, with a calibration error of ± 0.07 magnitudes. Once these constants are known, magnitudes of any object in the images can be computed.

The instrumental magnitude, r , is defined in Equation 2.2, where f is the flux in counts, and t is the exposure time in seconds. The instrumental magnitude r is then transformed into an apparent magnitude R via Equation 2.3, where ξ is the zero-point correction, $k'X$ is the airmass term (k' is the extinction coefficient) due to the fact that as the object gets closer to the horizon (i.e. airmass, X , increases), its light suffers more atmospheric attenuation, and $\epsilon(B - R)$ is the colour term accounting for wavelength-dependent scattering caused by the atmosphere. Upon calibration, it was

found that nights 1-6 had approximately the same solutions, while nights 7 and 8 had a different solution. The computed transformation coefficients are given in Table 2.1. The $(B - R)$ colour was taken as a nominal +1.50 based on the average galaxy colour derived from the limited number of B and R images.

$$r = -2.5 \log(f/t) \quad (2.2)$$

$$R = r + \xi + k'X + \epsilon(B - R) \quad (2.3)$$

Table 2.1: Apparent magnitude transformation coefficients

Nights	ξ (mag)	k' (mag/ X)	ϵ	$(B - R)$ (mag)
1-6	20.38	-0.116	0.016	+1.50
7-8	20.42	-0.132	0.079	+1.50

2.3.3 Host-Galaxy Magnitudes

Once the transformation coefficients have been computed, the apparent magnitudes of the host galaxies may be measured. This step was accomplished with PPP using circular apertures and an appropriately sized sky-background annulus. The galaxy's magnitude converged to a couple of hundredths of a magnitude within these apertures. Light from foreground stars was subtracted from the galaxy's integrated magnitude if the star was within the galaxy's aperture, and the magnitudes were corrected for Galactic absorption (as provided by the NASA/IPAC Extragalactic Database (NED), where $A_R = 0.55 A_B$).

2.4 Image Analysis

This section will describe the various methods used to analyze the data in order to determine the structural parameters of the host galaxies and to study their nearby environments. To accomplish this, image statistics were first acquired (Section 2.4.1), after which the light distributions of the host galaxies were fitted using elliptical isophotes (Section 2.4.2) which were then fitted to standard galaxy models (Section 2.4.3). Companion objects were then searched for (Section 2.4.4) and unusual morphologies of the hosts noted (Section 2.4.5). Finally, various parameters and statistics were computed based on this analysis in order to compare the two samples (Section 2.4.6).

2.4.1 Image Statistics and Editing

Image statistics provide very important parameters for analysis and reduction. These are measured using IRAF's `imexamine`. The mean background sky level and noise (standard deviation of the background level) were computed by measuring counts in roughly 40 5×5 boxes at blank areas on the image. The mean value was then subtracted from the image using `imarith`. The term *seeing* in astronomy is a measure of the image quality and refers to the apparent *disk* produced by turbulence in the Earth's atmosphere when observing a point source (such as a star). This disk is usually modeled by a Gaussian with a characteristic FWHM for all point sources on any given exposure (the exact shape is called the Point Spread Function (PSF)). The seeing was determined by measuring the FWHM of several bright, unsaturated stars on each image. The seeing varied between 1.4–3.0 arcseconds, with an average of 2.05 ± 0.42 arcseconds. The centroid of each host galaxy was also computed by using the centering routines in `imexamine`. Finally, any stars, ion events, blocked columns,

or satellite tracks that contaminated the host galaxy were replaced by a 4th order interpolated background using `imedit` (See Appendix A.1.3 for details of this task).

2.4.2 Elliptical Isophotal Analysis

At this point we wish to calculate the surface-brightness profile, ellipticity, and position angle of the major axis of each host galaxy. Surface brightness is a measure of intensity per unit area in an extended object and is often written in terms of magnitudes per square arcsecond. Ellipticity is defined as $\varepsilon = 1 - b/a$, where a is the semi-major axis length and b is the semi-minor axis length. Position angle is the direction in which the major axis points, and is measured from North through East. To accomplish this, IRAF's STSDAS/ELLIPSE task was used, which fits elliptical isophotes to the galaxy. This task returns a data file containing the following parameters as a function of the semi-major axis length: Intensity (in counts per pixel), ellipticity, position angle (orientation of the major-axis), ellipse center, ellipse harmonics (described below), number of iterations, stop code (reporting any problems during the computation), and all pertinent formal uncertainties.

The ELLIPSE task is an important part of the analysis and thus its algorithm will be discussed in some detail. Jedrzejewski (1987) described a variation of this algorithm in determining surface photometry of elliptical galaxies. Departures from a pure ellipse can be described by a series of coefficients to an orthogonal set of harmonic functions of the form:

$$A_n = \frac{1}{\pi} \int R(\varphi) \sin(n\varphi) d\varphi \quad B_n = \frac{1}{\pi} \int R(\varphi) \cos(n\varphi) d\varphi \quad (2.4)$$

where R are the intensity-contour points, and φ is the azimuthal angle. The first two orders of harmonics (A_1, B_1, A_2, B_2) indicate errors in the fitted ellipse, whereas the

third and fourth-order terms indicate an “egg-shaped”, “heart-shaped”, or “boxy-shaped” ellipse. The way this is implemented in the algorithm is that the intensity of the galaxy is sampled around the ellipse at equal intervals of the eccentric anomaly E at a specific semi-major radius. The following equation is then fitted by a weighted least-squares routine to solve for the harmonic coefficients and constant term:

$$I = I_0 + A_1 \sin(E) + B_1 \cos(E) + A_2 \sin(2E) + B_2 \cos(2E) \quad (2.5)$$

The ellipticity ε and the position angle θ of the ellipse are then adjusted to make the fit better (NB: ellipse centers were held fixed in our analysis) via:

$$\Delta\varepsilon = \frac{-2B_2(1 - \varepsilon)}{a_0 I'} \quad (2.6)$$

$$\Delta\theta = \frac{2A_2(1 - \varepsilon)}{a_0 I' [(1 - \varepsilon)^2 - 1]} \quad (2.7)$$

where

$$I' = \left. \frac{\partial I}{\partial a} \right|_{a_0} \quad (2.8)$$

That is, I' is the derivative of the intensity in the direction of the major axis evaluated at the semi-major length a_0 . This least squares and correction procedure is implemented iteratively until a sufficiently good fit is made (i.e. $I(E) = \text{constant}$). A minimum of 15 iterations are made, up to a maximum of 100. At this stage, the third and fourth-order harmonics are calculated via least squares from:

$$I = I_0 + A_3 \sin(3E) + B_3 \cos(3E) + A_4 \sin(4E) + B_4 \cos(4E) \quad (2.9)$$

at which point all parameters for that semi-major radius are written to a file. The error-bars in intensity are obtained from IRAF by computing the rms scatter of intensity along the fitted ellipse. The length of the semi-major axis is then increased by 10% and the whole procedure is repeated. This continues until the specified

maximum radius is reached; the procedure is then repeated from the initial radius until the minimum radius.

One potential problem that could arise from this algorithm arises from its interpolation scheme. For the inner 20 pixels, the algorithm uses a bilinear interpolation algorithm which can produce ellipticities that are systematically too low in the 5-10 pixel range. This arises from the nature of the interpolation introducing its own $\cos(2\varphi)$ term (i.e. B_2). This effect is most severe for galaxies that are flattened near the center; however, this is generally not a problem because seeing distorts the isophotal contours in the core in any case (as noted earlier, the seeing varied between 1.8 – 3.9 arcseconds).

For each host galaxy, the ellipse task was executed twice. In the first run, the centroid, ε , and θ were allowed to vary in order to confirm the centroid position found by `imexamine`. The results from the second run (in which we held the center fixed) were used in the subsequent analysis. Most galaxies were analyzed using `ellipse` with a minimum semi-major radius set to 1.8 pixels (using a smaller value results in numerical problems, and the inner few pixels give physically unrealistic results anyway). A few galaxies were fit using a third mode of `ellipse`, in which their centers were held fixed, $\varepsilon = 0$ and $\theta = 0^\circ$ (i.e. circular apertures), when the second run had extreme difficulty in fitting ellipses.

In some cases, the host galaxy is very close to a large companion galaxy. When this occurs, the two galaxies need to be *deblended* via the following process, which is illustrated using NGC 5541. Figure 2.2 shows the original image of both host and companion galaxies (all four panels use the same contour levels for visual uniformity). The first step involved isolating the companion galaxy by rotating the image 180° around the host galaxy's center and subtracting this from the original image I (call this new image B_1). Figure 2.3 shows NGC 5541 with the rotated host subtracted out).

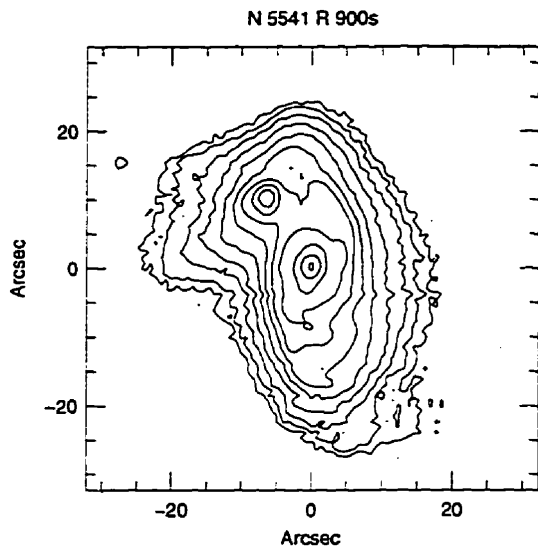


Figure 2.2: Sample deblending of NGC 5541, original image I

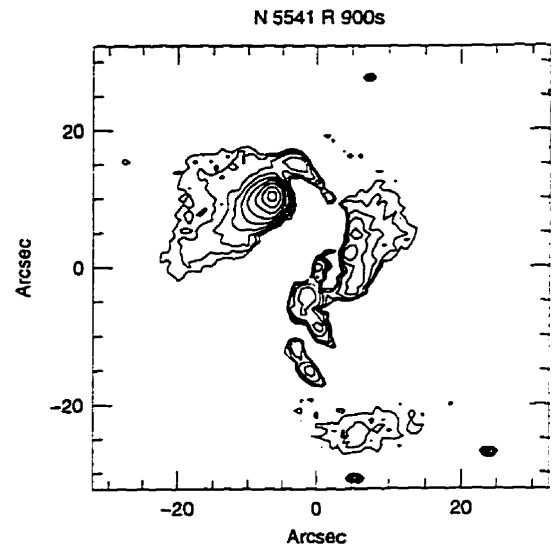


Figure 2.3: Sample deblending of NGC 5541 with companion isolated, image B_1

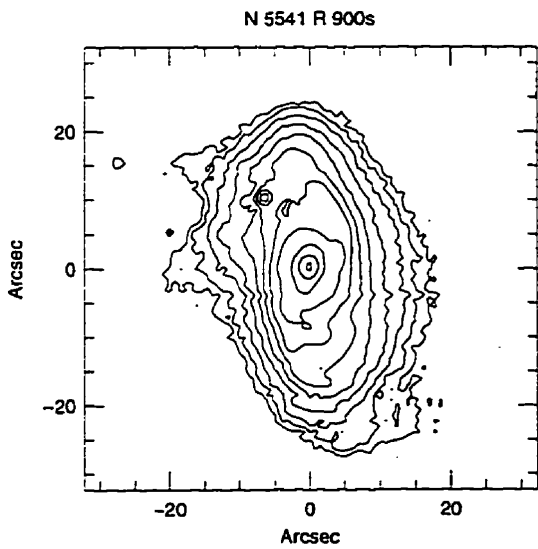


Figure 2.4: Sample deblending of NGC 5541 with host isolated, image A_1

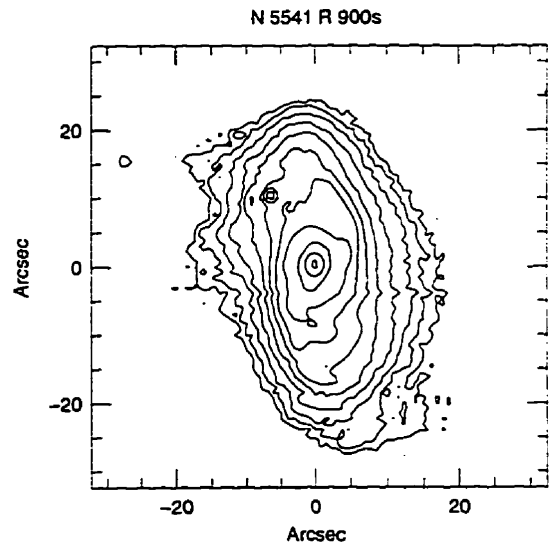


Figure 2.5: Sample deblending of NGC 5541 with clean host, image A_2

Ellipse would then be run on the companion galaxy in image B_1 , and a model galaxy B_1^{mod} would be constructed using the task `bmodel` (an IRAF routine which constructs an image based on results from `ellipse`). Model B_1^{mod} is then subtracted from the original image I resulting in image A_1 , thus isolating the host galaxy (Figure 2.4 shows the first-order isolated host galaxy of NGC 5541). Similarly, a model galaxy A_1^{mod} is constructed by running `ellipse` and `bmodel` on the host galaxy in image A_1 , which can then be subtracted from I to produce yet another image with the companion isolated. This process is performed iteratively until a clean profile of the isolated host is acquired (Figure 2.5 shows the clean image of NGC 5541).

2.4.3 Surface Brightness Profile Fitting

Now that the azimuthally averaged intensity as a function of the length of the semi-major axis has been measured for each host galaxy, the surface-brightness profile can be fitted to standard galaxy models (which were discussed in Section 1.2.1). We first used a three-component model consisting of an exponential disk (Freeman 1970), an $r^{1/4}$ bulge (de Vaucouleurs 1948), and a central Gaussian point source to model the star-like nuclei of the Seyferts. In linear units, the intensity f at any given radius r may then be expressed as:

$$f(r) = f_d e^{-r/r_0} + f_b e^{-7.688[(r/r_e)^{1/4} - 1]} + f_N e^{-r^2/2\sigma^2} \quad (2.10)$$

which can be converted to surface brightness (mag/arcsec²) via the transformation (cf. Equation 2.3):

$$\mu(r) = -2.5 \log \left(\frac{f(r)}{t \cdot A} \right) + \xi + k'X + \epsilon(B - R) \quad (2.11)$$

where A is the area subtended by each pixel (0.77 arcsec/px)². The fitting is restricted to these three standard models for consistency even though galaxies can be much

more complex (e.g., bars, rings, holes in disks, etc. Such features, however, require even more parameters to determine. There are also alternative functional forms for the bulge, though the de Vaucouleurs profile is appropriate since Seyfert galaxies are mostly “early-type” spirals with large bulges). The data are fit to Equation 2.10 using a chi-squared hypersurface minimization routine (Press et al. 1992). In this program the relative fluxes f_d , f_b , and f_N , and the scale radii r_0 and r_e are solved for, while σ is held constant since it is related to the seeing; by definition $\sigma = 0.42466 FWHM$. See Appendix A.2.1 for more details on this program. As soon as the function’s chi-squared reaches a global minimum, the parameters, their formal errors, and the reduced chi-squared are returned.

An alternative fitting method was also used for the Seyfert sample. This method involved fitting a two-component disk and bulge beginning 5 pixels from the center where the PSF is down to $\lesssim 2\%$ peak intensity for the median seeing. The quantity f_N is then computed by subtracting the extrapolated two-component fit from the data and interpreting the excess flux as being contributed by the PSF (see Appendix A.2.1 for more details). The issues of uniqueness of solutions and numerical stability can be addressed by comparing the results of the first and second methods.

Other studies have also been accomplished by examining the surface-brightness profiles of Seyfert galaxies. Alonso-Herrero, Ward, and Kotilainen (1996) and Kotilainen, Ward, and Williger (1993) for instance used a similar three-component, chi-squared minimization fitting routine. McLeod and Rieke (1995) on the other hand used an alternative technique in analyzing the surface brightness profiles by first performing PSF subtraction followed by a two-component fit.

2.4.4 Companion Galaxy Searching

At this point, we searched for optical companions to the hosts on the cropped images. As we approached this problem from a statistical viewpoint, we were not searching for physical companions, but merely for optical companions. Thus our lack of redshift or distance information for such galaxies is not problematic. The search for extra galaxies was performed by careful visual inspection using SAOimage with the assistance of IRAF's imexamine. All candidate objects were analyzed using the radial profile tool, and based on their FWHM and ε , were classified each as a star or galaxy. Objects in which the FWHM was less than the seeing were interpreted to be ion events; objects with a FWHM sufficiently greater than the seeing were interpreted as galaxies, and those with FWHM similar to the seeing were classified as stars (unless ε indicated otherwise).

The integrated intensity for all objects classified as galaxies was measured using an aperture of radius 7 pixels from within the radial-profile tool. If the galaxy was large, the aperture radius was increased appropriately to accommodate it. The centroid and flux of each galaxy were recorded so that the projected distances and magnitudes could be calculated later. Since a meaningful qualitative comparison is desired, we imposed a projected cut-off metric radius of 200 kpc (using $H_0 = 50 h \text{ km s}^{-1} \text{ Mpc}^{-1}$); this way we are searching for companions to a common, similar radius in the rest frame of the host galaxies.

2.4.5 Unsharp Masking and Morphology

We then looked at the general morphology and “interaction level” of all the hosts. This consisted of a two-phase visual inspection of the hosts to look for things such as: amorphous or unresolved features, spiral arms, bars, rings, distortions, faint disturbed

companions, bridges, tails, and jets. Phase one involved visual inspection of the sky-subtracted images. Phase two involved visual inspection of unsharp-masked images. Such images were created by taking the non-sky-subtracted images and convolving them with a flux-preserving Gaussian kernel with FWHM 4 times the seeing. The original image was then divided by the convolved image producing the “unsharp-masked” image (alternatively, the images could have been subtracted). This unsharp-masking

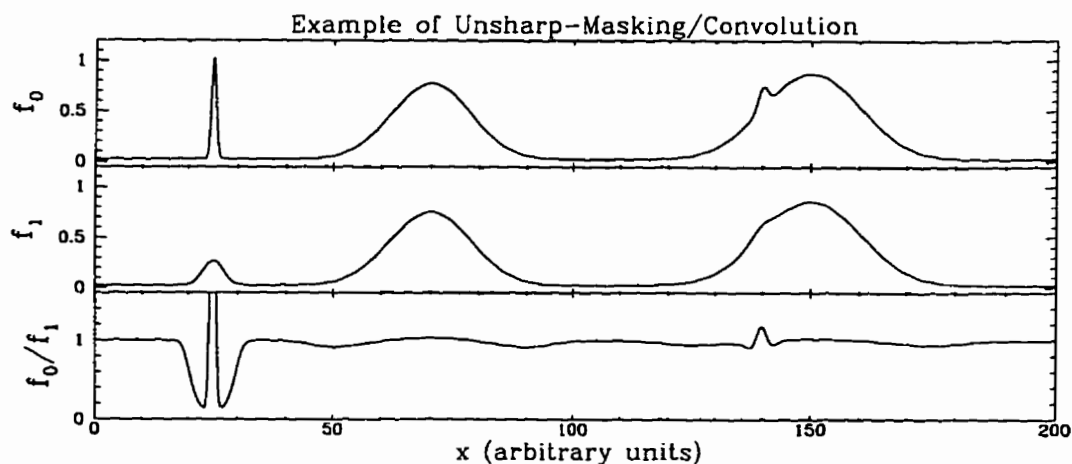


Figure 2.6: 1-D example of unsharp-masking/convolution

technique is illustrated in one dimension in Figure 2.6. The top panel represents an artificial original image which consists of a narrow Gaussian (representing a star), a broad Gaussian (representing a large galaxy), and a broad Gaussian with a narrower Gaussian superposed (representing a large galaxy with a close companion). The middle panel shows the image after it has been convolved with a Gaussian as described above. The bottom panel shows the division of the two images; note that the large galaxies nearly disappear, and that the star and companion galaxy are clearly evident. As seen from the example, unsharp-masking eliminates the low spatial-frequencies and enhances the high spatial-frequencies. Features such as spirals, bars, rings, and very

close companion galaxies all have their own unique signatures on unsharp-masked images as can be seen in the following examples. Figure 2.7 demonstrates how a bar and ring structure appear. Figure 2.8 illustrates the appearance of spiral arms. Figure 2.9 shows the signature of a close companion and a normal bright star. Figure 2.10 also demonstrates a close companion object. Morphological features were noted using this technique, and confirmed the features observed visually.

2.4.6 Galaxy Parameters and Statistics

Distances, magnitudes, luminosities, and gravitational tidal influences were then computed. This was done so that Seyfert galaxies can be compared to the control galaxies, as well as to compare Seyfert 1s and 2s. The first value computed was the distance to the host galaxies, from which can also be derived the image scales and thus the projected companion-host separation distance. The distance to the hosts (as a function of redshift) is given to a very good approximation by:

$$D = \frac{cz}{H_0} \quad \text{for} \quad z \ll 1 \quad (2.12)$$

where D is the distance, H_0 is Hubble's constant, and z is the redshift of the galaxy. In all the distance calculations, we use $H_0 = 50 h \text{ km s}^{-1} \text{ Mpc}^{-1}$, so that $c/H_0 = 5996 h^{-1} \text{ Mpc}$, where c is the speed of light and h is the dimensionless Hubble constant.

The projected separation distances s can then be derived from the image scale, and are given as: $s = \beta \cdot D$ where β is the angular separation given in radians. Now that the distance-type parameters have been determined, the absolute magnitudes of the hosts and companion galaxies (based on the projected distance), can be calculated via:

$$R - M_R = 5 \log \left(\frac{D}{10 \text{ pc}} \right) + A_{\text{gal}} \quad (2.13)$$

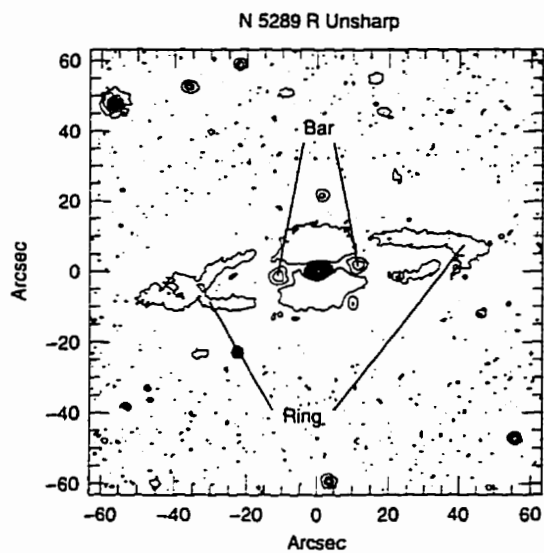


Figure 2.7: Sample unsharp-masked image of NGC 5289

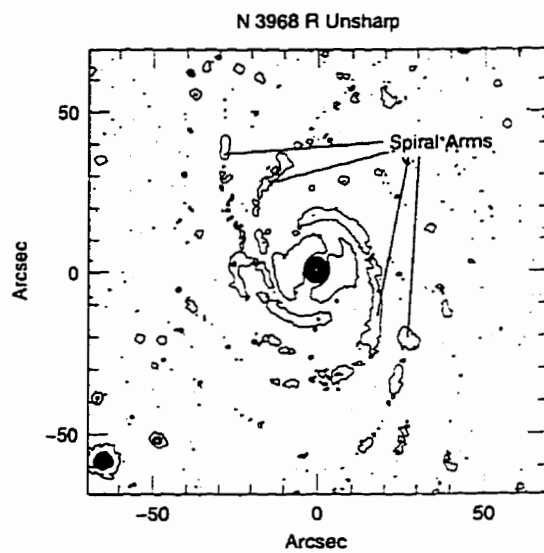


Figure 2.8: Sample unsharp-masked image of NGC 3968

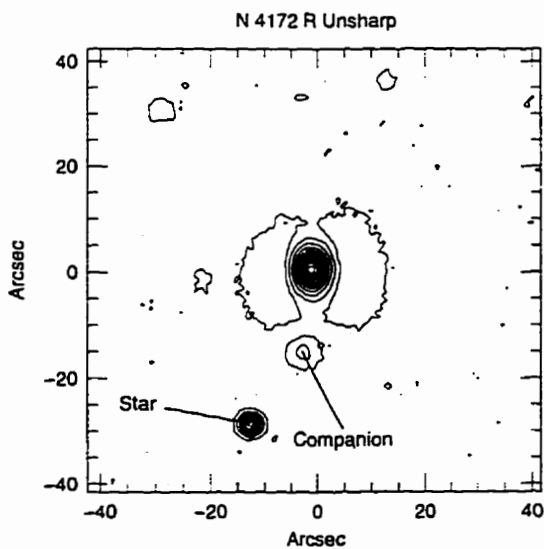


Figure 2.9: Sample unsharp-masked image of NGC 4172

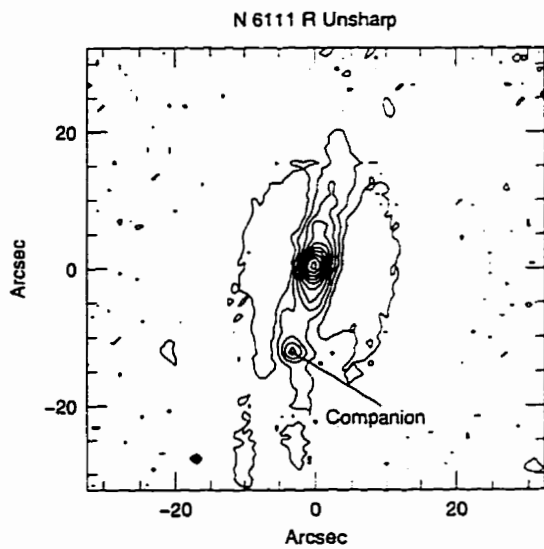


Figure 2.10: Sample unsharp-masked image of NGC 6111

where M_R is the absolute magnitude and A_{gal} is the extinction in our own Galaxy (in R-band). Using the galaxies' absolute magnitudes, we can now calculate their luminosities relative to L^* (which represents the luminosity of a typical large galaxy) which corresponds to $M_B^* = -20.6 + 5 \log(h)$ (Schechter 1976) using the same value for H_0 as this thesis. This transforms to $M_R^* = -22.1$ using $B - R = +1.5$ as a nominal average galaxy colour. The luminosity is then given by:

$$L = L^* \cdot 10^{-0.4(M_R - M_R^*)} \quad (2.14)$$

The next parameter that can be calculated is the tidal influence which the companions have on the host galaxy (based on their *projected* distances). Tidal force, Q , is proportional to M/s^3 where M is mass of the perturbing object and s is the separation distance. Assuming that the mass of a companion galaxy is proportional to its luminosity (i.e. constant mass-to-light ratio M/L), which is a reasonable approximation since we are concerned with the order of magnitude of the tidal parameter, we can thus define a maximum tidal influence as:

$$Q_i \propto \frac{L_i}{s_i^3} \quad (2.15)$$

where L_i is the luminosity of companion galaxy i , and s_i is its separation distance from the host. The full tidal influence on a host galaxy is then given by:

$$Q \propto \sum_{i=1}^N Q_i \quad (2.16)$$

where N is the number of companion galaxies around the host. Also calculated was the magnitude difference between the host and companions ($\Delta M_R = R_{\text{comp}} - R_{\text{host}}$).

Chapter 3

Discussion of Seyfert Galaxies

3.1 Introduction

Using the techniques outlined in Chapter 2, the reduction of the 32 Seyfert galaxies will be discussed in this chapter. Results of the image analysis including contour maps and surface-brightness profiles of the galaxies will be presented. Quantities derived and computed from this analysis such as magnitudes, distances, and properties of the galaxies will also be presented.

3.2 Analysis

This section will present images of the Seyfert galaxies, their surface-brightness profiles, and a brief discussion regarding the reduction of each galaxy. The images presented are displayed in terms of isophotal contours, where the lowest contour is at 3σ above the background, and the remaining contours are at increments of 0.2 magnitudes (i.e. intensity ratios of 1.20) unless otherwise noted. All contour maps have North up and East to the left. The surface-brightness profiles being presented have been converted into apparent magnitudes. The model components used in the fit are also shown. The dotted line represents the Gaussian PSF, the short-dashed line

represents the bulge component, the long-dashed line represents the disk component, while the solid line indicates the sum of the components; the data-points and their error-bars are the data that were returned from the ellipse task. The ellipticity profiles and position-angle (PA) profiles are also discussed, but appear in Appendix B. These plots delineate how the ellipticity of the galaxy and the PA of the major axis vary as a function of the semi-major axis length (in arcseconds). What follow in Section 3.2.1 are the galaxy contour images, surface-brightness profiles, and a description of each galaxy in the Seyfert data set.

3.2.1 The Galaxies

Mrk 0231 This is a disturbed galaxy that contains a tidal bridge to a companion galaxy $57''$ to the S. The surface-brightness profile (Figure 3.2) fits well, though the outer envelope seems a little brighter than expected, and no Gaussian PSF was required (perhaps due to the obvious tidal distortions). Based on the PA profile (Figure B.3), the elliptical contours do a complete twist around from center to edge. See Figure 3.1 for the contour map of Mrk 0231.

Mrk 0461 This galaxy appears as an ordinary spiral. Its surface-brightness profile (Figure 3.4) fits very well (using circular apertures from ellipse), using only bulge and disk components, with no need for a Gaussian PSF. The lack of a PSF is perhaps caused by some bar-type structure). The galaxy's PA (Figure B.1) is fairly steady, and its ellipticity varies as expected (though there is some hint of bar activity near $4''$). See Figure 3.3 for Mrk 0461's contour map.

Mrk 0471 This is a spiral galaxy with a bar. No Gaussian PSF was needed (due to the bar perhaps) in the fit to the surface-brightness profile (Figure 3.6), which fits

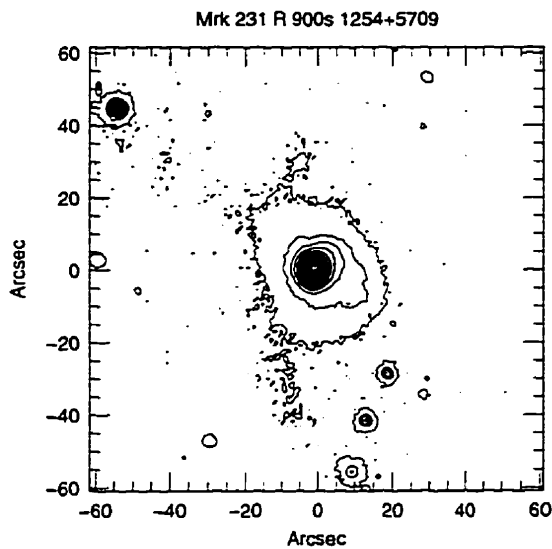


Figure 3.1: Intensity contour map of Mrk 0231

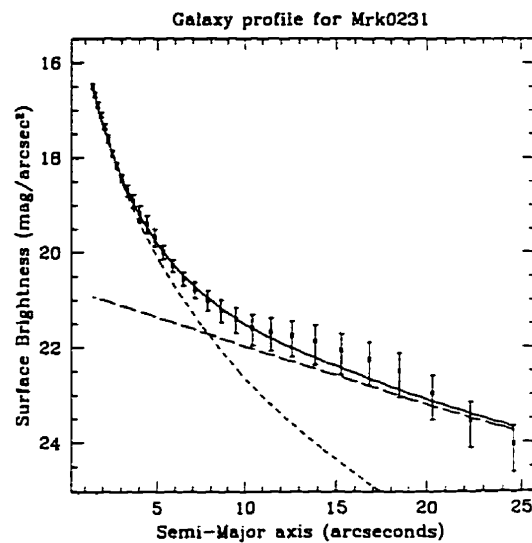


Figure 3.2: Radial profile and fit of Mrk 0231. $\chi^2_{\nu} = 0.31$

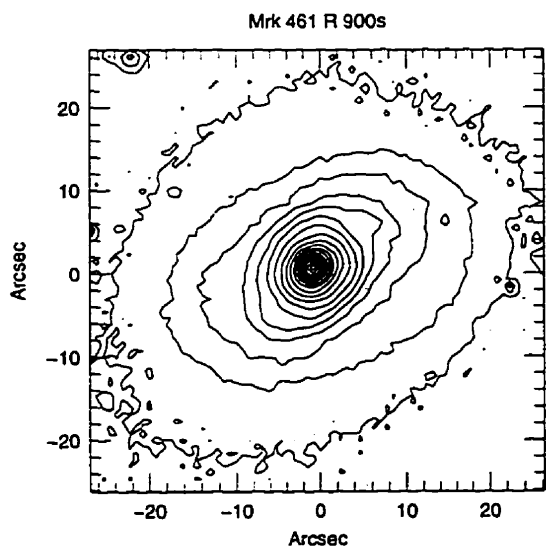


Figure 3.3: Intensity contour map of Mrk 0461

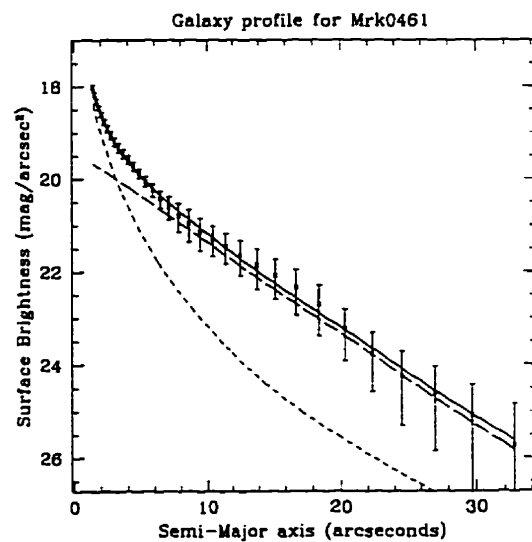


Figure 3.4: Radial profile and fit of Mrk 0461. $\chi^2_{\nu} = 0.07$

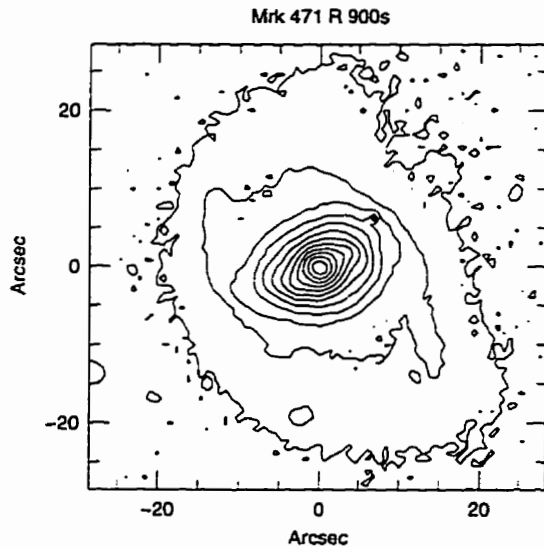


Figure 3.5: Intensity contour map of Mrk 0471

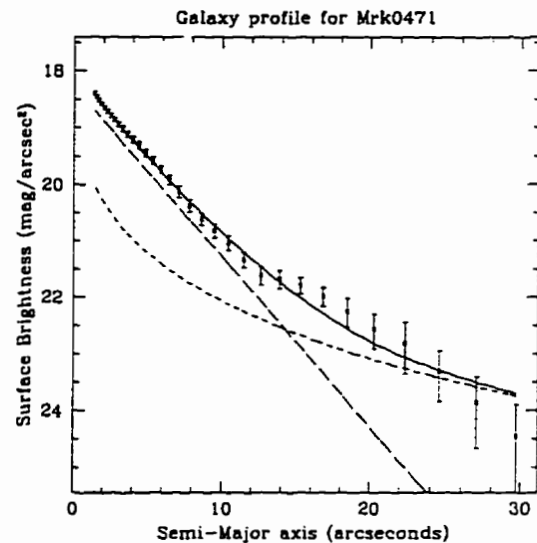


Figure 3.6: Radial profile and fit of Mrk 0471. $\chi^2_{\nu} = 0.67$

well with just a disk and bulge. The PA undergoes a perpendicular twist just after the bar at 10'' (Figure B.2). The contour map is found in Figure 3.5.

Mrk 0789 This is a very peculiar, distorted galaxy with some odd-shaped extended regions and an unusually shaped core (see Figure 3.7 for contour map). The object 20'' to the SE is a bright star. The surface-brightness profile (Figure 3.8) is somewhat noisy, but fits very well with all three components. Its PA is quite steady at about 50°, though its ellipticity varies across the galaxy (Figure B.4).

Mrk 0817 This galaxy appears as a normal spiral, with a close companion galaxy 11'' to the S (see Figure 3.9). The surface-brightness profile fits reasonably well with all three components (Figure 3.10). The ellipses were fit with the close companion removed. The galaxy's contours twist slowly throughout, though its ellipticity behaves reasonably well (Figure B.1).

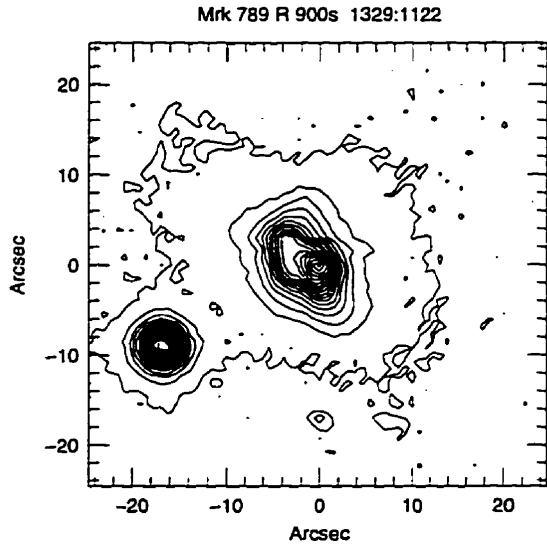


Figure 3.7: Intensity contour map of Mrk 0789

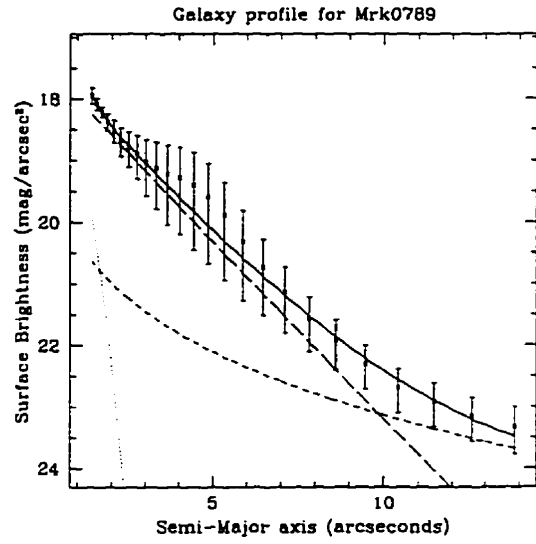


Figure 3.8: Radial profile and fit of Mrk 0789. $\chi^2_{\nu} = 0.11$

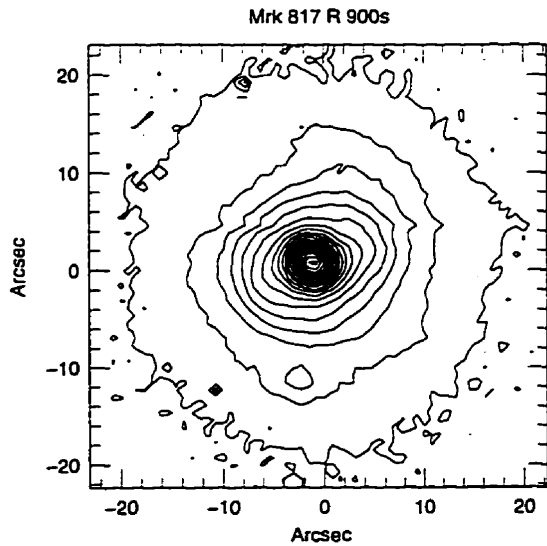


Figure 3.9: Intensity contour map of Mrk 0817

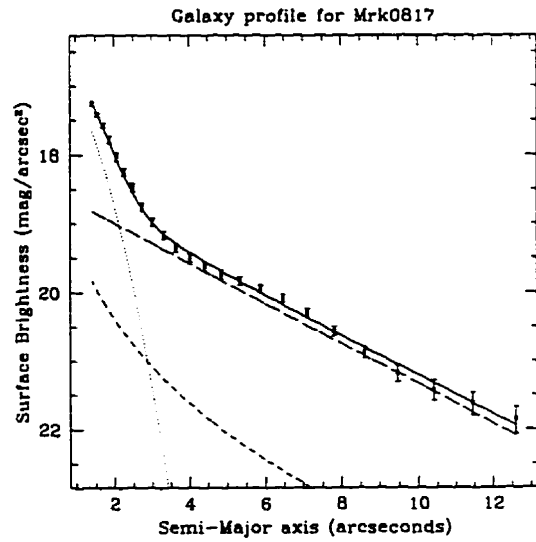


Figure 3.10: Radial profile and fit of Mrk 0817. $\chi^2_{\nu} = 0.98$

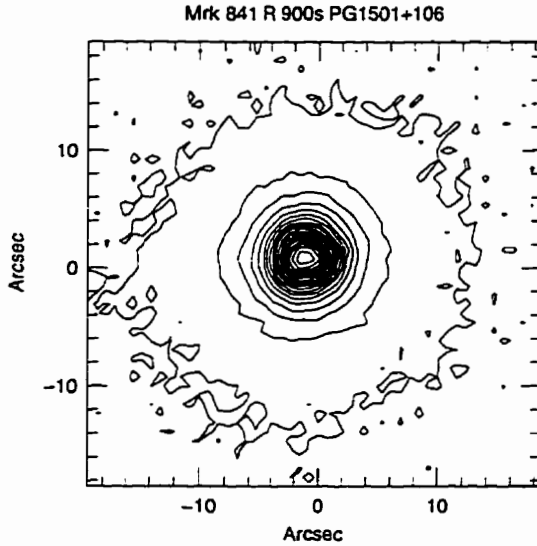


Figure 3.11: Intensity contour map of Mrk 0841

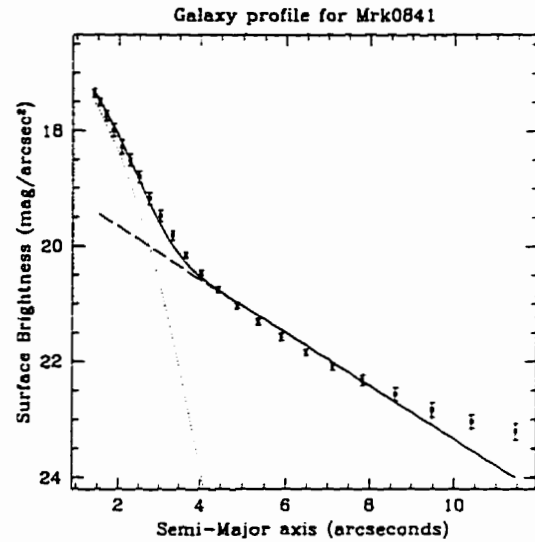


Figure 3.12: Radial profile and fit of Mrk 0841. $\chi^2_{\nu} = 4.02$

Mrk 0841 This is a plain-looking disk galaxy with a strong Gaussian PSF. The fit to the surface-brightness profile was poor numerically, though it appears acceptable (Figure 3.12). The ellipticity profile shows the galaxy to be very circular (Figure B.8), and hence the PA is irrelevant. The contour map of Mrk 0841 is found in Figure 3.11.

UGC 06100 This is a normal spiral galaxy; however, its surface-brightness profile fits well with a strong bulge component and no Gaussian PSF (Figure 3.14). UGC 06100's PA is very steady and its ellipticity behaves as expected (Figure B.2). An alternatively used name for this galaxy is A1058+455, and its contour map is found in Figure 3.13.

UGC 08621 This is a normal spiral galaxy with prominent spiral arms. Its surface-brightness profile fits well primarily with a disk component, though a Gaussian PSF is evident (Figure 3.16). The galaxy is roughly circular, and its PA appears to twist around with its spiral arms (Figure B.8). This galaxy is also called 1335+39, and its

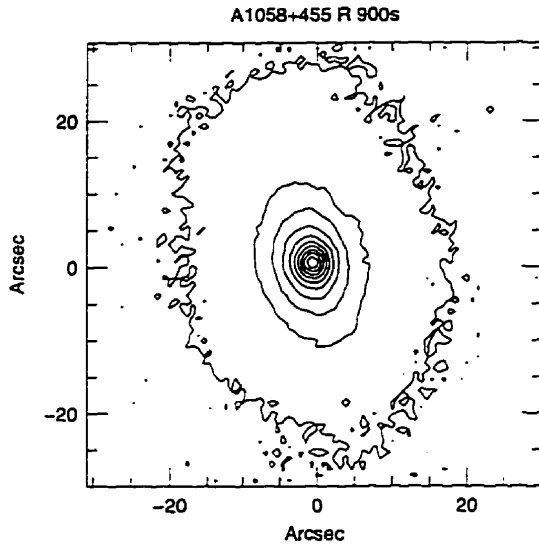


Figure 3.13: Intensity contour map of UGC 06100

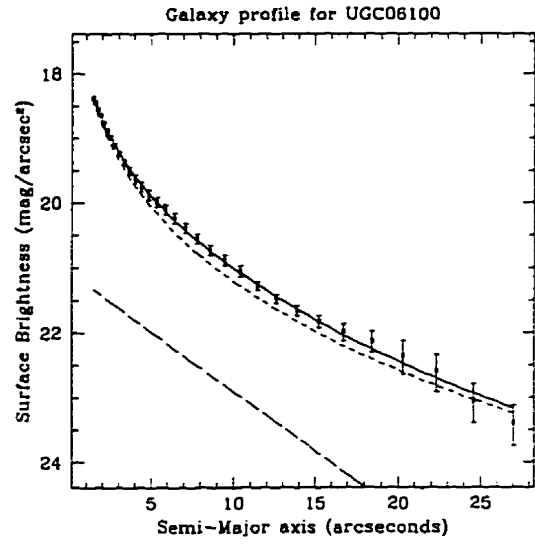


Figure 3.14: Radial profile and fit of UGC 06100. $\chi^2_{\nu} = 0.52$

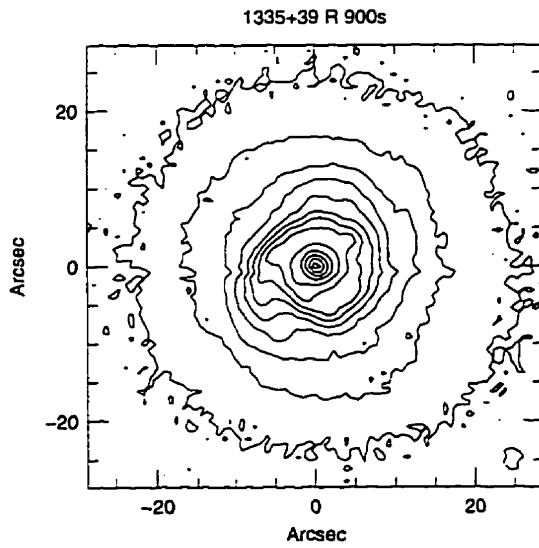


Figure 3.15: Intensity contour map of UGC 08621

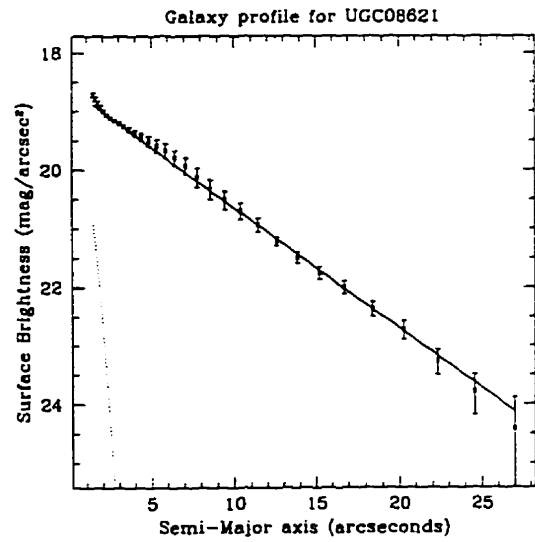


Figure 3.16: Radial profile and fit of UGC 08621. $\chi^2_{\nu} = 0.44$

contour map is found in Figure 3.15.

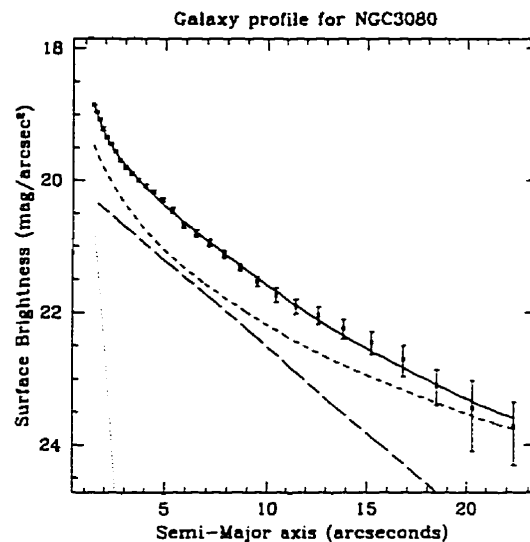
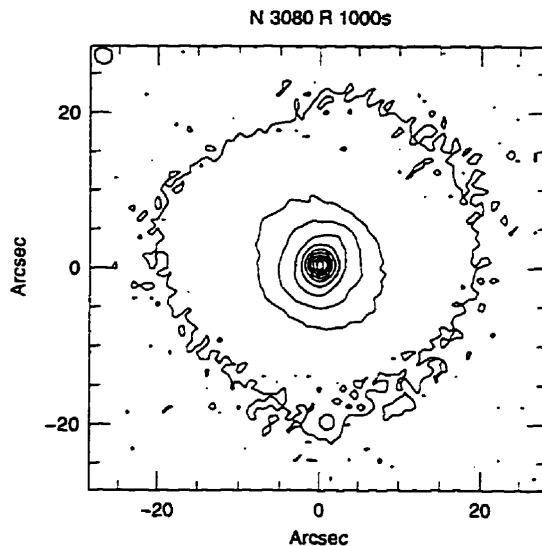


Figure 3.17: Intensity contour map of NGC 3080

Figure 3.18: Radial profile and fit of NGC 3080. $\chi^2_\nu = 1.17$

NGC 3080 This is a normal spiral galaxy with a small, close companion object (likely a faint star) to the S at 20". There is a very large companion galaxy 4.3' to the SW (UGC 05371, an interesting galaxy in itself). An adequate fit was made to the surface-brightness profile using all three components (Figure 3.18). There is a slight twist in the isophotes at 6", which is associated with a decrease in ellipticity (Figure B.1). The contour map of NGC 3080 is found in Figure 3.17.

NGC 3227 This is a large spiral galaxy with an large elliptical companion galaxy (NGC 3226) 2' NW. There is evidence of dust lanes and extended material surrounding the galaxy (possibly tidal in origin). The surface-brightness profile fits well, and used all three components (Figure 3.20). Outside of the core, the PA and ellipticity are fairly stable (Figure B.6). NGC 3227's contour map is in Figure 3.19.

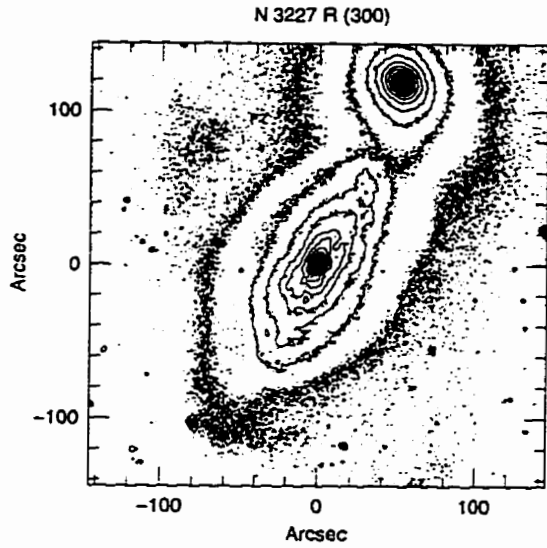


Figure 3.19: Intensity contour map of NGC 3227

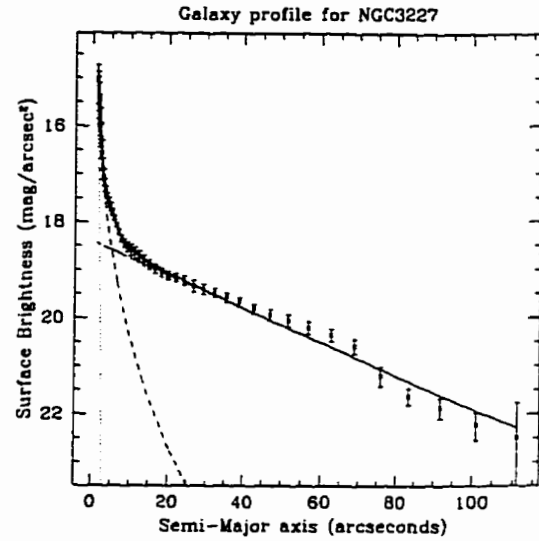


Figure 3.20: Radial profile and fit of NGC 3227. $\chi^2_{\nu} = 0.68$

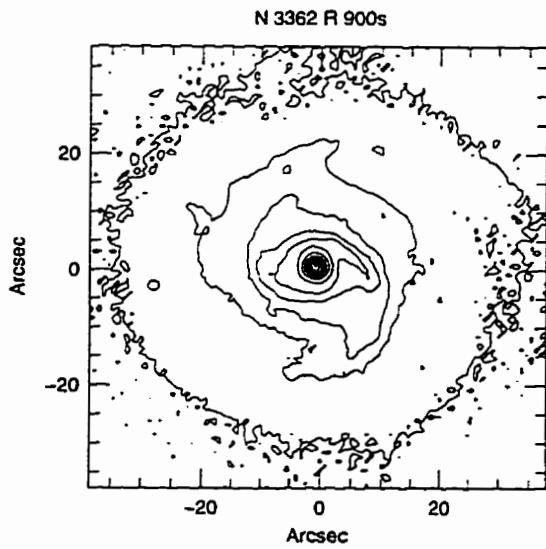


Figure 3.21: Intensity contour map of NGC 3362

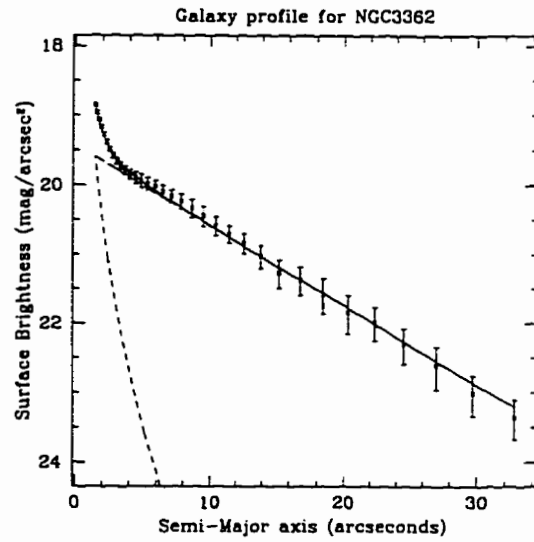


Figure 3.22: Radial profile and fit of NGC 3362. $\chi^2_{\nu} = 0.41$

NGC 3362 This is a spiral galaxy with bright spiral arms. The surface-brightness profile fits well, though it consisted only of a bulge and disk (Figure 3.22). The PA twists around over 90° with the spiral arms, while the ellipticity increases up to 0.4 and gradually becomes circular at the edge of the galaxy (Figure B.3). See Figure 3.21 for the contour map of NGC 3362.

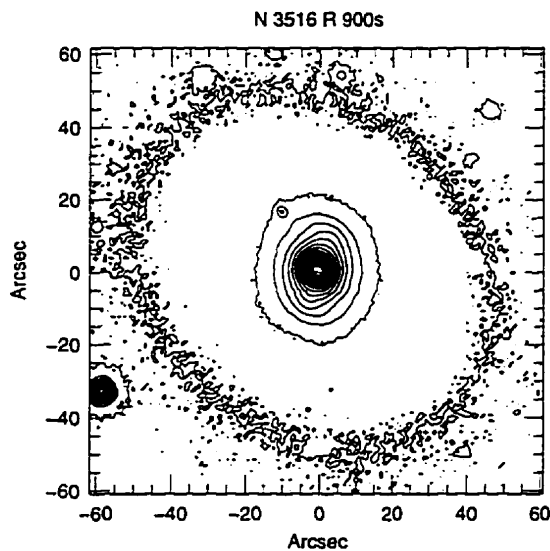


Figure 3.23: Intensity contour map of NGC 3516

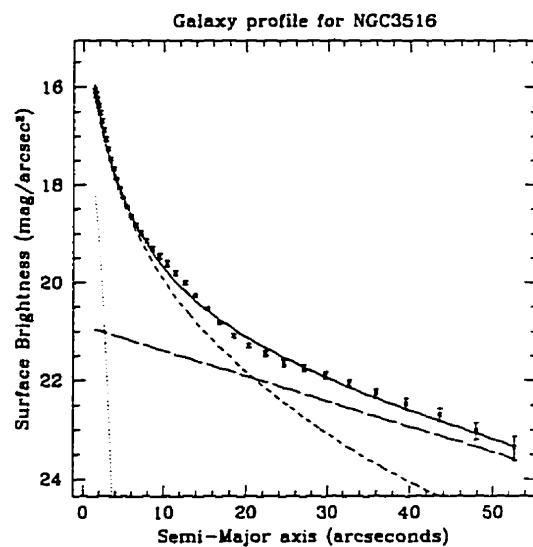


Figure 3.24: Radial profile and fit of NGC 3516. $\chi^2_{\nu} = 4.86$

NGC 3516 This is an ordinary spiral galaxy with very faint spiral arms. There are a number of close small companions, notably three at about $1'$ to the S, NE, and NW (see contour map: Figure 3.23). A few foreground stars were removed from the image prior to the isophotal analysis; however, the surface-brightness profile has a numerically poor fit (Figure 3.24), but visually appears acceptable. The isophotes twist back and forth once by about 60° (Figure B.2), with no particularly odd behaviour in ellipticity.

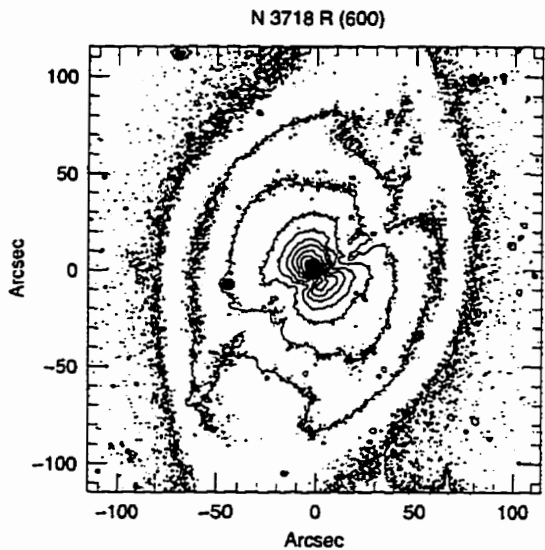


Figure 3.25: Intensity contour map of NGC 3718

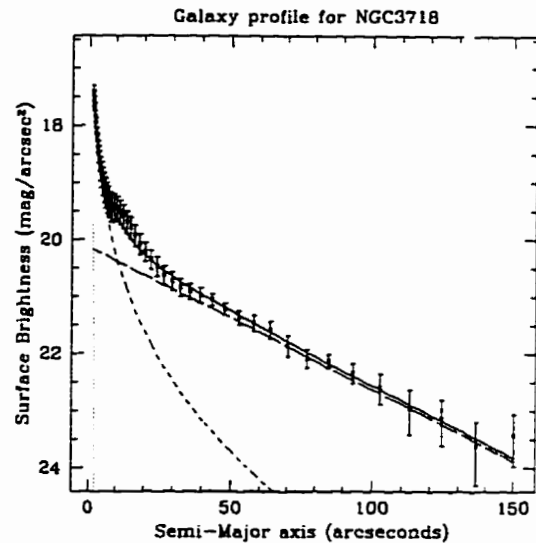


Figure 3.26: Radial profile and fit of NGC 3718. $\chi^2_\nu = 0.32$

NGC 3718 This is a distorted spiral galaxy with a dust lane through its center. There is a noticeable amount of extended material in the N and S directions as well. The surface-brightness profile fits well using all three components (Figure 3.26). The PA twists nearly 60° at $75''$ (Figure B.7), as the isophotes of the central region are almost perpendicular to those of the rest of the galaxy (Figure 3.25).

NGC 3786 This spiral galaxy has a faint ring present, as well as a large companion galaxy (NGC 3788) $1.4'$ to the N. There appears to be a tidal tail to the E caused by the interaction with NGC 3788. There is another companion galaxy $80''$ to the SW; the object $2'$ to the SE is a star. The surface-brightness profile fits reasonably well, though no Gaussian PSF was used, perhaps due to the ring and tidal distortions (Figure 3.28, the ring structure shows some artifacts at a radius of $20''$). The PA angle is quite steady, and the ellipticity behaves predictably as in Figure B.4. The contour map of NGC 3786 and NGC 3788 can be found in Figure 3.27.

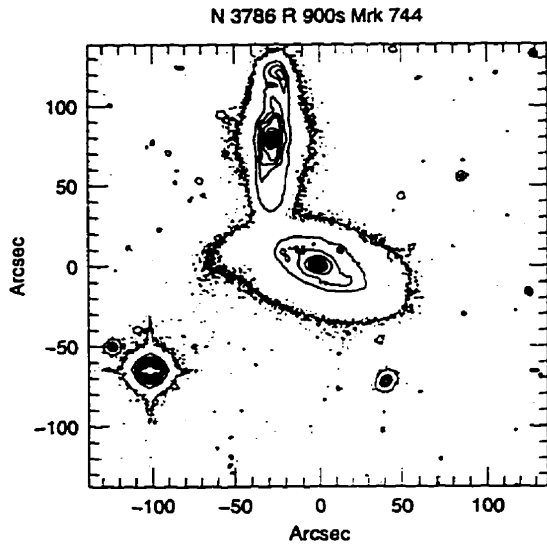


Figure 3.27: Intensity contour map of NGC 3786

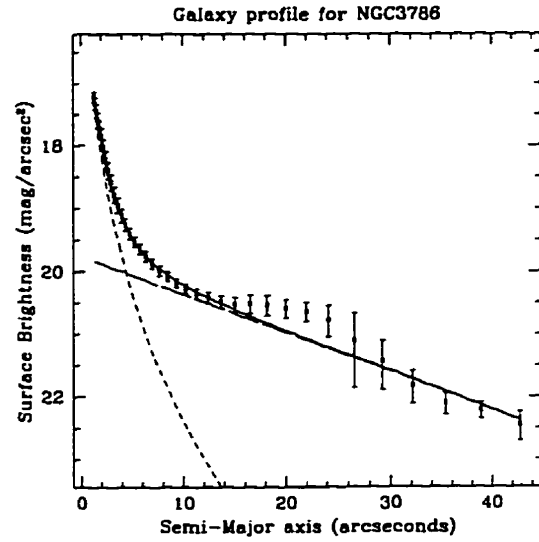


Figure 3.28: Radial profile and fit of NGC 3786. $\chi^2_{\nu} = 0.82$

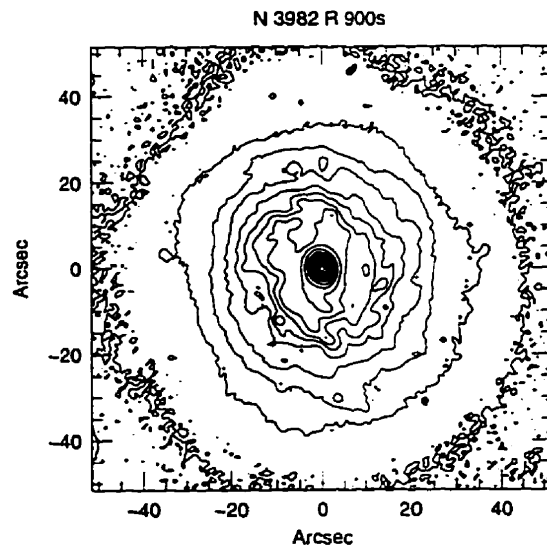


Figure 3.29: Intensity contour map of NGC 3982

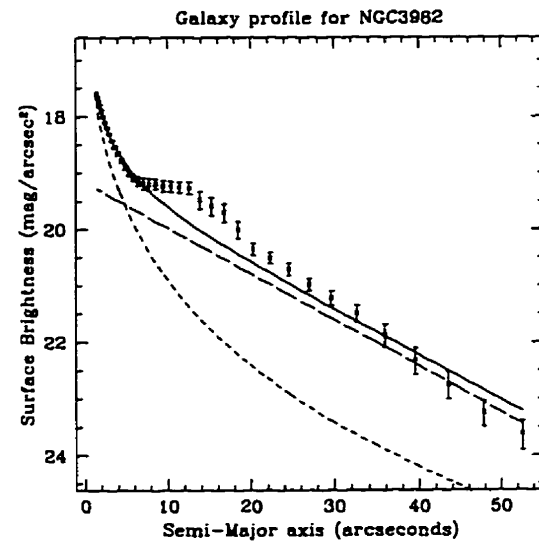


Figure 3.30: Radial profile and fit of NGC 3982. $\chi^2_{\nu} = 2.99$

NGC 3982 This galaxy has very pronounced spiral features. Its surface-brightness profile fits poorly (Figure 3.30), even after removing nine data points between 10–20'' (some kind of ring-type feature or disk-hole). Perhaps due to the peculiar nature of this galaxy, no Gaussian PSF was recovered. In this same region, the PA and ellipticity behave oddly as well, as the isophotes temporarily flatten and twist around (Figure B.5). See Figure 3.29 for the contour map of NGC 3982.

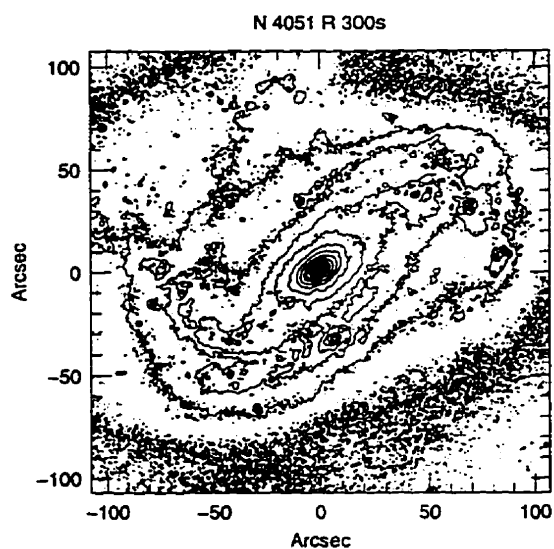


Figure 3.31: Intensity contour map of NGC 4051

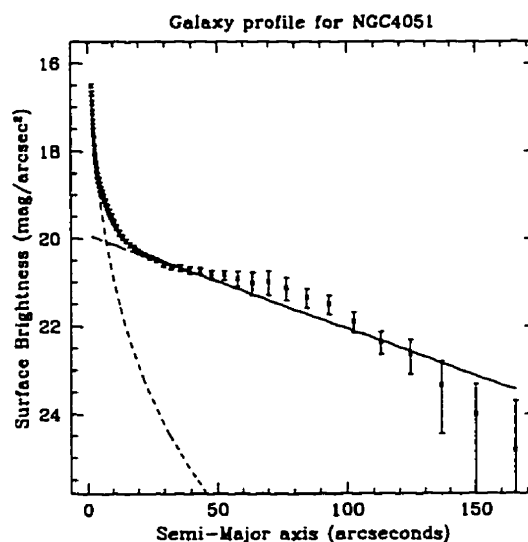


Figure 3.32: Radial profile and fit of NGC 4051. $\chi^2_{\nu} = 2.42$

NGC 4051 This galaxy has very prominent spiral arms with several large clumps in these arms. There is also a large, odd extended region in the NE, of unknown origin. The fit to the surface-brightness profile is somewhat poor (Figure 3.32), and no Gaussian PSF was recovered. The PA is quite steady (Figure B.7), though the isophotes flatten quite a bit due to the inclination of the galaxy (which is $i \approx 55^\circ$). The contour map of NGC 4051 can be found in Figure 3.31.

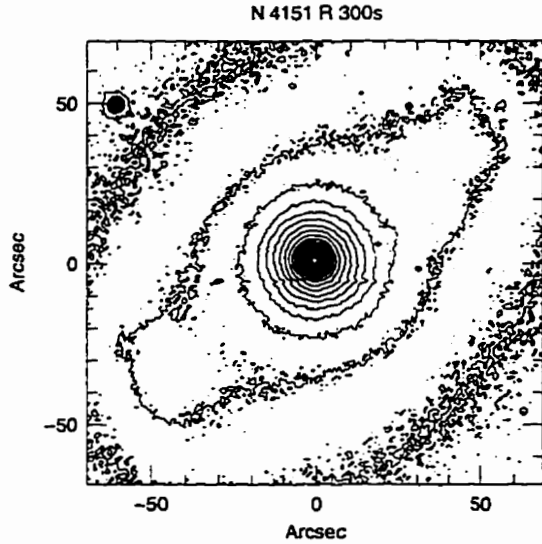


Figure 3.33: Intensity contour map of NGC 4151

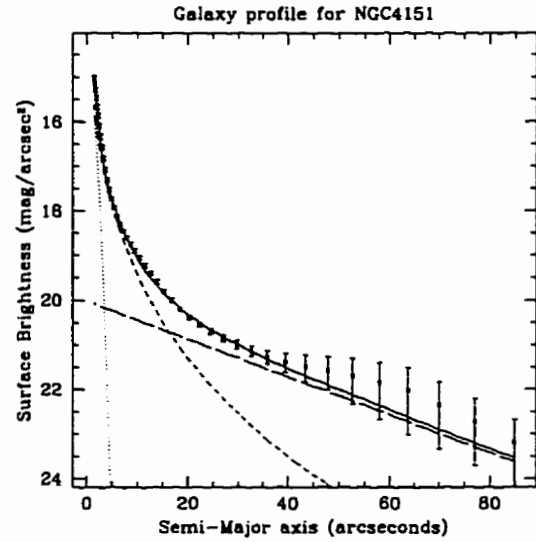


Figure 3.34: Radial profile and fit of NGC 4151. $\chi^2_{\nu} = 1.73$

NGC 4151 This is a spiral galaxy with a bar structure and a partial ring. There is a moderate sized spiral companion (NGC 4156), 5' NE. The surface-brightness profile fits adequately (Figure 3.34); the actual fit was executed on data acquired via circular apertures. The PA and ellipticity are very well behaved (the inner 20'' are meaningless for the PA, since the isophotes are very nearly circular in that region as seen in Figure B.5). NGC 4151's contour map can be found in Figure 3.33.

NGC 4235 This is a high-inclination ($i \approx 75^\circ$) spiral galaxy with noticeable dust lanes as well as a slight asymmetry in the NE edge of the galaxy. Nearly 50 stars were removed in the galaxy's vicinity in order to fit isophotes to the galaxy. The resulting surface-brightness profile fits very well, though using only bulge and disk components (Figure 3.36). The absence of the Gaussian PSF is perhaps indirectly due to the dust lane. The PA is extremely steady, and the ellipticity also behaves very well (Figure B.7). See Figure 3.35 for the contour map of NGC 4235.

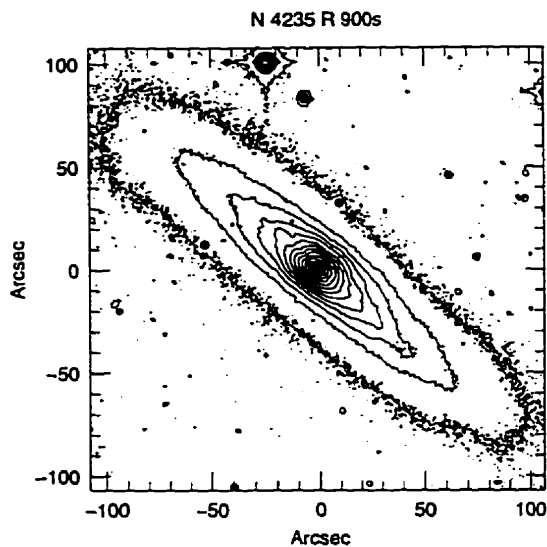


Figure 3.35: Intensity contour map of NGC 4235

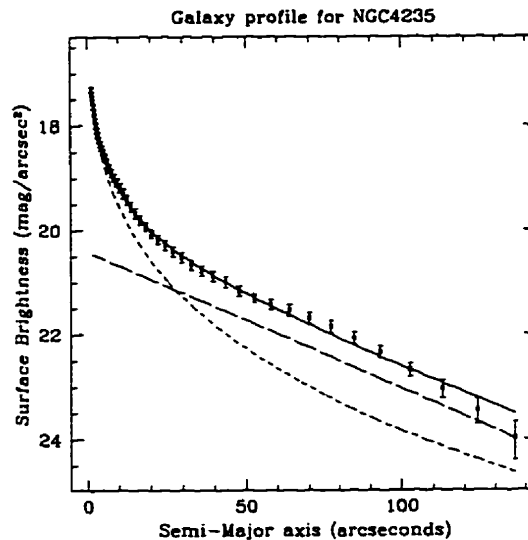


Figure 3.36: Radial profile and fit of NGC 4235. $\chi^2_{\nu} = 0.47$

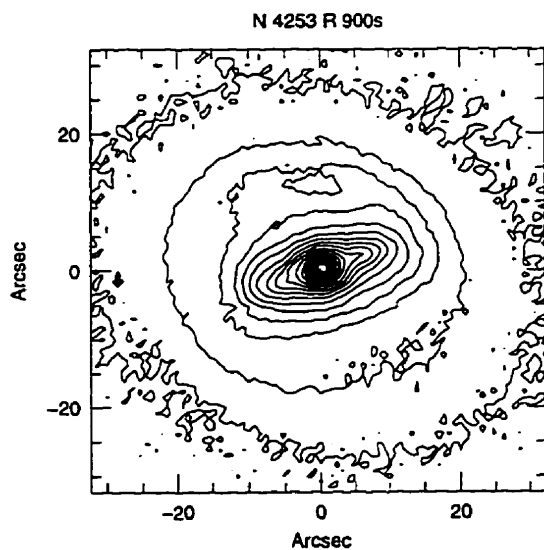


Figure 3.37: Intensity contour map of NGC 4253

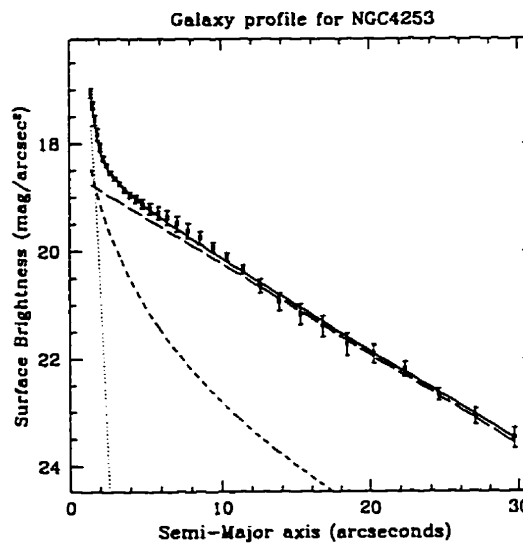


Figure 3.38: Radial profile and fit of NGC 4253. $\chi^2_{\nu} = 0.62$

NGC 4253 This spiral galaxy contains a bar and a faint partial ring. The surface-brightness profile fits well using all three components (Figure 3.38). The PA are fairly steady until $\sim 18''$ where the bar ends and the isophotes become circular in the outer region (Figure B.5). See Figure 3.37 for the contour map of NGC 4253.

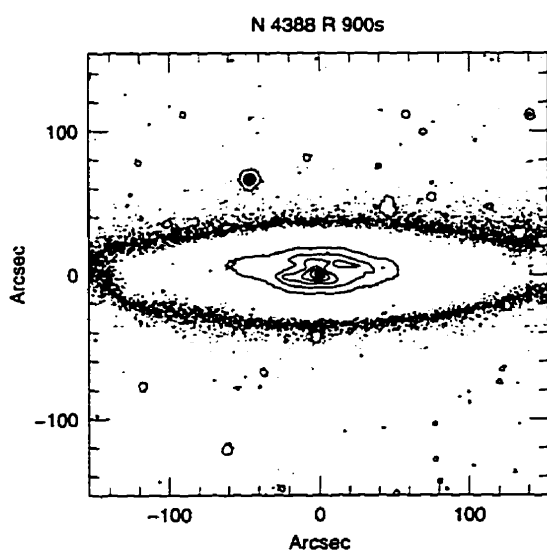


Figure 3.39: Intensity contour map of NGC 4388

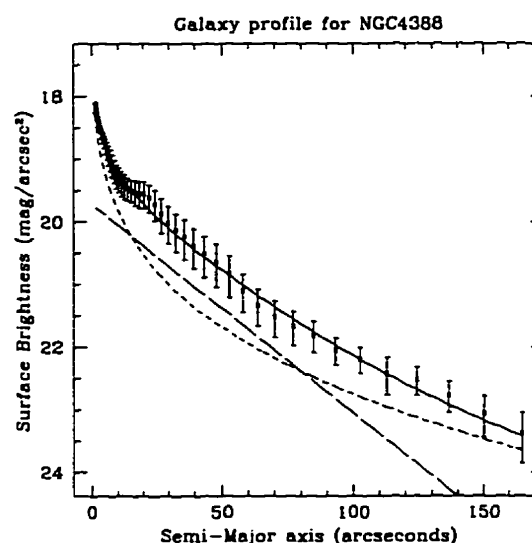


Figure 3.40: Radial profile and fit of NGC 4388. $\chi^2_{\nu} = 0.23$

NGC 4388 This is a high-inclination ($i \approx 75^\circ$) spiral galaxy with very prominent dust, and is located in the Virgo Cluster. Many stars were removed prior to isophotal analysis. The surface-brightness profile fits well with just two components (Figure 3.40), though it appears as though a Gaussian PSF would be needed if there was higher resolution data in the core. The PA is very steady, and the isophotes quickly become flattened, though there is a fair amount of noise in the inner $20''$ (Figure B.7). The contour map of NGC 4388 can be found in Figure 3.39.

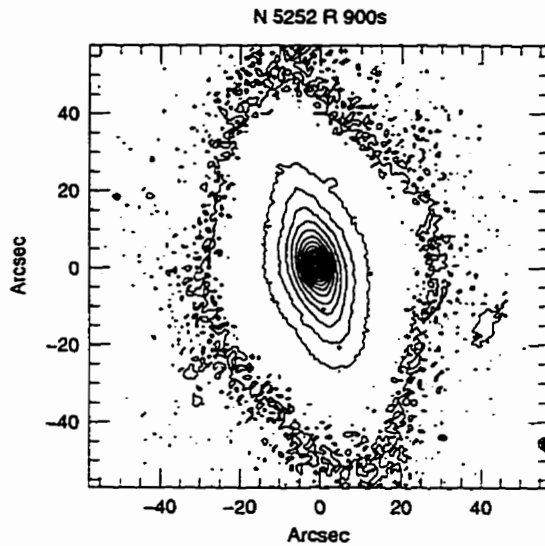


Figure 3.41: Intensity contour map of NGC 5252

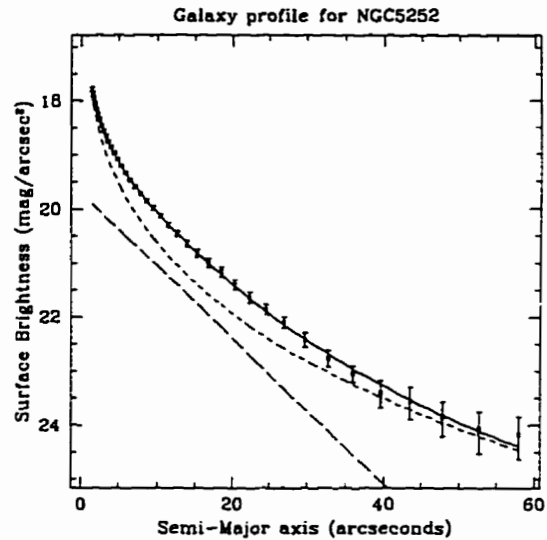


Figure 3.42: Radial profile and fit of NGC 5252. $\chi^2_{\nu} = 0.18$

NGC 5252 This galaxy has a somewhat pointed shape, and there are no obvious spiral arms. The surface-brightness profile fits very well to just bulge and disk components (Figure 3.42). A Gaussian PSF was not recovered since the bulge fits very well to the inner pixels. The isophotes are well behaved in terms of PA and ellipticity (Figure B.4). The contour map of NGC 5252 is found in Figure 3.41.

NGC 5256 This galaxy is obviously a merger/interaction in progress, and there are tidal tails streaming off in several directions (N, SW, SE). Due to the presence of the two nuclei in close proximity of each other and the irregular isophotes, I was unable to fit any elliptical isophotes to this galaxy. The contour map of NGC 5256 is found in Figure 3.43.

NGC 5273 This is an ordinary looking galaxy with no noticeable spiral arms. There is a moderate sized spiral galaxy located 3.3' away to the SE. The fit to the surface-brightness profile is poor, though it appears visually acceptable (Figure 3.45). The

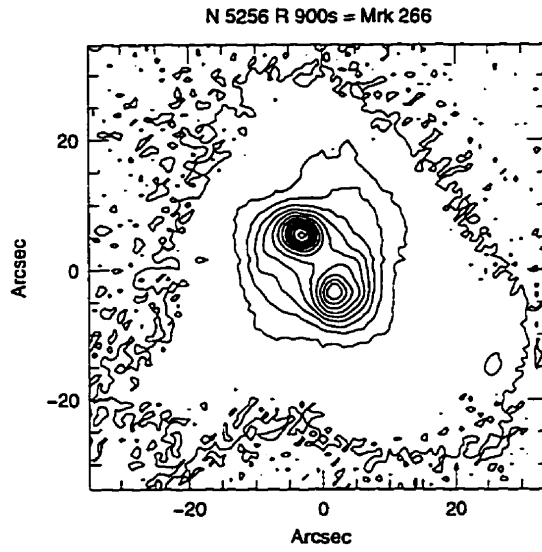


Figure 3.43: Intensity contour map of NGC 5256

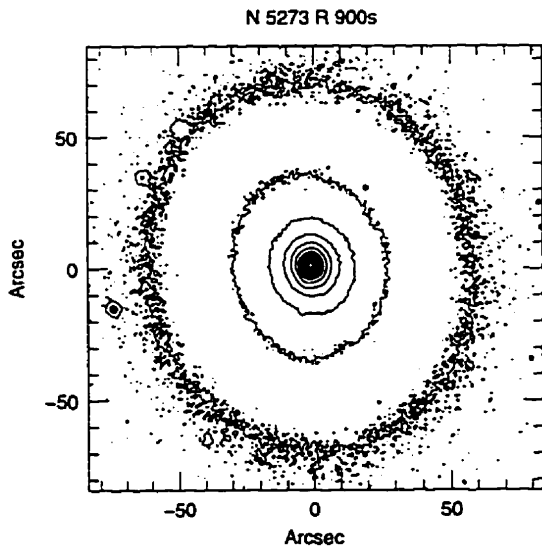


Figure 3.44: Intensity contour map of NGC 5273

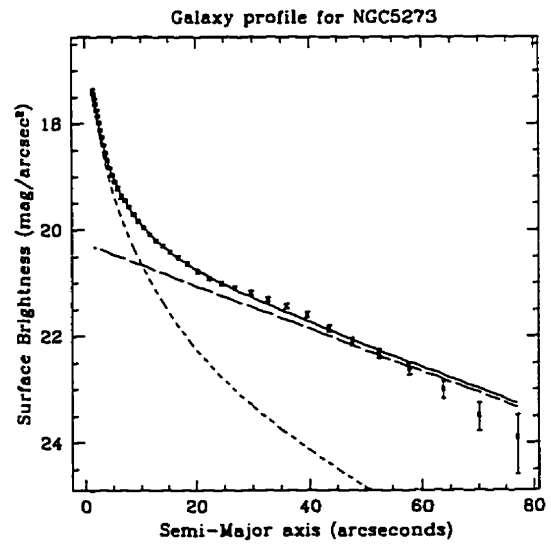


Figure 3.45: Radial profile and fit of NGC 5273. $\chi^2_\nu = 2.39$

fit was unable to recover a Gaussian PSF as the bulge appears to fit adequately to the central region. The PA and ellipticity of the galaxy are fairly well behaved (Figure B.8). NGC 5273's contour map is found in Figure 3.44.

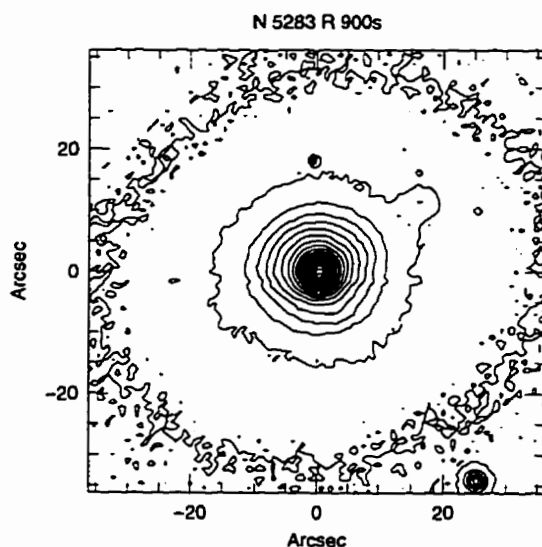


Figure 3.46: Intensity contour map of NGC 5283

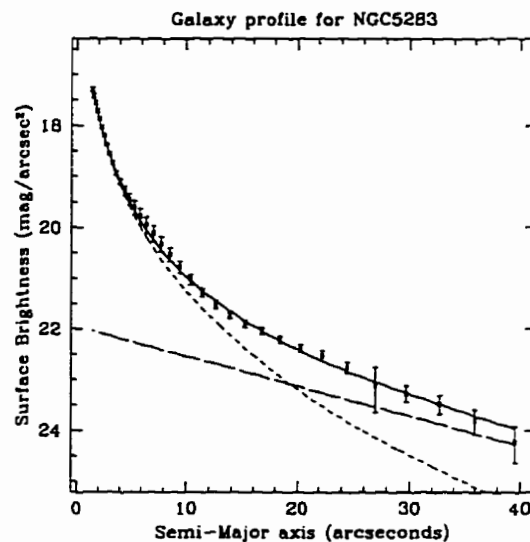


Figure 3.47: Radial profile and fit of NGC 5283. $\chi^2_{\nu} = 0.37$

NGC 5283 This object appears as a spiral galaxy with no obvious spiral arms. There is a small companion object very close, $19''$ to the NW. The surface-brightness profile fits very well using only a bulge and disk (Figure 3.47). It is unknown why a Gaussian PSF was not recovered, though the bulge fits well to the central region of the galaxy. The PA appears somewhat steady (within its error-bars, which are large), and ellipticity is well behaved (Figure B.8). The contour map of NGC 5283 is found in Figure 3.46.

NGC 5347 This spiral galaxy contains a prominent bar and ring. There is also a companion object (large clump in a spiral arm) $19''$ to the S. The surface-brightness profile fits well with all three components (Figure 3.49). The PA is very steady and

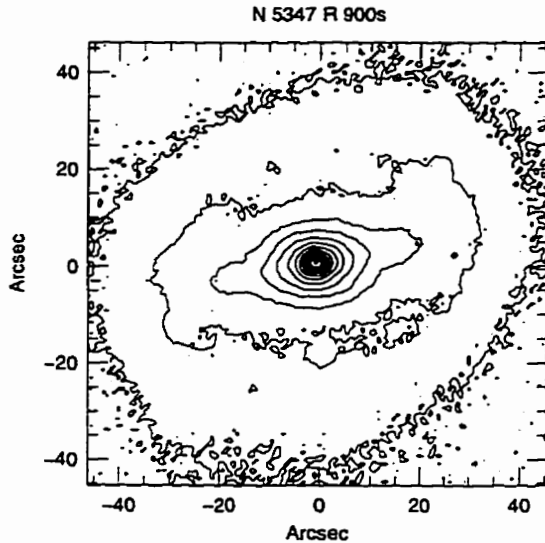


Figure 3.48: Intensity contour map of NGC 5347

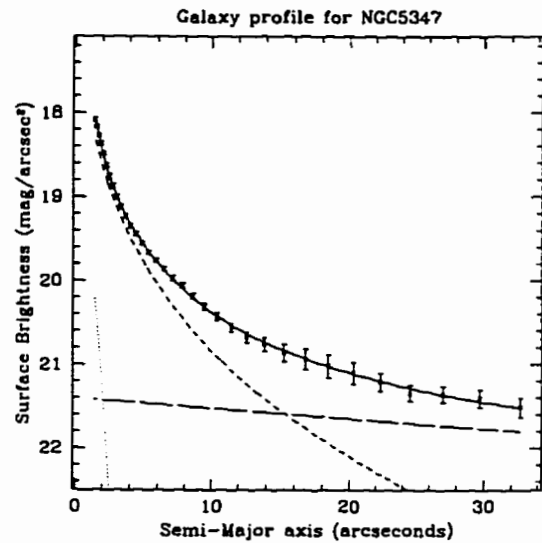


Figure 3.49: Radial profile and fit of NGC 5347. $\chi^2_{\nu} = 0.60$

the galaxy's ellipticity behaves as expected for a large bar (Figure B.4). NGC 5347's contour map can be found in Figure 3.48.

NGC 5548 This spiral galaxy is ringed. There also appears to be a faint outer ring (perhaps a remnant from some polar interaction). The fit to the surface-brightness profile is mediocre, and used only a combination of a bulge and a Gaussian PSF (Figure 3.51); odd that no disk component was needed. Ellipse had some trouble calculating some parameters of the isophotes outside of $20''$ (Figure B.3), but inside this region the PA is twisting slightly while the isophotes are expanding irregularly in several directions. See Figure 3.50 for the contour map of NGC 5548.

NGC 5674 This is a barred spiral galaxy with a ring. There was a certain amount of difficulty in fitting elliptical isophotes to this galaxy (outside of $15''$), as can be seen with the PA and ellipticity profiles in Figure B.6. The fit to the surface-brightness profile is poor, but is partly explained by the artifacts produced by the bar and ring

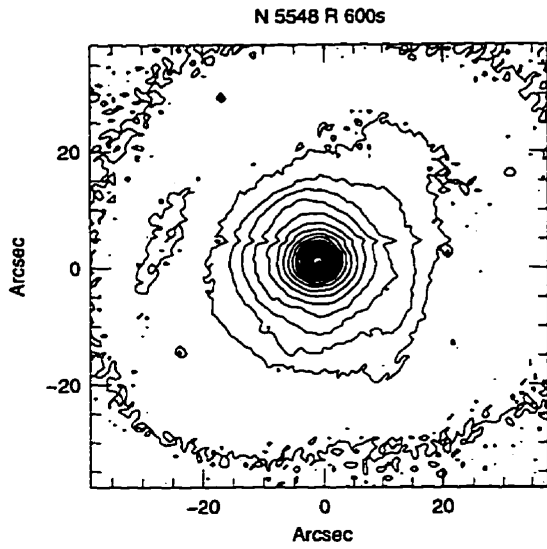


Figure 3.50: Intensity contour map of NGC 5548

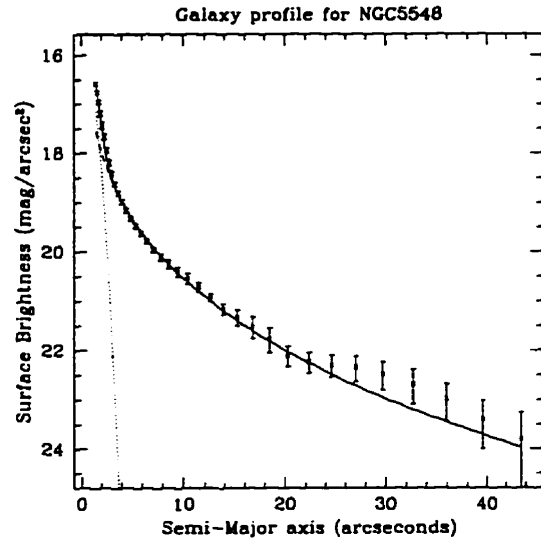


Figure 3.51: Radial profile and fit of NGC 5548. $\chi^2_\nu = 1.07$

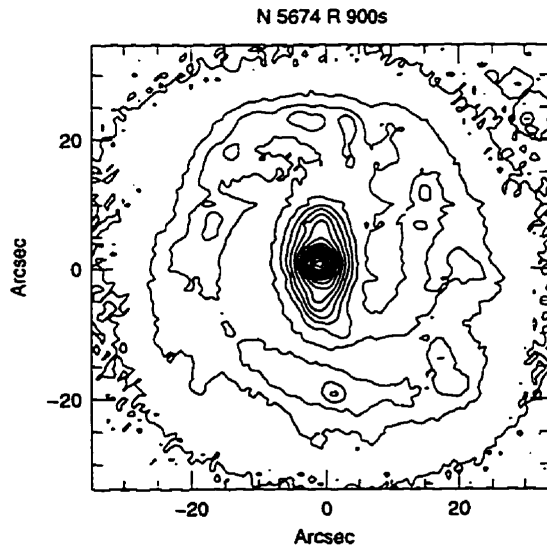


Figure 3.52: Intensity contour map of NGC 5674

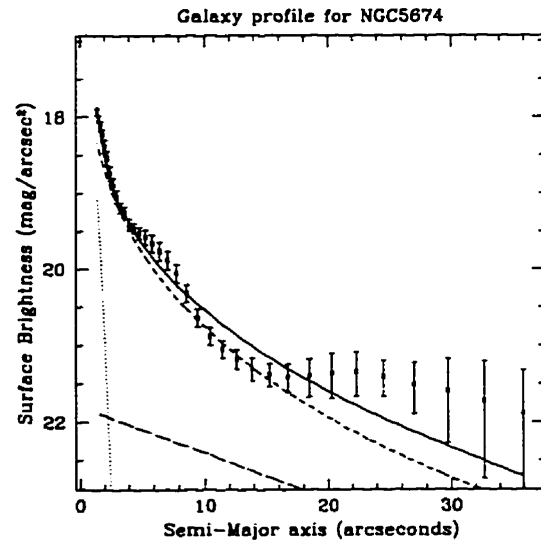


Figure 3.53: Radial profile and fit of NGC 5674. $\chi^2_\nu = 2.74$

(Figure 3.53). The contour map of NGC 5674 can be found in Figure 3.52.

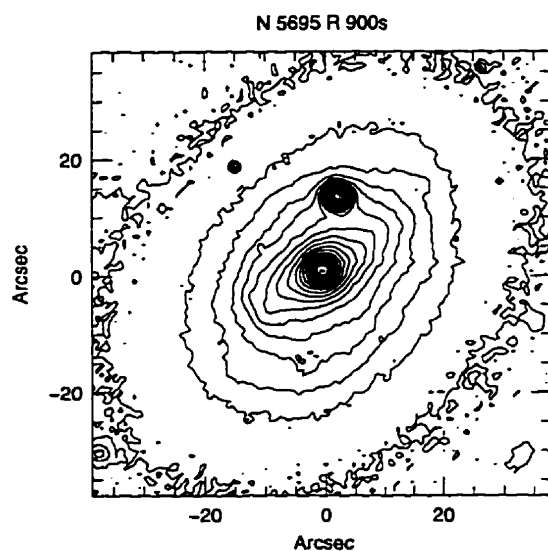


Figure 3.54: Intensity contour map of NGC 5695

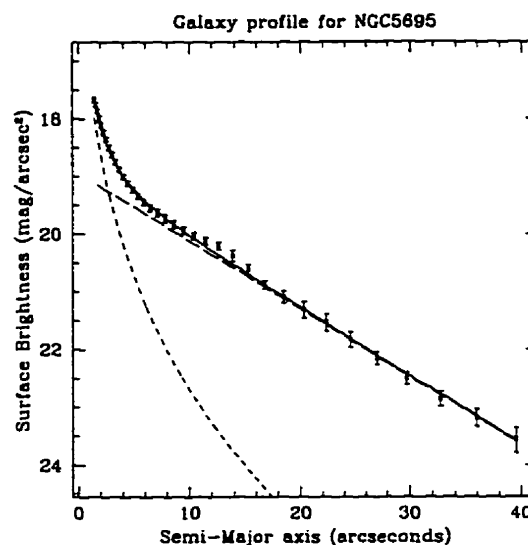


Figure 3.55: Radial profile and fit of NGC 5695. $\chi^2_{\nu} = 0.87$

NGC 5695 This spiral galaxy contains a hint of a bar. The star 15" N was removed prior to isophotal analysis. The surface-brightness profile fits well, but only used bulge and disk components (Figure 3.55). Perhaps the partial bar played some part in the inability to recover a central point source. The PA is steady, and the ellipticity behaves as expected for a barred galaxy (Figure B.5). See Figure 3.54 for the contour map of NGC 5695.

NGC 5929 This spiral galaxy is undergoing an interaction with a close ($< 30''$), spiral galaxy (NGC 5930). The fit to the surface-brightness profile is adequate; however, there was no disk component fit to it (Figure 3.57). The PA twists around slightly, but the ellipticity behaves appropriately (Figure B.6). The contour map of NGC 5929 can be found in Figure 3.56; note that NGC 5930 is at the center of the image.

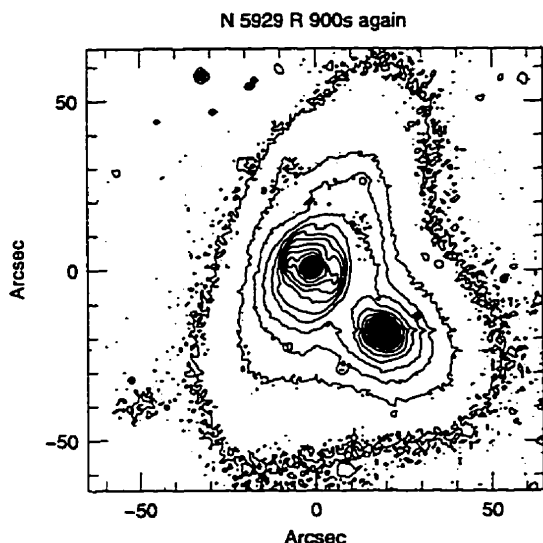


Figure 3.56: Intensity contour map of NGC 5929

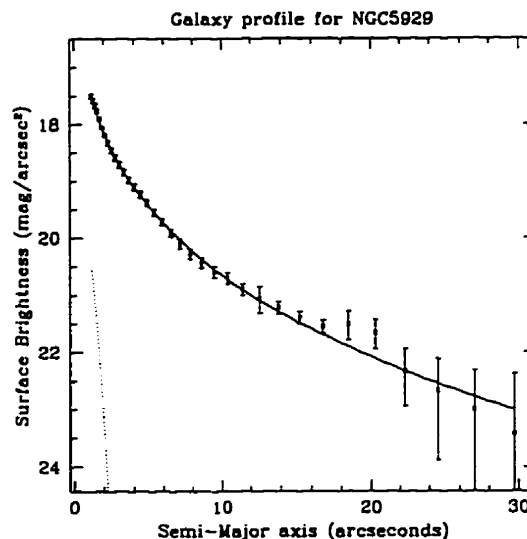


Figure 3.57: Radial profile and fit of NGC 5929. $\chi^2_{\nu} = 0.64$

NGC 5940 This spiral galaxy contains a pronounced bar. The surface-brightness profile fits very well, and uses all three components (Figure 3.59). The PA twists around with the bar and spiral arms, and the ellipticity behaves as a barred galaxy should (Figure B.6). NGC 5940's contour map can be found in Figure 3.58.

NGC 6104 This galaxy seems to be the result of two merging galaxies, currently surrounded by some kind of ring structure. Due to the confusion caused by the merger, no isophotes were fit to this galaxy, and thus no surface-brightness profile is available. See Figure 3.60 for the contour map of NGC 6104.

NGC 6814 This spiral galaxy has a partial bar and partial ring. The galaxy image was contaminated by numerous stars and a man-made satellite passing through, all of which were removed prior to isophotal analysis. The surface-brightness profile fits well, though it only utilized bulge and disk components (Figure 3.62). Perhaps the lack of a Gaussian PSF is due to either the interesting morphological features or the

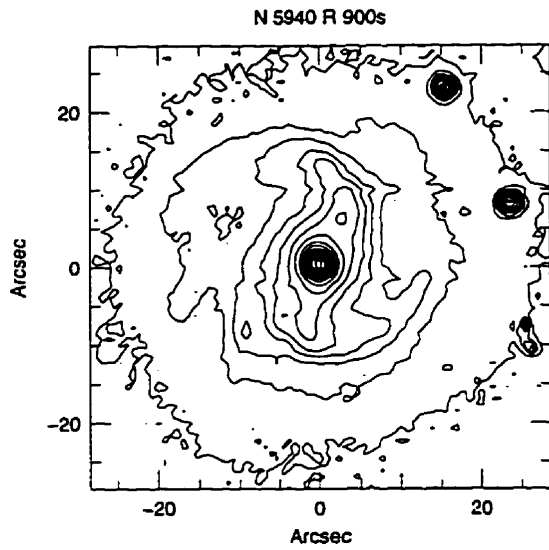


Figure 3.58: Intensity contour map of NGC 5940

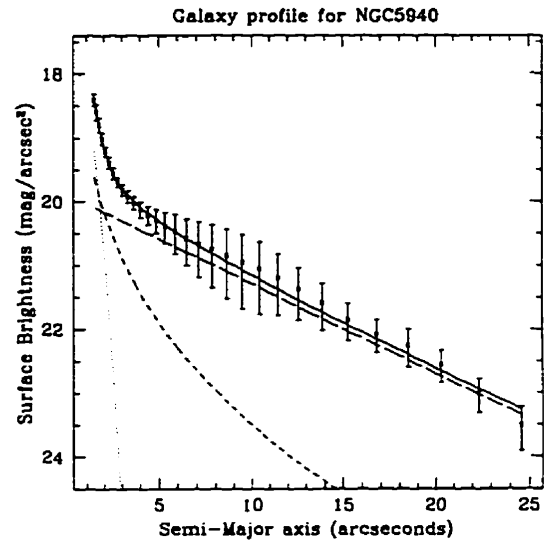


Figure 3.59: Radial profile and fit of NGC 5940. $\chi^2_{\nu} = 0.11$

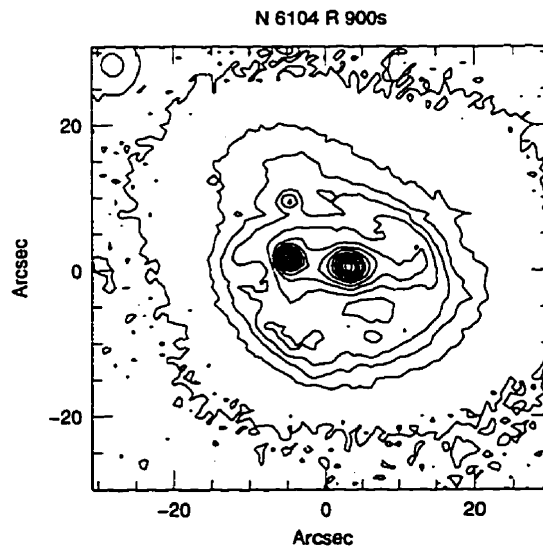


Figure 3.60: Intensity contour map of NGC 6104

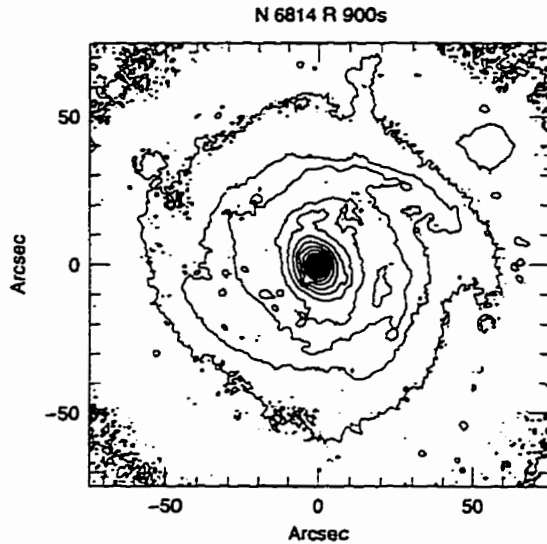


Figure 3.61: Intensity contour map of NGC 6814

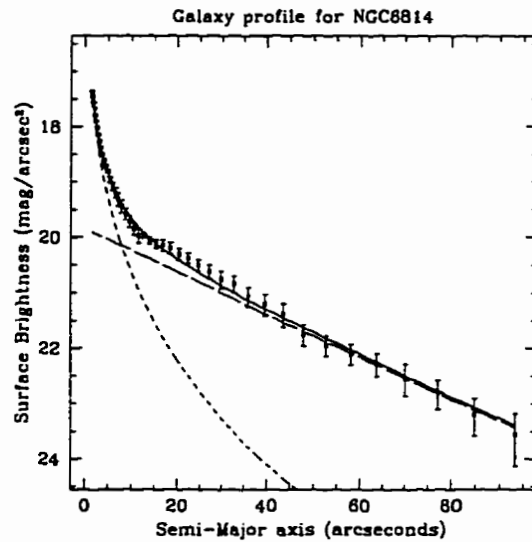


Figure 3.62: Radial profile and fit of NGC 6814. $\chi^2_\nu = 0.66$

image-editing process. The galaxy flattens into a partial bar at 20", and becomes circular beyond that, though the PA twists over a very large range (Figure B.3). The contour map of NGC 6814 can be found in Figure 3.61.

3.3 Summary of Seyfert Galaxy Properties

The following tables summarize much of the information about the individual Seyfert galaxies. Information regarding the basic properties of the host galaxies, image statistics, elliptical isophotal analysis parameters, surface brightness profile results, and companion statistics will be presented.

Table 3.1 shows some basic properties of the Seyfert galaxies, such as their location, magnitude, and redshift. Table 3.2 provides important image statistics for the Seyfert data, including the seeing and the airmass of the exposures. Table 3.3 gives some brief details of the isophotal analysis and the parameters used in the ellipse fitting. Table 3.4 provides the results from the three-component surface-brightness

profile fitting (method I), as well as the fractional luminosity contained in each component. In a similar format, Table 3.5 presents the results from the two-component surface-brightness profile fitting (method II, as outlined at the end of Section 2.4.3 and Section A.2.1), to provide a comparison with the three-component fit so that uniqueness of solutions can be noted. As can be seen, the disk parameters are much more stable than the bulge parameters. A further discussion of these fits follows in Section 5.2.2. Finally, Table 3.6 shows distance, luminosity and companion galaxy-related parameters of the hosts.

Table 3.1: Basic Properties of the Seyfert galaxies in the dataset

Name	$\alpha(1950.0)$	$\delta(1950.0)$	m_R	M_R	z	Type
Mrk 0231	12 ^h 54 ^m 05 ^s 0	+57°08'38"	12.66	-24.36	0.0422	1
Mrk 0461	13 ^h 45 ^m 04 ^s 4	+34°23'57"	13.35	-21.59	0.0162	2
Mrk 0471	14 ^h 20 ^m 46 ^s 8	+33°04'44"	13.46	-23.10	0.0342	1.8
Mrk 0789	13 ^h 29 ^m 55 ^s 4	+11°21'44"	14.06	-22.33	0.0316	1
Mrk 0817	14 ^h 34 ^m 57 ^s 9	+59°00'39"	13.25	-23.13	0.0315	1.5
Mrk 0841	15 ^h 01 ^m 36 ^s 3	+10°37'56"	13.86	-22.82	0.0362	1
UGC 06100	10 ^h 58 ^m 42 ^s 5	+45°55'22"	13.43	-22.79	0.0293	2
UGC 08621	13 ^h 35 ^m 28 ^s 5	+39°24'31"	13.10	-23.31	0.0201	1.8
NGC 3080	09 ^h 57 ^m 14 ^s 2	+13°17'03"	13.91	-22.73	0.0355	1
NGC 3227	10 ^h 20 ^m 46 ^s 8	+20°07'06"	10.52	-21.32	0.0039	1.5
NGC 3362	10 ^h 42 ^m 12 ^s 0	+06°52'00"	12.74	-23.36	0.0277	2
NGC 3516	11 ^h 03 ^m 22 ^s 8	+72°50'20"	11.39	-22.22	0.0088	1.5
NGC 3718	11 ^h 29 ^m 49 ^s 9	+53°20'39"	10.50	-20.97	0.0033	1
NGC 3786	11 ^h 37 ^m 04 ^s 9	+32°11'11"	12.07	-21.57	0.0089	1.8
NGC 3982	11 ^h 53 ^m 53 ^s 0	+55°24'00"	11.28	-20.45	0.0037	2
NGC 4051	12 ^h 00 ^m 36 ^s 4	+44°48'35"	10.40	-20.39	0.0024	1
NGC 4151	12 ^h 08 ^m 01 ^s 1	+39°41'02"	10.32	-21.16	0.0033	1.5
NGC 4235	12 ^h 14 ^m 36 ^s 7	+07°28'09"	11.02	-22.38	0.0080	1
NGC 4253	12 ^h 15 ^m 55 ^s 6	+30°05'26"	12.54	-21.90	0.0129	1.5
NGC 4388	12 ^h 23 ^m 12 ^s 0	+12°56'00"	10.51	-23.01	0.0084	2
NGC 5252	13 ^h 35 ^m 42 ^s 0	+04°47'00"	12.70	-23.01	0.0230	1.9
NGC 5256	13 ^h 36 ^m 14 ^s 7	+48°31'53"	13.27	-22.85	0.0279	2
NGC 5273	13 ^h 39 ^m 55 ^s 1	+35°54'21"	11.57	-20.04	0.0035	1.9
NGC 5283	13 ^h 39 ^m 41 ^s 4	+67°55'27"	12.78	-20.88	0.0090	2
NGC 5347	13 ^h 51 ^m 05 ^s 4	+33°44'00"	12.43	-20.92	0.0078	2
NGC 5548	14 ^h 15 ^m 43 ^s 5	+25°22'01"	12.35	-23.96	0.0192	1.5
NGC 5674	14 ^h 31 ^m 22 ^s 5	+05°40'38"	12.60	-23.27	0.0249	1.9
NGC 5695	14 ^h 35 ^m 19 ^s 7	+36°47'02"	12.48	-22.16	0.0141	2
NGC 5929	15 ^h 24 ^m 18 ^s 9	+41°50'41"	11.86	-21.68	0.0085	2
NGC 5940	15 ^h 28 ^m 51 ^s 5	+07°37'37"	13.26	-23.29	0.0341	1
NGC 6104	16 ^h 14 ^m 40 ^s 1	+35°49'50"	13.21	-22.92	0.0280	1.5
NGC 6814	19 ^h 39 ^m 55 ^s 8	-10°26'33"	10.40	-22.07	0.0052	1

Column 1, name of the galaxy; columns 2-3, the Right Ascension and Declination of they galaxy (from NED); column 4, the apparent magnitude of the host, as measured by M.M. DeRobertis (Paper I); column 5, the absolute magnitude of the host; column 6, the redshift (from NED); and column 7, the Seyfert Type of the galaxy (from NED).

Table 3.2: Image statistics of the Seyfert galaxies

Name	seeing (")	sky ($\frac{\text{mag}}{\text{arcsec}^2}$)	sky σ (ADU)	X	exptime (s)
Mrk 0231	2.30 \pm 0.04	20.09	8.6	1.15	900
Mrk 0461	1.74 \pm 0.08	20.69	6.8	1.06	900
Mrk 0471	2.03 \pm 0.05	20.30	7.6	1.22	900
Mrk 0789	1.57 \pm 0.05	20.61	6.9	1.07	900
Mrk 0817	2.38 \pm 0.06	20.53	6.7	1.20	900
Mrk 0841	2.58 \pm 0.12	20.62	6.7	1.20	900
UGC 06100	2.27 \pm 0.04	19.62	10.5	1.09	900
UGC 08621	1.86 \pm 0.05	20.59	6.8	1.02	900
NGC 3080	1.81 \pm 0.02	19.83	9.7	1.23	900
NGC 3227	1.65 \pm 0.06	20.26	4.8	1.26	300
NGC 3362	1.54 \pm 0.04	20.20	8.1	1.19	900
NGC 3516	2.26 \pm 0.04	19.75	10.3	1.42	900
NGC 3718	1.45 \pm 0.05	20.58	5.8	1.14	600
NGC 3786	2.30 \pm 0.09	19.76	9.9	1.02	900
NGC 3982	1.95 \pm 0.05	20.44	7.4	1.10	900
NGC 4051	1.34 \pm 0.08	20.66	3.9	1.12	300
NGC 4151	2.64 \pm 0.06	19.98	4.8	1.03	226
NGC 4235	1.42 \pm 0.05	20.45	7.4	1.12	900
NGC 4253	1.46 \pm 0.11	20.64	6.6	1.17	900
NGC 4388	2.92 \pm 0.11	19.15	13.0	1.26	900
NGC 5252	1.55 \pm 0.08	20.49	7.0	1.27	900
NGC 5256	2.33 \pm 0.09	20.14	8.3	1.11	900
NGC 5273	2.20 \pm 0.05	19.86	9.6	1.16	900
NGC 5283	1.89 \pm 0.04	20.52	7.2	1.24	1000
NGC 5347	2.34 \pm 0.04	20.15	8.6	1.08	900
NGC 5548	2.15 \pm 0.09	20.69	5.3	1.16	600
NGC 5674	1.85 \pm 0.12	20.66	6.6	1.19	900
NGC 5695	2.21 \pm 0.07	20.82	6.2	1.11	900
NGC 5929	1.68 \pm 0.08	20.71	5.2	1.19	600
NGC 5940	1.89 \pm 0.08	20.74	6.4	1.24	900
NGC 6104	1.71 \pm 0.05	20.78	6.1	1.12	900
NGC 6814	2.01 \pm 0.08	20.52	7.1	1.36	900

Column 1, name; column 2, seeing (this is the FWHM of the PSF); column 3, sky background level; column 4, noise in the image (which I refer to as “sky σ ”); column 5, the airmass at the time of exposure; and column 6, the exposure time.

Table 3.3: Ellipse parameters for the Seyfert galaxies

Name	a_{max} (")	$\langle \varepsilon \rangle$ (1-b/a)	$\langle PA \rangle$ (N-E)
Mrk 0231	25	0.25	-140
Mrk 0461	33	0.3	-50
Mrk 0471	30	0.3	30
Mrk 0789	15	0.3	50
Mrk 0817	13	0.2	130
Mrk 0841	12	0.05	-70
UGC 06100	28	0.35	10
UGC 08621	28	0.05	30
NGC 3080	22	0.1	60
NGC 3227	112	0.5	-30
NGC 3362	35	0.1	40
NGC 3516	53	0.2	40
NGC 3718	159	0.4	-10
NGC 3786	43	0.5	70
NGC 3982	53	0.1	10
NGC 4051	166	0.4	110
NGC 4151	85	0.4	-50
NGC 4235	137	0.75	50
NGC 4253	30	0.2	-75
NGC 4388	166	0.75	-90
NGC 5252	59	0.45	10
NGC 5256	-	-	-
NGC 5273	78	0.15	10
NGC 5283	40	0.15	-70
NGC 5347	36	0.6	100
NGC 5548	44	0.05	80
NGC 5674	36	0.45	00
NGC 5695	40	0.3	-40
NGC 5929	30	0.1	40
NGC 5940	25	0.3	10
NGC 6104	-	-	-
NGC 6814	94	0.1	00

Column 1, name; column 2, maximum semi-major axis length used in the ellipse fitting; column 3, approximate ellipticity of the galaxy near the outer edge of the profile; and column 4; approximate Position Angle of the major-axis of the galaxy near the edge.

Table 3.4: surface-brightness profile parameters for the Seyfert galaxies

Name	r_0 (kpc)	r_e (kpc)	μ_d (mag/arcsec ²)	μ_b	μ_N	χ^2_ν	LD (%)	LB (%)	LN (%)
Mrk 0231	10.1	0.8	20.76	14.98	–	0.31	13	87	00
Mrk 0461	2.5	0.9	19.38	18.90	–	0.07	59	41	00
Mrk 0471	3.4	55.4	18.28	25.07	–	0.67	62	38	00
Mrk 0789	1.6	24.5	17.45	25.03	17.48	0.11	73	18	09
Mrk 0817	3.2	4.6	18.41	22.21	16.60	0.98	61	12	27
Mrk 0841	2.3	–	18.74	–	16.59	4.02	38	00	62
UGC 06100	4.8	14.5	21.07	22.34	–	0.52	13	87	00
UGC 08621	3.0	–	18.59	–	19.18	0.44	99	00	01
NGC 3080	4.1	19.0	19.93	23.49	18.89	1.17	36	60	03
NGC 3227	3.5	0.3	18.40	16.87	14.05	0.68	88	09	03
NGC 3362	7.2	0.4	19.43	17.51	–	0.41	92	08	00
NGC 3516	5.3	1.3	20.88	18.38	16.96	4.86	26	71	03
NGC 3718	4.1	2.0	20.13	21.74	16.83	0.32	82	17	01
NGC 3786	4.5	0.5	19.76	17.92	–	0.82	78	22	00
NGC 3982	1.4	1.3	19.16	21.23	–	2.99	71	29	00
NGC 4051	3.5	0.3	19.91	18.51	–	2.42	92	08	00
NGC 4151	2.4	0.5	20.02	17.96	14.96	1.73	42	48	10
NGC 4235	9.5	11.9	20.41	22.34	–	0.47	54	46	00
NGC 4253	2.3	1.1	18.52	19.93	14.78	0.62	65	15	20
NGC 4388	7.8	57.2	19.72	24.38	–	0.23	47	53	00
NGC 5252	5.2	13.4	19.70	22.03	–	0.18	31	69	00
NGC 5256	–	–	–	–	–	–	–	–	–
NGC 5273	2.8	1.0	20.26	20.55	–	2.39	71	29	00
NGC 5283	4.8	1.1	21.95	19.33	–	0.37	23	77	00
NGC 5347	19.8	5.6	21.40	22.55	19.10	0.60	51	48	01
NGC 5548	–	7.3	–	21.15	15.78	1.07	00	82	18
NGC 5674	12.3	22.0	21.79	22.85	17.33	2.74	20	76	04
NGC 5695	3.7	0.8	18.95	18.70	–	0.87	80	20	00
NGC 5929	–	3.6	–	21.45	19.08	0.64	00	99	01
NGC 5940	7.2	4.4	19.89	21.80	17.52	0.11	73	19	08
NGC 6104	–	–	–	–	–	–	–	–	–
NGC 6814	4.2	1.5	19.85	20.70	–	0.66	80	20	00

Column 1, name; column 2, scale radius of the disk; column 3, effective radius of the bulge; column 4, central surface brightness of the disk; column 5, effective surface brightness of the bulge; column 6, central surface brightness of the Gaussian PSF; column 7, the reduced chi-squared goodness of fit of the model; columns 8-10, the fractional luminosity contained in each the disk, bulge, and PSF respectively.

Table 3.5: surface-brightness profile parameters for the Seyfert galaxies, method II.

Name	r_0 (kpc)	r_e (kpc)	μ_d mag/arcsec ²	μ_b mag/arcsec ²	μ_N mag/arcsec ²	χ^2_ν	LD (%)	LB (%)	LN (%)
Mrk 0231	9.6	0.7	20.60	14.69	19.15	0.34	13	86	01
Mrk 0461	2.6	0.3	19.36	15.60	–	0.07	41	59	00
Mrk 0471	3.0	24.3	18.32	23.36	–	0.81	44	56	00
Mrk 0789	1.2	20.1	16.16	24.52	–	0.07	86	14	00
Mrk 0817	3.3	5.1	18.44	22.47	16.51	1.69	60	11	29
Mrk 0841	2.4	6.4	18.91	24.20	16.57	8.70	33	05	62
UGC 06100	4.0	18.2	20.17	22.88	18.74	0.24	21	76	03
UGC 08621	2.9	–	18.49	–	20.36	0.21	100	00	00
NGC 3080	3.4	20.5	19.92	23.38	19.97	0.57	25	74	01
NGC 3227	3.5	0.2	18.39	16.04	14.25	0.85	87	10	02
NGC 3362	6.9	–	19.33	–	16.28	0.10	91	00	09
NGC 3516	14.3	2.1	22.53	19.28	15.66	4.20	14	77	09
NGC 3718	4.3	11.8	20.84	23.72	14.26	0.21	42	54	04
NGC 3786	4.2	0.1	19.60	14.05	–	0.92	59	41	00
NGC 3982	1.3	1.0	18.79	21.43	17.09	2.07	82	16	02
NGC 4051	4.1	0.7	20.12	20.46	13.40	1.25	86	09	05
NGC 4151	3.9	0.8	20.78	18.93	14.65	1.21	36	51	13
NGC 4235	9.6	10.5	20.37	22.17	–	0.53	56	44	00
NGC 4253	2.2	1.3	18.33	21.25	14.22	0.38	65	05	30
NGC 4388	7.3	69.3	19.78	24.51	–	0.19	40	60	00
NGC 5252	5.8	10.8	19.80	21.70	–	0.14	36	64	00
NGC 5256	–	–	–	–	–	–	–	–	–
NGC 5273	2.6	0.7	20.09	20.15	–	1.24	74	26	00
NGC 5283	4.5	1.0	21.76	19.02	–	0.47	24	76	00
NGC 5347	99.9	8.4	21.93	23.02	18.48	0.22	41	58	01
NGC 5548	16.0	7.3	23.02	21.23	15.65	0.29	10	71	19
NGC 5674	–	19.7	–	22.55	17.47	2.67	00	96	04
NGC 5695	3.5	0.2	18.72	18.26	16.46	0.45	90	01	09
NGC 5929	–	4.0	–	21.62	17.88	0.63	00	98	02
NGC 5940	6.5	2.2	19.50	23.23	16.88	0.11	85	01	14
NGC 6104	–	–	–	–	–	–	–	–	–
NGC 6814	3.6	0.1	19.45	12.82	–	0.24	56	44	00

Column 1, name; column 2, scale radius of the disk; column 3, effective radius of the bulge; column 4, central surface brightness of the disk; column 5, effective surface brightness of the bulge; column 6, central surface brightness of the Gaussian PSF; column 7, the reduced chi-squared goodness of fit of the model; columns 8-10, the fractional luminosity contained in each the disk, bulge, and PSF respectively.

Table 3.6: Distance and luminosity parameters for the Seyfert galaxies

Name	d_β (Mpc)	imscale (kpc/'')	A_{gal} (mag)	L (L^*)	N	Q (L^*/Mpc^3)
Mrk 0231	235	1.142	0.00	6.91	3	3.29×10^2
Mrk 0461	94	0.458	0.00	0.59	27	2.88×10^3
Mrk 0471	193	0.938	0.00	2.23	11	1.51×10^3
Mrk 0789	179	0.870	0.00	1.11	11	3.29×10^2
Mrk 0817	179	0.868	0.00	2.32	18	6.04×10^3
Mrk 0841	204	0.988	0.04	1.72	10	1.18×10^2
UGC 06100	167	0.810	0.00	1.71	8	6.27×10^2
UGC 08621	116	0.565	0.00	1.13	16	2.98×10^2
NGC 3080	200	0.971	0.03	1.58	10	4.08×10^2
NGC 3227	23	0.113	0.01	0.49	8	3.01×10^4
NGC 3362	158	0.768	0.03	2.90	13	3.84×10^2
NGC 3516	52	0.252	0.05	1.08	8	1.27×10^3
NGC 3718	20	0.095	0.00	0.35	28	6.59×10^2
NGC 3786	53	0.255	0.00	0.59	6	6.39×10^4
NGC 3982	22	0.106	0.00	0.22	21	1.45×10^3
NGC 4051	14	0.070	0.00	0.21	8	1.55×10^4
NGC 4151	20	0.095	0.00	0.42	5	1.81×10^3
NGC 4235	47	0.230	0.00	1.26	15	1.96×10^2
NGC 4253	76	0.366	0.05	0.80	10	2.69×10^2
NGC 4388	50	0.240	0.06	2.23	11	1.99×10^3
NGC 5252	133	0.643	0.01	2.11	14	3.89×10^2
NGC 5256	159	0.773	0.00	1.81	10	1.54×10^7
NGC 5273	21	0.101	0.00	0.15	10	2.88×10^3
NGC 5283	53	0.198	0.02	0.32	12	9.65×10^3
NGC 5347	46	0.223	0.00	0.33	7	7.59×10^3
NGC 5548	111	0.540	0.00	2.06	15	4.31×10^2
NGC 5674	143	0.694	0.03	2.70	8	5.43×10^3
NGC 5695	82	0.400	0.00	1.00	4	1.83×10^2
NGC 5929	50	0.244	0.03	0.66	6	8.26×10^5
NGC 5940	193	0.935	0.05	2.67	6	1.61×10^2
NGC 6104	160	0.775	0.00	1.92	13	9.02×10^6
NGC 6814	31	0.149	0.34	0.95	8	2.46×10^3

Column 1, name; column 2, distance, based on angular distance derived from the galaxy's redshift; column 3, image scale, based on projected distance at the distance of the host galaxy; column 4, R -band Galactic extinction (from NED); column 5, absolute R luminosity; column 6, number of optical companion galaxies found; and column 7, cumulative tidal effect of the companion galaxies upon the host.

Chapter 4

Discussion of Control Galaxies

4.1 Introduction

Using the techniques outlined in Chapter 2, the reduction of the 49 control galaxies will be discussed in this chapter. Results of the image analysis including contour maps and surface-brightness profiles of the galaxies will be presented. Quantities derived and computed from this analysis such as magnitudes, distances, and properties of the galaxies will also be presented.

4.2 Analysis

This section will present images of the control galaxies, their surface-brightness profiles, and a brief discussion regarding the reduction of each galaxy. The presentation of this data is in the same format and style as in Chapter 3, and similarly includes a discussion about morphology, surface-brightness profile goodness of fit, and isophotal behaviour. What follows in Section 4.2.1, are the galaxy contour images, surface-brightness profiles, and a description of each galaxy in the Seyfert data set.

4.2.1 The Galaxies

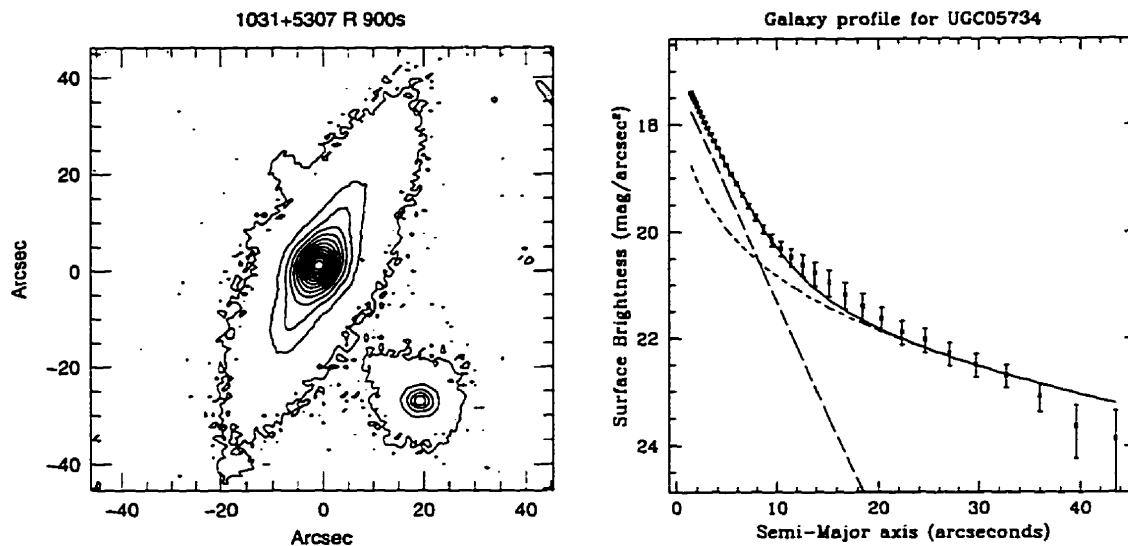


Figure 4.1: Intensity contour map of UGC 05734

Figure 4.2: Radial profile and fit of UGC 05734. $\chi^2_\nu = 0.58$

UGC 05734 This spiral galaxy has a hint of a bar. There are several small close companion galaxies. The surface-brightness profile fits well, though it could be improved with better data (Figure 4.2). The PA is very steady, and the ellipticity also behaves well (Figure B.20). An alternatively used name of this galaxy is 1031+5307. See Figure 4.1 for the contour map of UGC 05734.

UGC 07064 This spiral contains both a bar and a ring. The fit to the surface-brightness profile is poor, even after removing six data points from the ring (Figure 4.4). The PA twists slightly with the bar in the inner 10'' (Figure B.12). UGC 07064's alternative name is 1202+3127. The contour map of UGC 07064 is found in Figure 4.3.

UGC 09295 This spiral galaxy is very plain looking. The fit to the surface-brightness profile is poor, which contains some unusual fluctuations, and consists of only a disk component (Figure 4.6). The PA is very steady, and the ellipticity behaves as expected (Figure B.11). An alternative name for UGC 09295 is 1426+7010.

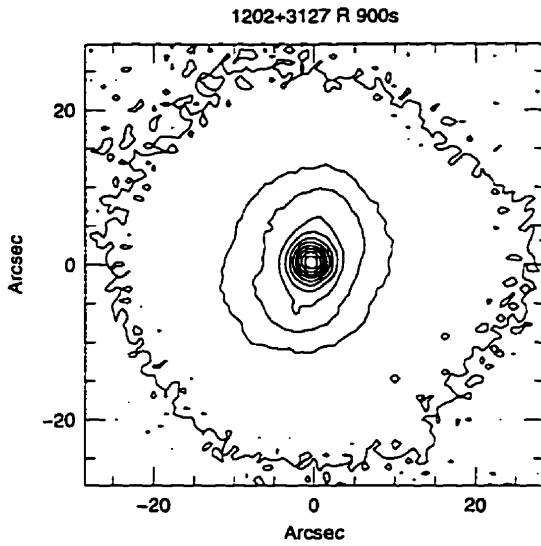


Figure 4.3: Intensity contour map of UGC 07064

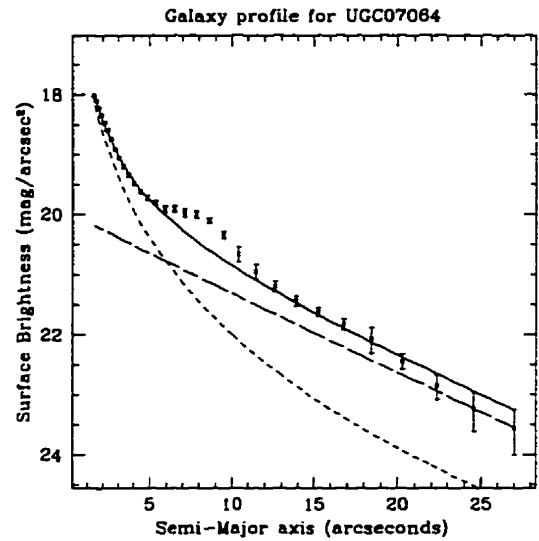


Figure 4.4: Radial profile and fit of UGC 07064. $\chi^2_{\nu} = 2.12$

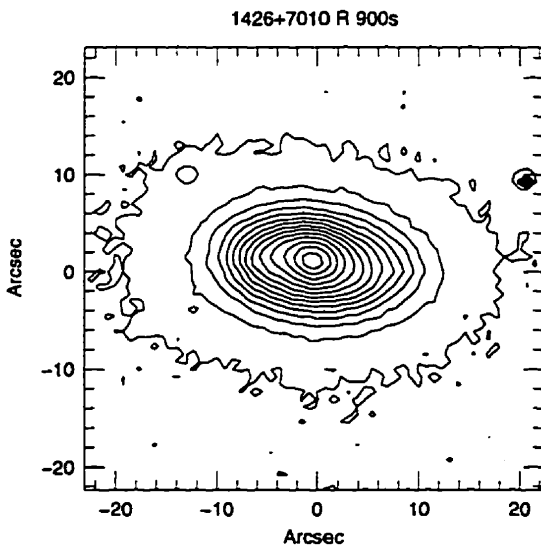


Figure 4.5: Intensity contour map of UGC 09295

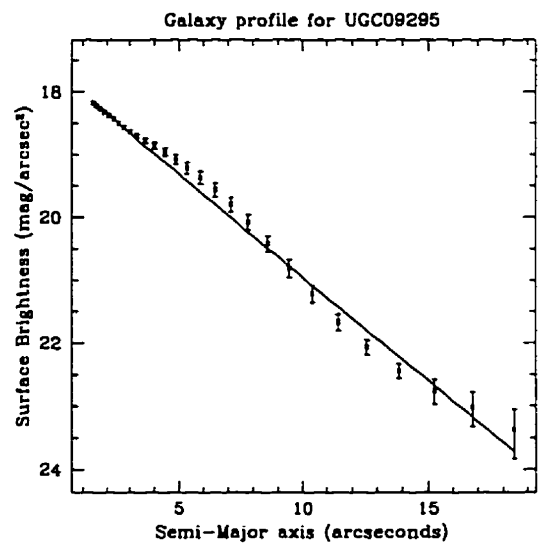


Figure 4.6: Radial profile and fit of UGC 09295. $\chi^2_{\nu} = 3.17$

UGC 09295's contour map is found in Figure 4.5.

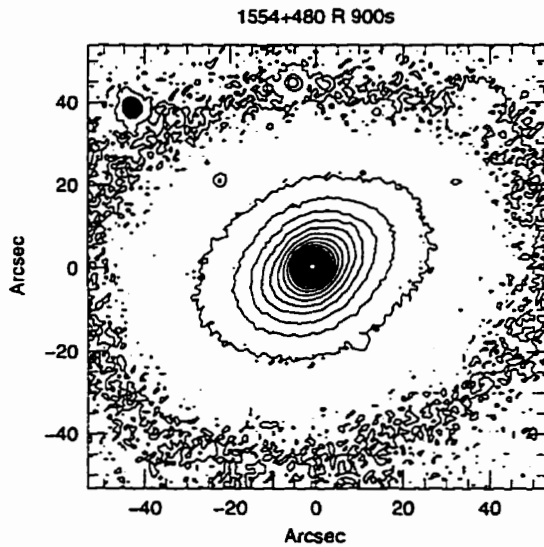


Figure 4.7: Intensity contour map of UGC 10097

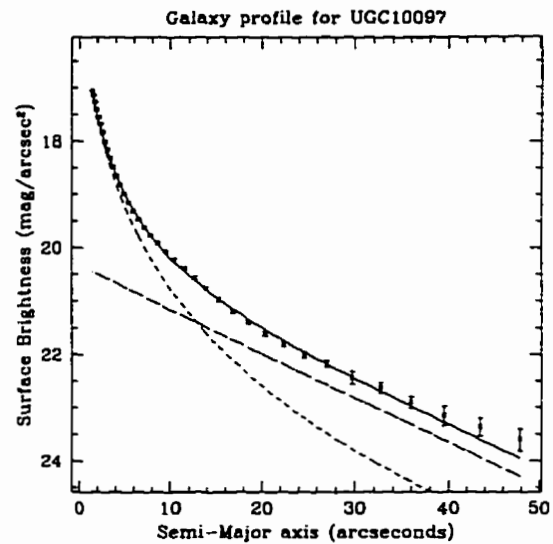


Figure 4.8: Radial profile and fit of UGC 10097. $\chi^2_{\nu} = 2.74$

UGC 10097 This is a normal looking spiral galaxy, with a close small companion galaxy 40" to the N. The fit to the surface-brightness profile is numerically poor, though it visually appears very acceptable (Figure 4.8). The PA twists very slightly throughout the galaxy, and the ellipticity appears well behaved (Figure B.12). An alternative name for this galaxy is 1554+480. The contour map of UGC 10097 is found in Figure 4.7.

UGC 10407 This galaxy is undergoing a merger or interaction, there is evidence of about three nuclei, and the resulting galaxy is very asymmetrically shaped. As a result, no isophotal analysis was performed on this galaxy, and thus no surface-brightness profile is available; however, its contour map can be seen in Figure 4.9. This galaxy is also called 1626+420.

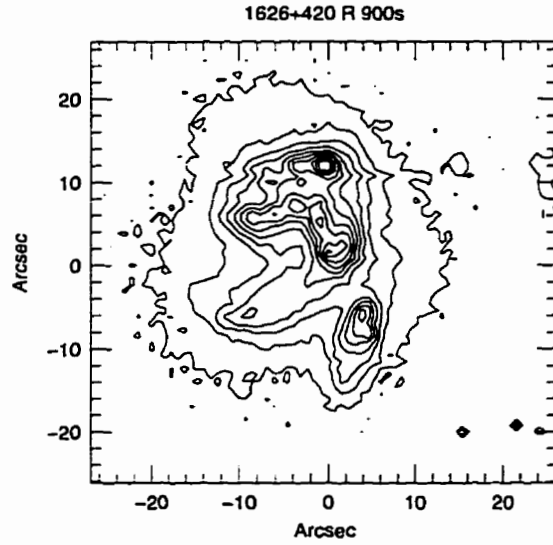


Figure 4.9: Intensity contour map of UGC 10407

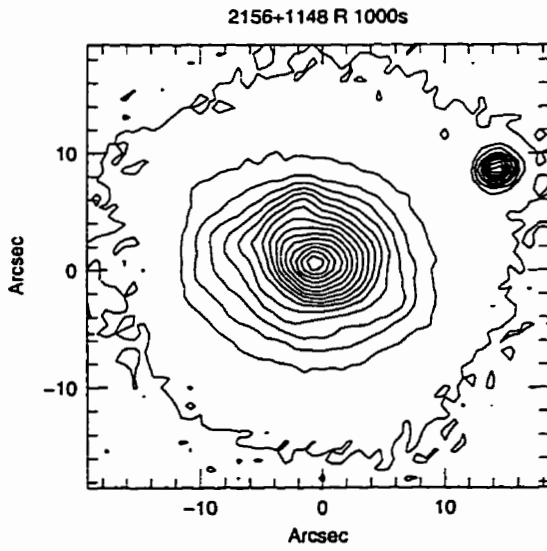


Figure 4.10: Intensity contour map of UGC 11865

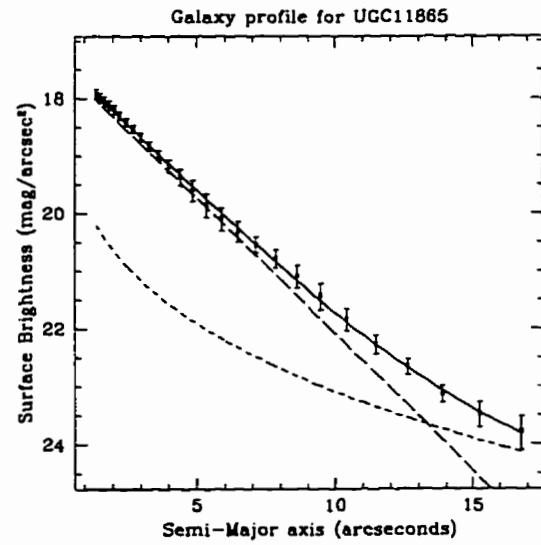


Figure 4.11: Radial profile and fit of UGC 11865. $\chi^2_\nu = 0.11$

UGC 11865 This spiral galaxy has a peculiar, asymmetric shape. There are a couple of small, very close companions within 10'' of the host, though the object 18'' to the NW is a foreground star. The surface-brightness profile fits very well, with a dominant disk component (Figure 4.11). The PA and ellipticity vary somewhat across the galaxy, following the asymmetries of the isophotes (Figure B.21). An alternative name of this galaxy 2156+1148; its contour map can be found in Figure 4.10.

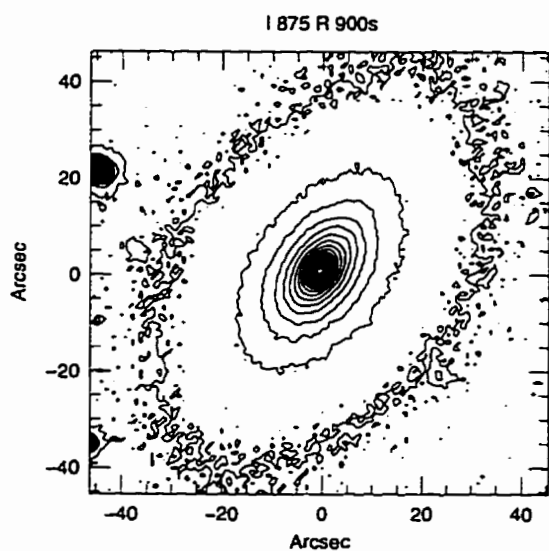


Figure 4.12: Intensity contour map of IC 875

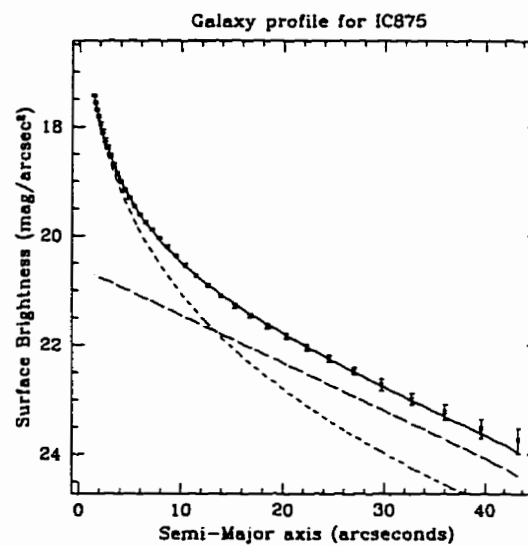


Figure 4.13: Radial profile and fit of IC 875. $\chi^2_{\nu} = 0.75$

IC 875 This galaxy is a very ordinary looking galaxy. There is a small companion 30'' away to the SW. The surface-brightness profile fits well as can be seen in Figure 4.13. The PA is very steady and the ellipticity behaves very well (Figure B.9). IC 875's contour map can be found in Figure 4.12.

IC 1141 This is a normal spiral galaxy. The surface-brightness profile fits well (Figure 4.15); the star to the SW was removed before the fit was performed. The

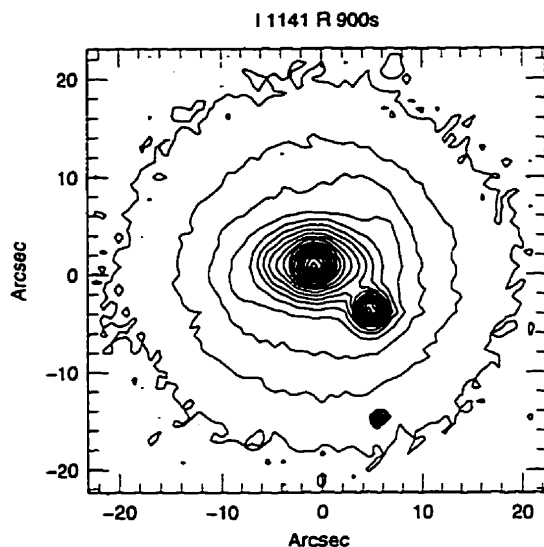


Figure 4.14: Intensity contour map of IC 1141

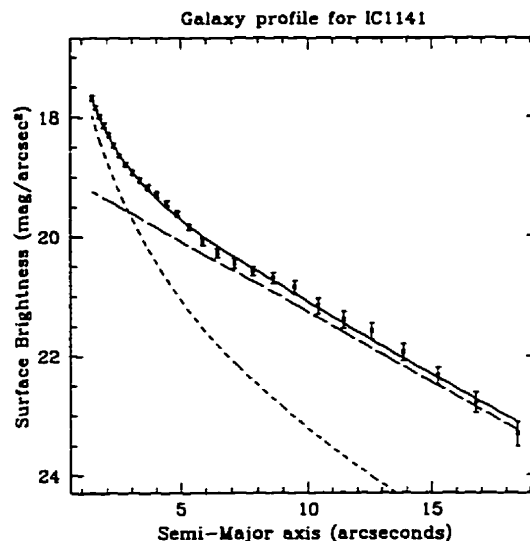


Figure 4.15: Radial profile and fit of IC 1141. $\chi^2_{\nu} = 0.85$

PA profile is steady, and the ellipticity behaves reasonably well (Figure B.11). The contour map of IC 1141 can be seen in Figure 4.14.

NGC 3169 This is a spiral galaxy with prominent dust lanes, and a very large companion galaxy (NGC 3166) 7.5' away (60 kpc projected distance) to the W. There are extended regions of the galaxy which may be tidally induced by NGC 3166. The fit to the surface-brightness profile is relatively poor (Figure 4.17), though it could be partly explained by perturbations from NGC 3166. The PA is very steady, though the ellipticity takes an unusual dip at 30" (Figure B.11). NGC 3169's contour map can be seen in Figure 4.16.

NGC 3492 This is a merging/interacting galaxy with two nuclei present, as well as a very close companion galaxy (12" SW, 12 kpc projected distance). The SW companion was deblended from the host prior to analysis, and the isophotal analysis was performed using a minimum radius outside of the double nuclei (starting at 5").

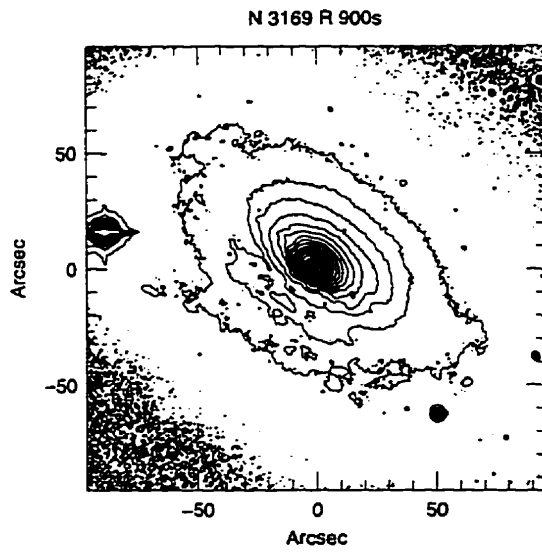


Figure 4.16: Intensity contour map of NGC 3169

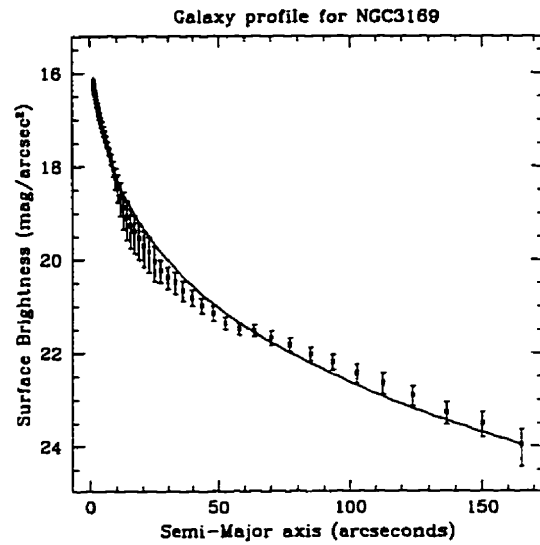


Figure 4.17: Radial profile and fit of NGC 3169. $\chi^2_{\nu} = 2.04$

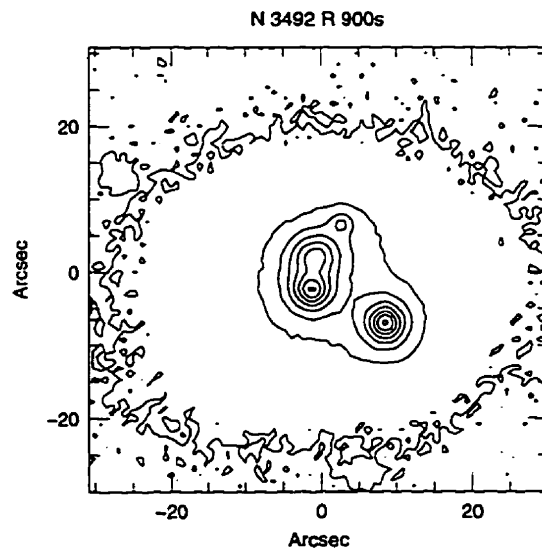


Figure 4.18: Intensity contour map of NGC 3492

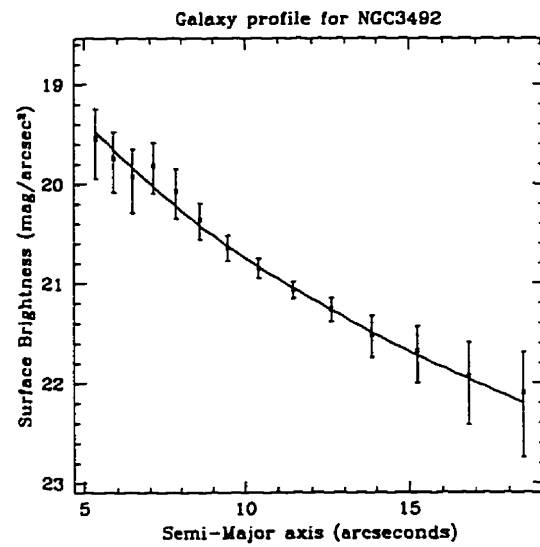


Figure 4.19: Radial profile and fit of NGC 3492. $\chi^2_{\nu} = 0.20$

The surface-brightness profile fits very well with just a bulge component (Figure 4.19), though a sole disk component would fit reasonably well also. The PA twists slightly in this range, and the ellipticity behaves well (Figure B.9). The contour map of NGC 3492 can be found in Figure 4.18.

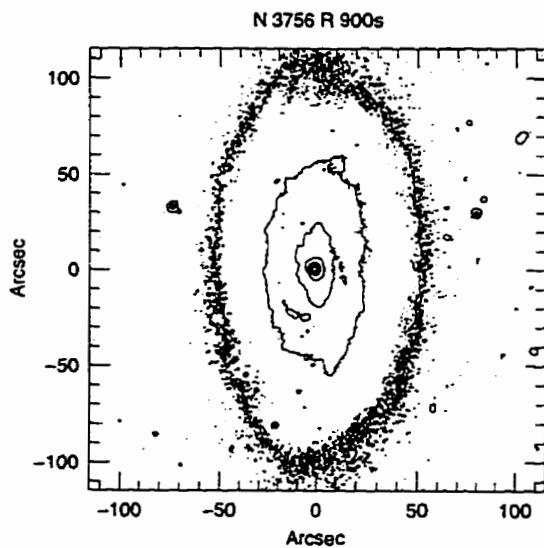


Figure 4.20: Intensity contour map of NGC 3756

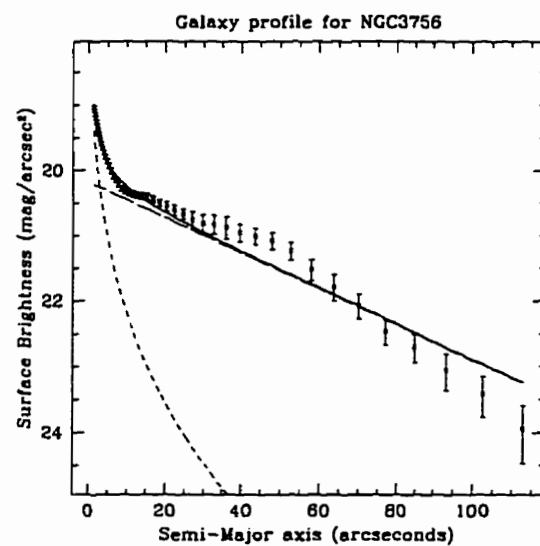


Figure 4.21: Radial profile and fit of NGC 3756. $\chi^2_{\nu} = 2.45$

NGC 3756 This is a relatively normal spiral galaxy. There are some isophotal irregularities at $40''$. The fit to the surface-brightness profile is poor, caused by some of the isophotal asymmetries (Figure 4.21). The PA is mostly steady, and the ellipticity behaves well (Figure B.16). See Figure 4.20 for the contour map of NGC 3756.

NGC 3825 This spiral galaxy contains a prominent bar. The fit to the surface-brightness profile is numerically very poor (Figure 4.23), even after removing 5 data points caused by the bar at $10''$; however, the fit appears visually acceptable. The PA twists nearly 180° as the isophotes follow the bar and the spiral arms, and the ellipticity fluctuates following the same features (Figure B.17). The contour map of

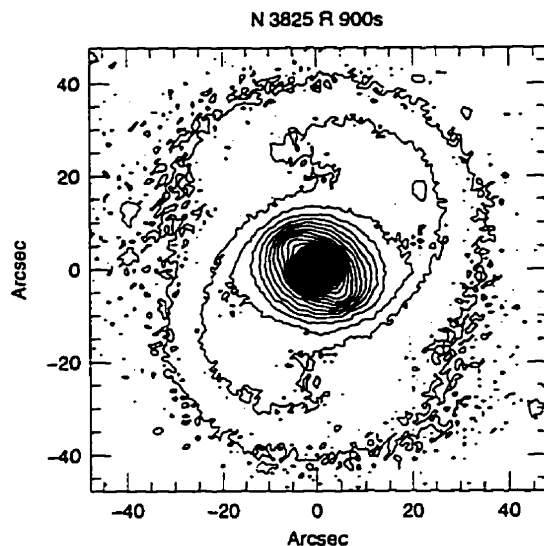


Figure 4.22: Intensity contour map of NGC 3825

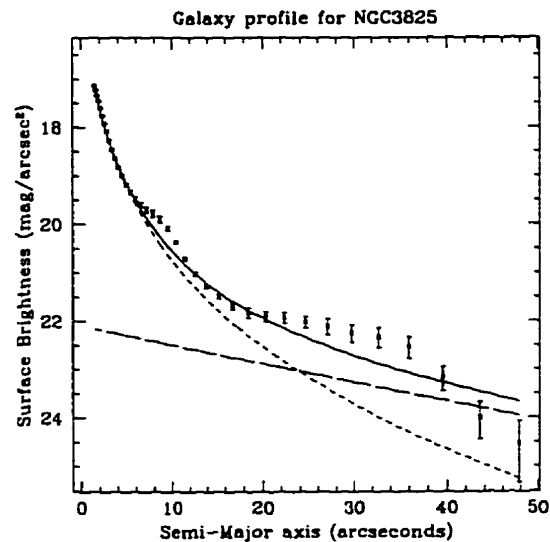


Figure 4.23: Radial profile and fit of NGC 3825. $\chi^2_\nu = 5.08$

NGC 3825 is found in Figure 4.22; please note the the contour levels are at 0.10 magnitude increments.

NGC 3938 This galaxy has bright, clumpy spiral arms, with many small close companions (most likely large spiral clumps or H II regions). The fit to the surface-brightness profile is mediocre (Figure 4.25). The PA fluctuates all over the place, and the ellipticity behaves somewhat oddly as well (Figure B.12). NGC 3938's contour map can be found in Figure 4.24.

NGC 3968 This spiral galaxy contains a bar. The fit to the surface-brightness profile is numerically poor, though acceptable visually (Figure 4.27). The PA undergoes a very rapid perpendicular twist where the bar ends at 20'' (Figure B.17). See Figure 4.26 for NGC 3968's contour map.

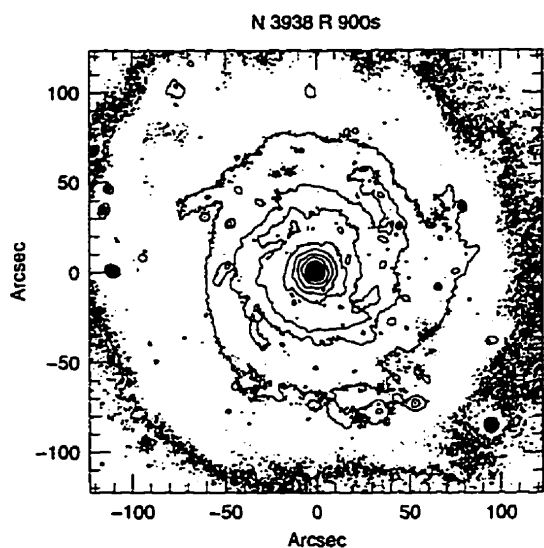


Figure 4.24: Intensity contour map of NGC 3938

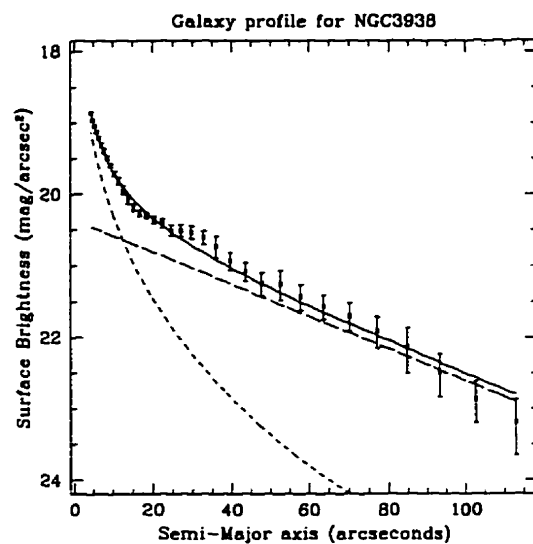


Figure 4.25: Radial profile and fit of NGC 3938. $\chi^2_{\nu} = 1.37$

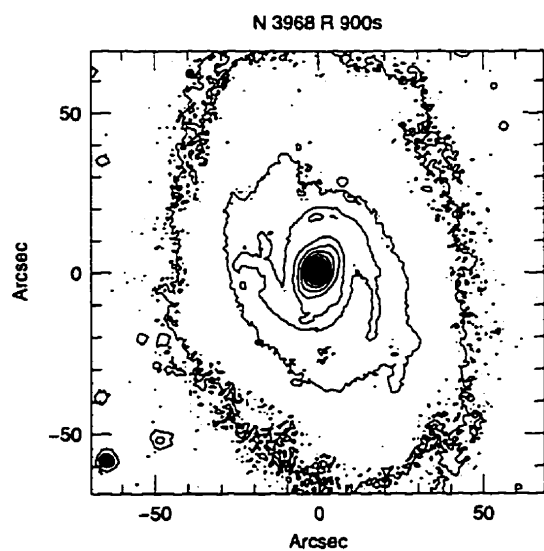


Figure 4.26: Intensity contour map of NGC 3968

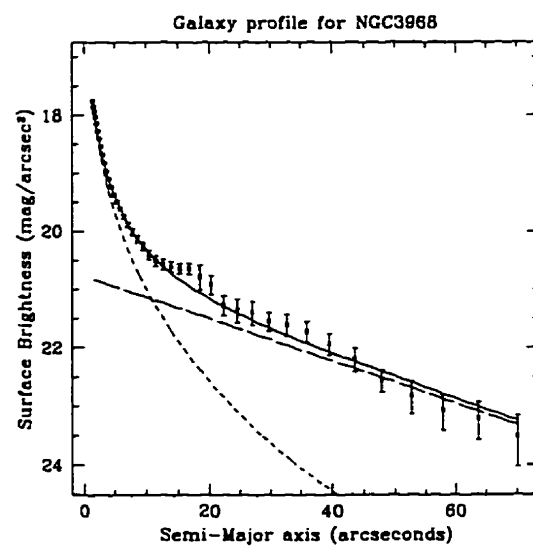


Figure 4.27: Radial profile and fit of NGC 3968. $\chi^2_{\nu} = 2.39$

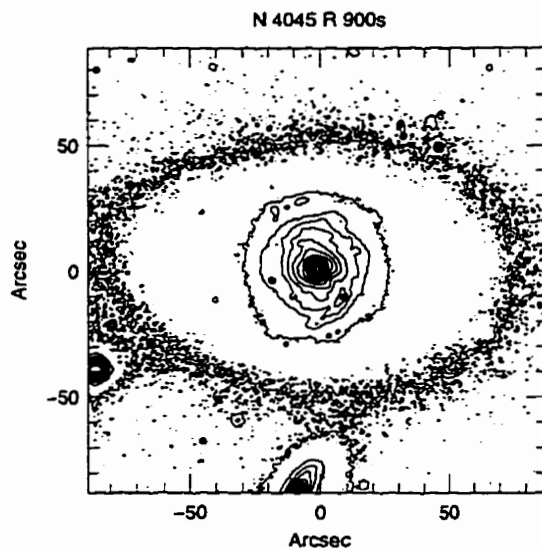


Figure 4.28: Intensity contour map of NGC 4045

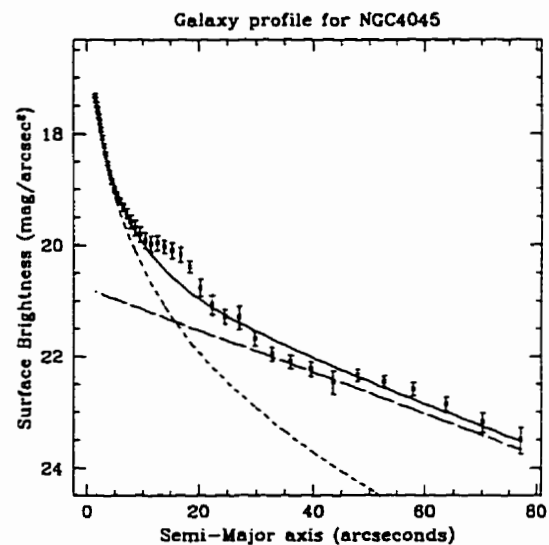


Figure 4.29: Radial profile and fit of NGC 4045. $\chi^2_{\nu} = 2.67$

NGC 4045 This spiral galaxy contains a partial bar and an extended envelope. There is a close companion galaxy to the S at $1.5'$. Numerically, the surface-brightness profile fits poorly, though it is visually acceptable (Figure 4.29). The PA twist around several times, and the ellipticity varies drastically at the same location (Figure B.13). The contour map of NGC 4045 can be found in Figure 4.28.

NGC 4048 This spiral galaxy contains an object that looks like a warped bar. There are two close companions about $30''$ away to the SE and NW. Due to the presence of this warped bar, the fit to the surface-brightness profile is poor, and consists of only a disk component (Figure 4.31). The PA remains steady throughout the bar, and the ellipticity behaves reasonably well (Figure B.19). NGC 4048's contour map is found in Figure 4.30.

NGC 4088 This spiral galaxy has a bar, and an extended feature to the NE. The noise is very bad in this image, and as a consequence, the surface-brightness profile fits

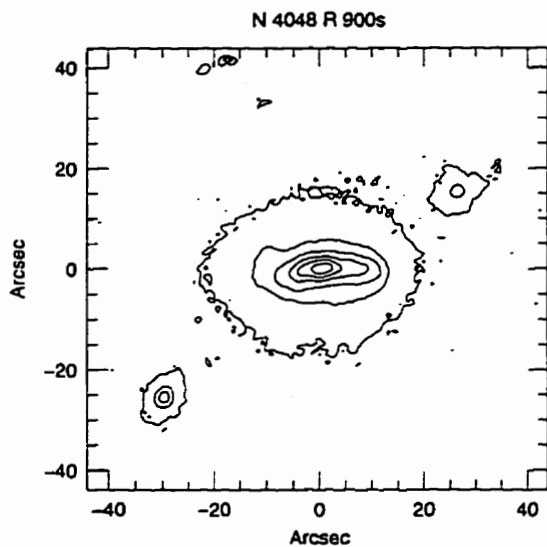


Figure 4.30: Intensity contour map of NGC 4048

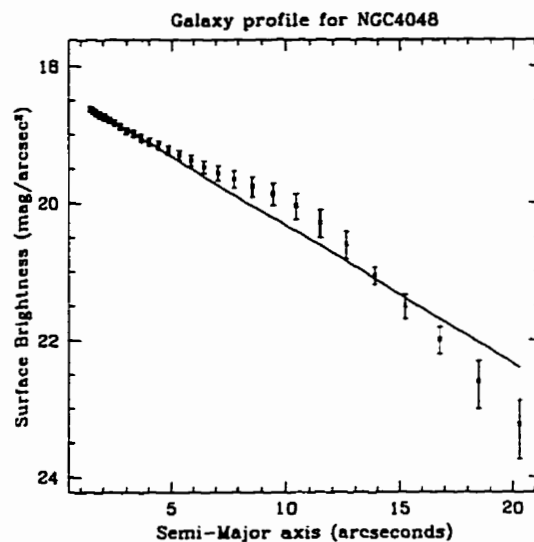


Figure 4.31: Radial profile and fit of NGC 4048. $\chi^2_{\nu} = 2.03$

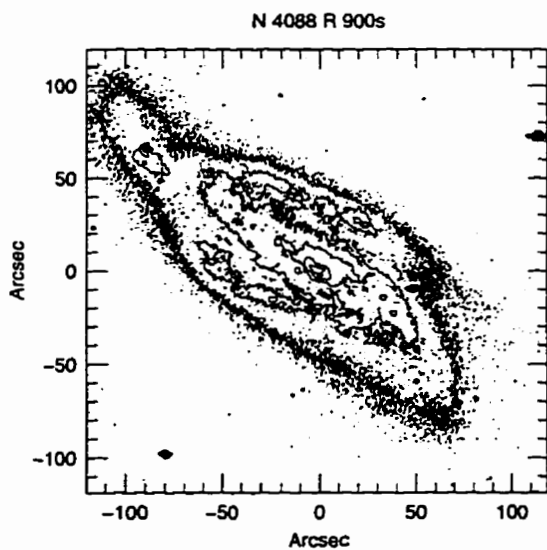


Figure 4.32: Intensity contour map of NGC 4088

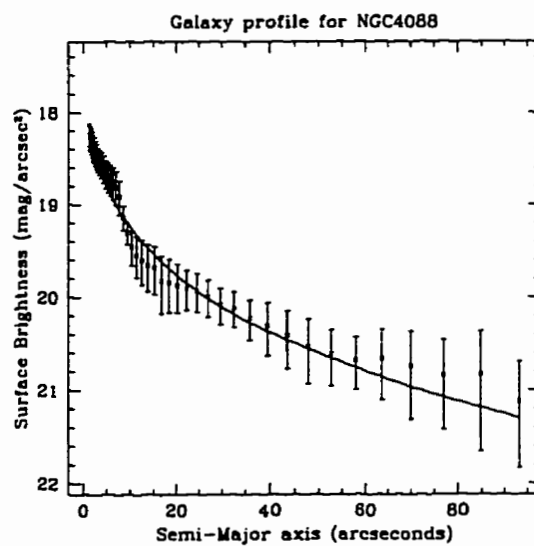


Figure 4.33: Radial profile and fit of NGC 4088. $\chi^2_{\nu} = 0.40$

well numerically, but the resulting parameters are somewhat unrealistic (Figure 4.33). The PA twists somewhat in the inner 20", after which the PA and ellipticity data become bad (Figure B.18). The contour map of NGC 4088 can be found in Figure 4.32, please note that the contour levels are at 0.5 magnitude increments.

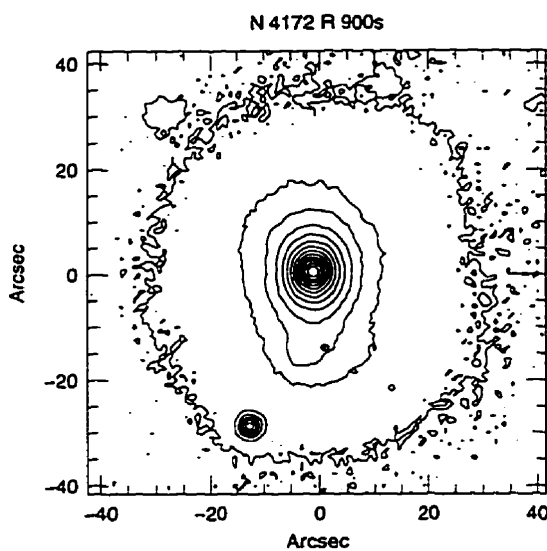


Figure 4.34: Intensity contour map of NGC 4172

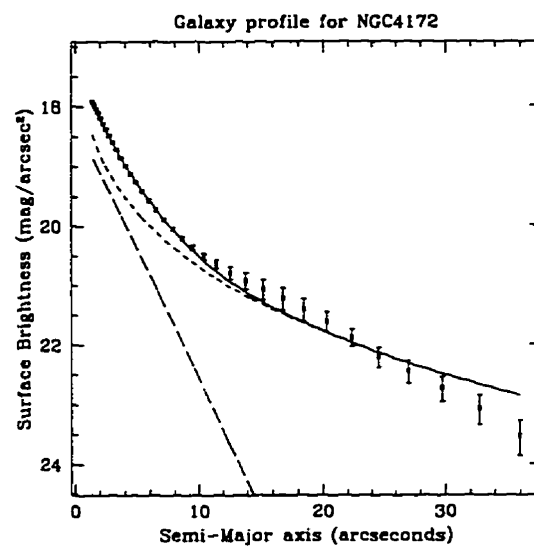


Figure 4.35: Radial profile and fit of NGC 4172. $\chi^2_{\nu} = 1.83$

NGC 4172 This appears to be a normal spiral galaxy with a very close companion 15" to the S; the object 30" to the S is a star. The fit to the surface-brightness profile is somewhat poor, being too bright at the outer edges (Figure 4.35). The PA is very steady and the ellipticity behaves well, though it flattens at 20" due to the companion (Figure B.10). See Figure 4.34 for the contour map of NGC 4172.

NGC 4224 This spiral galaxy has a prominent dust lane. The surface-brightness profile fits well (Figure 4.37, the kink in the profile at 7" is caused by poor fitting of the elliptical isophotes due to the dust lane cutting through that region). The PA is

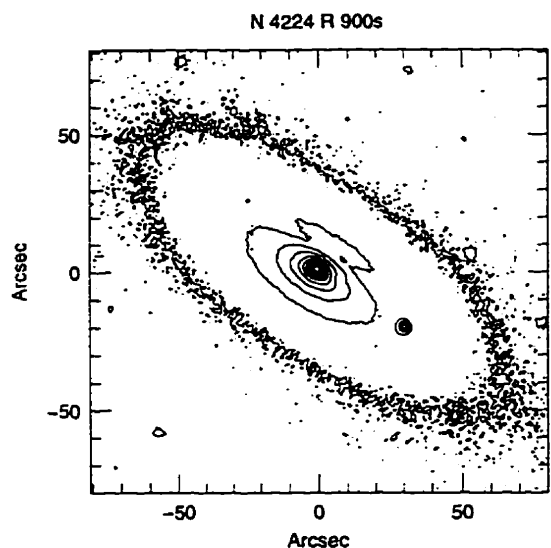


Figure 4.36: Intensity contour map of NGC 4224

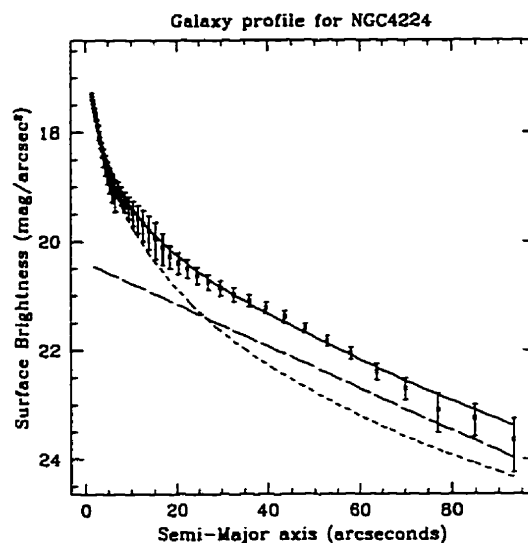


Figure 4.37: Radial profile and fit of NGC 4224. $\chi^2_{\nu} = 0.68$

very steady, and the ellipticity behaves reasonably well (Figure B.17). NGC 4224's contour map can be found in Figure 4.36.

NGC 4352 This is a seemingly normal galaxy, with no apparent companions anywhere near it. The fit to the surface-brightness profile is very poor, but appears mediocre except at the galaxy edge (Figure 4.39). The PA is very steady and the ellipticity also behaves very well (Figure B.14). The contour map of NGC 4352 can be found in Figure 4.38.

NGC 4375 This is a spiral galaxy with a very faint ring. The fit to the surface-brightness profile is numerically poor, though it appears acceptable (Figure 4.41, the bump in the profile at 10'' is likely caused by the faint ring). The PA twists by 50° just past the ring, though the ellipticity behaves reasonably well (Figure B.10). See Figure 4.40 for the contour map of NGC 4375.

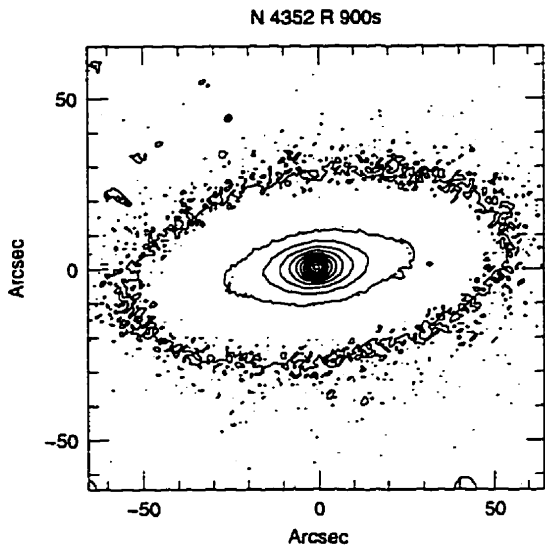


Figure 4.38: Intensity contour map of NGC 4352

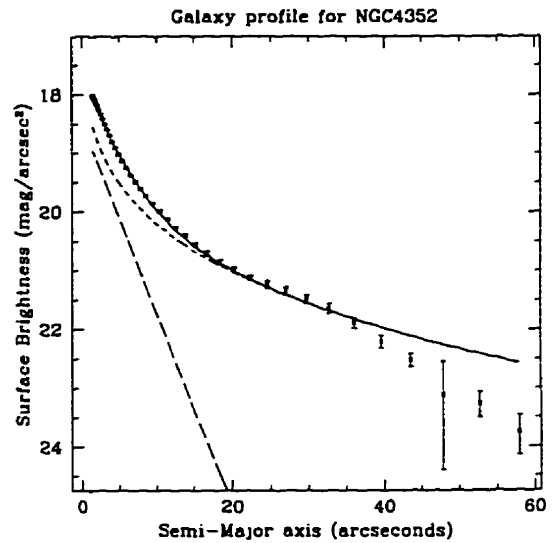


Figure 4.39: Radial profile and fit of NGC 4352. $\chi^2_{\nu} = 10.45$

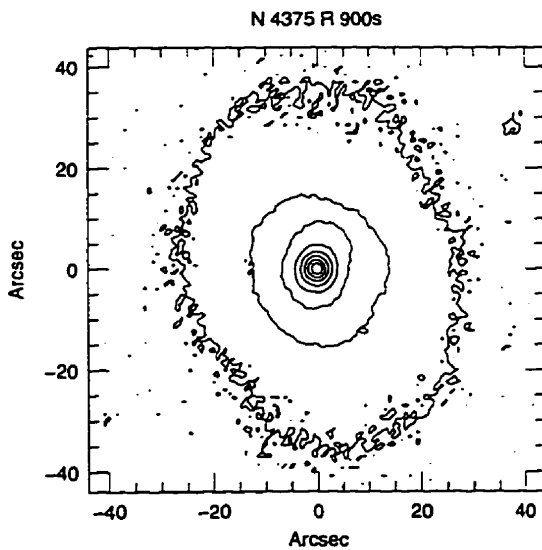


Figure 4.40: Intensity contour map of NGC 4375

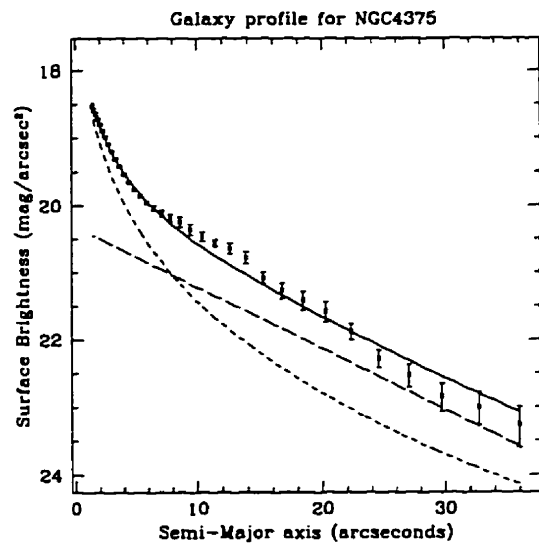


Figure 4.41: Radial profile and fit of NGC 4375. $\chi^2_{\nu} = 4.36$

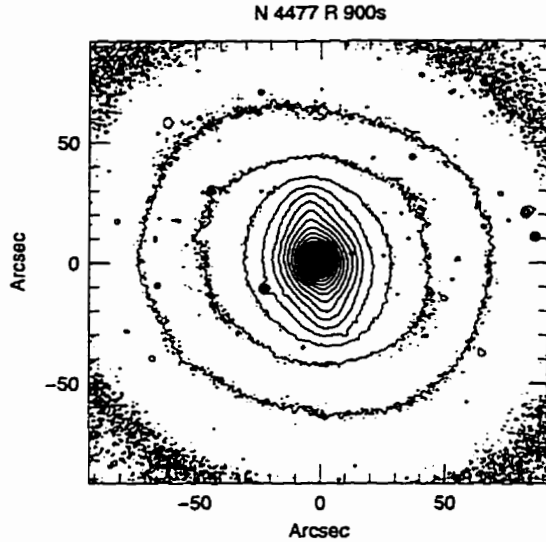


Figure 4.42: Intensity contour map of NGC 4477

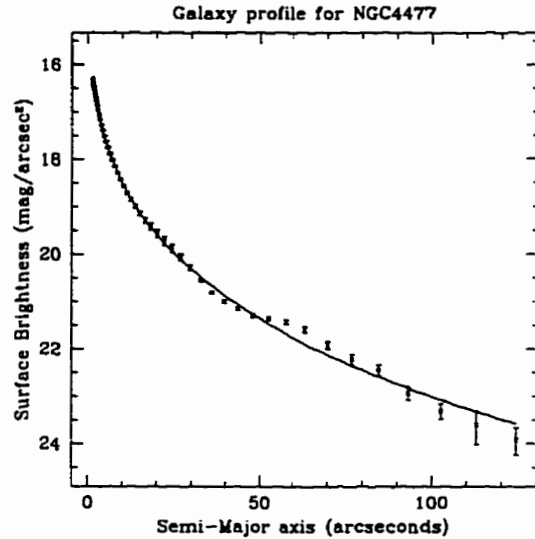


Figure 4.43: Radial profile and fit of NGC 4477. $\chi^2_\nu = 8.42$

NGC 4477 This is a barred spiral galaxy with a large companion $5.3'$ to the SE. The surface-brightness profile fits very poorly numerically, using only a bulge component, though the fit is visually acceptable (Figure 4.43). The PA twists 60° after the bar, and the ellipticity behaves as expected for a bar (Figure B.10). The contour map of NGC 4477 can be found in Figure 4.42.

NGC 4799 This is a normal spiral galaxy. The objects $14''$ E and $50''$ SE are stars. The surface-brightness profile fits well (Figure 4.45). The PA is very steady, and the ellipticity behaves very well (Figure B.18). See Figure 4.44 for the contour map of NGC 4799.

NGC 4944 This is a normal spiral galaxy, though not much more can be said because of the high level of noise in the image. The fit to the surface-brightness profile is mediocre (Figure 4.47). The PA is very steady, and the ellipticity is very well behaved (Figure B.18). NGC 4944's contour map can be found in Figure 4.46.

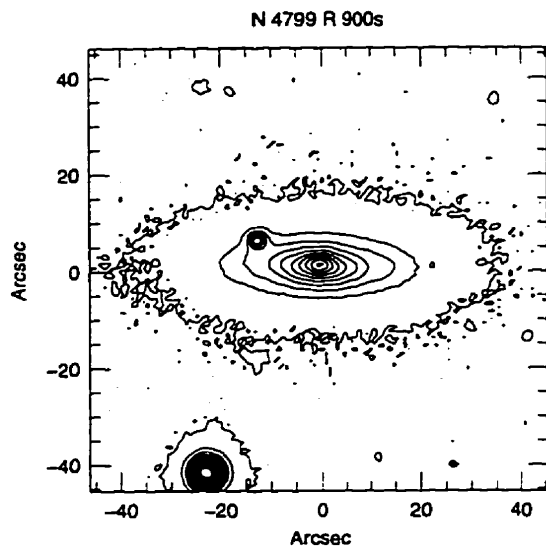


Figure 4.44: Intensity contour map of NGC 4799

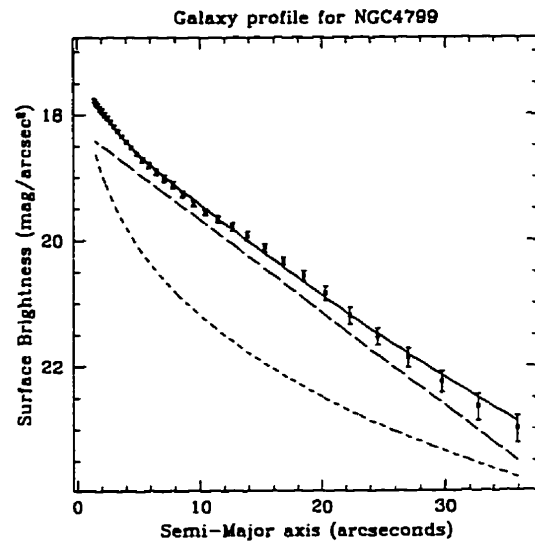


Figure 4.45: Radial profile and fit of NGC 4799. $\chi^2_{\nu} = 0.84$

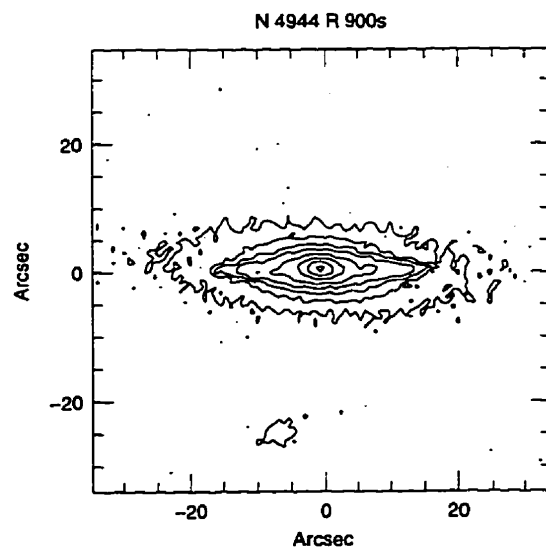


Figure 4.46: Intensity contour map of NGC 4944

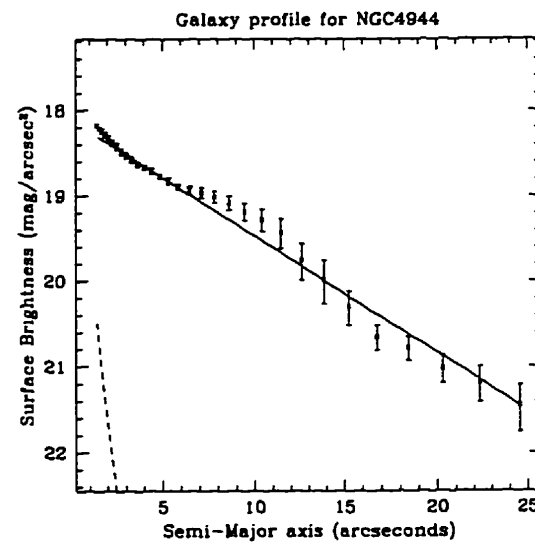


Figure 4.47: Radial profile and fit of NGC 4944. $\chi^2_{\nu} = 1.40$

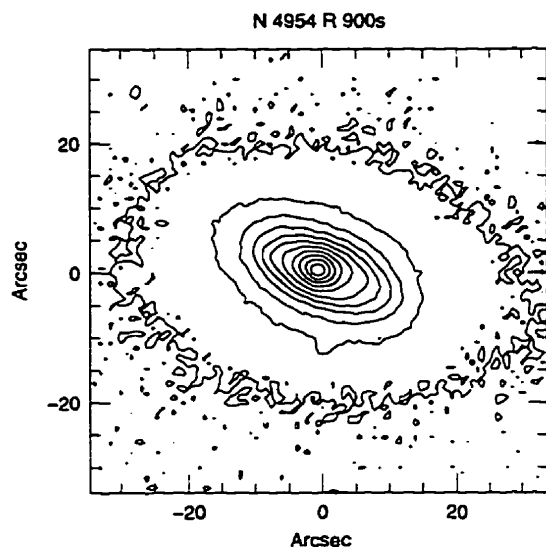


Figure 4.48: Intensity contour map of NGC 4954

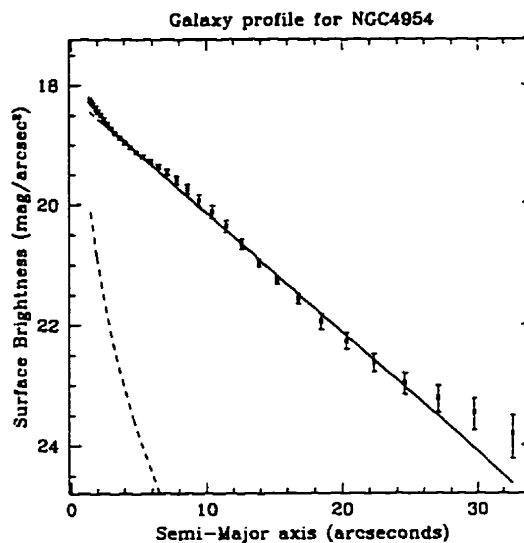


Figure 4.49: Radial profile and fit of NGC 4954. $\chi^2_{\nu} = 1.35$

NGC 4954 This is a spiral galaxy with a couple of nearby, fair-sized companions. The surface-brightness profile fits adequately (Figure 4.49). The PA is fairly steady, and the ellipticity behaves well (Figure B.15). The contour map of NGC 4954 can be found in Figure 4.48.

NGC 5289 This spiral galaxy contains a bar and a ring, with a very close small companion $14''$ (3 kpc projected distance) to the SW. The fit to the surface-brightness profile is very poor, though it can be partly explained by the presence of the bar and ring (Figure 4.51). The PA is very steady, but the ellipticity takes an odd dip at $20''$ (Figure B.18). See Figure 4.50 for the contour map of NGC 5289.

NGC 5375 This is a spiral galaxy containing a bar (which has clumps on the ends). The fit to the surface-brightness profile is numerically poor, but visually acceptable (Figure 4.53). The PA twists slightly within the bar, and the ellipticity indicates the presence of the bar also (Figure B.16). NGC 5375's contour map can be found in

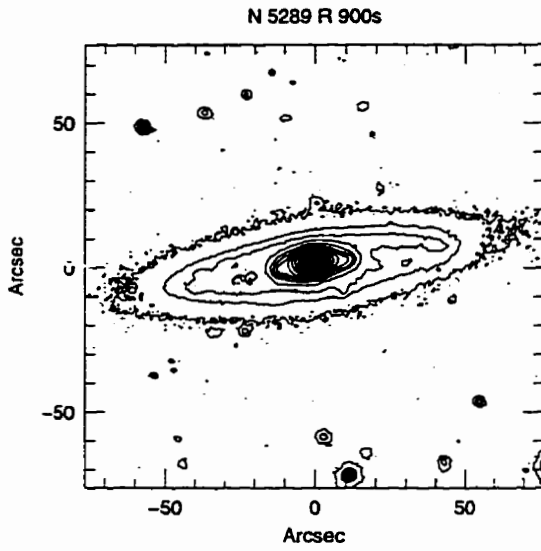


Figure 4.50: Intensity contour map of NGC 5289

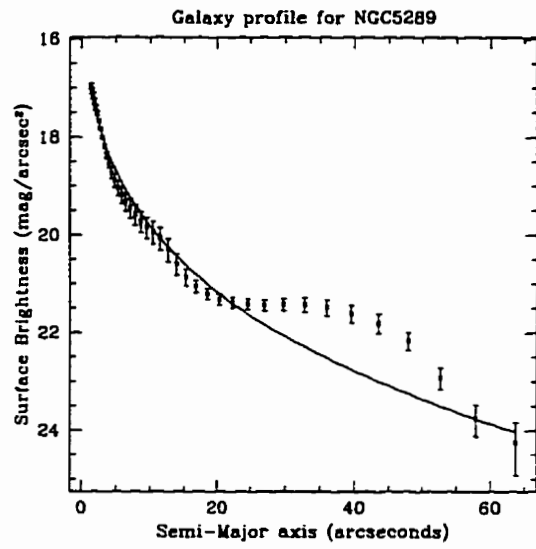


Figure 4.51: Radial profile and fit of NGC 5289. $\chi^2_\nu = 5.02$

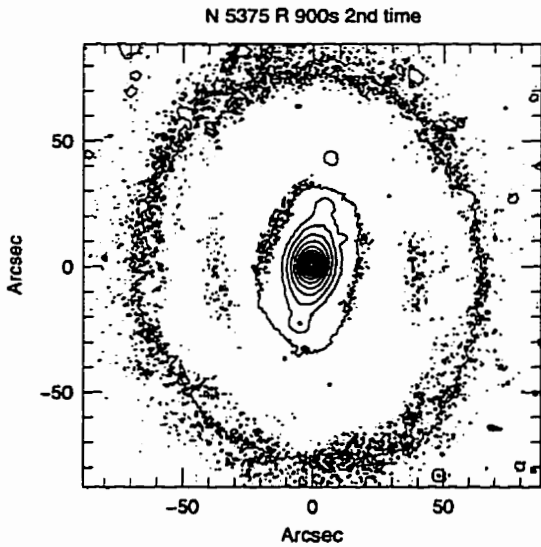


Figure 4.52: Intensity contour map of NGC 5375

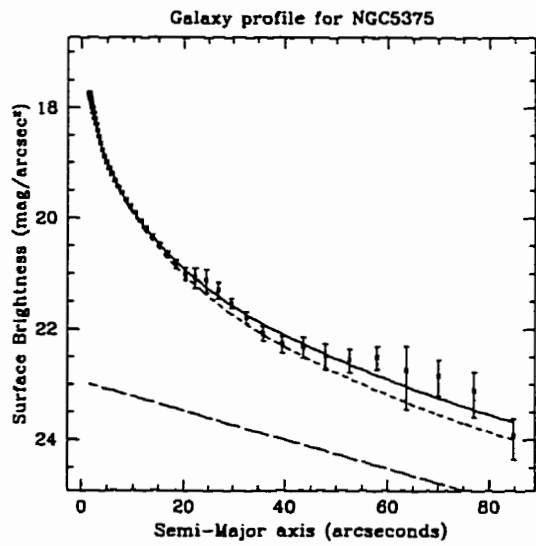


Figure 4.53: Radial profile and fit of NGC 5375. $\chi^2_\nu = 2.17$

Figure 4.52.

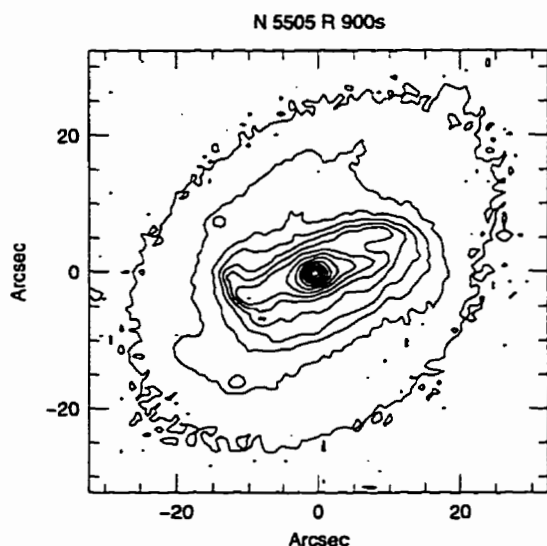


Figure 4.54: Intensity contour map of NGC 5505

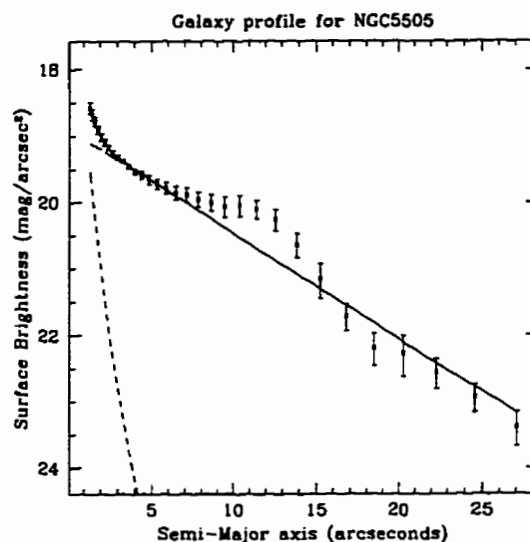


Figure 4.55: Radial profile and fit of NGC 5505. $\chi^2_{\nu} = 1.96$

NGC 5505 This spiral galaxy contains a prominent bar. The surface-brightness profile fits poorly, but is partly explainable by the presence of the bar (Figure 4.55). The PA twists slightly throughout the galaxy, and the ellipticity behaves as expected (Figure B.19). The contour map of NGC 5505 can be found in Figure 4.54.

NGC 5515 This galaxy is a spiral with a very faint ring. The star 23" to the NW was removed prior to isophotal analysis. The surface-brightness profile fits well (Figure 4.57). The PA is very steady, and the ellipticity is well behaved (Figure B.14). See Figure 4.56 for the contour map of NGC 5515.

NGC 5541 This spiral galaxy is undergoing an interaction with a very close companion galaxy 15" NE. The bright star 23" to the S was removed before any isophotal

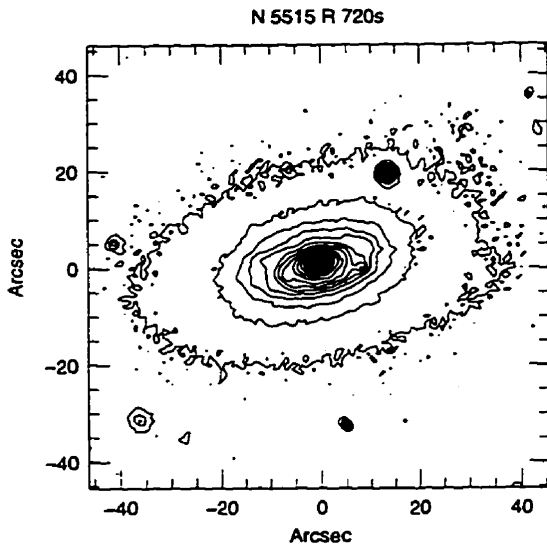


Figure 4.56: Intensity contour map of NGC 5515

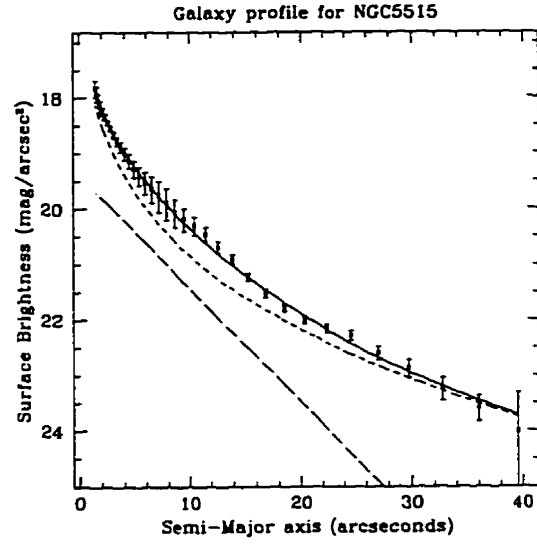


Figure 4.57: Radial profile and fit of NGC 5515. $\chi^2_\nu = 0.47$

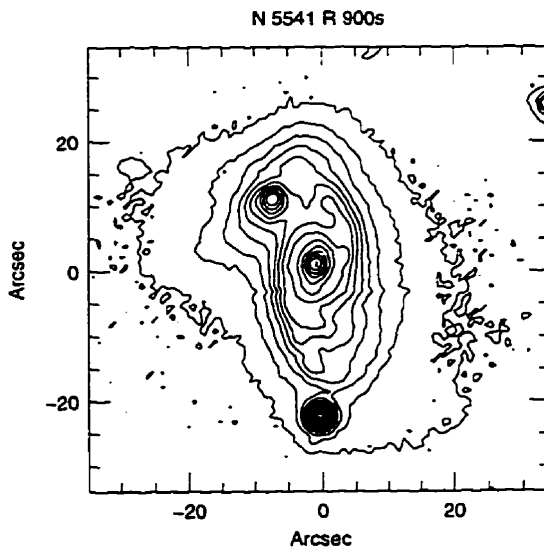


Figure 4.58: Intensity contour map of NGC 5541

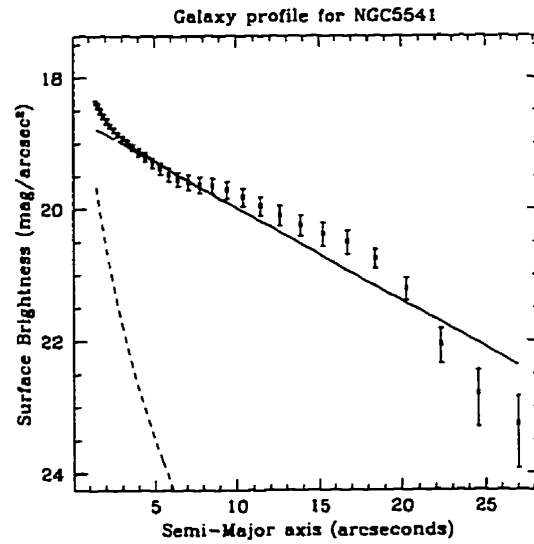


Figure 4.59: Radial profile and fit of NGC 5541. $\chi^2_\nu = 1.93$

analysis. The fit to the surface-brightness profile is somewhat poor, perhaps explainable due to the interaction perturbing the system (Figure 4.59). The PA is relatively steady, and the ellipticity behaves well, though there is a dip at 6" (Figure B.16). NGC 5541's contour map can be found in Figure 4.58.

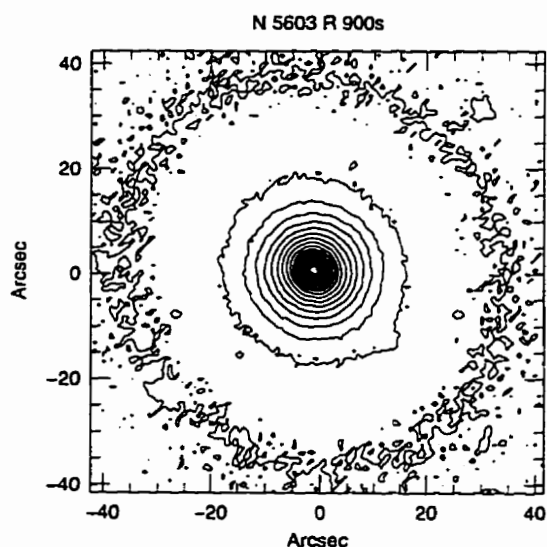


Figure 4.60: Intensity contour map of NGC 5603

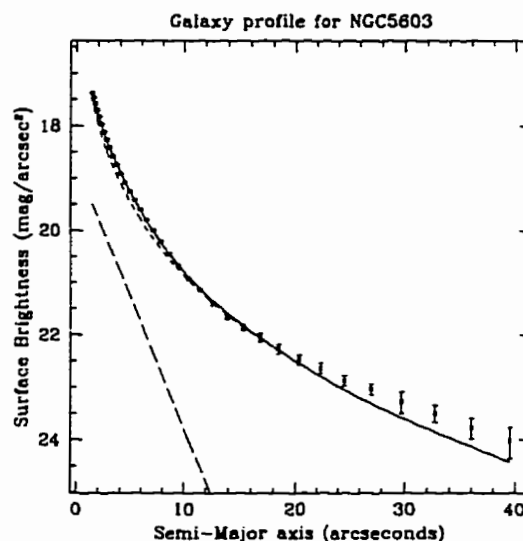


Figure 4.61: Radial profile and fit of NGC 5603. $\chi^2_\nu = 2.32$

NGC 5603 This is a plain looking galaxy with a couple of large, distant companions. The fit to the surface-brightness profile is poor, though it appears acceptable (Figure 4.61). The PA is fairly steady, and the ellipticity is well behaved (Figure B.21). The contour map of NGC 5603 is found in Figure 4.60.

NGC 5644 This is another plain looking galaxy with distant large companions. The objects 22" NE and 38" E are foreground stars. The surface-brightness profile fit is numerically very poor, but is visually very acceptable (Figure 4.63). The PA and ellipticity are both quite steady (Figure B.21). See Figure 4.62 for the contour map of NGC 5644.

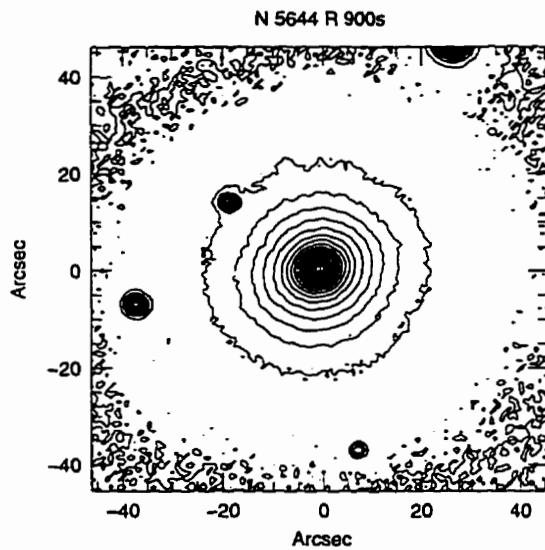


Figure 4.62: Intensity contour map of NGC 5644

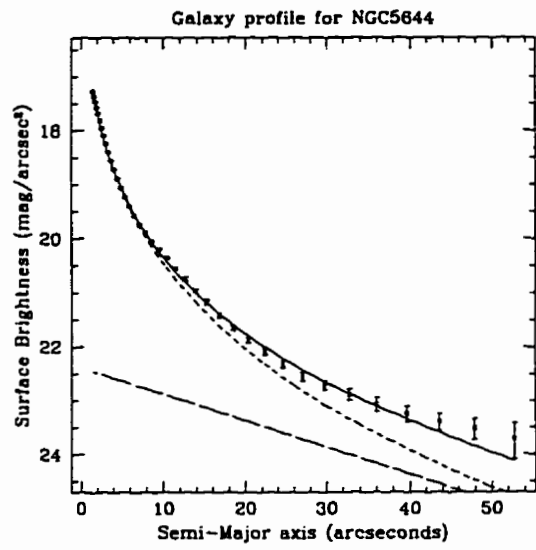


Figure 4.63: Radial profile and fit of NGC 5644. $\chi^2_{\nu} = 4.91$

NGC 5690 This is a spiral galaxy with dust and a lot of spiral clumps. There were several contaminating stars that were removed before analysis, as well as an E-W diffraction spike from a particularly bright star. The surface-brightness profile fits well, partly due to the noise level though (Figure 4.65). The PA is very steady, and the ellipticity is fairly steady as well (Figure B.19) indicating an inclination of $i \approx 70^\circ$. NGC 5690's contour map can be seen in Figure 4.64.

NGC 5772 This is a normal spiral galaxy with no interesting features. The surface-brightness profile fits very poorly numerically, though it appears quite acceptable (Figure 4.67). The PA is very steady, and the ellipticity behaves well (Figure B.15). The contour map of NGC 5772 can be found in Figure 4.66.

NGC 5806 This is a spiral galaxy with a hint of a bar; there are two very close companion objects within $1'$. The fit to the surface-brightness profile is very poor numerically, but it appears visually acceptable (Figure 4.69). The PA is very steady, but

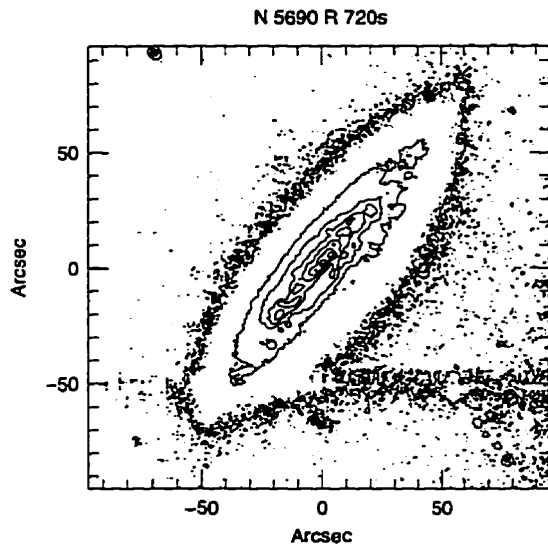


Figure 4.64: Intensity contour map of NGC 5690

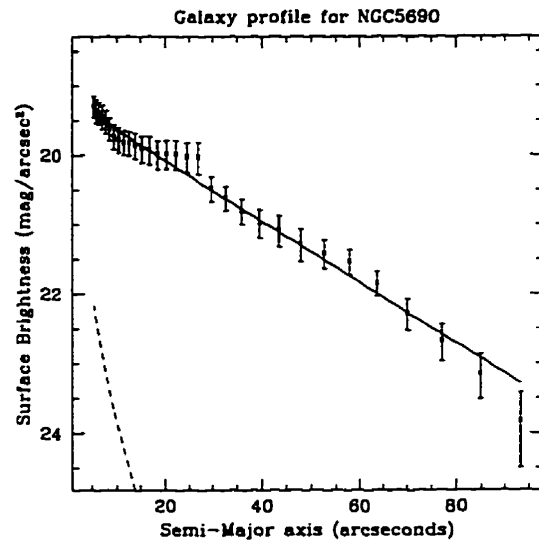


Figure 4.65: Radial profile and fit of NGC 5690. $\chi^2_{\nu} = 0.47$

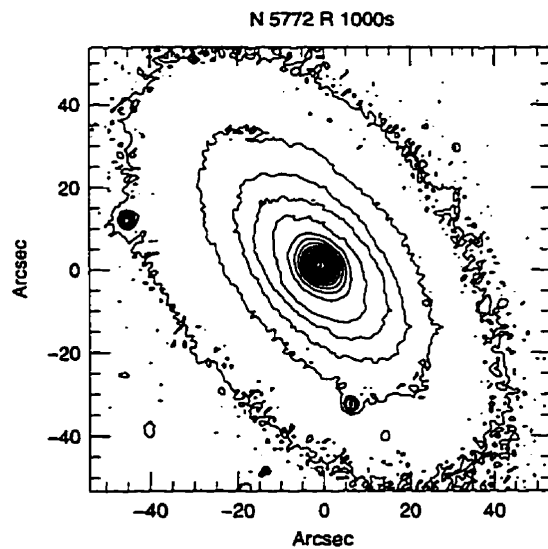


Figure 4.66: Intensity contour map of NGC 5772

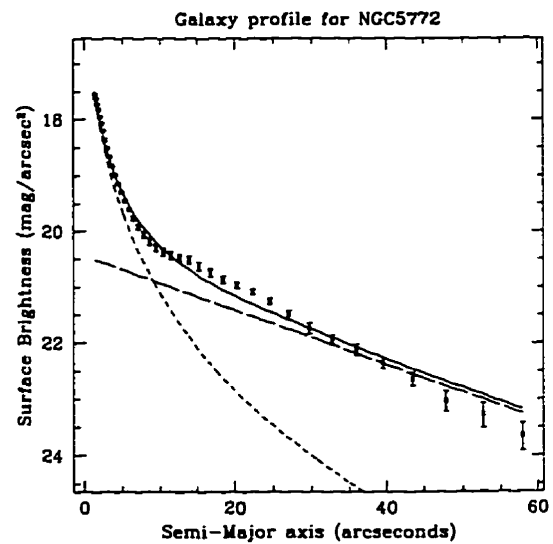


Figure 4.67: Radial profile and fit of NGC 5772. $\chi^2_{\nu} = 10.32$

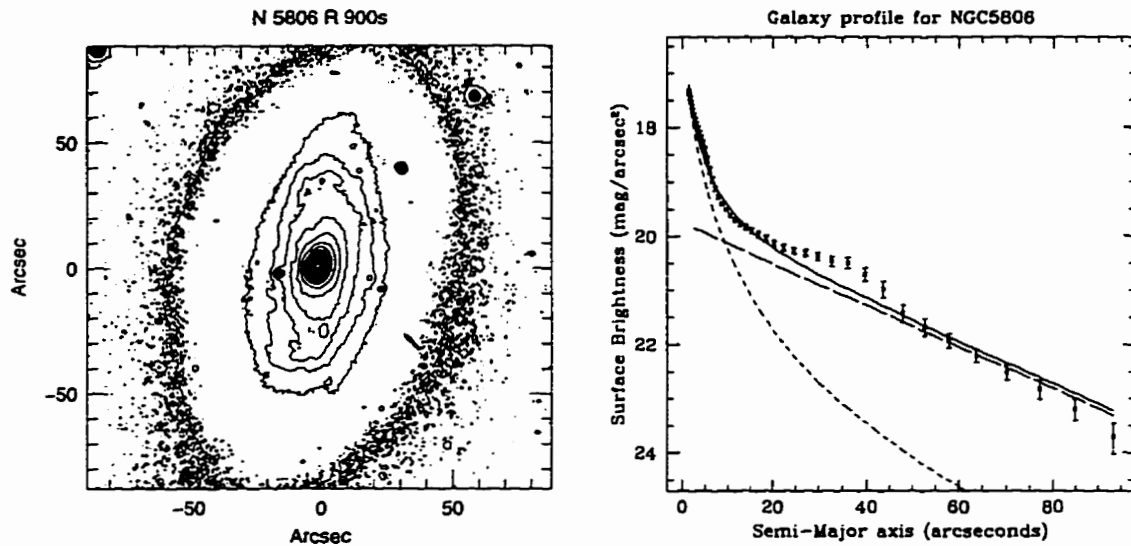


Figure 4.68: Intensity contour map of NGC 5806

Figure 4.69: Radial profile and fit of NGC 5806. $\chi^2_{\nu} = 7.42$

the ellipticity shows some amount of fluctuation throughout the galaxy (Figure B.14). See Figure 4.68 for the contour map of NGC 5806.

NGC 5876 This spiral galaxy contains a bar and a ring. The fit to the surface-brightness profile is numerically very poor, though it appears acceptable (Figure 4.71). The PA undergoes a moderate twist at 15" following the bar. The ellipticity also takes a jump at the same location due to the bar (Figure B.15). The contour map of NGC 5876 can be found in Figure 4.70.

NGC 5908 This spiral galaxy is nearly edge-on ($i \gtrsim 75^\circ$) and contains a prominent dust lane. The surface-brightness profile fits very well (Figure 4.73). The PA is very steady, and the ellipticity behaves as expected for an edge-on galaxy (Figure B.19). NGC 5908's contour map can be found in Figure 4.72.

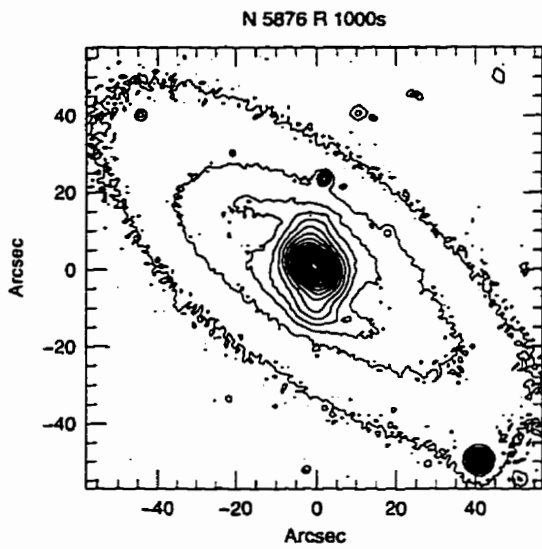


Figure 4.70: Intensity contour map of NGC 5876

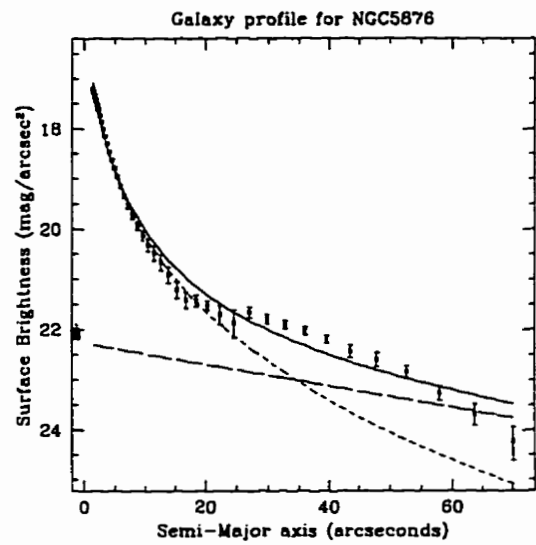


Figure 4.71: Radial profile and fit of NGC 5876. $\chi^2_{\nu} = 6.78$

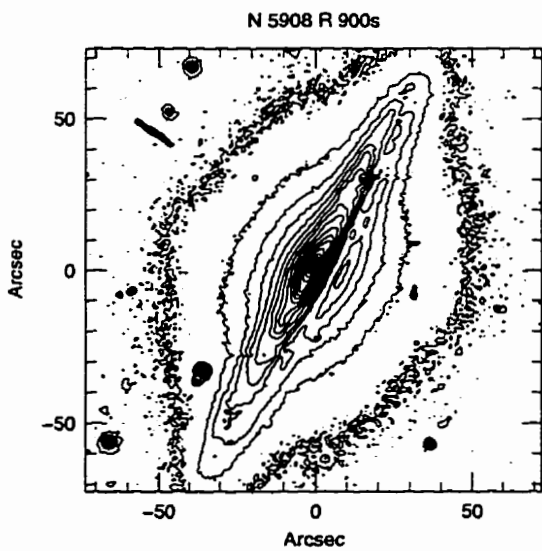


Figure 4.72: Intensity contour map of NGC 5908

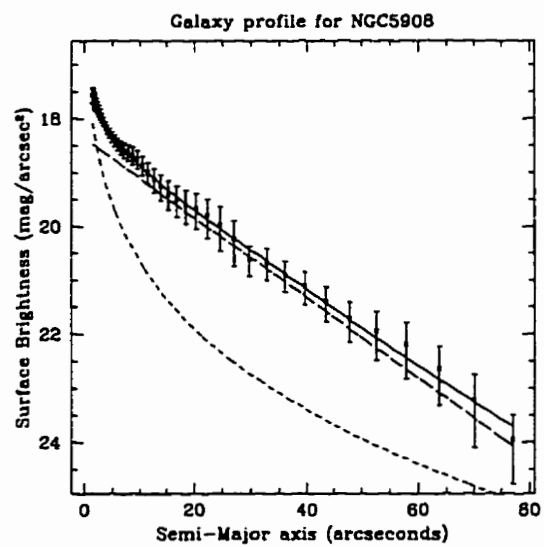


Figure 4.73: Radial profile and fit of NGC 5908. $\chi^2_{\nu} = 0.07$

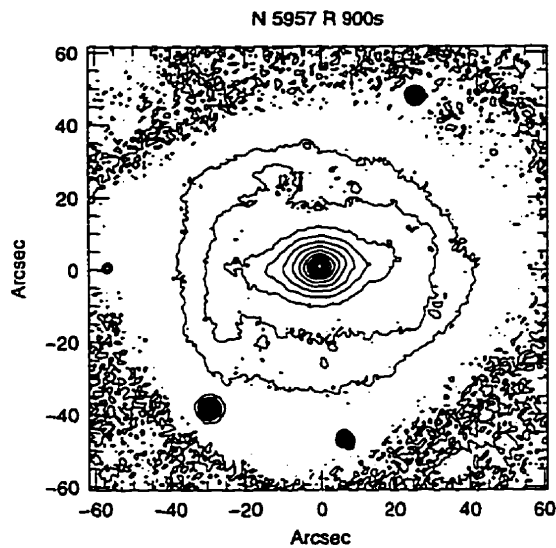


Figure 4.74: Intensity contour map of NGC 5957

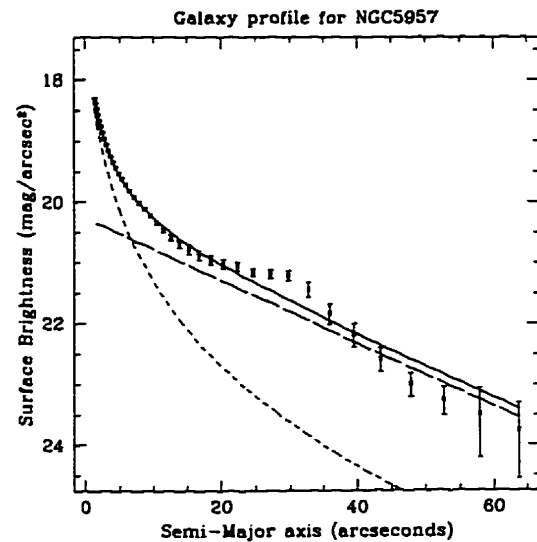


Figure 4.75: Radial profile and fit of NGC 5957. $\chi^2_{\nu} = 2.16$

NGC 5957 This is a spiral galaxy with a bar and ring. The fit to the surface-brightness profile is mediocre, partially due to the ring and bar (Figure 4.75). The PA is fairly steady, though the ellipticity steadily increases until the end of the bar where the ring starts (Figure B.17). See Figure 4.74 for the contour map of NGC 5957.

NGC 5980 This is a normal spiral galaxy with a small, close companion 32" to the SE. The surface-brightness profile fits adequately (Figure 4.77). The PA is very steady, and the ellipticity is very well behaved (Figure B.15). The contour map of NGC 5980 can be found in Figure 4.76.

NGC 6001 This spiral galaxy contains a partial bar and prominent arms. The surface-brightness profile fits well (Figure 4.79). The PA undergoes a 90° twist during the transition from bar to disk, and the ellipticity demonstrates this as well (Figure B.13). NGC 6001's contour map can be found in Figure 4.78.

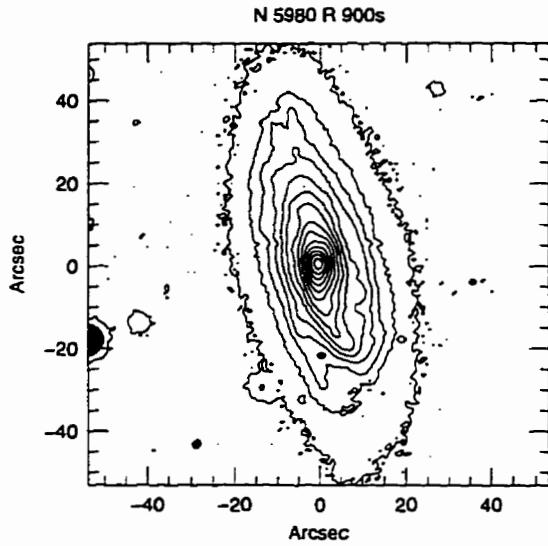


Figure 4.76: Intensity contour map of NGC 5980

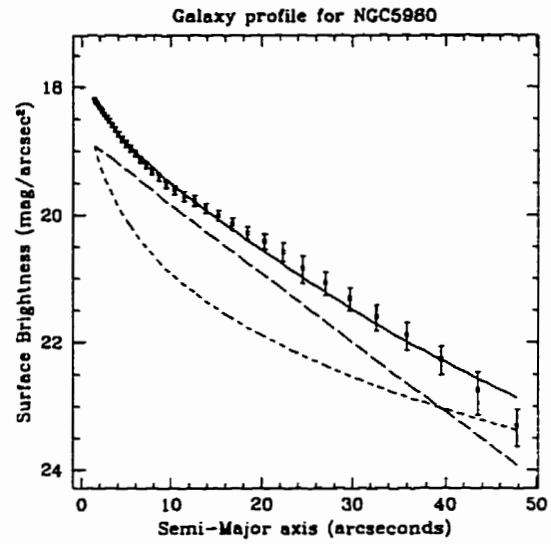


Figure 4.77: Radial profile and fit of NGC 5980. $\chi^2_{\nu} = 1.17$

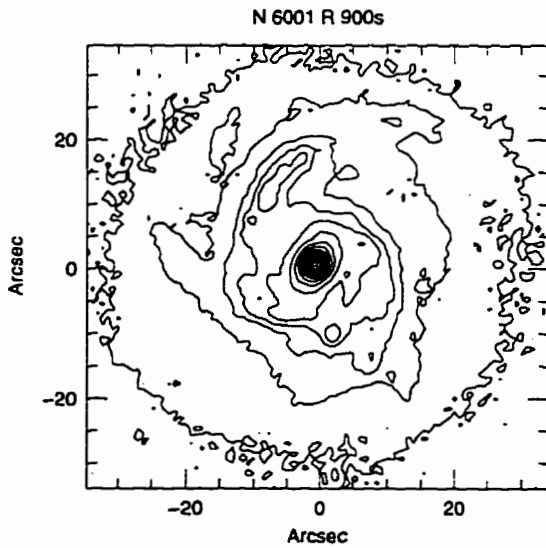


Figure 4.78: Intensity contour map of NGC 6001

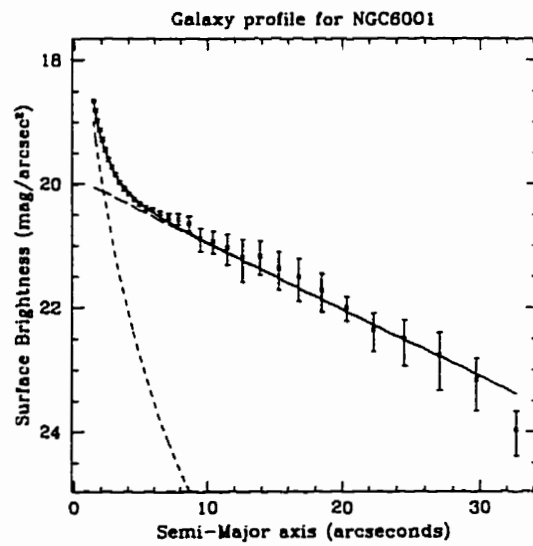


Figure 4.79: Radial profile and fit of NGC 6001. $\chi^2_{\nu} = 0.95$

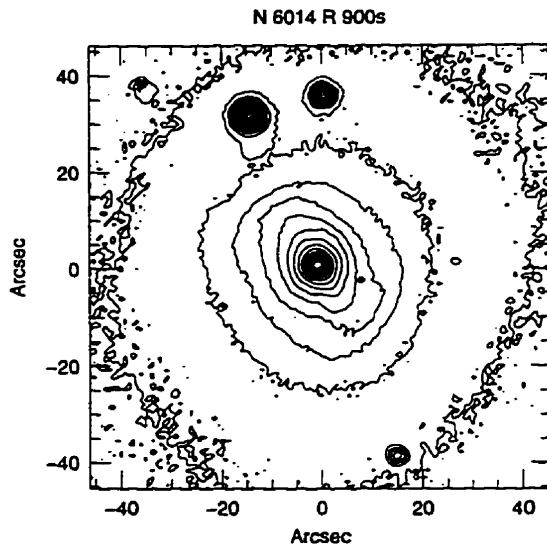


Figure 4.80: Intensity contour map of NGC 6014

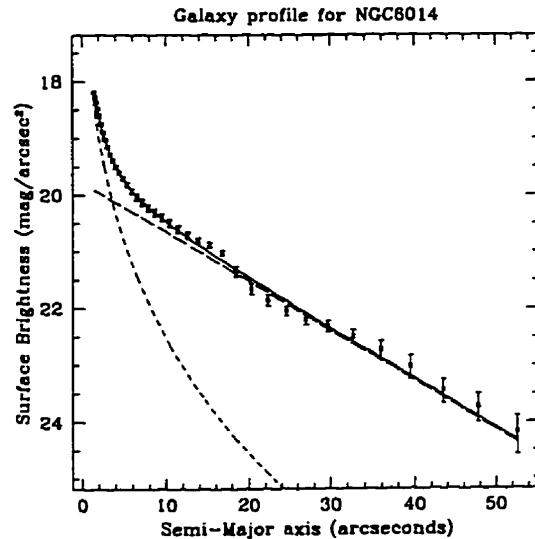


Figure 4.81: Radial profile and fit of NGC 6014. $\chi^2_\nu = 1.93$

NGC 6014 This spiral galaxy has a bar and a partial ring. The objects 35'' to the N are stars and were removed prior to isophotal analysis. The fit to the surface-brightness profile is mediocre, though it appears very acceptable (Figure 4.81). The PA twists from the bar to the rest of the galaxy, and the ellipticity follows this trend as well (Figure B.10). See Figure 4.80 for the contour map of NGC 6014.

NGC 6030 This is a normal looking galaxy. The fit to the surface-brightness profile is poor numerically (due to small error-bars), though it is acceptable visually (Figure 4.83). The PA is very steady, and the ellipticity behaves very well (Figure B.11). The contour map of NGC 6030 can be found in Figure 4.82.

NGC 6085 This is a normal spiral galaxy that is in a rich environment, but there are no noticeable close companion objects. The fit to the surface-brightness profile is very poor; however, it appears visually acceptable (Figure 4.85). There is a slight twist in the PA at 12'', and there is an odd dip in the ellipticity at the same location

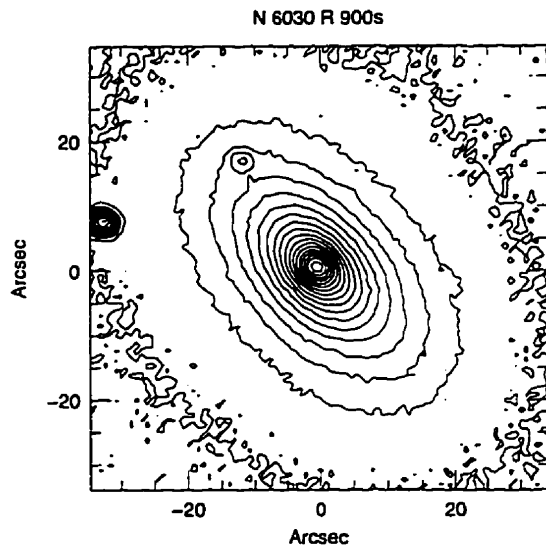


Figure 4.82: Intensity contour map of NGC 6030

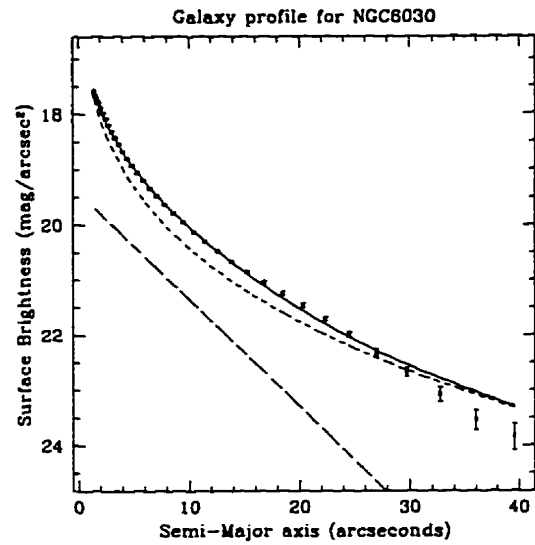


Figure 4.83: Radial profile and fit of NGC 6030. $\chi^2_{\nu} = 4.92$

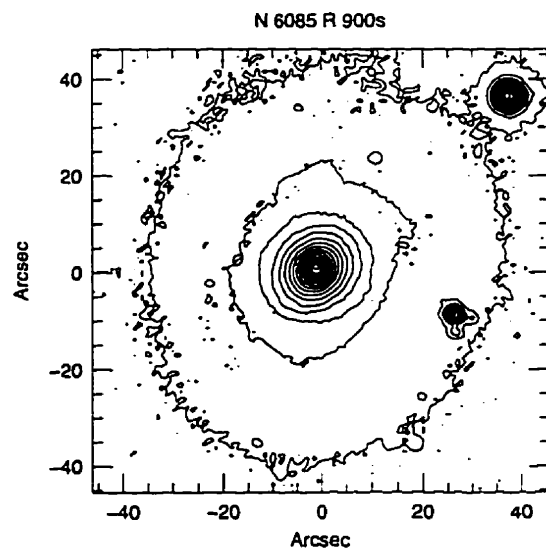


Figure 4.84: Intensity contour map of NGC 6085

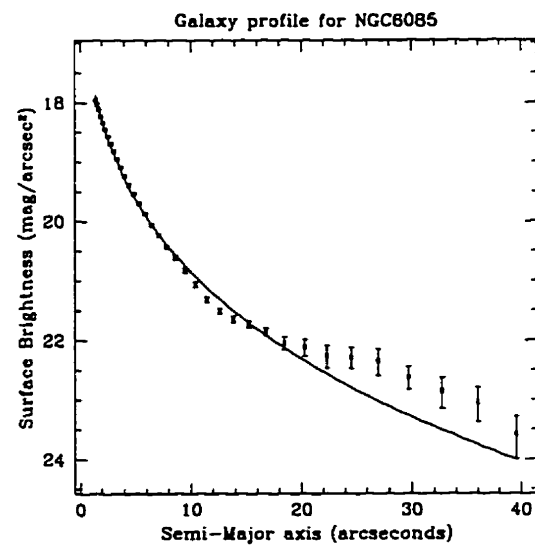


Figure 4.85: Radial profile and fit of NGC 6085. $\chi^2_{\nu} = 6.80$

(Figure B.13). NGC 6085's contour map can be found in Figure 4.84.

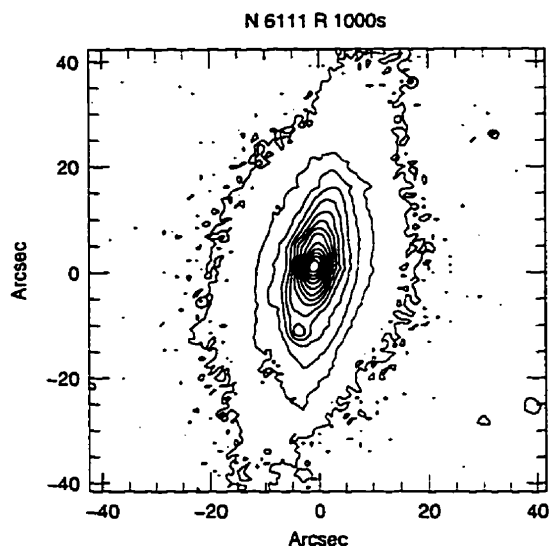


Figure 4.86: Intensity contour map of NGC 6111

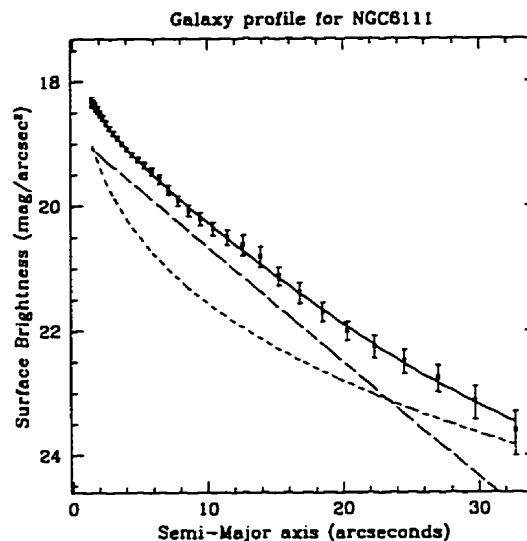


Figure 4.87: Radial profile and fit of NGC 6111. $\chi^2_{\nu} = 0.19$

NGC 6111 This is a fairly normal spiral galaxy which has a very close companion object 13" (4 kpc projected distance) to the S. The surface-brightness profile fits very well (Figure 4.87). The PA is very steady, and the ellipticity is reasonably well behaved (Figure B.14). See Figure 4.86 for the contour map of NGC 6111.

NGC 6126 This is a normal spiral galaxy with a very close small companion object 19" (17 kpc projected distance) to the NW. The surface-brightness profile fits well, as can be seen in Figure 4.89. Since the ellipticity indicates a very round isophotes, the PA does not provide much information (Figure B.21). The contour map of NGC 6126 can be found in Figure 4.88.

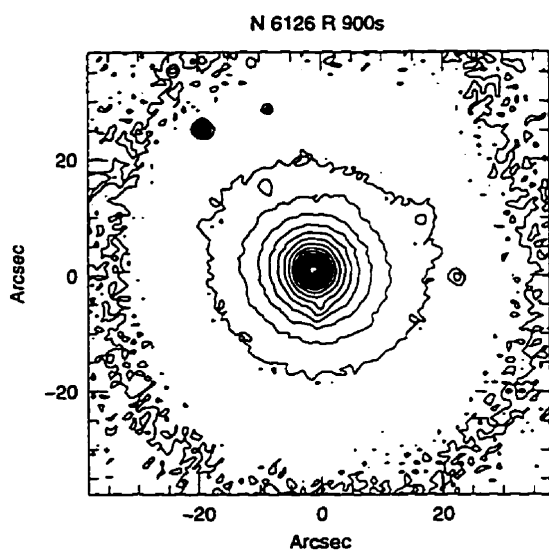


Figure 4.88: Intensity contour map of NGC 6126

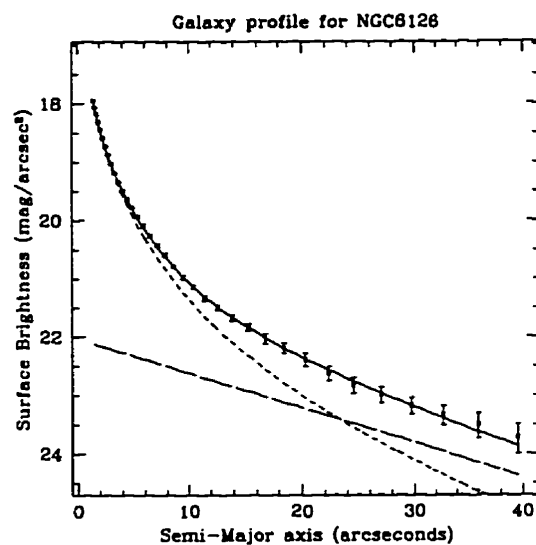


Figure 4.89: Radial profile and fit of NGC 6126. $\chi^2_{\nu} = 0.65$

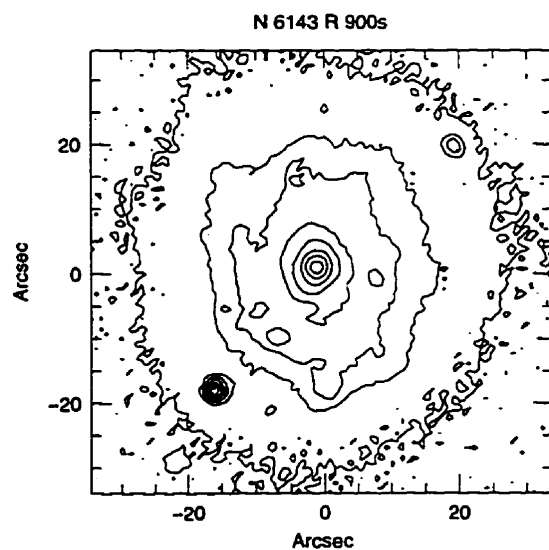


Figure 4.90: Intensity contour map of NGC 6143

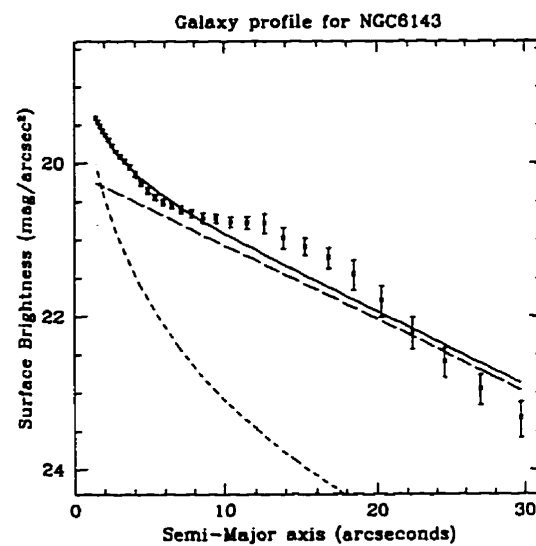


Figure 4.91: Radial profile and fit of NGC 6143. $\chi^2_{\nu} = 3.58$

NGC 6143 This is a spiral galaxy with clumpy spiral arms and a close companion 30'' to the NW; the object 25'' to the SE is a foreground star. The fit to the surface-brightness profile is poor, partly explained by the bump in the profile caused by the spiral arm clumps (Figure 4.91). The PA twists around slightly and erratically, and the ellipticity behaves in a similar manner (Figure B.16). NGC 6143's contour map can be seen in Figure 4.90.

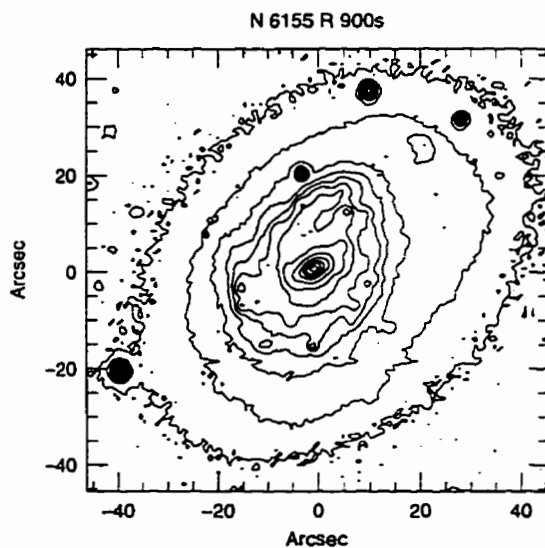


Figure 4.92: Intensity contour map of NGC 6155

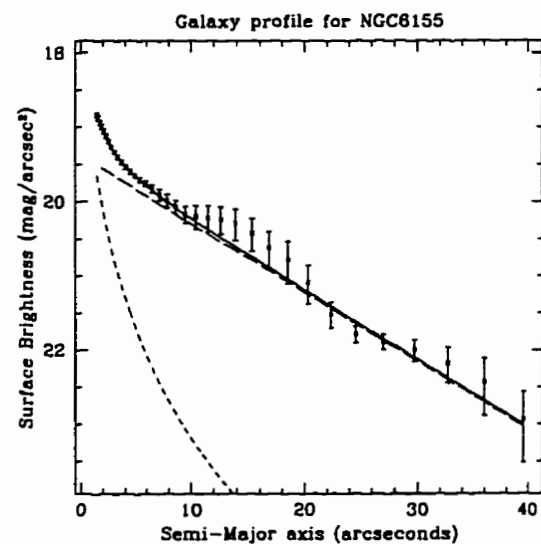


Figure 4.93: Radial profile and fit of NGC 6155. $\chi^2_{\nu} = 0.58$

NGC 6155 This spiral galaxy contains a bar, and there is a small companion object 30'' (8 kpc projected distance) away to the NW. The surface-brightness profile fits well (Figure 4.93). The PA twists 50° due to the presence of the bar, and the ellipticity is somewhat steady but noisy (Figure B.9). See Figure 4.92 for the contour map of NGC 6155.

NGC 6196 This is a normal looking (perhaps elliptical) galaxy; there are a couple of nearby companion objects within 1.5'. The fit to the surface-brightness profile

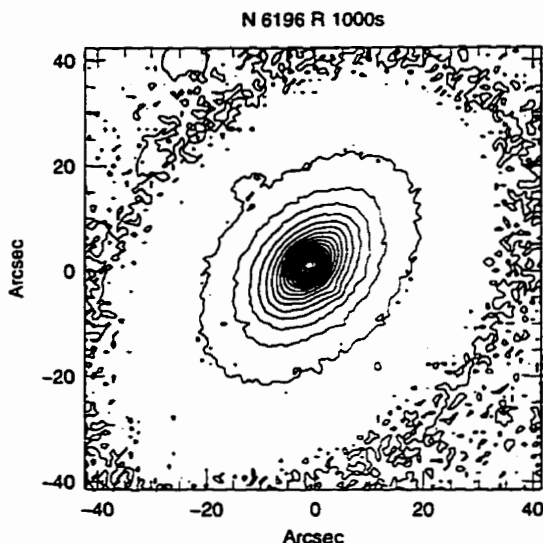


Figure 4.94: Intensity contour map of NGC 6196

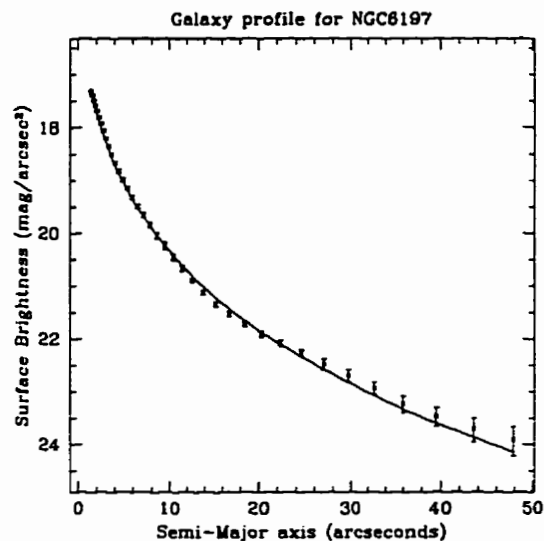


Figure 4.95: Radial profile and fit of NGC 6196. $\chi^2_{\nu} = 4.45$

is numerically poor (due to the small error-bars), though it is visually acceptable (Figure 4.95). The PA is very steady, and the ellipticity behaves well (Figure B.9). the contour map of NGC 6196 can be found in Figure 4.94.

NGC 6764 This spiral galaxy contains a bar, and there is a fair-sized companion less than $3'$ away, as well as a close, small companion $25''$ (6 kpc projected distance) to the N. Many foreground stars were removed prior to isophotal analysis. The surface-brightness profile fits well, as can be seen in Figure 4.97. The PA is very steady, and the ellipticity is well behaved (Figure B.20). NGC 6764's contour map can be seen in Figure 4.96.

4.3 Summary of Control Galaxy Properties

The following tables summarize much of the information about the individual control galaxies. Information regarding the basic properties of the host galaxies, image

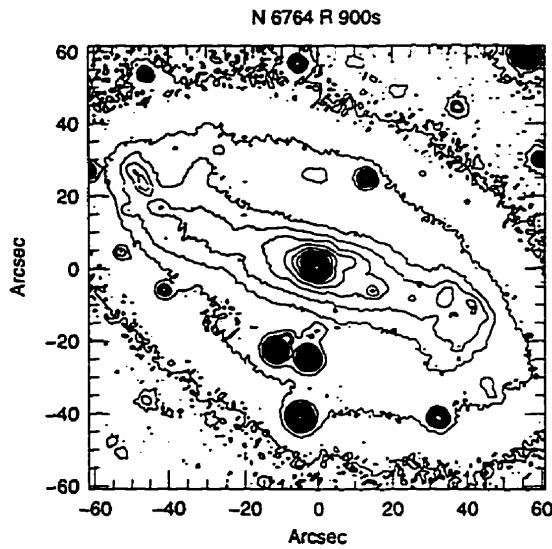


Figure 4.96: Intensity contour map of NGC 6764

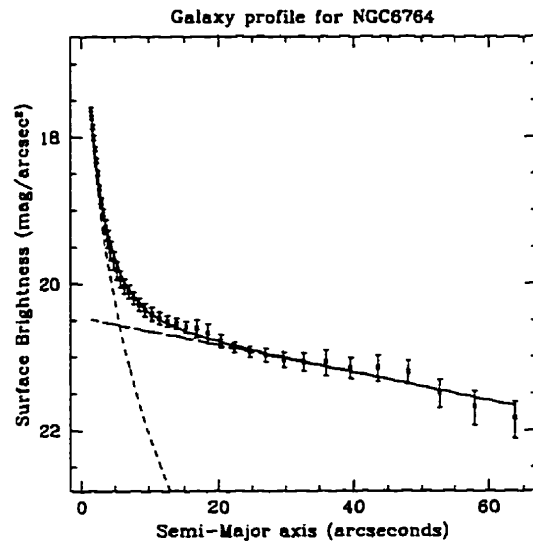


Figure 4.97: Radial profile and fit of NGC 6764. $\chi^2_{\nu} = 0.53$

statistics, elliptical isophotal analysis parameters, surface brightness profile results, and companion statistics will be presented.

Table 4.1 shows some basic properties of the control sample galaxies, such as their location, magnitude, and redshift. Table 4.2 provides important image statistics for the control data, including the seeing and the airmass of the exposures. Table 4.3 gives some brief details of the isophotal analysis and the parameters used in the ellipse fitting. Table 4.4 provides the results from the three-component surface-brightness profile fitting, as well as the fractional luminosity contained in each component. Finally, Table 4.5 shows distance, luminosity and companion galaxy-related parameters of the hosts.

Table 4.1: Basic properties of the control galaxies in the dataset

Name	$\alpha(1950.0)$	$\delta(1950.0)$	m_R	M_R	z
UGC 05734	10 ^h 31 ^m 08 ^s .3	+53°07'47"	12.65	-23.02	0.0237
UGC 07064	12 ^h 02 ^m 10 ^s .2	+31°27'20"	13.12	-22.67	0.0250
UGC 09295	14 ^h 26 ^m 48 ^s .3	+70°09'35"	13.56	-22.72	0.0313
UGC 10097	15 ^h 54 ^m 12 ^s .7	+48°00'41"	12.09	-23.26	0.0200
UGC 10407	16 ^h 26 ^m 48 ^s .3	+41°19'38"	13.97	-22.07	0.0283
UGC 11865	21 ^h 56 ^m 09 ^s .3	+11°47'53"	13.52	-22.93	0.0317
IC 875	13 ^h 15 ^m 08 ^s .2	+57°48'09"	12.79	-20.91	0.0093
IC 1141	15 ^h 47 ^m 25 ^s .5	+12°33'03"	13.41	-21.35	0.0149
NGC 3169	10 ^h 11 ^m 38 ^s .0	+03°43'13"	10.13	-21.92	0.0043
NGC 3492	10 ^h 58 ^m 20 ^s .3	+10°46'28"	13.35	-23.16	0.0354
NGC 3756	11 ^h 34 ^m 04 ^s .8	+54°34'24"	11.06	-20.98	0.0043
NGC 3825	11 ^h 39 ^m 48 ^s .9	+10°32'30"	12.39	-23.17	0.0217
NGC 3938	11 ^h 50 ^m 13 ^s .4	+44°23'55"	10.43	-20.61	0.0027
NGC 3968	11 ^h 52 ^m 54 ^s .7	+12°14'55"	11.82	-23.63	0.0213
NGC 4045	12 ^h 00 ^m 08 ^s .2	+02°15'26"	11.52	-21.42	0.0065
NGC 4048	12 ^h 00 ^m 16 ^s .4	+18°17'40"	13.23	-21.63	0.0159
NGC 4088	12 ^h 03 ^m 03 ^s .1	+50°49'13"	10.05	-20.83	0.0025
NGC 4172	12 ^h 09 ^m 46 ^s .0	+56°27'22"	12.75	-23.47	0.0309
NGC 4224	12 ^h 14 ^m 00 ^s .6	+07°44'24"	11.28	-22.30	0.0088
NGC 4352	12 ^h 21 ^m 32 ^s .2	+11°29'45"	12.22	-20.88	0.0070
NGC 4375	12 ^h 22 ^m 30 ^s .5	+28°50'06"	12.67	-23.56	0.0302
NGC 4477	12 ^h 27 ^m 30 ^s .7	+13°54'45"	10.24	-21.91	0.0045
NGC 4799	12 ^h 52 ^m 42 ^s .5	+03°10'03"	12.62	-21.12	0.0094
NGC 4944	13 ^h 01 ^m 25 ^s .9	+28°27'13"	12.75	-22.94	0.0237
NGC 4954	13 ^h 00 ^m 54 ^s .9	+75°40'21"	13.03	-23.21	0.0309

Column 1, name; columns 2-3, the Right Ascension and Declination of they galaxy (from NED); column 4, the apparent magnitude of the host, as measured by M.M. DeRobertis (Paper I); column 5, the absolute magnitude of the host; column 6, the redshift (from NED).

Table 4.1: continued

Name	$\alpha(1950.0)$	$\delta(1950.0)$	m_R	M_R	z
NGC 5289	13 ^h 43 ^m 01 ^s .1	+41°45'11"	12.30	-21.18	0.0084
NGC 5375	13 ^h 54 ^m 40 ^s .6	+29°24'26"	12.08	-21.27	0.0079
NGC 5505	14 ^h 10 ^m 06 ^s .6	+13°32'19"	13.19	-21.41	0.0142
NGC 5515	14 ^h 10 ^m 34 ^s .2	+39°32'38"	12.98	-22.84	0.0254
NGC 5541	14 ^h 14 ^m 28 ^s .9	+39°49'12"	12.87	-22.97	0.0257
NGC 5603	14 ^h 21 ^m 00 ^s .9	+40°36'15"	12.86	-22.33	0.0188
NGC 5644	14 ^h 28 ^m 00 ^s .5	+12°08'58"	11.65	-24.17	0.0254
NGC 5690	14 ^h 35 ^m 09 ^s .3	+02°30'14"	11.79	-20.96	0.0058
NGC 5772	14 ^h 49 ^m 44 ^s .1	+40°48'14"	12.22	-22.72	0.0165
NGC 5806	14 ^h 57 ^m 28 ^s .4	+02°05'20"	11.16	-21.07	0.0045
NGC 5876	15 ^h 08 ^m 07 ^s .4	+54°41'48"	12.16	-21.94	0.0112
NGC 5908	15 ^h 15 ^m 23 ^s .0	+55°35'37"	11.42	-22.64	0.0110
NGC 5957	15 ^h 33 ^m 01 ^s .0	+12°12'46"	12.00	-20.85	0.0061
NGC 5980	15 ^h 39 ^m 11 ^s .6	+15°56'58"	12.26	-22.28	0.0136
NGC 6001	15 ^h 45 ^m 39 ^s .0	+28°46'00"	13.21	-23.20	0.0332
NGC 6014	15 ^h 53 ^m 29 ^s .4	+06°04'40"	12.62	-20.86	0.0081
NGC 6030	15 ^h 59 ^m 36 ^s .5	+18°05'56"	11.80	-22.94	0.0150
NGC 6085	16 ^h 10 ^m 35 ^s .0	+29°29'31"	13.09	-23.37	0.0340
NGC 6111	16 ^h 13 ^m 52 ^s .5	+62°39'41"	13.22	-20.59	0.0098
NGC 6126	16 ^h 19 ^m 38 ^s .9	+36°29'37"	13.33	-23.00	0.0326
NGC 6143	16 ^h 20 ^m 35 ^s .7	+55°12'11"	13.17	-21.87	0.0175
NGC 6155	16 ^h 24 ^m 43 ^s .6	+48°28'41"	12.37	-21.03	0.0081
NGC 6196	16 ^h 36 ^m 05 ^s .8	+36°10'16"	12.33	-23.94	0.0314
NGC 6764	19 ^h 07 ^m 01 ^s .2	+50°51'08"	11.76	-21.72	0.0079

Table 4.2: Image statistics of the control galaxies

Name	seeing (")	sky ($\frac{\text{mag}}{\text{arcsec}^2}$)	sky σ (ADU)	X	exptime (s)
UGC 05734	2.34 ± 0.04	19.55	11.2	1.11	900
UGC 07064	2.44 ± 0.07	19.54	10.8	1.07	900
UGC 09295	2.29 ± 0.05	20.60	6.9	1.29	900
UGC 10097	2.11 ± 0.05	20.85	6.2	1.16	900
UGC 10407	1.34 ± 0.05	20.83	7.5	1.24	900
UGC 11865	1.75 ± 0.03	20.52	7.0	1.36	1000
IC 875	1.80 ± 0.05	20.66	6.9	1.12	900
IC 1141	1.79 ± 0.03	20.47	7.2	1.27	900
NGC 3169	1.53 ± 0.05	20.09	8.4	1.39	900
NGC 3492	2.20 ± 0.05	18.98	14.4	1.13	900
NGC 3756	2.26 ± 0.03	19.75	9.6	1.12	900
NGC 3825	1.88 ± 0.05	20.27	7.7	1.10	900
NGC 3938	2.20 ± 0.07	20.44	7.4	1.06	900
NGC 3968	1.97 ± 0.08	20.29	8.0	1.16	900
NGC 4045	1.72 ± 0.05	20.21	7.9	1.30	900
NGC 4048	1.81 ± 0.03	19.22	12.9	1.09	900
NGC 4088	1.71 ± 0.14	20.68	42.6	1.17	900
NGC 4172	2.79 ± 0.04	20.06	8.5	1.12	900
NGC 4224	2.48 ± 0.04	18.99	13.9	1.22	900
NGC 4352	3.13 ± 0.05	19.71	9.9	1.13	900
NGC 4375	2.56 ± 0.08	19.47	11.1	1.11	900
NGC 4477	1.64 ± 0.05	20.55	7.2	1.07	900
NGC 4799	2.39 ± 0.07	19.17	13.2	1.37	900
NGC 4944	2.67 ± 0.25	19.28	85.4	1.04	900
NGC 4954	2.28 ± 0.05	19.98	8.6	1.42	900

Column 1, name; column 2, seeing (this is the FWHM of the PSF); column 3, sky background level; column 4, noise in the image ("sky σ "); column 5, the airmass at the time of exposure; and column 6, the exposure time.

Table 4.2: continued

Name	seeing (")	sky $\left(\frac{\text{mag}}{\text{arcsec}^2}\right)$	sky σ (ADU)	X	exptime (s)
NGC 5289	1.84 ± 0.08	20.71	6.5	1.04	900
NGC 5375	2.75 ± 0.12	20.26	7.8	1.14	900
NGC 5505	1.57 ± 0.15	20.70	6.3	1.08	900
NGC 5515	1.33 ± 0.05	20.62	6.4	1.77	720
NGC 5541	1.99 ± 0.05	20.47	7.3	1.30	900
NGC 5603	2.02 ± 0.08	20.82	6.3	1.08	900
NGC 5644	2.07 ± 0.08	20.68	6.6	1.08	900
NGC 5690	1.53 ± 0.05	20.07	7.3	2.86	720
NGC 5772	2.40 ± 0.08	20.74	6.7	1.22	1000
NGC 5806	1.92 ± 0.05	20.29	7.7	1.56	900
NGC 5876	2.06 ± 0.05	20.73	6.7	1.33	900
NGC 5908	1.72 ± 0.06	20.82	6.5	1.11	900
NGC 5957	1.97 ± 0.10	20.72	6.3	1.23	900
NGC 5980	2.69 ± 0.11	20.70	6.6	1.12	900
NGC 6001	1.71 ± 0.07	20.88	6.3	1.02	900
NGC 6014	2.52 ± 0.11	20.66	6.5	1.16	900
NGC 6030	2.66 ± 0.12	20.80	6.1	1.08	900
NGC 6085	1.76 ± 0.08	20.67	6.6	1.24	900
NGC 6111	1.93 ± 0.05	20.75	6.4	1.29	1000
NGC 6126	1.52 ± 0.04	20.82	6.3	1.15	900
NGC 6143	1.97 ± 0.06	20.33	7.3	1.28	900
NGC 6155	1.58 ± 0.05	20.95	6.0	1.20	900
NGC 6196	2.39 ± 0.11	20.83	6.4	1.13	1000
NGC 6764	2.55 ± 0.12	20.83	6.1	1.06	900

Table 4.3: Ellipse parameters for the control galaxies

Name	a_{max} (")	$\langle \epsilon \rangle$ (1-b/a)	$\langle PA \rangle$ (N-E)
UGC 05734	44	0.6	155
UGC 07064	28	0.1	40
UGC 09295	18	0.4	85
UGC 10097	49	0.25	-70
UGC 10407	-	-	-
UGC 11865	17	0.1	80
IC 875	44	0.4	145
IC 1141	18	0.2	90
NGC 3169	166	0.3	60
NGC 3492	18	0.4	140
NGC 3756	116	0.5	0
NGC 3825	49	0.2	-20
NGC 3938	113	0.1	0
NGC 3968	71	0.35	10
NGC 4045	78	0.35	-90
NGC 4048	21	0.3	95
NGC 4088	96	0.55	60
NGC 4172	36	0.2	5
NGC 4224	94	0.6	50
NGC 4352	59	0.5	100
NGC 4375	36	0.25	20
NGC 4477	125	0.15	50
NGC 4799	36	0.6	88
NGC 4944	25	0.7	90
NGC 4954	33	0.35	80

Column 1, name; column 2, maximum semi-major axis length used in the ellipse fitting; column 3, approximate ellipticity of the galaxy near the outer edge of the profile; and column 4, approximate Position Angle of the major-axis of the galaxy near the edge.

Table 4.3: continued

Name	a_{max} (")	$\langle \varepsilon \rangle$ ($1-b/a$)	$\langle PA \rangle$ (N-E)
NGC 5289	64	0.7	100
NGC 5375	85	0.5	0
NGC 5505	28	0.3	130
NGC 5515	40	0.45	100
NGC 5541	28	0.4	10
NGC 5603	40	0.1	30
NGC 5644	53	0.1	110
NGC 5690	94	0.7	140
NGC 5772	59	0.45	35
NGC 5806	94	0.4	170
NGC 5876	71	0.55	50
NGC 5908	78	0.6	150
NGC 5957	64	0.2	-80
NGC 5980	49	0.6	10
NGC 6001	33	0.1	10
NGC 6014	53	0.15	0
NGC 6030	40	0.3	40
NGC 6085	40	0.15	100
NGC 6111	33	0.5	170
NGC 6126	40	0.15	10
NGC 6143	30	0.2	0
NGC 6155	40	0.3	140
NGC 6196	49	0.3	140
NGC 6764	78	0.75	-110

Table 4.4: surface-brightness profile parameters for the control galaxies

Name	r_0 (kpc)	r_e (kpc)	μ_d (mag/arcsec ²)	μ_b	χ^2_ν	LD (%)	LB (%)
UGC 05734	1.7	38.3	17.16	23.79	0.58	37	63
UGC 07064	5.7	3.4	20.00	20.33	2.12	51	49
UGC 09295	2.9	–	17.68	–	3.17	100	00
UGC 10097	7.3	3.2	20.33	19.53	2.74	39	61
UGC 10407	–	–	–	–	–	–	–
UGC 11865	2.0	13.7	17.37	23.98	0.11	83	17
IC 875	3.3	1.8	20.59	20.17	0.75	38	62
IC 1141	1.9	0.6	18.91	18.04	0.85	54	46
NGC 3169	–	6.0	–	20.97	2.04	00	100
NGC 3492	–	7.9	–	20.30	0.20	00	100
NGC 3756	4.9	2.2	20.18	23.32	2.45	95	05
NGC 3825	17.0	3.7	22.11	19.67	5.08	25	75
NGC 3938	3.8	2.5	20.36	22.38	1.37	77	23
NGC 3968	17.8	6.0	20.77	21.01	2.39	69	31
NGC 4045	5.4	2.2	20.78	20.75	2.67	57	43
NGC 4048	2.4	–	18.31	–	2.03	100	00
NGC 4088	–	59.9	–	24.81	0.40	00	100
NGC 4172	2.1	38.2	18.23	23.30	1.83	17	83
NGC 4224	7.1	8.3	20.39	21.86	0.68	46	54
NGC 4352	0.7	28.7	18.50	24.26	10.45	10	90
NGC 4375	10.0	15.1	20.31	22.59	4.36	53	47
NGC 4477	–	5.5	–	21.02	8.42	00	100
NGC 4799	2.0	6.0	18.20	22.72	0.84	74	26
NGC 4944	5.3	0.2	18.11	15.80	1.40	97	03
NGC 4954	4.7	0.5	18.16	18.15	1.35	95	05

column 1, name; column 2, scale radius of the disk; column 3, effective radius of the bulge; column 4, central surface brightness of the disk; column 5, effective surface brightness of the bulge; column 6, the reduced chi-squared goodness of fit of the model; and columns 7-8): the fractional luminosity contained in each of the disk and bulge respectively.

Table 4.4: continued

Name	r_0 (kpc)	r_e (kpc)	μ_d (mag/arcsec ²)	μ_b (mag/arcsec ²)	χ^2_ν	LD (%)	LB (%)
NGC 5289	-	4.4	-	21.01	5.02	00	100
NGC 5375	9.4	10.0	22.95	22.51	2.17	13	87
NGC 5505	2.7	0.1	18.87	12.06	1.96	64	36
NGC 5515	3.8	13.7	19.41	22.12	0.47	27	73
NGC 5541	5.5	0.4	18.58	17.44	1.93	94	06
NGC 5603	1.1	4.5	18.78	20.55	2.32	09	91
NGC 5644	15.5	7.0	22.38	20.44	4.91	15	85
NGC 5690	4.1	0.5	19.20	20.65	0.47	99	01
NGC 5772	10.4	3.2	20.45	20.28	10.32	66	34
NGC 5806	3.7	1.8	19.75	20.94	7.42	76	24
NGC 5876	16.4	4.0	22.28	20.58	6.78	31	69
NGC 5908	4.6	7.9	18.36	22.38	0.07	82	18
NGC 5957	3.7	2.9	20.27	22.32	2.16	74	26
NGC 5980	3.9	27.0	18.77	24.14	1.17	66	34
NGC 6001	9.3	0.5	19.90	16.93	0.95	82	18
NGC 6014	2.9	0.9	19.79	20.17	1.93	81	19
NGC 6030	2.4	8.2	19.41	21.69	4.92	21	79
NGC 6085	-	12.9	-	21.50	6.80	00	100
NGC 6111	1.7	7.1	18.82	23.29	0.19	61	39
NGC 6126	16.4	7.4	22.03	20.94	0.65	27	73
NGC 6143	5.6	6.0	20.12	23.48	3.58	84	16
NGC 6155	2.7	1.6	19.37	22.33	0.58	92	08
NGC 6196	-	10.4	-	20.72	4.45	00	100
NGC 6764	13.0	0.7	20.46	19.02	0.53	92	08

Table 4.5: Distance and luminosity parameters for the control galaxies

Name	d_β (Mpc)	imscale (kpc/'')	A_{gal} (mag)	L (L^*)	N	Q (L^*/Mpc^3)
UGC 05734	136	0.661	0.00	2.34	14	1.33×10^4
UGC 07064	144	0.696	0.00	1.68	11	1.05×10^4
UGC 09295	178	0.862	0.03	1.77	7	5.34×10^2
UGC 10097	116	0.561	0.03	2.91	16	7.66×10^2
UGC 10407	162	0.783	0.00	0.97	16	1.47×10^6
UGC 11865	180	0.873	0.17	2.14	12	2.47×10^5
IC 875	55	0.266	0.00	0.33	10	1.17×10^3
IC 1141	87	0.422	0.06	0.50	15	2.30×10^2
NGC 3169	26	0.125	0.01	0.85	27	5.20×10^3
NGC 3492	200	0.969	0.01	2.66	16	3.23×10^5
NGC 3756	26	0.125	0.00	0.36	9	3.72×10^2
NGC 3825	125	0.608	0.07	2.68	33	1.69×10^3
NGC 3938	16	0.078	0.00	0.25	22	1.44×10^4
NGC 3968	123	0.597	0.00	4.10	15	9.48×10^2
NGC 4045	39	0.187	0.01	0.53	6	9.91×10^3
NGC 4048	93	0.449	0.02	0.65	4	1.07×10^4
NGC 4088	15	0.073	0.01	0.31	1	1.72×10^2
NGC 4172	176	0.852	0.00	3.54	10	1.97×10^4
NGC 4224	52	0.252	0.00	1.20	10	6.67×10^2
NGC 4352	41	0.201	0.01	0.32	0	-
NGC 4375	172	0.834	0.05	3.82	5	1.17×10^3
NGC 4477	27	0.130	0.01	0.84	9	2.32×10^3
NGC 4799	55	0.269	0.02	0.41	7	8.98×10^2
NGC 4944	136	0.661	0.02	2.18	3	8.41×10^3
NGC 4954	176	0.852	0.02	2.79	5	6.30×10^3

Column 1, name; column 2, distance, based on angular distance derived from the galaxy's redshift; column 3, image scale, based on projected distance at the distance of the host galaxy; column 4, R -band Galactic extinction (from NED); column 5, absolute R luminosity; column 6, number of optical companion galaxies found; and column 7, cumulative tidal effect of the companion galaxies upon the host.

Table 4.5: continued

Name	d_β (Mpc)	imscale (kpc/'')	A_{gal} (mag)	L (L^*)	N	Q (L^*/Mpc^3)
NGC 5289	50	0.240	0.00	0.43	10	2.51×10^4
NGC 5375	47	0.226	0.00	0.46	11	3.35×10^4
NGC 5505	83	0.403	0.00	0.53	4	2.76×10^2
NGC 5515	146	0.706	0.00	1.97	5	1.66×10^2
NGC 5541	147	0.714	0.00	2.23	13	1.92×10^5
NGC 5603	109	0.529	0.00	1.24	20	1.91×10^3
NGC 5644	146	0.706	0.00	6.72	11	5.09×10^2
NGC 5690	34	0.168	0.07	0.35	4	8.71×10^2
NGC 5772	96	0.466	0.03	1.78	7	6.66×10^1
NGC 5806	27	0.130	0.09	0.39	13	1.85×10^4
NGC 5876	66	0.319	0.01	0.87	7	1.78×10^2
NGC 5908	65	0.314	0.01	1.65	8	3.62×10^2
NGC 5957	36	0.175	0.06	0.32	6	2.07×10^2
NGC 5980	80	0.386	0.03	1.18	7	1.14×10^3
NGC 6001	188	0.912	0.04	2.76	12	7.71×10^2
NGC 6014	48	0.232	0.08	0.32	4	6.61×10^2
NGC 6030	88	0.425	0.03	2.17	8	1.35×10^3
NGC 6085	192	0.932	0.04	3.22	12	9.17×10^2
NGC 6111	58	0.281	0.00	0.25	13	3.38×10^4
NGC 6126	185	0.896	0.00	2.30	8	1.38×10^3
NGC 6143	102	0.494	0.00	0.81	20	3.04×10^3
NGC 6155	48	0.232	0.00	0.37	15	3.49×10^3
NGC 6196	178	0.865	0.01	5.43	9	1.74×10^3
NGC 6764	47	0.226	0.13	0.70	10	1.05×10^4

Chapter 5

Comparison Between Seyfert and Control Galaxies

5.1 Introduction

With the analysis of the Seyfert and the control samples complete, a comparison between their properties and the nearby environments of the galaxies can be undertaken. This chapter will compare the two samples in terms of a wide variety of parameters. Section 5.2.1 will describe the distribution of parameters related to the selection of the host galaxies based on redshift and luminosity. Section 5.2.2 will compare the surface-brightness profile parameters from the isophotal analysis and discuss the problems associated with multi-component fitting. Section 5.3.1 will compare the nearby environments of the hosts by examining properties of the optical companion galaxies found around the host galaxies. Section 5.3.2 will discuss the frequency with which disturbed morphologies occur within the host galaxies. Finally, Section 5.4 will summarize the comparison of the Seyfert galaxies and the control galaxies.

5.2 Distribution of Host Galaxy Properties

5.2.1 Host Galaxies

As mentioned in Chapter 1, the control galaxies were selected based on their redshift, morphology, and luminosity. The following histograms illustrate the distributions of some of these properties. All the histograms in this chapter follow the same format: the x-axis (abscissa) is the parameter whose distribution is being considered, and the y-axis (ordinate) shows the relative frequency of that parameter. The left panel shows the relative frequency for all the data (Seyfert + control), the middle panel shows the relative frequency for the Seyfert data (Seyfert 1 as a solid line, Seyfert 2 as a dotted line), and the right panel shows the relative frequency for the control galaxy data. The histograms have been normalized such that $\int f dx = 1$. The distributions have been compared by using the Kolmogorov-Smirnov (K-S) test in which the *null hypothesis* is that the two properties being compared are from the same underlying population. Mention will be made only if the K-S test rejects the null hypothesis at a confidence level of 95% or greater.

Figure 5.1 shows the distribution of redshifts of the hosts. As can be seen, the redshift distributions of the Seyferts and control galaxies are similar, as also shown by the K-S test. The distribution of distances calculated from Equation 2.12 (in units of Mpc) can be seen in Figure 5.2.

The distribution of the apparent magnitudes of the hosts as measured by M.M. De Robertis (Paper I) with PPP can be seen in Figure 5.3. Using the distances to the host galaxy, the absolute magnitude of the galaxy is computed using Equation 2.13, and the distribution of absolute magnitude can be seen in Figure 5.4. The K-S test shows that the distributions are similar for both the Seyfert and control galaxies.

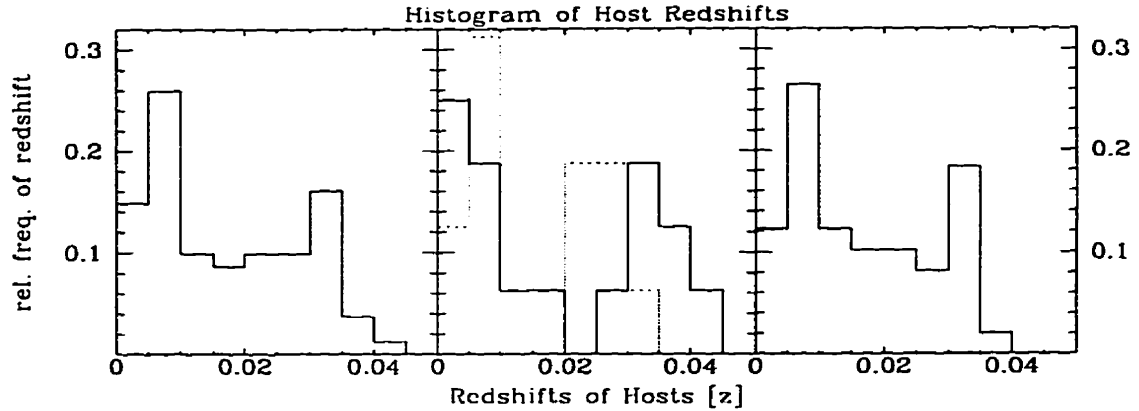


Figure 5.1: Distribution of host galaxy redshift. Left panel: all hosts. middle panel: Seyferts (solid: Sy1, dotted: Sy2). right panel: Control hosts.

The distribution of ellipticities of the hosts are found in Figure 5.5. The distributions are similar as demonstrated by the K-S test, so any affect caused by tilt extinction will be present in both samples. Tilt extinction is being neglected since it is difficult to measure and so is much less tractable to include.

As can be seen from the basic properties of the host galaxies, a fair comparison can be made between the two samples since the distributions are similar. Though there are slight differences in the distributions of redshift and apparent magnitude between the Seyfert 1s and 2s, a fair comparison can still be made.

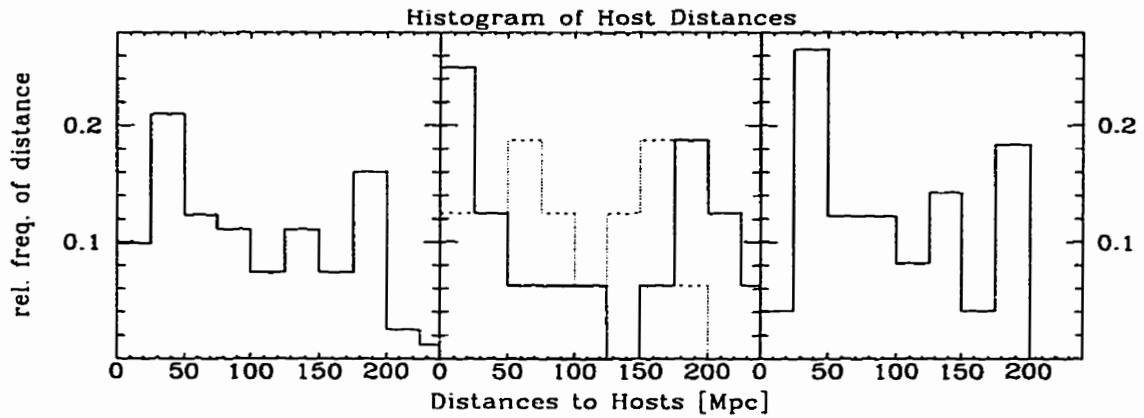


Figure 5.2: Distribution of host galaxy distances (distances are given in h^{-1} Mpc). Left panel: all hosts. middle panel: Seyferts (solid: Sy1, dotted: Sy2). right panel: Control hosts.

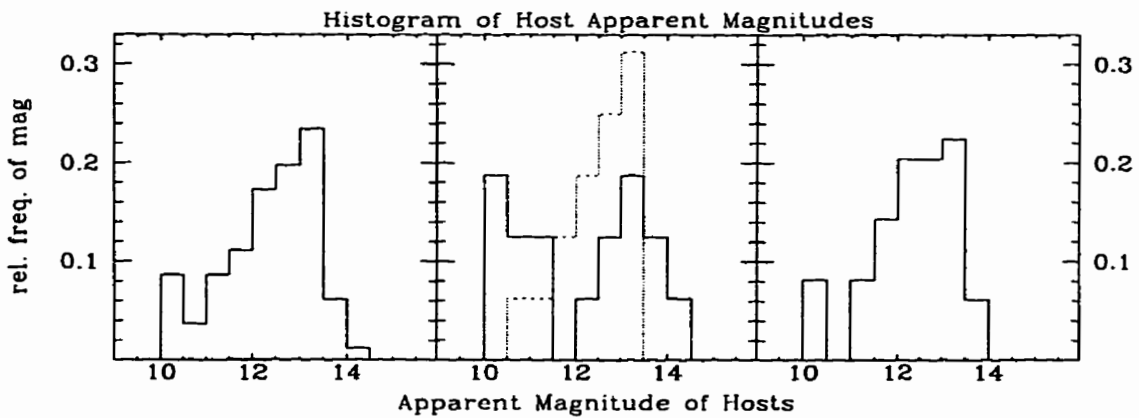


Figure 5.3: Distribution of apparent magnitudes of host galaxies. Left panel: all hosts. middle panel: Seyferts (solid: Sy1, dotted: Sy2). right panel: Control hosts.

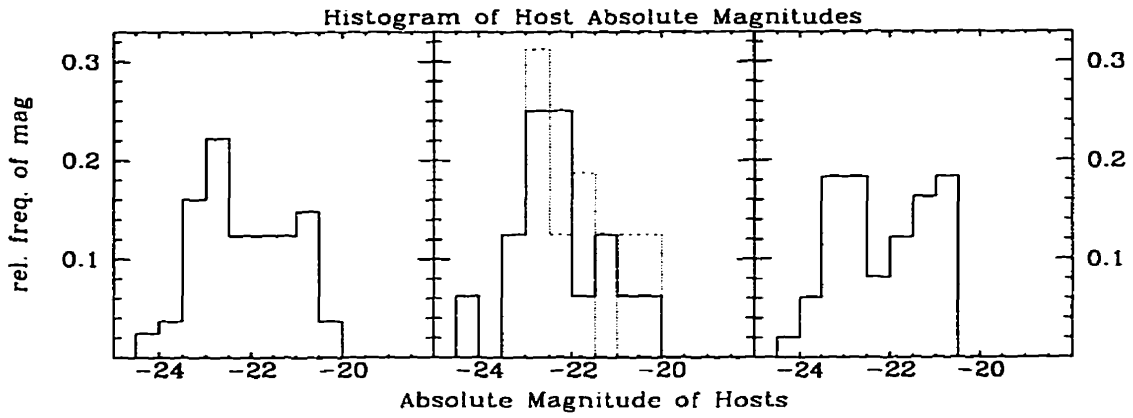


Figure 5.4: Distribution of absolute magnitudes of host galaxies. Left panel: all hosts. middle panel: Seyferts (solid: Sy1, dotted: Sy2). right panel: Control hosts.

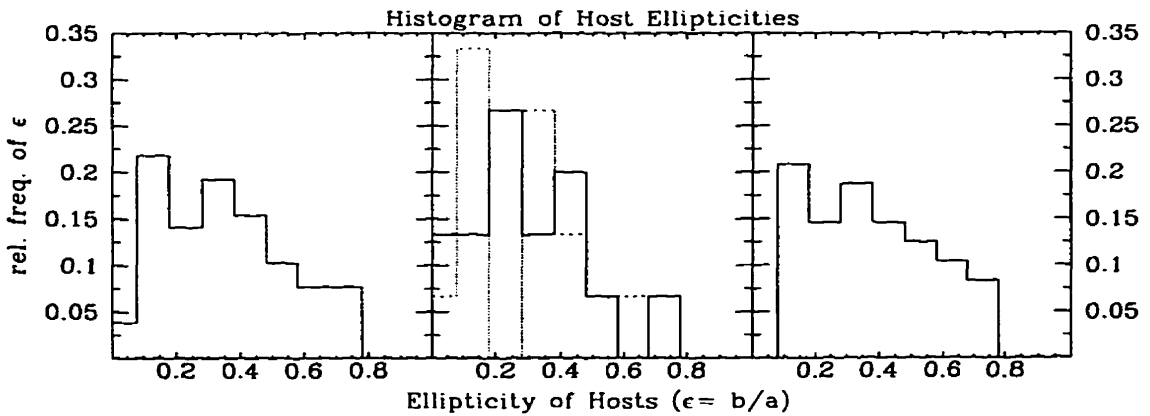


Figure 5.5: Distribution of ellipticities of host galaxies. Left panel: all hosts. middle panel: Seyferts (solid: Sy1, dotted: Sy2). right panel: Control hosts.

5.2.2 Distribution of parameters from surface-brightness profile fitting

This section presents the distribution of parameters measured from the 3-component surface-brightness profile-fitting routines. Both the disk and bulge parameters will be shown. Figure 5.6 displays the distribution of the disk scale radii r_0 (in kpc), and Figure 5.7 shows the distribution of the bulge effective radii r_e (in kpc) of the host galaxies. The distribution of disk central surface brightness μ_d (mag/arcsec²) can be seen in Figure 5.8, and the distribution of bulge effective surface brightness μ_b (mag/arcsec²) is presented in Figure 5.9.

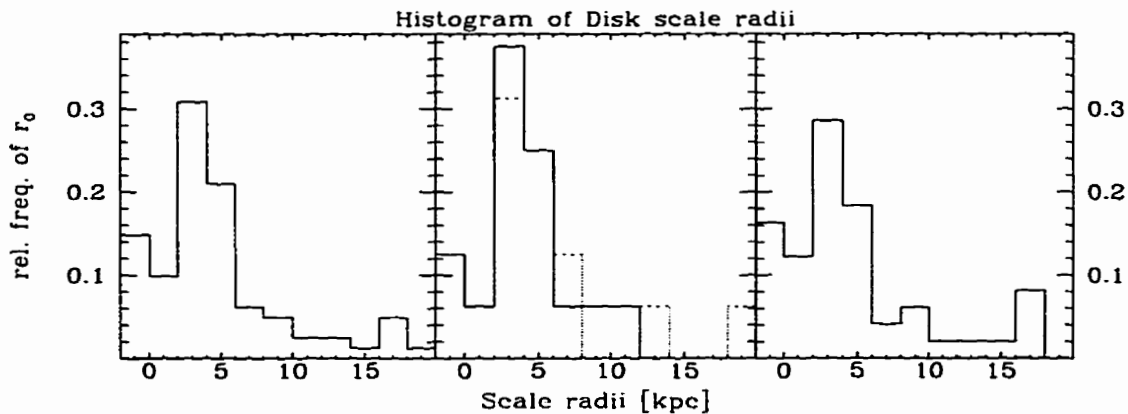


Figure 5.6: Distribution of fitted scale radii r_0 (kpc). Left panel: all hosts. middle panel: Seyferts (solid: Sy1, dotted: Sy2). right panel: Control hosts.

The four parameters have a somewhat similar distribution for the Seyfert and control hosts, as well as between the Seyfert 1s and 2s according to the K-S test, except for the bulge radii (for which the Seyfert versus the control distribution is rejected at the 97% level). The mean scale radii are $\langle r_0 \rangle = 5.2 \pm 0.7$ kpc for the Seyferts, and $\langle r_0 \rangle = 6.0 \pm 0.8$ kpc for the control galaxies (the uncertainties given are the rms of the mean). The mean disk surface brightness for both the Seyfert and the

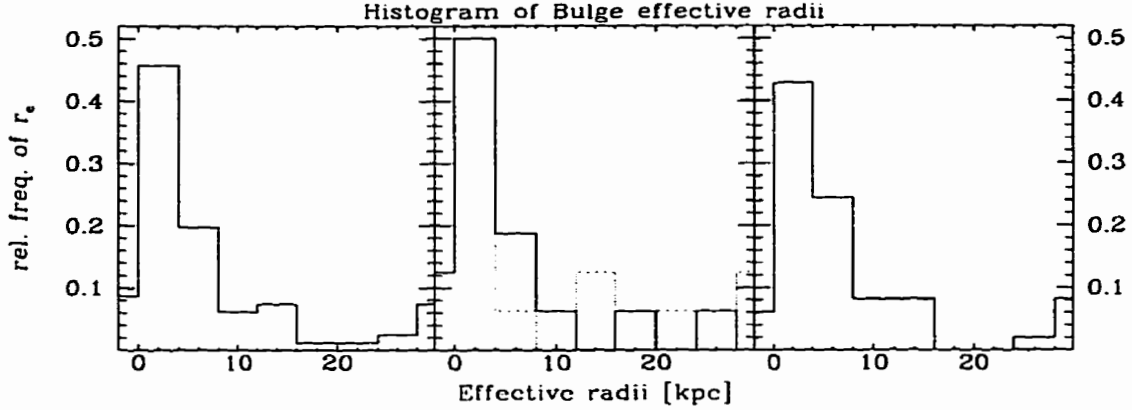


Figure 5.7: Distribution of fitted effective radii r_e (kpc). Left panel: all hosts. middle panel: Seyferts (solid: Sy1, dotted: Sy2). right panel: Control hosts.

control hosts are $\langle \mu_d \rangle = 19.74 \pm 0.21$ mag/arcsec² and $\langle \mu_d \rangle = 19.67 \pm 0.22$ mag/arcsec² respectively. The mean bulge effective radii are $\langle r_e \rangle = 9.2 \pm 2.8$ kpc for the Seyferts, and $\langle r_e \rangle = 8.6 \pm 1.8$ kpc for the control galaxies. The mean bulge surface brightness for both the Seyfert and the control hosts are $\langle \mu_b \rangle = 20.71 \pm 0.48$ mag/arcsec² and $\langle \mu_b \rangle = 21.01 \pm 0.35$ mag/arcsec² respectively. The average fraction of luminosity from the three components in the Seyfert galaxies was 54% from the disk, 40% from the bulge, and 6% from the PSF. The control galaxies in comparison, had average luminosity fractions of 53% from the disk and 47% from the bulge. These similarities indicate yet again that the control sample can be fairly compared with the Seyfert sample. The difference in the distribution of the bulge radii is noticeable for small r_e and arises since the bulge and the Gaussian PSF are difficult to distinguish between.

With multi-component non-linear fits, issues of confidence, numerical stability, and uniqueness arise. Fitting a disk and bulge simultaneously is generally considered relatively straightforward, whereas fitting three components simultaneously carries with it some risk. The three-component fitting I performed is indeed sensitive to the

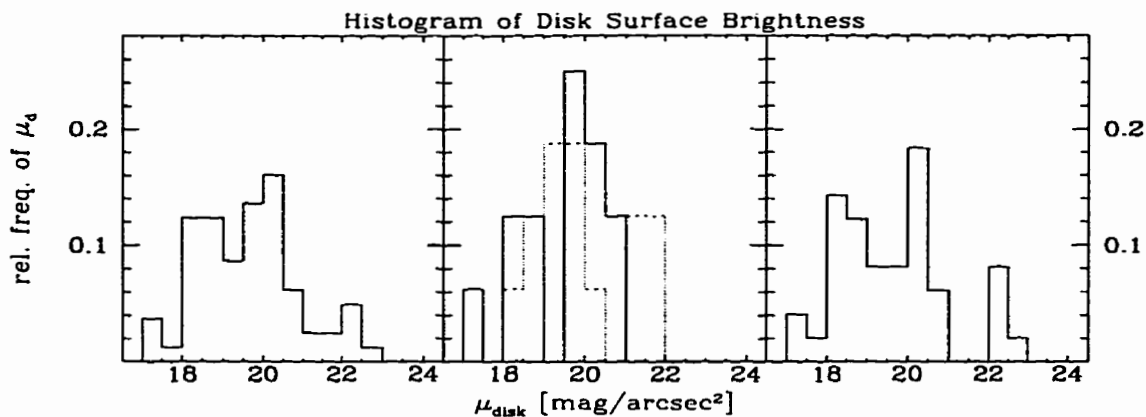


Figure 5.8: Distribution of fitted disk surface brightness μ_d (mag/arcsec²). Left panel: all hosts. middle panel: Seyferts (solid: Sy1, dotted: Sy2). right panel: Control hosts.

quality of the data and the initial “guesses” of the parameters, as the chi-squared hypersurface can be complicated. With such a large parameter-space, there can be many local minima in the hypersurface, and so it may be difficult to find the global minimum. There are two further complications regarding the third component (the PSF) in these fits:

1. The data from `Ellipse` starts at 1.8 pixels from the intensity centroid. At that radius, the PSF is typically down to 20% of its peak value, and so we are trying to fit the lower-intensity “wings” of the PSF.
2. For the inner pixels, the PSF and bulge component are both very similar in that they are strongly peaked at the center. Due to this, the parameters μ_N , μ_b and r_e are strongly correlated.

In order to test the stability and uniqueness of the three-component fits, they were redone using an inner radius of 5 pixels using only bulge and disk components. A Gaussian PSF is down to 2% or less peak intensity at that radius, so this is reasonable. It was found that the disk parameters are quite stable, but that the bulge parameters

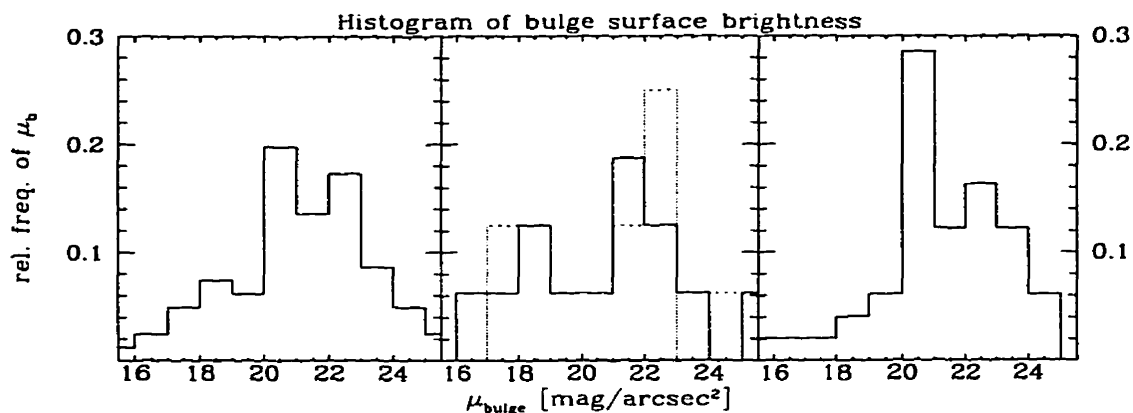


Figure 5.9: Distribution of fitted bulge surface brightness μ_b (mag/arcsec²). Left panel: all hosts. middle panel: Seyferts (solid: Sy1, dotted: Sy2). right panel: Control hosts.

show a fair amount of variability in some galaxies.

There are obvious limitations to fitting three-component models in this fashion, though there are problems with any procedure which fits parameters simultaneously. An alternative empirical method of extracting the three components is to find a bright unsaturated star on the image (a good PSF), and to subtract scaled versions of this from the nucleus until some pre-determined criteria are met. In this manner the PSF parameters are then known, and the resulting surface-brightness profile follows a standard two-component fit. We chose not to pursue this method both because it is time-intensive and because there is still a significant degree of subjectivity associated with it.

Finally, I would like to note the frequency with which the PSF does not fit at all. The three-component fits were only performed for the Seyfert galaxy profiles, where we expect to find a PSF component due to its bright star-like nucleus. Of these fits, a PSF was recovered in 11 of 15 Seyfert 1s, but only in 4 of 15 Seyfert 2s. This is explainable by the observational evidence that Seyfert 1s are brighter than

Seyfert 2s (Yee 1983), and thus it is more difficult to fit a PSF to Seyfert 2s. When the alternative method of fitting the three components is performed the situation becomes slightly better, in which 12 of 15 Seyfert 1s and 8 of 15 Seyfert 2s were fit with a PSF.

5.3 Distribution of Environmental Properties

5.3.1 Properties Derived from Companion Galaxy Data

This section presents information regarding the companions around the host galaxies and their “projected” properties. The first point I would like to stress is that these galaxies are not necessarily physical companions, some are optical, and thus the projected separation distances are a minimum. For the 32 Seyfert hosts, 371 optical companion galaxies were found (averaging 11.6 companions/host), while for the 49 control hosts, 657 optical companions were found (averaging 13.4 companions/host). In order to provide a fair comparison between the two samples we will only consider those galaxies which are within 200 kpc (projected distance); this ensures that the comparison is being performed using companions within a similar radius in the rest frame of the hosts. Within 200 kpc, 359 optical companions were found around the Seyfert hosts (11.2 ± 1.0 companions/host; Sy1: 175, Sy2: 184), and 520 optical companions were found around the control hosts (10.6 ± 0.9 companions/host. As in the previous section, the uncertainties are the rms of the mean). Figure 5.10 shows the relative frequency of the number of companions around each host, and as the K-S test shows, the distributions are similar for the two samples.

The distribution of projected separation distance from the companions to the host

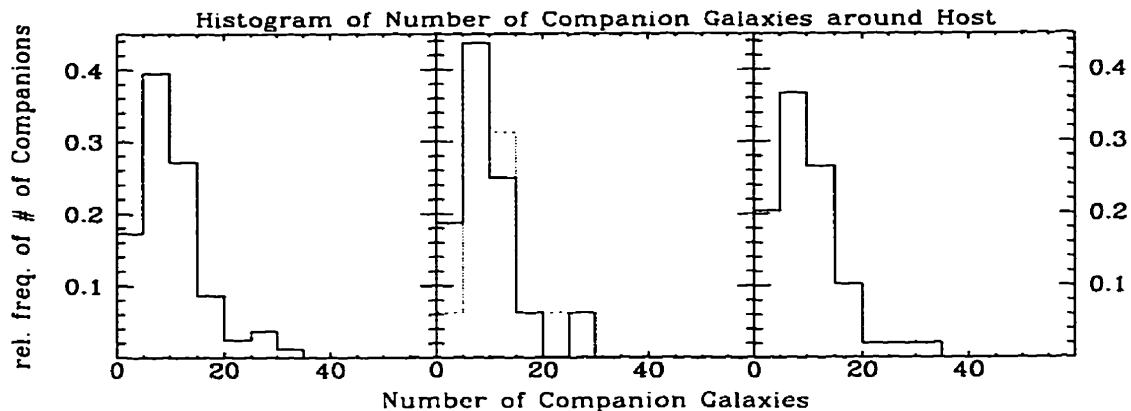


Figure 5.10: Distribution of the number of companion galaxies around the hosts. Left panel: all hosts. middle panel: Seyferts (solid: Sy1, dotted: Sy2). right panel: Control hosts.

galaxies is presented in Figure 5.11 (in kpc). The K-S test shows that both distributions are similar, though the Seyfert galaxies appear to have a slightly higher frequency of companions within 50 kpc (which may be important tidally). As would be expected, the companions are found randomly with respect to position angle around the hosts, as can be seen in Figure 5.12 (measured from North through East). As the histogram is binned into 45° intervals, one expects a flat distribution with a relative frequency of 0.125 in each bin, which one observes.

Based on the integrated flux of the companion galaxies, various magnitude and luminosity parameters can be computed. The logarithm of the distribution of the companion galaxies' apparent magnitudes is presented in Figure 5.13. Both samples have a similar distribution as demonstrated by the K-S test, in which the relative frequency of objects between 12 – 19 magnitude roughly follows a power-law, as one expects from the luminosity function for galaxies (Schechter 1976). At a magnitude of approximately $R = +19$ the distribution turns over and rapidly drops to zero,

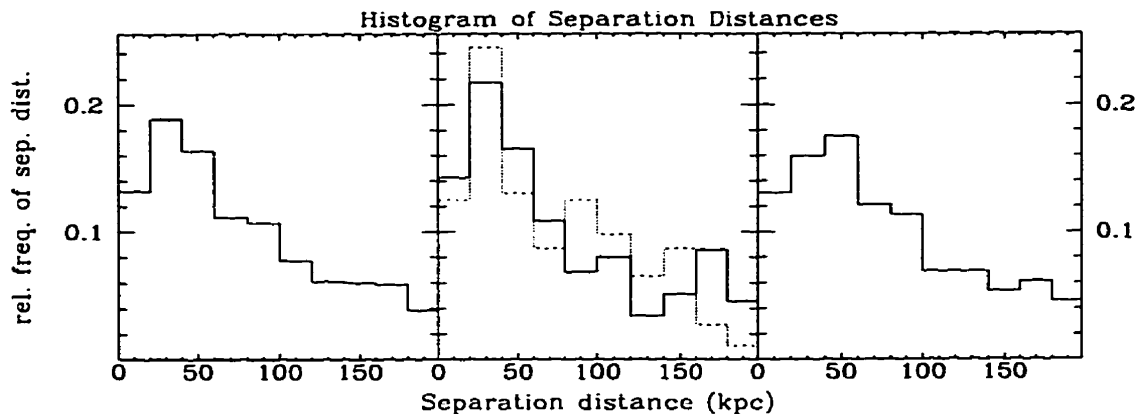


Figure 5.11: Distribution of companion galaxy separation distances (in kpc). Left panel: all hosts. middle panel: Seyferts (solid: Sy1, dotted: Sy2). right panel: Control hosts.

indicating the magnitude at which incompleteness sets in and thus the limiting magnitude to which I could detect faint companion galaxies efficiently. This illustrates that the galaxy counts are roughly complete down to 19th magnitude, after which the counts are incomplete. The magnitude difference between the host galaxy and its companion galaxies can then be computed via $R_{comp} - R_{host}$, and the distribution of Δm can be seen in Figure 5.14. Again, both the Seyfert and control companion distributions are similar (though the null hypothesis is rejected at the 99.9% level for comparison between the Seyfert 1s and 2s). There are differences between the Seyfert 1s and 2s in that the Seyfert 2s have an excess of companions in the $\Delta m = 5.5 - 7$ range, while the Seyfert 1s have an excess of companions in the $\Delta m = 7 - 9$ range. Using the distances to the host galaxies, the absolute magnitudes of the companions can be calculated (based on the assumption that the companion galaxies are located at the same distance from us as the host). The distribution of the projected absolute magnitudes of the companion galaxies is presented in Figure 5.15; to a first approximation the Seyfert and control companions have a similar distribution, though the

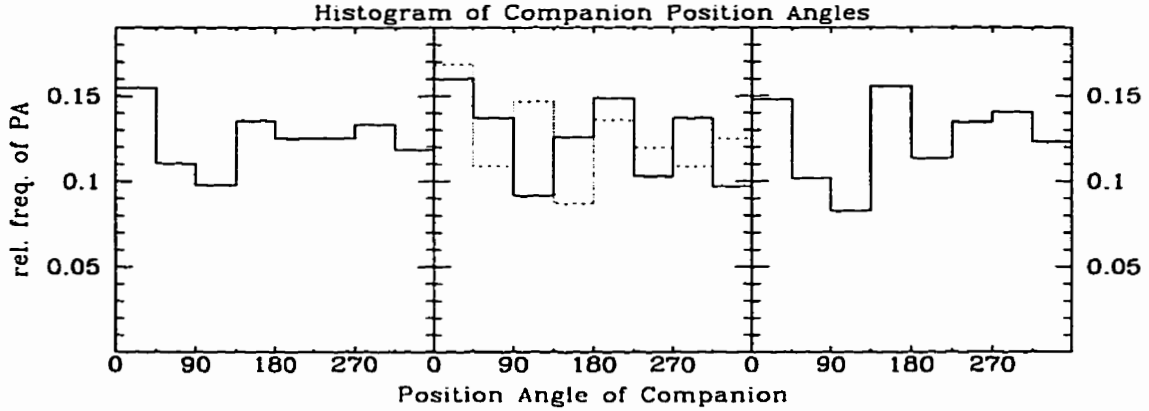


Figure 5.12: Distribution of Position Angle of companions with respect to host [North through East]. Left panel: all hosts. middle panel: Seyferts (solid: Sy1, dotted: Sy2). right panel: Control hosts.

differences between the Seyfert 1s and 2s (as noted with the Δm parameter), are apparent in this parameter as well (Seyfert 1s and 2s distribution rejected at the 98% level).

Now that the “absolute” magnitudes of the companions galaxies have been calculated, their luminosities can be computed. Using $M_R^* = -22.1$ (Schechter 1976) which is equivalent to L^* , the distribution of companion galaxy luminosities can be seen in Figure 5.16. From the luminosity, the “tidal” parameter for each companion galaxy can be calculated as described in Section 2.4.6. Figure 5.17 contains the distribution of the individual companion galaxy tidal parameters, and Figure 5.18 presents the distribution of the cumulative tidal parameter $Q = \sum Q_i$ for each host galaxy. The K-S test shows that the distribution of Q_i is similar for both the Seyfert and control companion galaxies, as is also the case for Q . Unlike the distribution absolute magnitude, the Seyfert 1s and 2s companions have similar distributions of the tidal parameter according to the K-S test. There are, however, a few hosts (both samples) in which $Q > 10^5 L^*/\text{Mpc}^3$, consisting of severely disturbed systems (Seyfert:

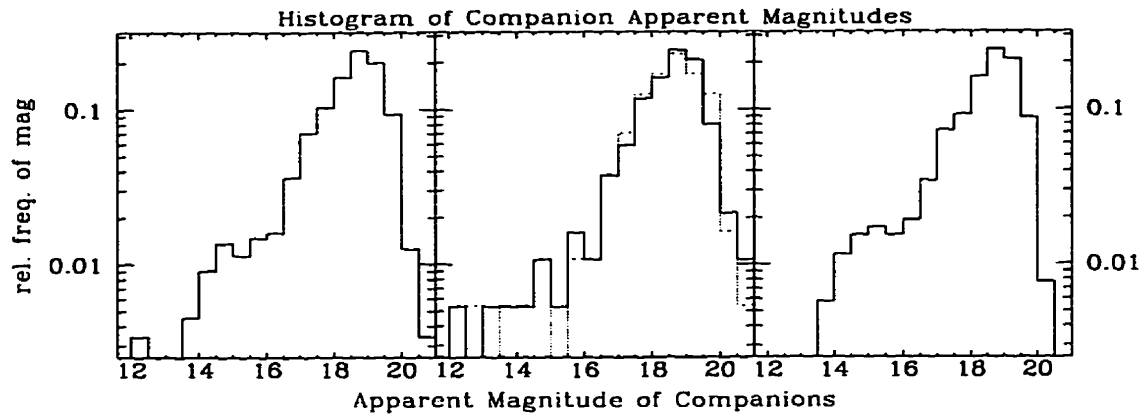


Figure 5.13: Distribution of apparent magnitudes of the companion galaxies. Left panel: all hosts. middle panel: Seyferts (solid: Sy1, dotted: Sy2). right panel: Control hosts.

NGC 5256, NGC 5929, NGC 6104. Control: UGC 10407, UGC 11865, UGC 3492, and NGC 5541).

As seen with all the parameters related to the optical companions of the host galaxies, the environments of Seyfert galaxies and the control galaxies are fairly similar. There is a difference in the distribution of faint galaxies around Seyfert 1s compared to Seyfert 2s, though when considered together, the Seyfert and control companion distributions are similar. There is also no obvious difference in the tidal influences the companion galaxies have on the hosts, though both samples have their share of very tidally disturbed systems ($\sim 8\%$).

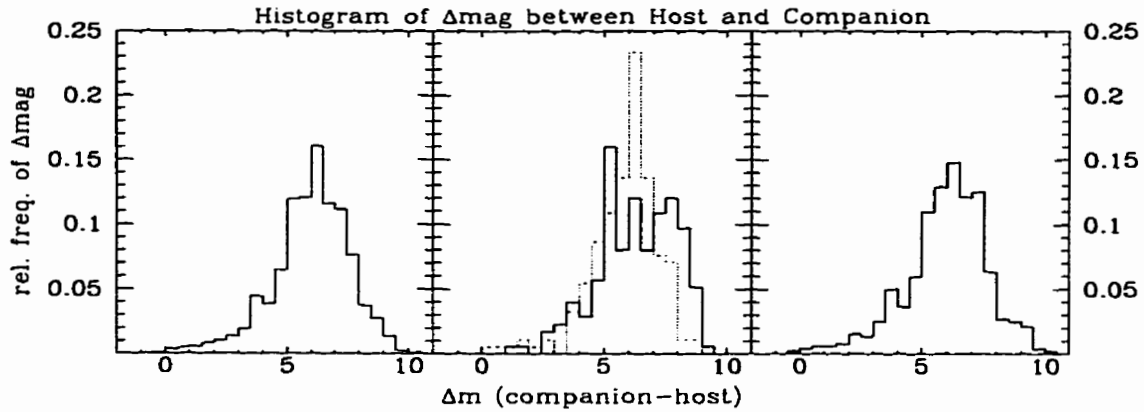


Figure 5.14: Distribution of Δmag between host galaxy and companion galaxies ($R_{comp} - R_{host}$). Left panel: all hosts. middle panel: Seyferts (solid: Sy1, dotted: Sy2). right panel: Control hosts.

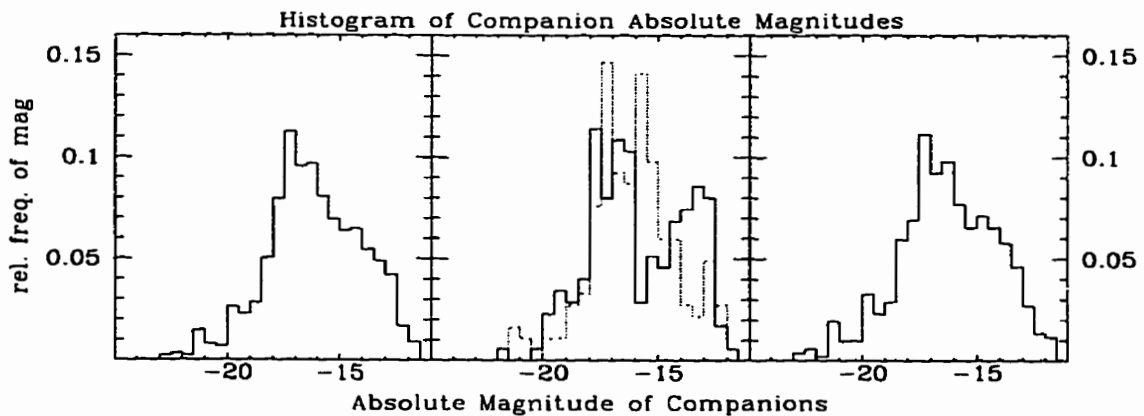


Figure 5.15: Distribution of absolute magnitudes of the companion galaxies (assuming distance same as that of host). Left panel: all hosts. middle panel: Seyferts (solid: Sy1, dotted: Sy2). right panel: Control hosts.

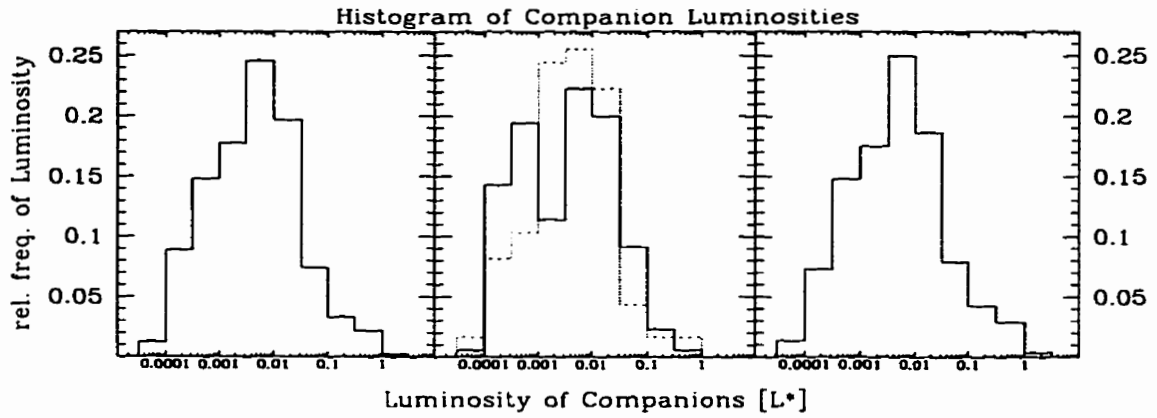


Figure 5.16: Distribution of companion galaxy luminosities (L^*). Left panel: all hosts. middle panel: Seyferts (solid: Sy1, dotted: Sy2). right panel: Control hosts.

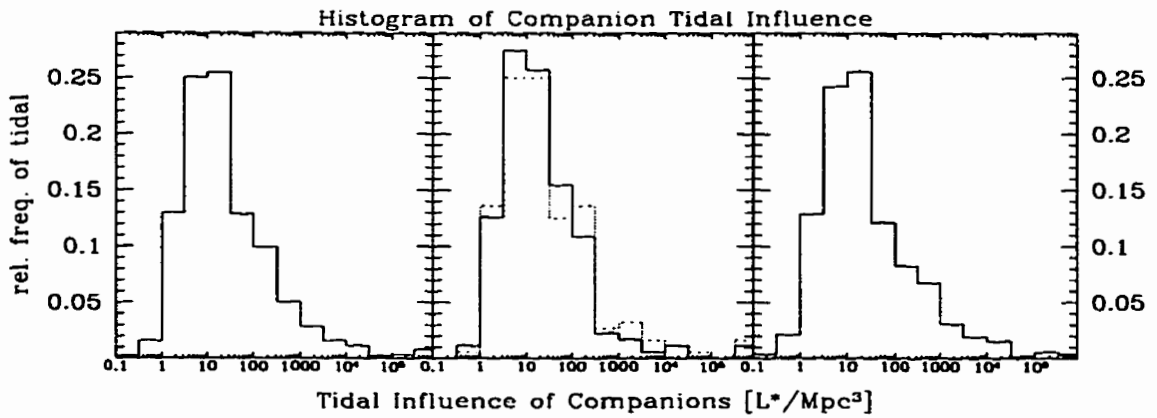


Figure 5.17: Tidal parameters of the companion galaxies. Left panel: all hosts. middle panel: Seyferts (solid: Sy1, dotted: Sy2). right panel: Control hosts.

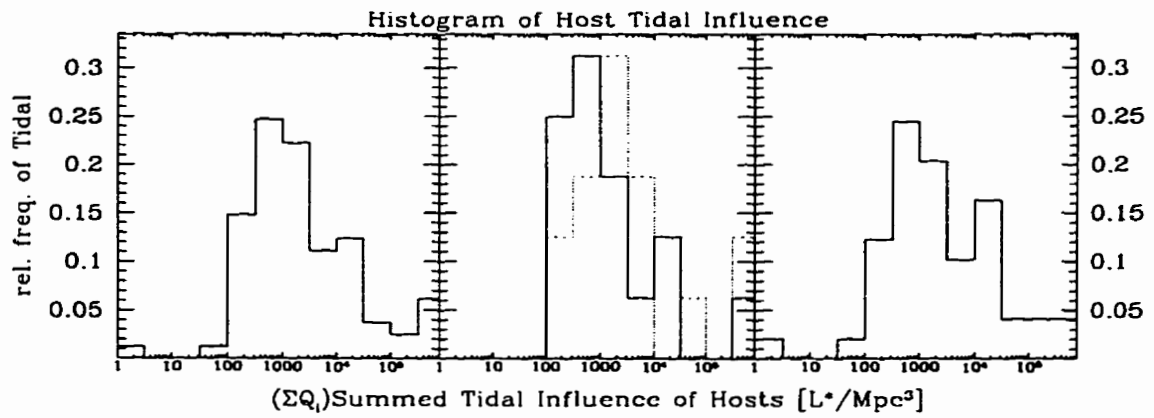


Figure 5.18: Summed tidal parameters of the companion galaxies for the hosts ($Q = \Sigma Q_i$). Left panel: all hosts. middle panel: Seyferts (solid: Sy1, dotted: Sy2). right panel: Control hosts.

5.3.2 Host Galaxy Morphological Disturbances

Light asymmetries and morphological disturbances of the host galaxies are another aspect of the environment of the host galaxies which can be examined. There are various morphological features which *may* be a symptom of a recent interaction or merger or evidence for a radial flow of material.

As mentioned earlier, bars are thought to be an efficient mechanism of transporting gas to the inner regions of a galaxy, thus fueling a possible AGN (Athanasoula 1992; Shlosman and Noguchi 1993). As such, it is instructive to note the frequency of bars in the host galaxies. Rings can be a symptom of a recent interaction in which a companion object passes right through the host galaxy (e.g., Combes et al. 1991). Any other form of distortion or disturbance in the galaxy may also be a sign of some kind of interaction, and may appear as tidal tails, bridges, prominent dust lanes, or other significant light asymmetries. Another sign of a recent interaction may be extreme twisting of isophotes (i.e. position angle profile changes by a large amount, say 45°). Tables 5.1 and 5.2 show the frequency of morphological disturbances in both the Seyfert host and the control host respectively detected in this analysis. A (\checkmark) indicates that the feature was noticed in the galaxy, and (\dagger) indicates that a partial feature was observed. A “B” shows the presence of bars in the host galaxy, an “R” rings, a “D” distortions of some other variety, “ Θ ”, illustrates which galaxies have position-angle profiles which have “excursions” of more than 45° , and finally, an “A” shows the occurrence of any of the previous disturbances (i.e. bar and/or ring and/or distortions).

Table 5.3 summarizes the frequency of bars, rings, and other distortions. It presents the number of galaxies containing the feature (including partial features in parentheses) as well as the fraction of galaxies with that feature. As can be seen,

Table 5.1: Seyfert hosts: Bars, rings and distortions

Name	B	R	D	Θ	A
Mrk 0231			✓	✓	✓
Mrk 0461	✓				✓
Mrk 0471	✓			✓	✓
Mrk 0789			✓		✓
Mrk 0817					
Mrk 0841					
UGC 06100	†				†
UGC 08621				✓	✓
NGC 3080				✓	✓
NGC 3227			✓		✓
NGC 3362				✓	✓
NGC 3516				✓	✓
NGC 3718			†	✓	✓
NGC 3786		†	✓		✓
NGC 3982			†	✓	✓
NGC 4051			✓		✓
NGC 4151	✓	†		✓	✓
NGC 4235			†		†
NGC 4253	✓	†			✓
NGC 4388			†		†
NGC 5252					
NGC 5256			✓		✓
NGC 5273					
NGC 5283					
NGC 5347	✓	✓			✓
NGC 5548		✓	✓	✓	✓
NGC 5674	✓	✓			✓
NGC 5695	†				†
NGC 5929					
NGC 5940	✓				✓
NGC 6104		✓	✓		✓
NGC 6814	†	†			†

Table 5.2: Control hosts: Bars, rings and distortions

Name	B	R	D	Θ	A	Name	B	R	D	Θ	A
UGC 05734	†				†	NGC 4954					
UGC 07064	✓	✓			✓	NGC 5289	✓	✓			✓
UGC 09295						NGC 5375	✓				✓
UGC 10097						NGC 5505	✓				✓
UGC 10407			✓		✓	NGC 5515		†			†
UGC 11865			✓		✓	NGC 5541			✓		✓
IC 875						NGC 5603					
IC 1141						NGC 5644					
NGC 3169			✓		✓	NGC 5690			✓		✓
NGC 3492			✓		✓	NGC 5772					
NGC 3756						NGC 5806	†				†
NGC 3825	✓			✓	✓	NGC 5876	✓	✓		✓	✓
NGC 3938				✓	✓	NGC 5908			†		†
NGC 3968	✓			✓	✓	NGC 5957	✓	✓			✓
NGC 4045	†		✓	✓	✓	NGC 5980					
NGC 4048	✓		✓		✓	NGC 6001	†			✓	✓
NGC 4088	✓		✓		✓	NGC 6014	†	†		✓	✓
NGC 4172						NGC 6030					
NGC 4224			†		†	NGC 6085					
NGC 4352						NGC 6111					
NGC 4375		†		✓	✓	NGC 6126					
NGC 4477	†			✓	✓	NGC 6143			✓		✓
NGC 4799						NGC 6155	✓			✓	✓
NGC 4944						NGC 6196					
						NGC 6764	✓				✓

Table 5.3: Frequency of bars, rings and distortions

	Seyfert		Control	
	#	%	#	%
Bars	7(10)	22(31)	12(18)	24(37)
Rings	4(8)	13(25)	4(7)	8(14)
Dist.	8(12)	25(38)	11(13)	22(27)
Θ	10	33	11	22
Any	21(26)	66(81)	26(31)	53(63)

there are slightly different ratios of galaxies that contain bars or rings in both samples. However, a large fraction of the galaxies in both samples contain some form of disturbance, though a slightly larger fraction of Seyfert galaxies contain a disturbance. This indicates that the environments of Seyfert galaxies are similar to control galaxies in terms of possible morphological disturbances.

5.4 Summary

A summary can now be made regarding the properties and the environment of Seyfert galaxies as compared to control sample of galaxies. As seen in previous sections, the Seyfert galaxies and the control galaxies were selected to have similar redshifts, morphologies, and luminosities. These two samples of galaxies were then found to have similar surface photometry parameters resulting from the isophotal analysis, indicating that a fair comparison can be made between the two samples. The Seyfert and control hosts were also seen to be in similar environments with regard to the number of optical companion galaxies, and their corresponding projected luminosities and tidal influence. Finally, we saw that both sets of galaxies are also very similar in that the same fraction contains some form of morphological disturbance. The concluding chapter will attempt to address these similarities in terms of the Unified Model and the interaction hypothesis.

Chapter 6

Conclusions

In studying 32 Seyfert galaxies and a control sample of 49 non-active galaxies, we sought to test the interaction model for activity in galactic nuclei. The AGN “engine” consists of the accretion of material onto a supermassive black hole. The interaction hypothesis describes the mechanism by which the fuel reaches the accretion disk and central engine. This model proposes that material is transported to the inner region of the galaxy via a perturbing interaction (either a tidal perturbation or a cannibalistic merger). In this model, Seyfert galaxies should then have an excess of companion galaxies as compared to normal galaxies. In testing this hypothesis, this thesis examined the morphologies and optical companion galaxies of Seyfert galaxies and a control sample of normal galaxies in order to compare the environments of Seyfert galaxies to that of normal galaxies, and found that the environments are similar. The two samples were matched in redshift, morphological class, and luminosity in order to minimize any biases that may arise due to unknown selection effects, and the host-galaxy properties were then examined to determine if a fair comparison could be made between the two samples.

The process of investigating the nearby environments of the galaxies involved several steps. The surface-brightness profiles were measured using the elliptical isophotal

routines in IRAF, which were then fit with a disk and a bulge component (and a Gaussian PSF in the case of the Seyfert galaxies). Optical companions were then visually searched for and their relevant parameters were measured (i.e. position and apparent magnitude). Finally, unusual host-galaxy morphologies were examined by visual inspection and using unsharp-masking techniques to find features such as bars and rings.

The surface-brightness profile-fitting parameters for the Seyfert and control galaxies were compared. The radial and intensity parameters (τ_0 , r_e , μ_d , and μ_b) were found to have similar distributions in the two galaxy samples, thus indicating that the control sample is a fair one. It was acknowledged that the three-component fitting technique used for the Seyfert galaxies can be problematic and that there may be better ways of achieving more consistent fits. As expected, however, Seyfert 1s were much more successful at having the nuclear component fit, which confirms observations that Seyfert 1s have a more dominant nucleus than Seyfert 2s. Other than this difference, the other surface brightness profile parameters were similar for both the Seyfert 1s and 2s.

Similarities were also found in the environments of the sample galaxies via companion galaxy counts. Counts of optical companion galaxies around the host galaxies resulted in an average of 11.2 ± 1.0 companions/Seyfert galaxy and 10.6 ± 0.9 companions/control galaxy when a maximum search radius of 200 kpc was imposed. The distributions of the various parameters derived from the companions were similar for both the Seyfert and the control samples, which included angular distribution, apparent and absolute magnitudes, luminosities, and maximal tidal influence. The similarity in these parameters indicates that the nearby environments of Seyfert galaxies are similar to that of the control galaxies. One difference was noted, however; Seyfert 1s and 2s had somewhat different distributions of Δm (difference in apparent magnitude

between the companion galaxies and their hosts), although it is not known whether this is significant in terms of the interaction hypothesis. Unlike Paper II, it was found that Seyfert 1s and 2s had a similar number of companion galaxies (perhaps because this companion search went $\gtrsim 6$ magnitudes dimmer than the host galaxies).

The frequency of disturbed morphologies such as bars, rings, and position angle excursions was also examined. It was found that the control galaxies had roughly the same fraction of disturbed galaxies as did the Seyfert sample. The fraction of “disturbed” galaxies was found to be roughly 2/3 for the control sample and 3/4 for the Seyfert sample. This is another indication that the environments of Seyfert galaxies are roughly similar to normal galaxies, just as in Paper II, which finds that Seyfert galaxies are not found in richer environments as compared to the control sample.

Based on this analysis, Seyfert galaxies and the control galaxies occupy similar environments, and exhibit a similar frequency of disturbances. This similarity has a few implications for the interaction hypothesis. Since the Seyfert galaxies and the control galaxies occur in similar environments this could indicate that galaxy-galaxy interactions do not necessarily initiate activity in AGNs but, rather, may contribute to increased star formation in the host (e.g., Larson and Tinsley 1978). This is not to say that perturbing interactions do not initiate activity, but rather these may not be necessary, and that there may be other mechanisms which are not yet understood that can also lead to activity. If there is not enough material being transported to the innermost region of the galaxy due to a perturbing interaction then there will not be any activity; though if material does get to the inner parsec there will be activity provided a SBH exists. There are Seyfert galaxies that do not appear to be morphologically disturbed, so there may be alternative mechanisms for transporting gas to the inner galaxy and thus initiating activity. Clearly, the interaction model

needs to be studied in more detail to determine whether it is reasonable hypothesis, or whether the theory needs to be modified. One suggestion put forth by Paper II is that “minor mergers” may play an important role in the activity of low-luminosity AGNs such as Seyferts, since minor mergers should occur more frequently than major interactions and can drive a sufficient quantity of fuel into the central region of the host.

More research needs to be done in the area of Seyfert galaxies and their environments since there is no clear consensus yet regarding the interaction hypothesis. In order to accomplish this, one should acquire higher resolution images in several passbands of a large number of Seyfert galaxies and control galaxies (using the adaptive optics bonnet at CFHT perhaps) in order to detect very small and close disturbances. Using a large sample of galaxies will improve the statistical uncertainties, thus sharpening the comparison between the two samples. Multiple-colour images provide information on the nature of the galaxies (such an analysis is currently in progress using two colours, B and R , by S. Virani). Higher quality surface-brightness profiles could then be extracted from the data and several methods of radial profile fitting could then be used (simultaneous three-component fitting, two-component fitting, and PSF subtraction followed by two-component fitting) to acquire consistent results. The search for optical companion galaxies could then be undertaken via visual inspection as well as using an automated technique (with human intervention) in order to accurately determine the properties of these objects. Spectra could also be obtained of the host galaxies and their optical companion galaxies in order to further classify the objects and get their redshifts. In this way, distances to the optical companions could be computed, and it can be determined whether the objects are actually physical companion galaxies. Moreover, the kinematics and dynamics of these systems could also be determined. Explicit knowledge of the physical companions

could then be used to calculate more accurate tidal forces that these objects have on the hosts. Also required is an improved understanding of the theory behind the interaction hypothesis (e.g., incorporating dissipative inflow of gas into the centers of galaxies via stellar and gaseous bars) so that the observations more closely match theory.

In closing, there is much research that must be undertaken before we can fully understand AGNs, which involves detailed observations of the nearby and large-scale environments of these galaxies as well as the examination of the galaxies themselves.

Bibliography

- Adams, T. 1977. ApJS, 33, 19.
- Alonso-Herrero, A., Ward, M. J., & Kotilainen, J. K. 1996. MNRAS, 278, 902.
- Antonucci, R. & Miller, J. 1985. ApJ, 297, 621.
- Antonucci, R. R. 1993. ARA&A, 31, 473.
- Athanassoula, E. 1992. MNRAS, 259, 345.
- Barnes, J. & Hernquist, L. 1991. ApJ, 370, L65.
- Bekki, K. & Noguchi, M. 1994. A&A, 290, 7.
- Blandford, R., Netzer, H., & Woltjer, L. 1990. *Active Galactic Nuclei' Saas-Fee Advanced Course 20*. Springer-Verlag.
- Combes, F., Boissé, P., Mazure, A., & Blanchard, A. 1991. *Galaxies and Cosmology*. Springer-Verlag.
- Dahari, O. 1984, July. AJ, 89, 966.
- Dahari, O. 1985. AJ, 90, 1772.
- de Vaucouleurs, G. 1948. Ann. d'Astrophys., 11, 247.
- de Vaucouleurs, G. 1959. Hdb. d. Phys., 53, 311.
- DeRobertis, M. M., Hayhoe, K., & Yee, H. 1997. ApJS. Submitted (Paper I).
- DeRobertis, M. M., Yee, H., & Hayhoe, K. 1997. ApJ. Submitted (Paper II).

- Freeman, K. 1970. ApJ, 160, 811.
- Fuentes-Williams, T. & Stocke, J. T. 1988. AJ, 96, 1235.
- Hubble, E. 1930. ApJ, 71, 231.
- Huchra, J. & Burg, R. 1992. ApJ, 393, 90.
- Jedrzejewski, R. I. 1987. MNRAS, 226, 747.
- Keel, W. C. 1996. AJ, 111, 696.
- Keel, W. C., Kennicutt, Jr., R. C., Hummel, E., & van der Hulst, J. 1985. AJ, 90, 708.
- King, I. 1966. AJ, 71, 64.
- Kollatschny, W. & Fricke, K. 1989. A&A, 219, 34.
- Kotilainen, J., Ward, M., & Williger, G. 1993. MNRAS, 263, 655.
- Kukula, M., Pedlar, A., Unger, S., Baum, S., & O'Dea, C. 1994. ApSS, 216, 371.
- Landolt, A. 1992. AJ, 104, 340.
- Larson, R. & Tinsley, B. 1978. ApJ, 219, 46.
- Laurikainen, E. & Salo, H. 1995. A&A, 293, 683.
- Laurikainen, E., Salo, H., Teerikorpi, P., & Petrov, G. 1994. A&AS, 108, 491.
- MacKenty, J. W. 1989. ApJ, 343, 125.
- MacKenty, J. W. 1990. ApJS, 72, 231.
- McLeod, K. & Rieke, G. 1995. ApJ, 441, 96.
- Nesci, R. 1986. A&A, 160, 259.
- Osterbrock, D. E. 1989. *Astrophysics of Gaseous Nebulae and Active Galactic Nuclei*. University Science Books.

- Osterbrock, D. E. 1993. ApJ, 404, 551.
- Osterbrock, D. E. & Martel, A. 1993. ApJ, 414, 552.
- Press, W., Flannery, B., Teudolsky, S., & Vetterling, W. 1992. *Numerical Recipes in C: The Art of Scientific Computing* (2 ed.). Cambridge University Press.
- Rafanelli, P., Violato, M., & Baruffolo, A. 1995. AJ, 109, 1546.
- Ransom, R. R. 1997, August. private communication.
- Robson, I. 1996. *Active Galactic Nuclei*. John Wiley & Sons.
- Schechter, P. 1976. ApJ, 203, 297.
- Seyfert, C. K. 1943. ApJ, 97, 28.
- Seyfert, C. K. 1947. PASP, 59, 35.
- Shane, C. 1975. In A. Sandage, M. Sandage, and J. Kristian (Eds.), *Stars and Stellar Systems*, Volume IX. Univ. of Chicago.
- Shlosman, I. & Noguchi, M. 1993. ApJ, 414, 474.
- Toomre, A. & Toomre, J. 1972. ApJ, 178, 623.
- Ward, M. J. 1996. *Vistas in Astron.*, 40, 233.
- Yee, H. 1983. ApJ, 272, 473.
- Yee, H. 1991. PASP, 103, 396.

Appendix A

Programs Used for Analysis

A.1 ★ IRAF Packages

Image Reduction and Analysis Facility (IRAF) is a commonly used software package in astronomy. What follows are descriptions of the important routines (`Imexamine`, `Ellipse`, `Imedit`, `Imarith`, `Gauss`) used during the reduction and analysis. Also provided are an example of the important parameters used while executing each task.

A.1.1 `Imexamine`

The `imexamine` task is used to determine statistical information about image sections. The statistics tool (`m` key) returns the mean, standard deviation, maximum and minimum within a $n \times n$ pixel box (we have set $n = 5$), and is useful for determining properties such as the background sky level and noise. Surface plots (`s`) and contour plots (`e`) in a 15×15 pixel box are a convenient way of looking at the data. A very important tool is the radial profile tool (`r`), which is a very flexible tool since the radius to which data is measured is completely configurable by the user. This tool locates the nearest peak to the image cursor, then determines the centroid of this peak, plots a radial profile of the data around this point, and fits a Gaussian to this

profile returning numerous parameters (centroid, FWHM, peak, ellipticity, position angle, and integrated flux). Below are the parameter lists for the `imexamine` task as well as the parameter list for radial profile sub-task (`rimexamine`).

Imexamine parameters

<code>input = "n6764r"</code>	images to be examined
<code>(logfile = "imexam.log")</code>	logfile
<code>(ncstat = 5)</code>	number of columns for statistics
<code>(nlstat = 5)</code>	number of lines for statistics
<code>(use_display = yes)</code>	enable direct display interaction

Rimexamine parameters

<code>(xlabel = "Radius")</code>	X-axis label
<code>(ylabel = "Pixel Value")</code>	Y-axis label
<code>(fitplot = yes)</code>	Overplot gaussian fit?
<code>(center = yes)</code>	Center object in aperture?
<code>(background = yes)</code>	Fit and subtract background?
<code>(radius = 7.)</code>	Object radius
<code>(buffer = 1.)</code>	Background buffer width
<code>(width = 2.)</code>	Background width
<code>(xorder = 4)</code>	Background x order
<code>(yorder = 4)</code>	Background y order
<code>(rplot = 9.)</code>	Plotting radius

A.1.2 STSDAS/Isophote/Ellipse

The `Ellipse` task contained in the `Isophote` package of the STSDAS (Space Telescope Science Data Analysis System) package fits elliptical isophotes to an image. Details of the algorithm were described in Section 2.4.2 and the important fitting parameters are listed below.

Ellipse parameters

<code>input = "n3982"</code>	input image name
<code>output = "gal.tab"</code>	output table name
<code>a0 = 8.4</code>	initial semi-major axis
<code>mina = 1.7</code>	minimum semi-major axis
<code>maxa = 53.</code>	maximum semi-major axis
<code>(harmonics = "none")</code>	optional harmonic numbers
<code>(x0 = INDEF)</code>	initial ellipse center
<code>(y0 = INDEF)</code>	
<code>(eps0 = INDEF)</code>	initial ellipticity
<code>(teta0 = INDEF)</code>	initial position angle
<code>(hcenter = yes)</code>	hold center fixed ?
<code>(heps = no)</code>	hold ellipticity fixed ?

(hteta = no)	hold position angle fixed ?
(astep = 0.1)	step between successive ellipses
(linear = no)	linear astep ?
(minit = 15)	minimum no. of iterations
(maxit = 100)	maximum no. of iterations
(lslope = 0.)	limit for acceptable slope
(conver = 0.)	convergency sensitivity control
(clip = 0.02)	fraction of points to clip off
(maxrit = INDEF)	max. semi-major axis for iterative mode
(integrmode = "bi-linear")	area integration mode

A.1.3 Imedit

The imedit task can be used to delete unwanted stars and ion events as well as touch-up other defects in the image. This task is performed interactively in real time so the user can see the changes as they are being done. The main tool in this task is the background replacement routine. With this routine, the user specifies the radius of a circular aperture which is surrounded by circular annulus. The pixels within the aperture are then replaced by a background surface based on the pixels in the annulus; Gaussian noise is added to the replacement pixels. The polynomial order of the background surface is set by the user, and was set to 3rd-order for this research.

Imedit parameters

input = "n3169r"	Images to be edited
output = "_n3169"	Output images
(aperture = "circular")	Aperture type
(radius = 4.)	Substitution radius
(search = 0.)	Search radius
(buffer = 2.)	Background buffer width
(width = 2.)	Background width
(xorder = 4)	Background x order
(yorder = 4)	Background y order
(value = 0.)	Constant value substitution
(sigma = 6.6)	Added noise sigma
(command = "display \$image 1 erase=\$erase fill=yes order=0 >& dev\$null")	Display command

A.1.4 Iarith

The `imarith` task is used to perform image arithmetic. This can either be accomplished with an image and a constant or with two images. In the case of two images, the specified operation is performed on a pixel-to-pixel basis (similar to matrix addition and subtraction, though it applies to multiplication and division as well). This task is useful for removing the background sky level from an image, as well as dividing an image by a smoothed image for unsharp-masking.

Imarith parameters

<code>operand1 = "n6111r2"</code>	Operand image or numerical constant
<code>op = "/"</code>	Operator
<code>operand2 = "n6111gau"</code>	Operand image or numerical constant
<code>result = "lpf"</code>	Resultant image

A.1.5 Gauss

The `Gauss` task convolves an image with a flux-preserving Gaussian kernel in which the width σ is specified by the user. This task is useful for unsharp-masking, as well as for smoothing images in general.

Gauss parameters

<code>input = "orig"</code>	Input images to be fit
<code>output = "gau"</code>	Output images
<code>sigma = 4.434</code>	Sigma of Gaussian along major axis of ellipse
<code>(ratio = 1.)</code>	Ratio of sigma in y to x
<code>(theta = 0.)</code>	Position angle of ellipse
<code>(nsigma = 5.)</code>	Extent of Gaussian kernel in sigma
<code>(bilinear = yes)</code>	Use bilinear approximation to Gaussian kernel

A.2 User-Supplied Programs

These are programs the author wrote to perform surface-brightness profile fitting and to compute the many host and companion galaxy parameters.

A.2.1 galprof and splitprof

Galprof and splitprof fit analytic functions to the radial surface-brightness profiles of galaxies (i.e. after they have been fit with ellipse). The main chi-squared minimization routine is based on the algorithm in *Numerical Recipes* by Press et al. (1992). The algorithm fits an analytic function with unknown parameters to a data set, adjusting the parameters until the chi-squared reaches a minimum. The function used for the galaxy surface-brightness profiles is found in Equation 2.10. The algorithm also requires the first derivatives of the parameters in order to adjust the parameters during each iteration such that the chi-squared decreases. These derivatives have the following functional form:

$$\frac{\partial f}{\partial f_N} = e^{-r^2/2\sigma^2} \quad (\text{A.1})$$

$$\frac{\partial f}{\partial \sigma} = f_N e^{-r^2/2\sigma^2} \frac{r^2}{\sigma^3} \quad (\text{A.2})$$

$$\frac{\partial f}{\partial f_b} = e^{-7.688[(r/r_e)^{1/4}-1]} \quad (\text{A.3})$$

$$\frac{\partial f}{\partial r_e} = f_b e^{-7.688[(r/r_e)^{1/4}-1]} \cdot 1.922 r^{1/4} r_e^{-5/4} \quad (\text{A.4})$$

$$\frac{\partial f}{\partial f_d} = e^{-r/r_0} \quad (\text{A.5})$$

$$\frac{\partial f}{\partial r_0} = f_d e^{-r/r_0} \cdot \frac{r}{r_0^2} \quad (\text{A.6})$$

The program splitprof takes the output parameters from galprof and creates a data-file that contains the flux that is contributed by each of the three components (disk, bulge, and Gaussian PSF). When the alternate two-component fitting is performed on the Seyfert data, splitprof is modified to compute the contribution by the Gaussian PSF by integrating the flux left over between 1.8 pixels and 5.2 pixels.

This is accomplished by first realizing that the flux in a Gaussian PSF annulus is given by:

$$F_{ring} = 2\pi f_N \sigma^2 [e^{-a^2/2\sigma^2} - e^{-b^2/2\sigma^2}] \quad (\text{A.7})$$

where a and b are the inner and outer radii of the annulus. Thus the parameter in question is given by:

$$f_N = \frac{F_{ring}}{2\pi\sigma^2 [e^{-a^2/2\sigma^2} - e^{-b^2/2\sigma^2}]} \quad (\text{A.8})$$

where F_{ring} is computed from the data via numerical integration using the trapezoidal method:

$$F_{ring} = \sum_{i=1}^n \frac{h_i}{2} [f_i + f_{i+1}] \quad (\text{A.9})$$

where $h_i = r_{i+1} - r_i$ and $f_i = 2\pi r_i I_i$ where I_i is the “left over” flux and $r_1 = a$ and $r_{n+1} = b$. Thus the PSF parameter can be computed by integrating the data-points and substituting the result into Equation A.8.

A.2.2 raddist

This program computes various statistics about the host galaxies and its companion galaxies. This program correlates the companion galaxy files with the galaxy information files to produce various quantities such as apparent magnitude, absolute magnitude, luminosity, separation distance, and tidal influence of the companion galaxies, as well as the distance, luminosity, surface brightness, and the fraction of luminosity due to each component for each of the host galaxies.

The fraction of light contributed from each component is computed by first calculating the integrated flux (out to a maximum radius m) of each component. This is given by:

$$\mathcal{F} = \int_0^m 2\pi r I(r) dr \quad (\text{A.10})$$

which corresponds to the following for the Gaussian PSF, the disk, and the bulge:

$$\mathcal{F}_{\text{psf}} = 2\pi f_N \sigma^2 \left[1 - e^{-m^2/2\sigma^2} \right] \quad (\text{A.11})$$

$$\mathcal{F}_{\text{disk}} = 2\pi f_d r_0^2 \left[1 - \frac{m}{r_0} e^{-m/r_0} - e^{-m/r_0} \right] \quad (\text{A.12})$$

$$\begin{aligned} \mathcal{F}_{\text{bulge}} = \frac{8\pi f_b e^a r_e^2}{a^8} & \left[5040 - y^7 e^{-y} - 7y^6 e^{-y} - 42y^5 e^{-y} - 210y^4 e^{-y} \right. \\ & \left. - 840y^3 e^{-y} - 2520y^2 e^{-y} - 5040y e^{-y} - 5040e^{-y} \right] \end{aligned} \quad (\text{A.13})$$

where $a = 7.688$ and $y = a(m/r_e)^{1/4}$. The fractional luminosity is then computed by dividing the component's flux by the total flux ($\mathcal{F}_{\text{psf}} + \mathcal{F}_{\text{disk}} + \mathcal{F}_{\text{bulge}}$).

The other parameters output by this program are computed as outlined in Chapter 2.4.6, at which point they can be compared as in Chapter 5.

Appendix B

Ellipticity and Position Angle Plots

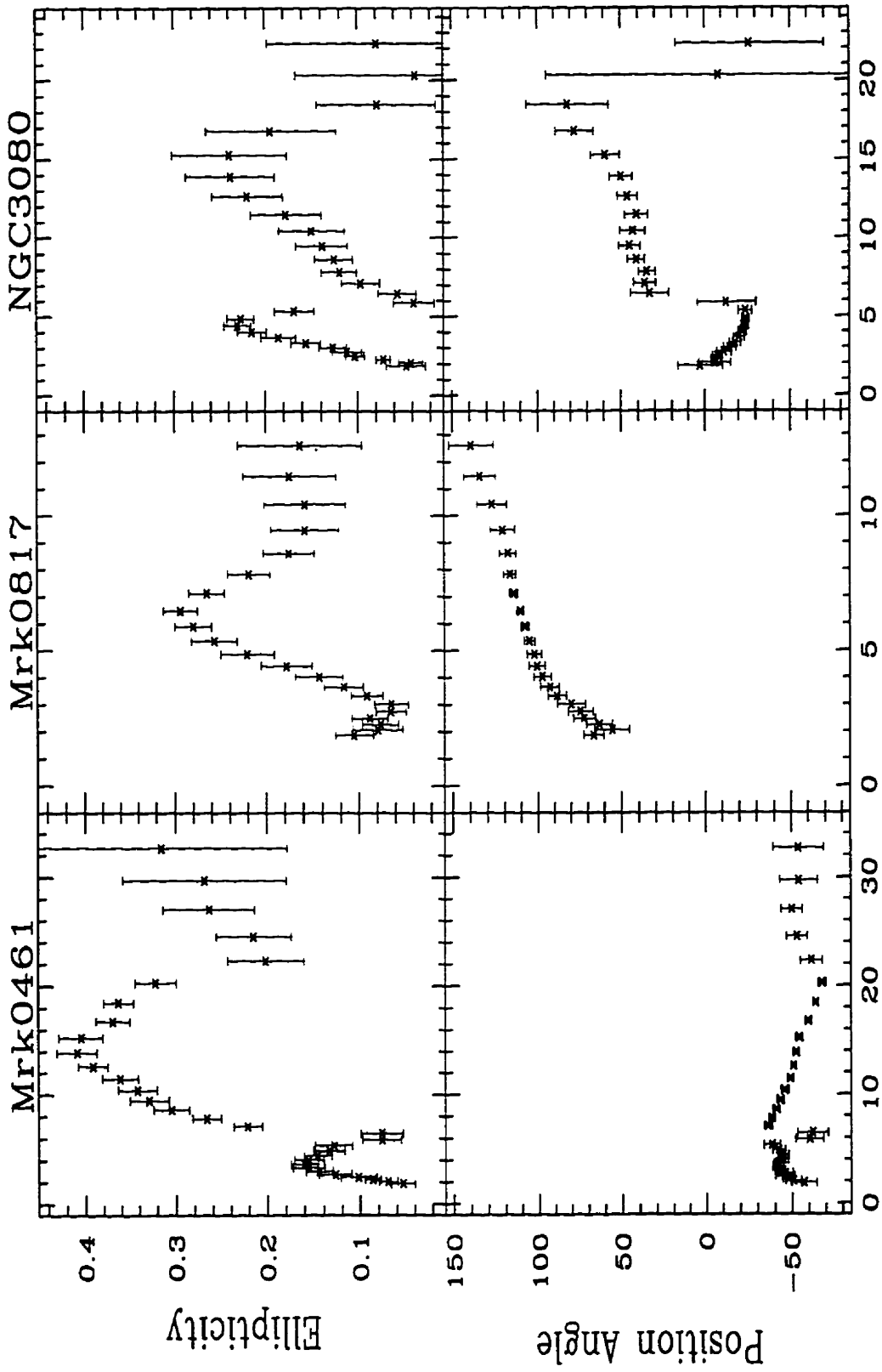
What follows are the ellipticity profiles and the position-angle profiles for the host galaxies of both the Seyfert and control samples. The data were provided by the `ellipse` task in IRAF. Ellipticity is given by $\epsilon = 1 - b/a$ and position angle is given as from North through East.

B.1 Seyfert Data Set

The plots for the Seyfert samples are presented in Figures B.1 through Figures B.8.

B.2 Control Data Set

The plots for the control samples are presented in Figures B.9 through Figures B.21.



Semi-Major axis (arcseconds)

Figure B.1: Ellipticity and position angles of three Seyfert galaxies

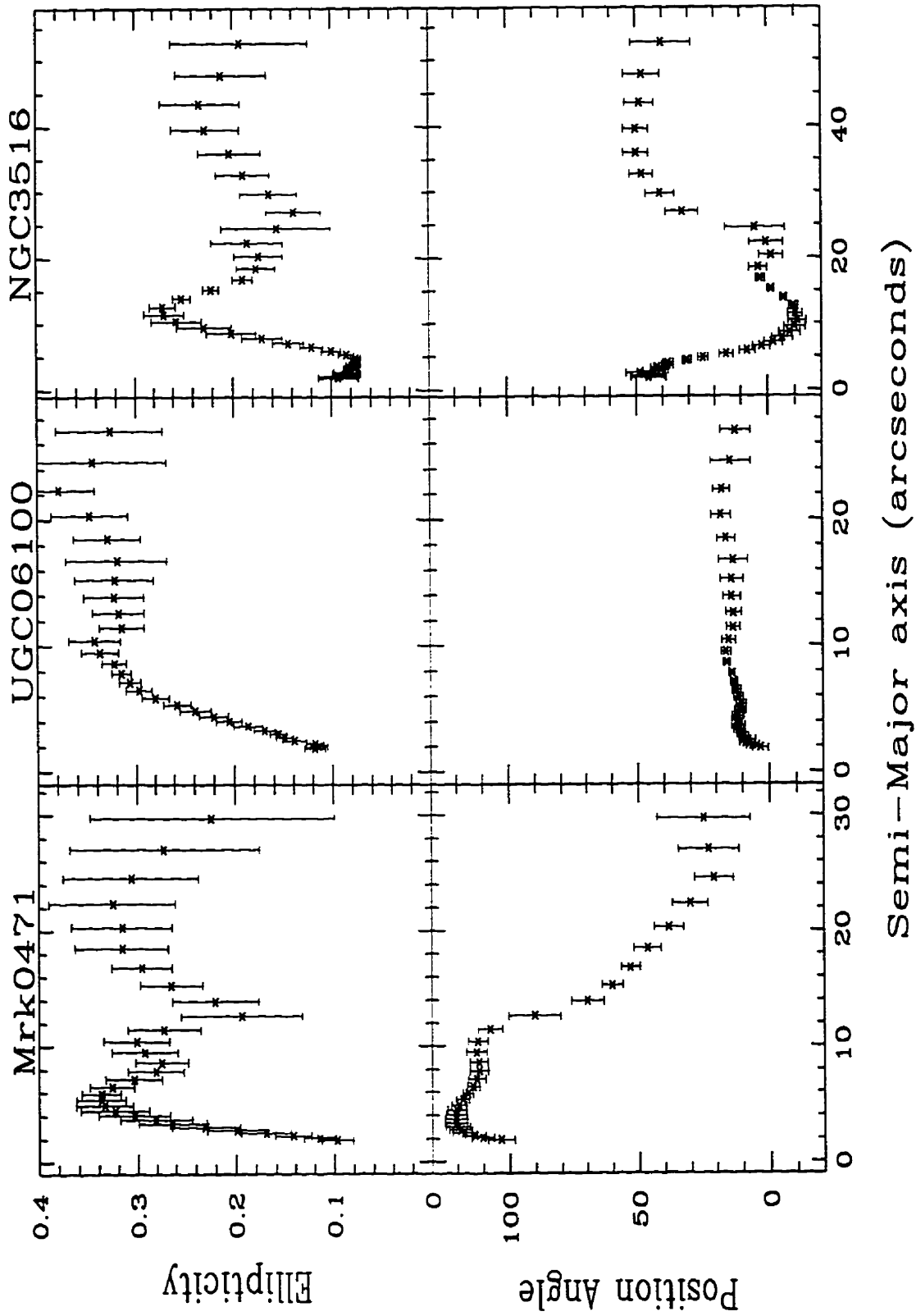


Figure B.2: Ellipticity and position angles of three Seyfert galaxies

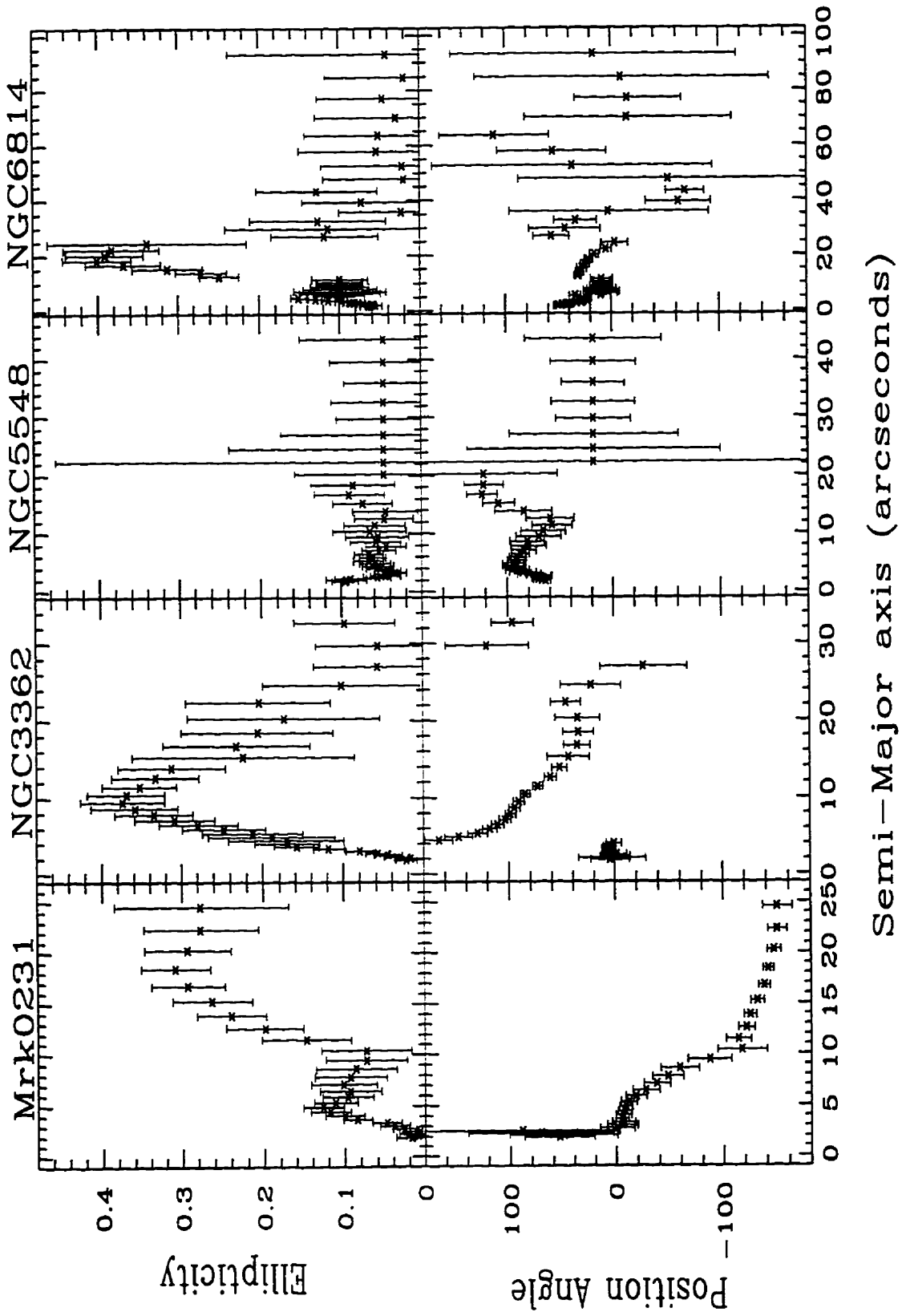


Figure B.3: Ellipticity and position angles of four Seyfert galaxies

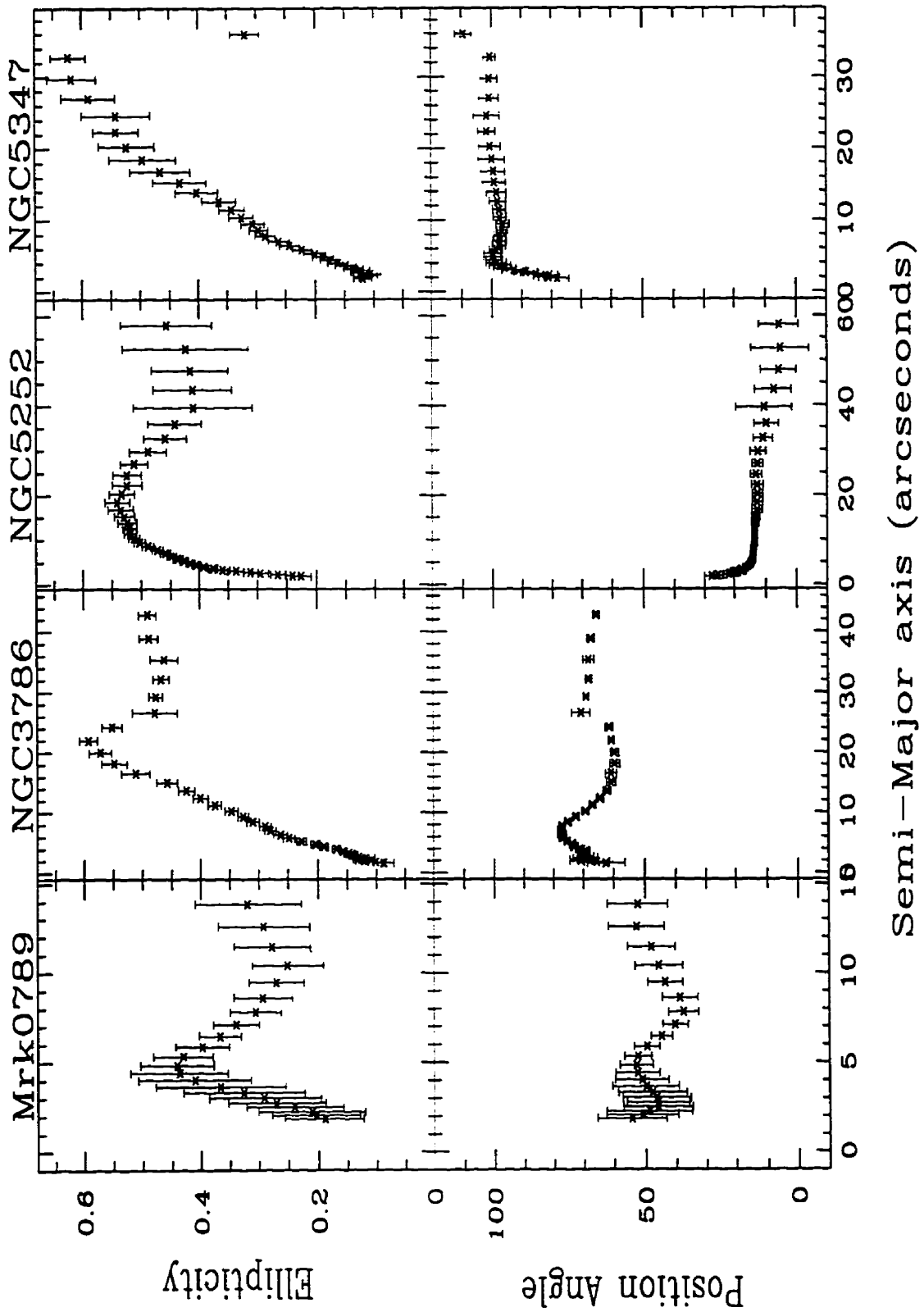
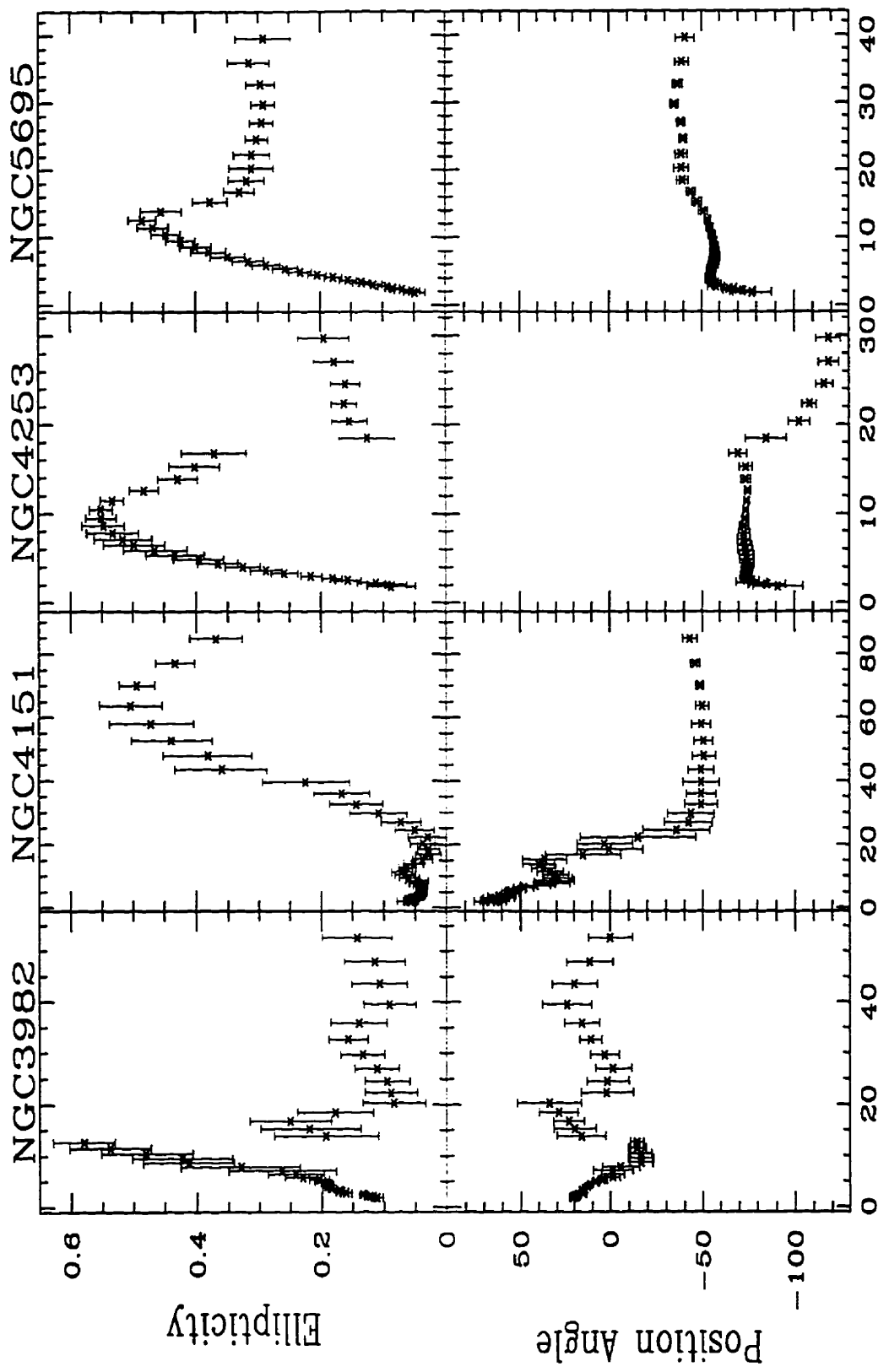


Figure B.4: Ellipticity and position angles of four Seyfert galaxies



Semi-Major axis (arcseconds)

Figure B.5: Ellipticity and position angles of four Seyfert galaxies

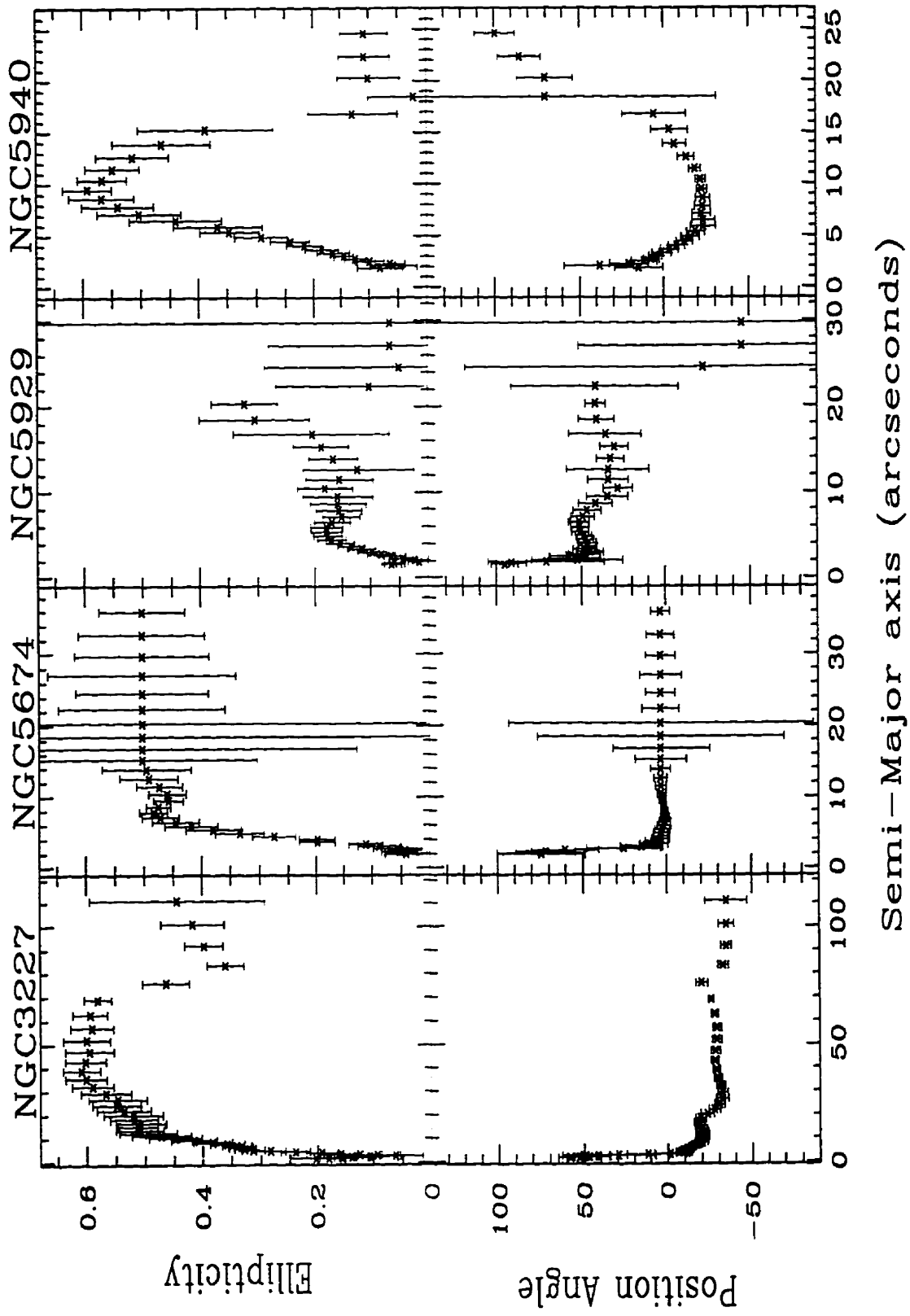


Figure B.6: Ellipticity and position angles of four Seyfert galaxies

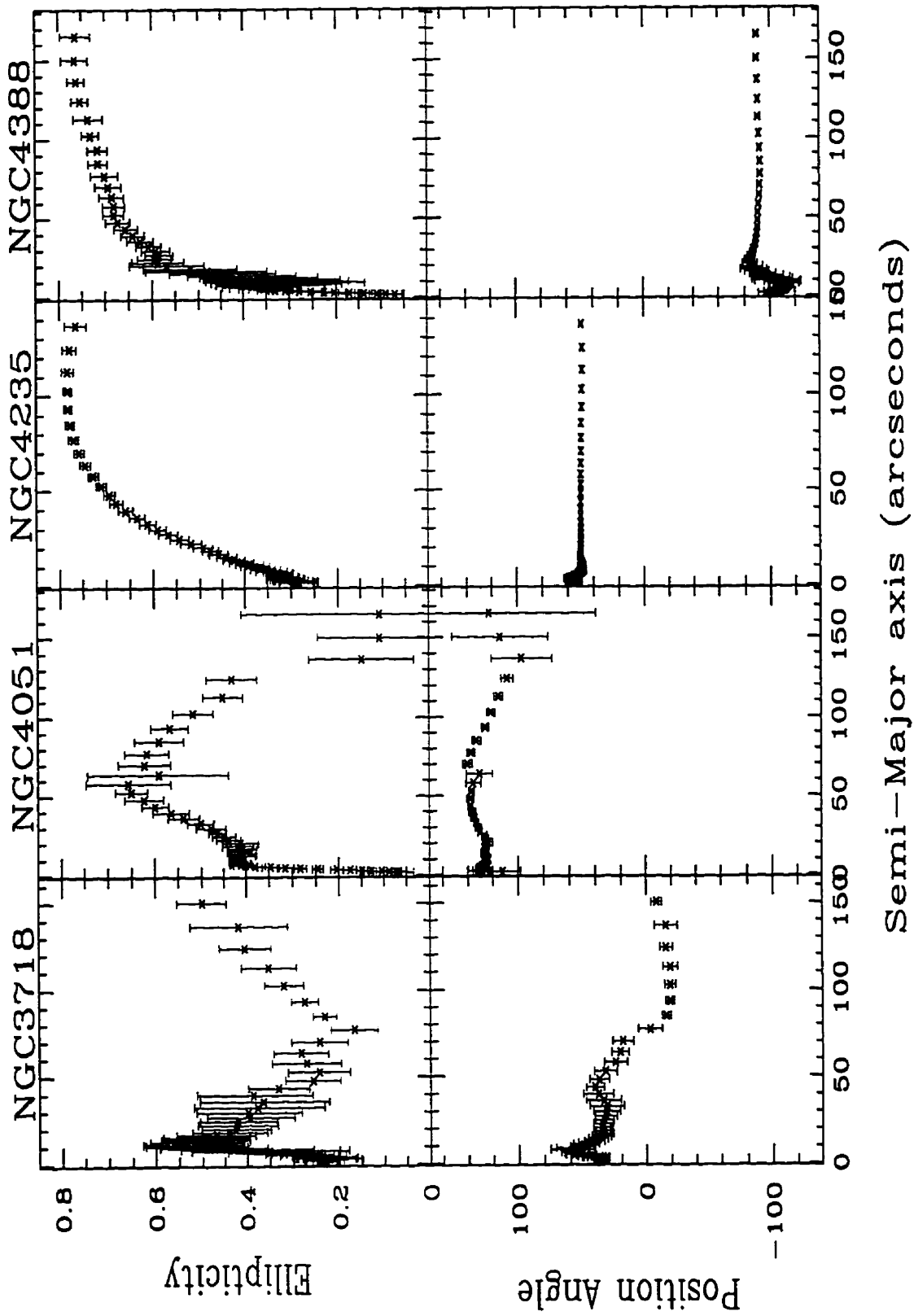


Figure B.7: Ellipticity and position angles of four Seyfert galaxies

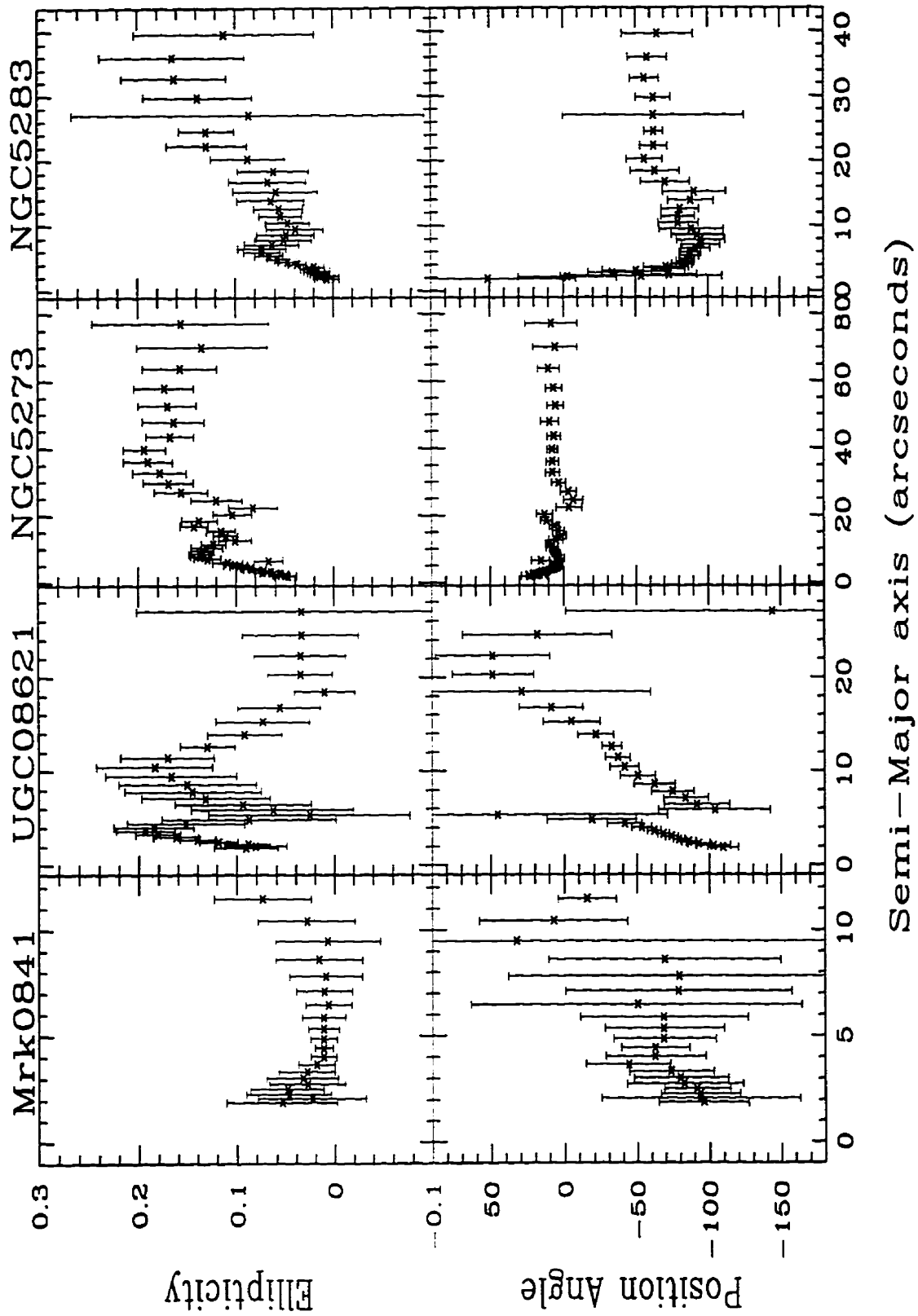


Figure B.8: Ellipticity and position angles of four Seyfert galaxies

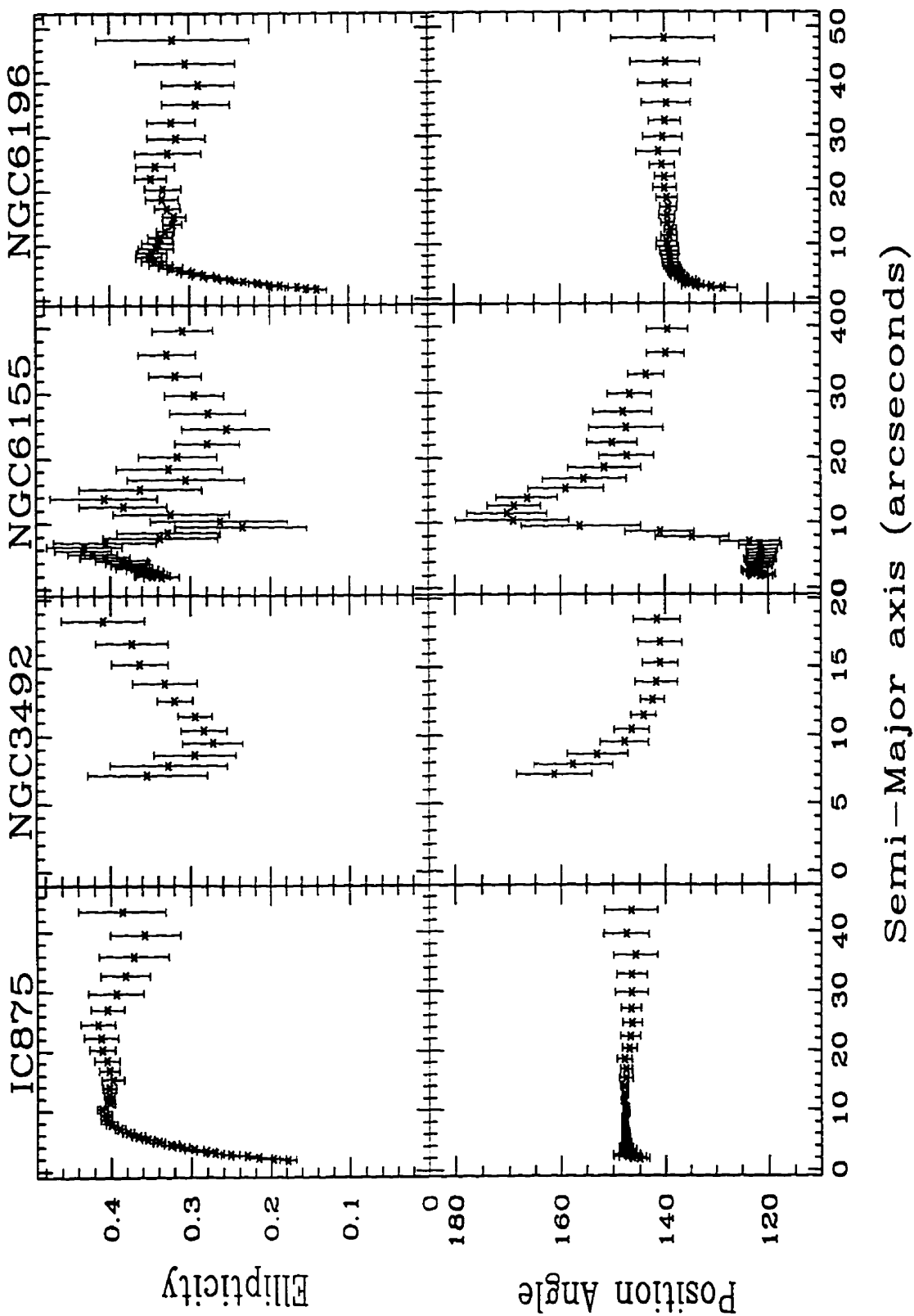


Figure B.9: Ellipticity and position angles of four galaxies

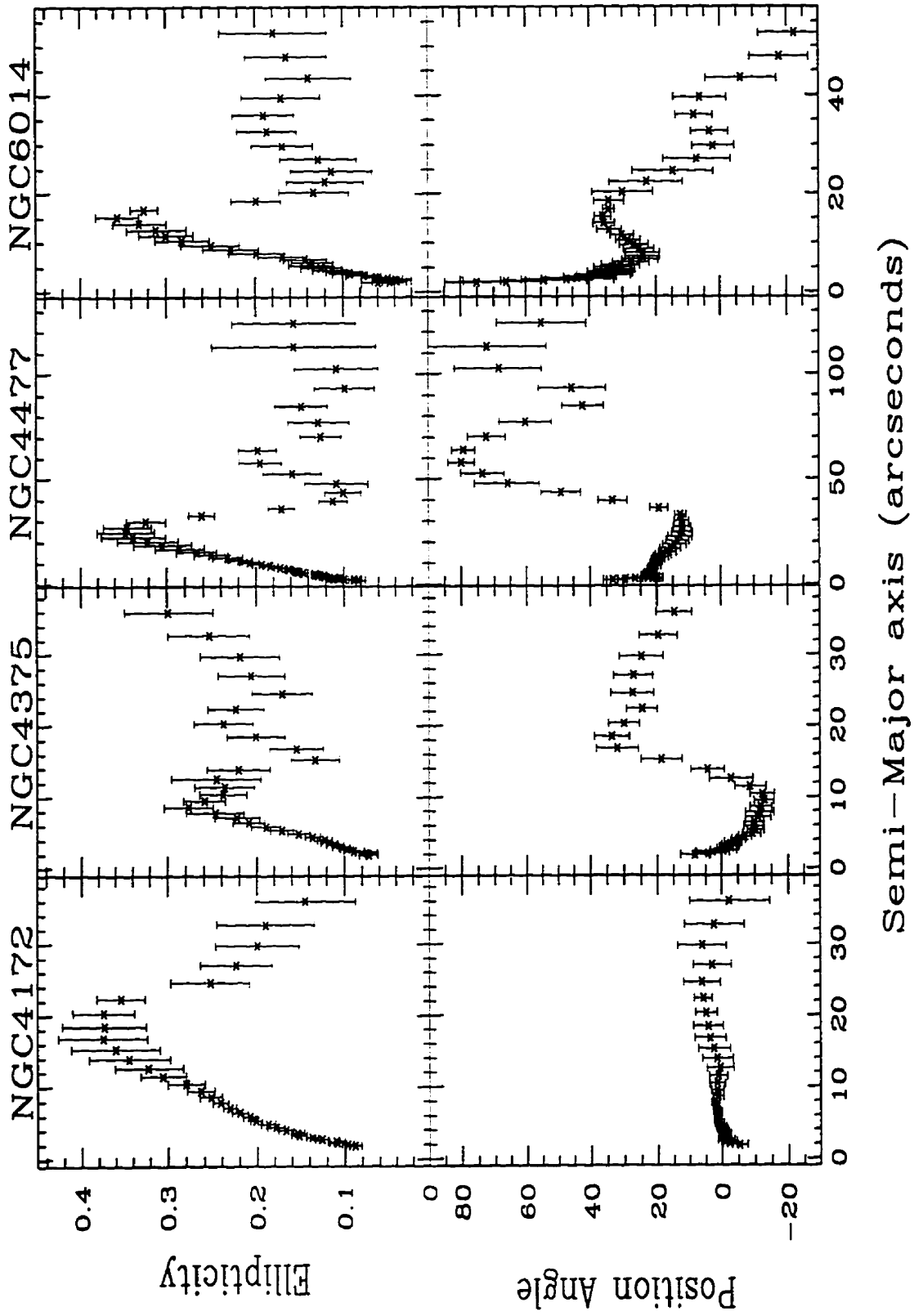


Figure B.10: Ellipticity and position angles of four galaxies

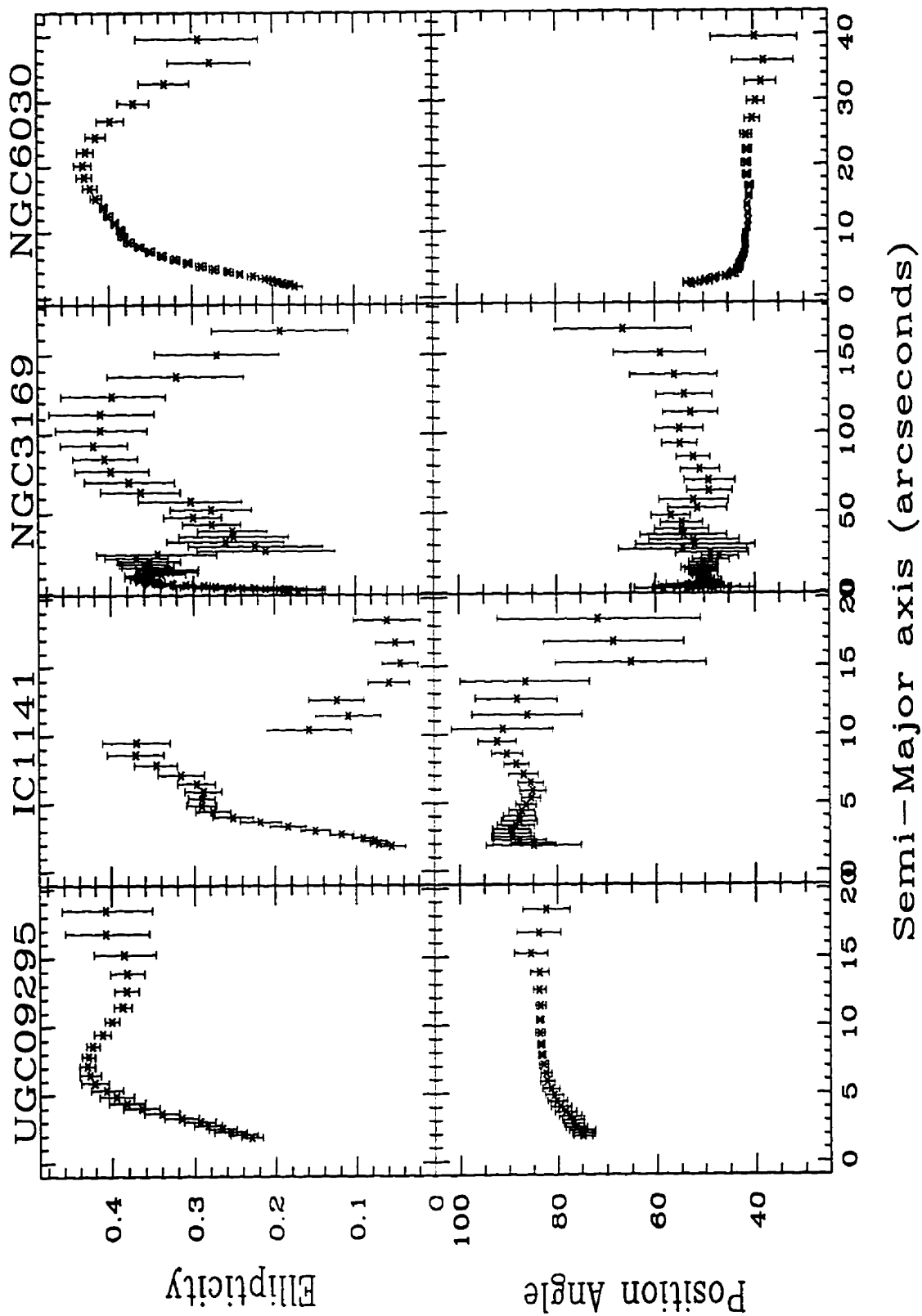


Figure B.11: Ellipticity and position angles of four galaxies

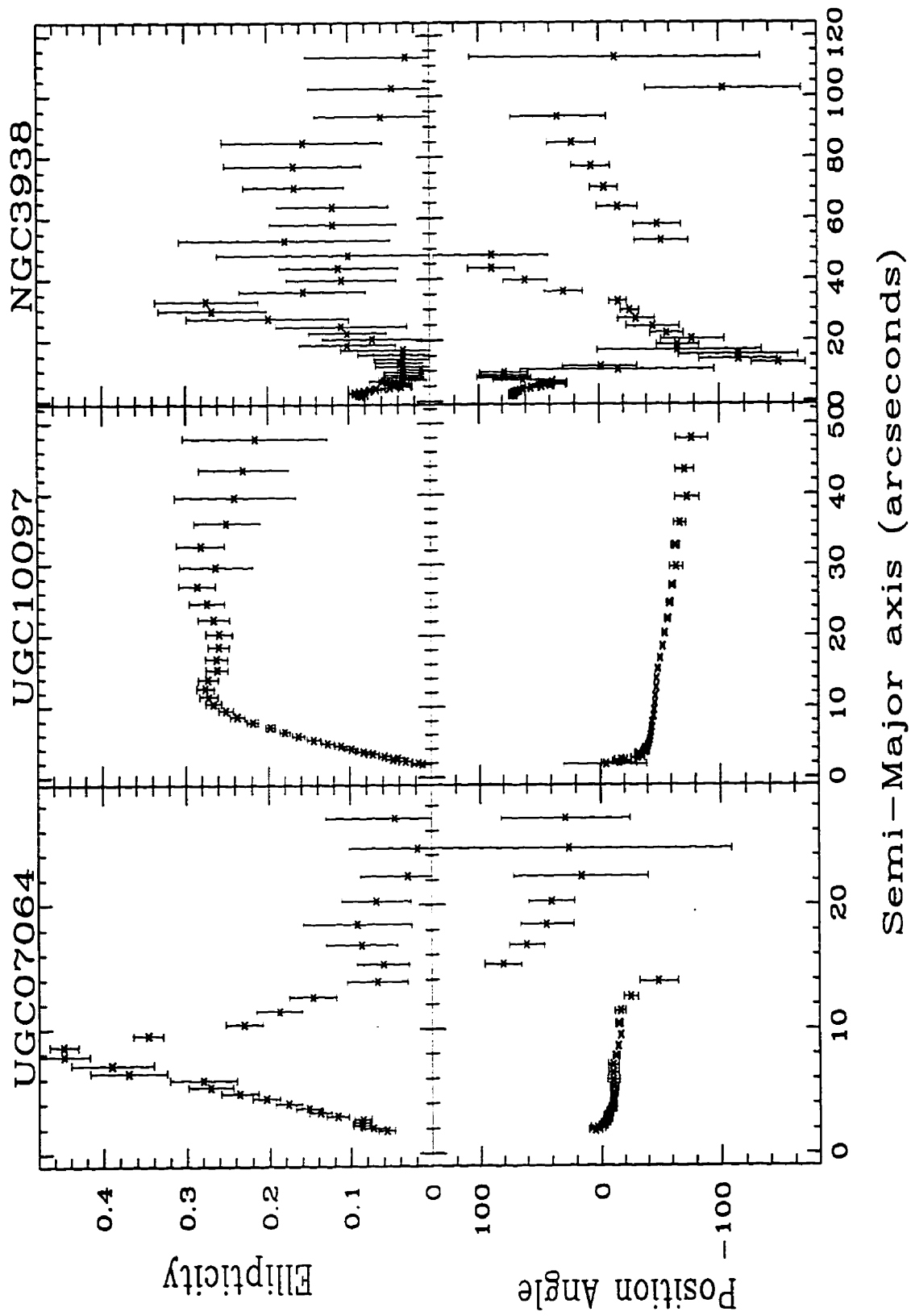


Figure B.12: Ellipticity and position angles of three galaxies

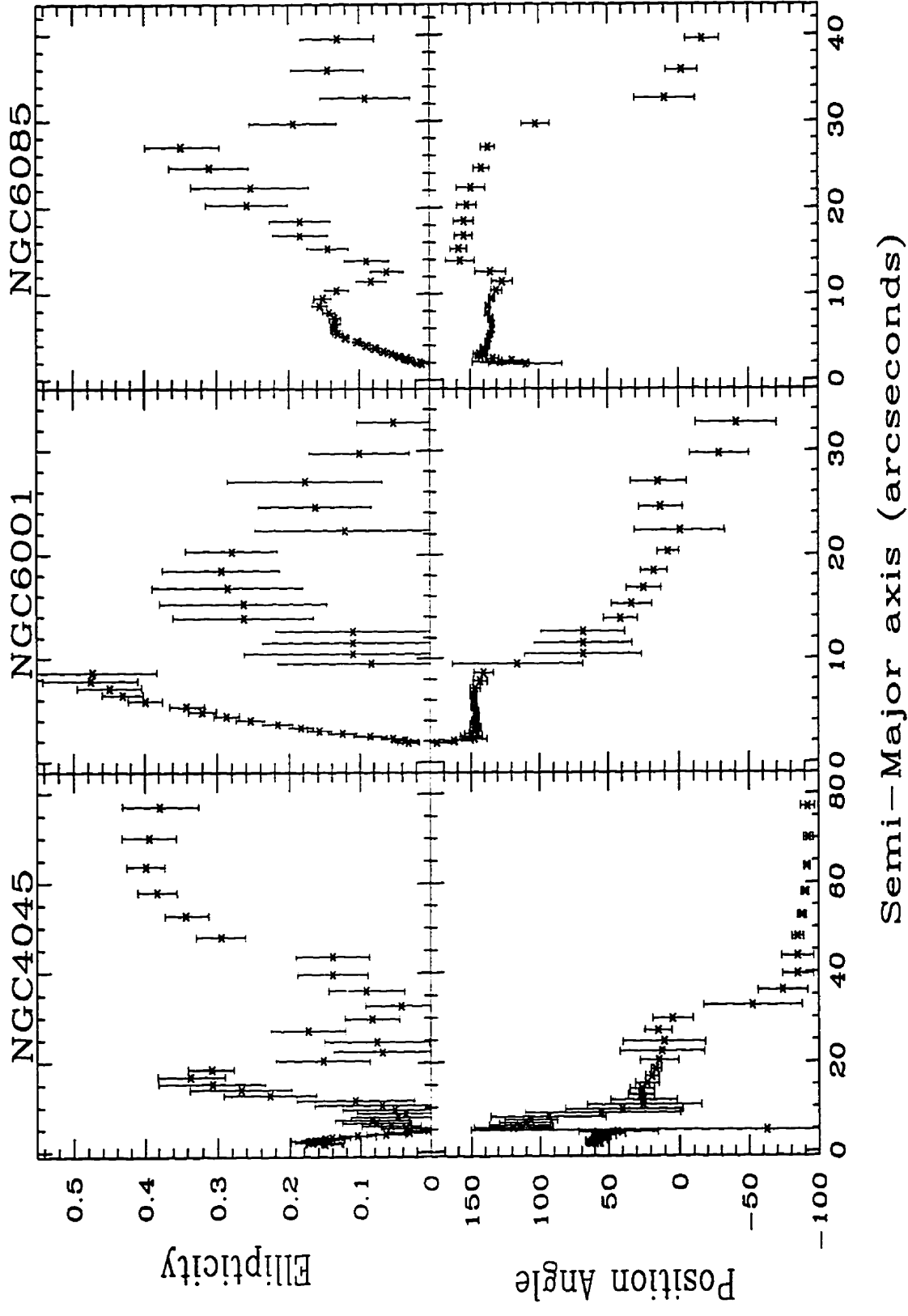


Figure B.13: Ellipticity and position angles of three galaxies

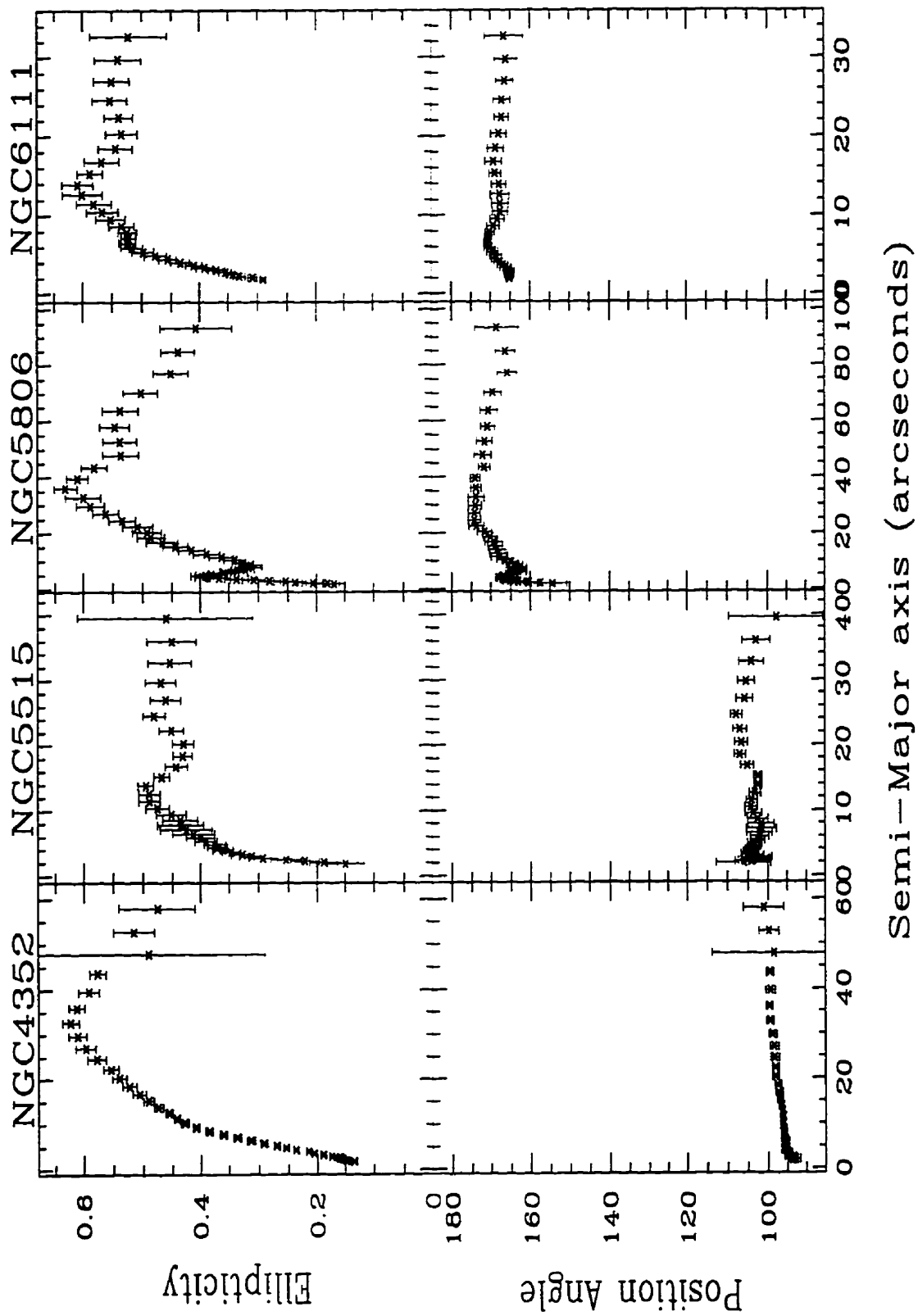
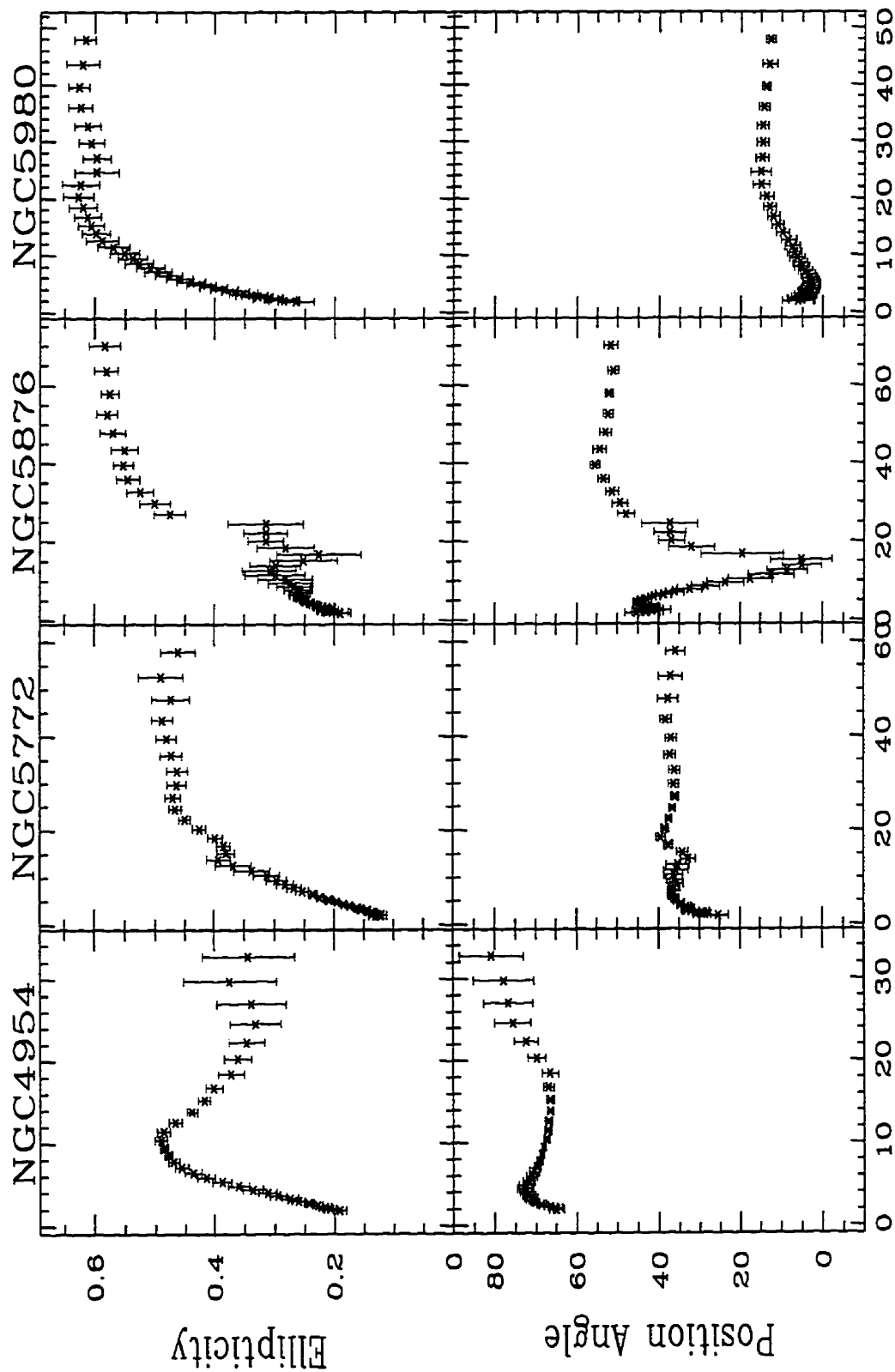


Figure B.14: Ellipticity and position angles of four galaxies



Semi-Major axis (arcseconds)

Figure B.15: Ellipticity and position angles of four galaxies

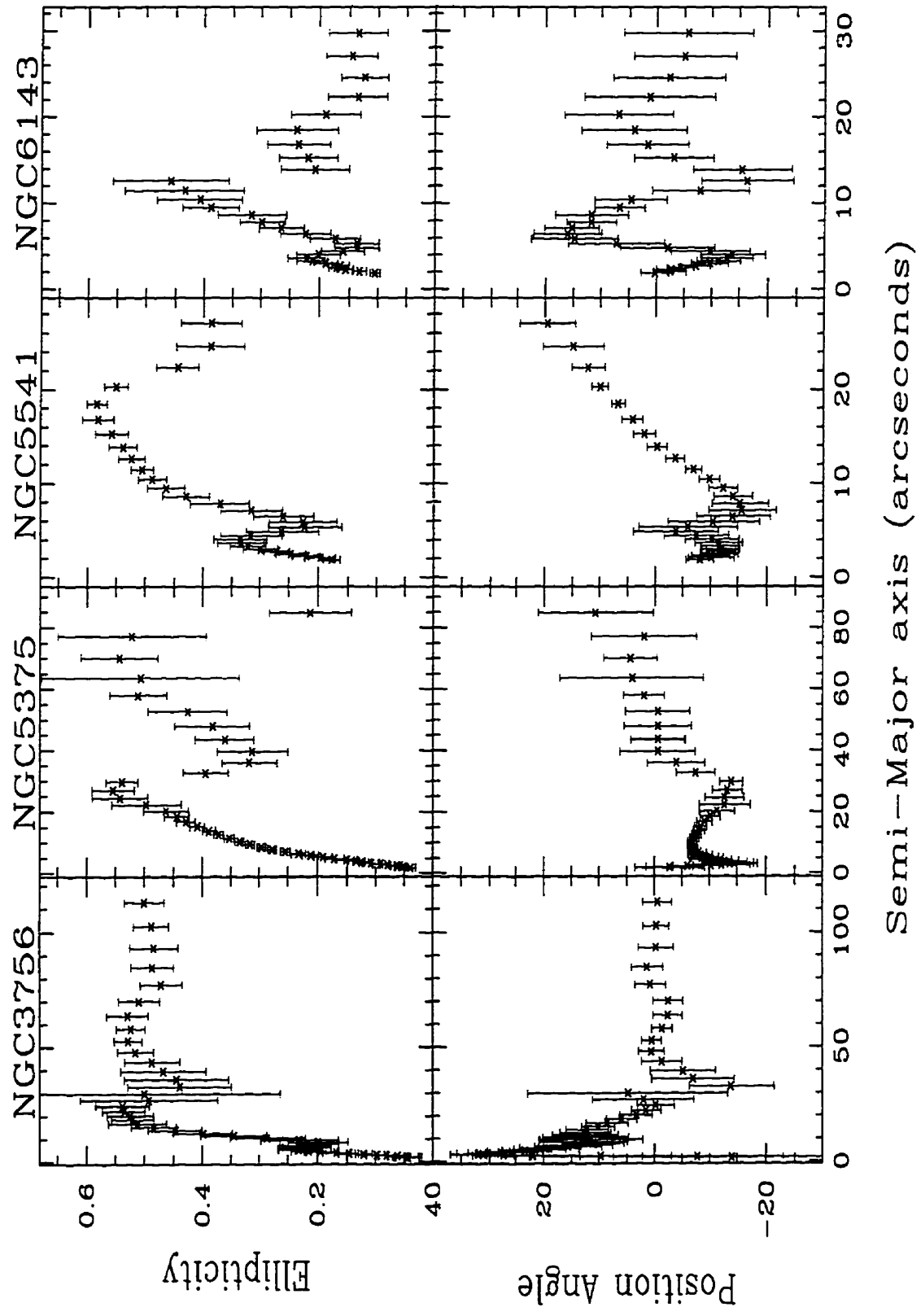


Figure B.16: Ellipticity and position angles of four galaxies

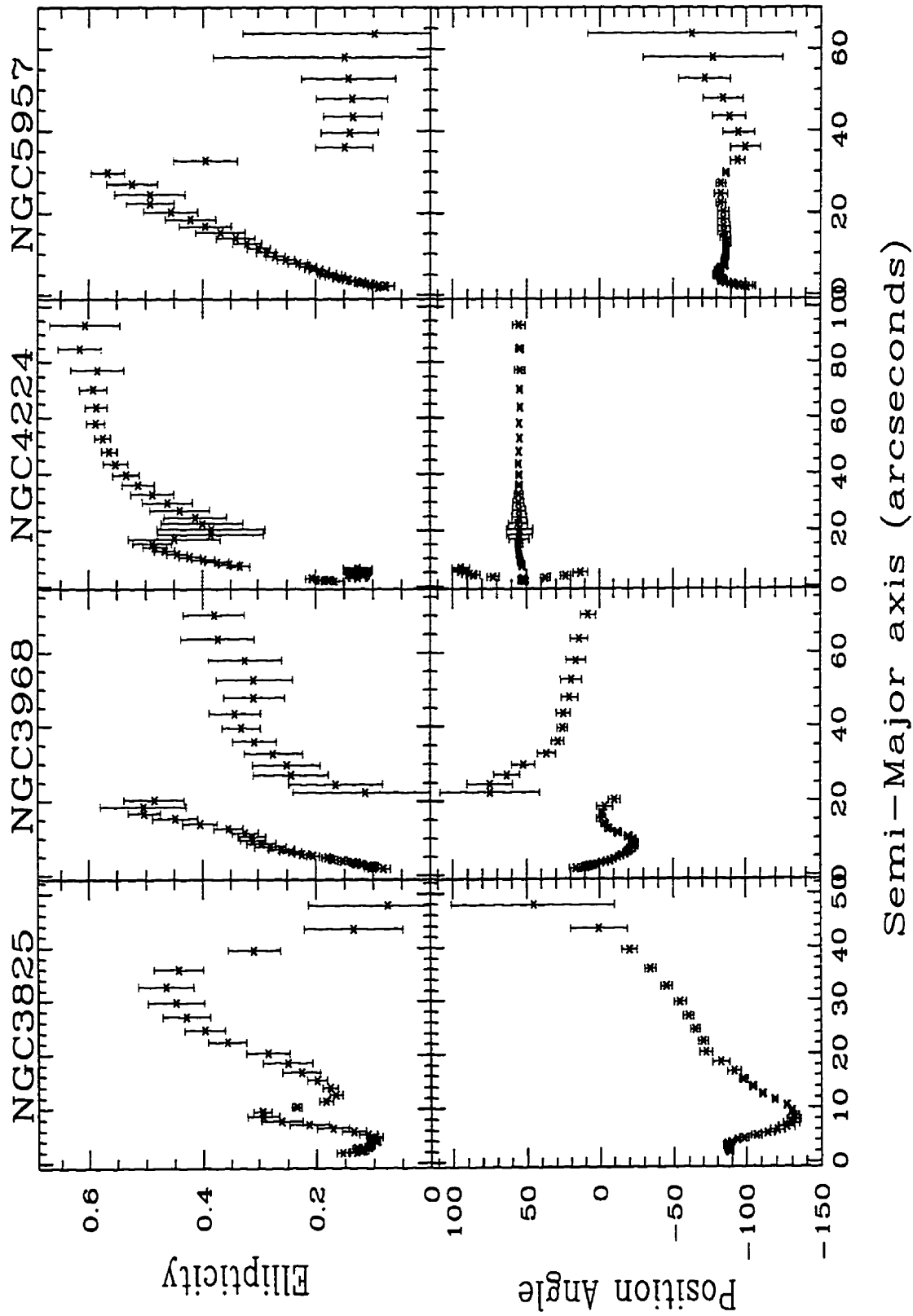


Figure B.17: Ellipticity and position angles of four galaxies

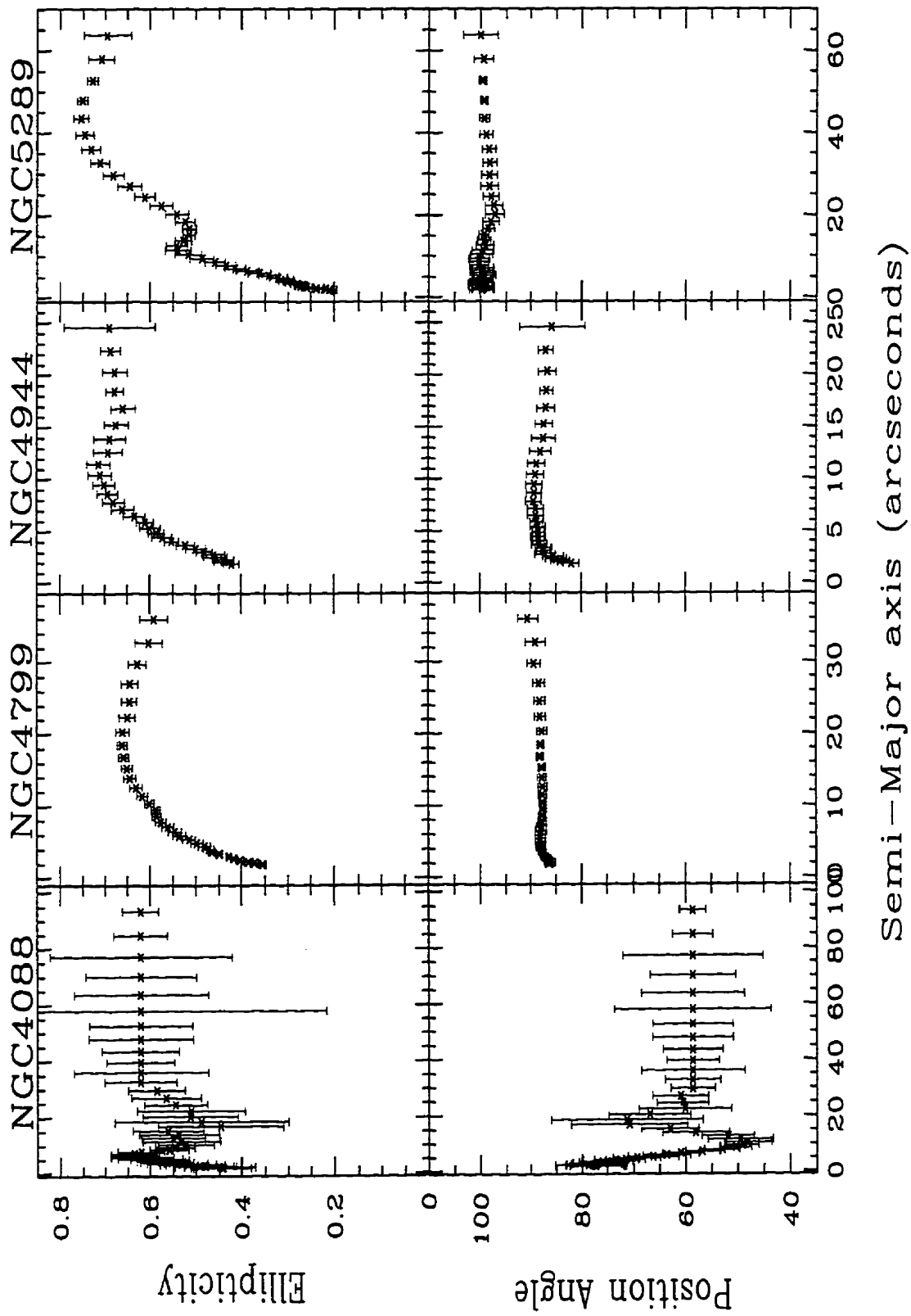
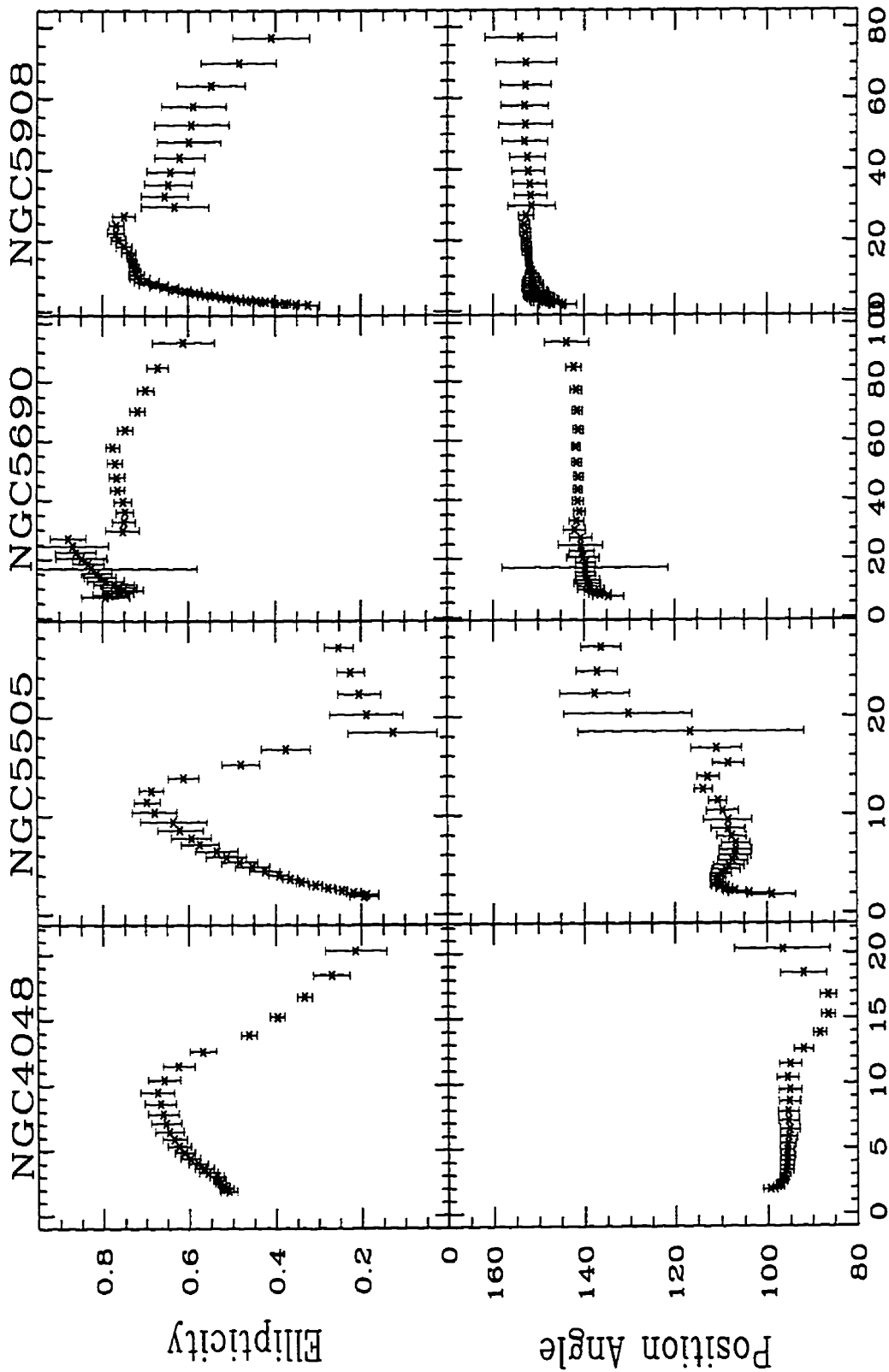


Figure B.18: Ellipticity and position angles of four galaxies



Semi-Major axis (arcseconds)

Figure B.19: Ellipticity and position angles of four galaxies

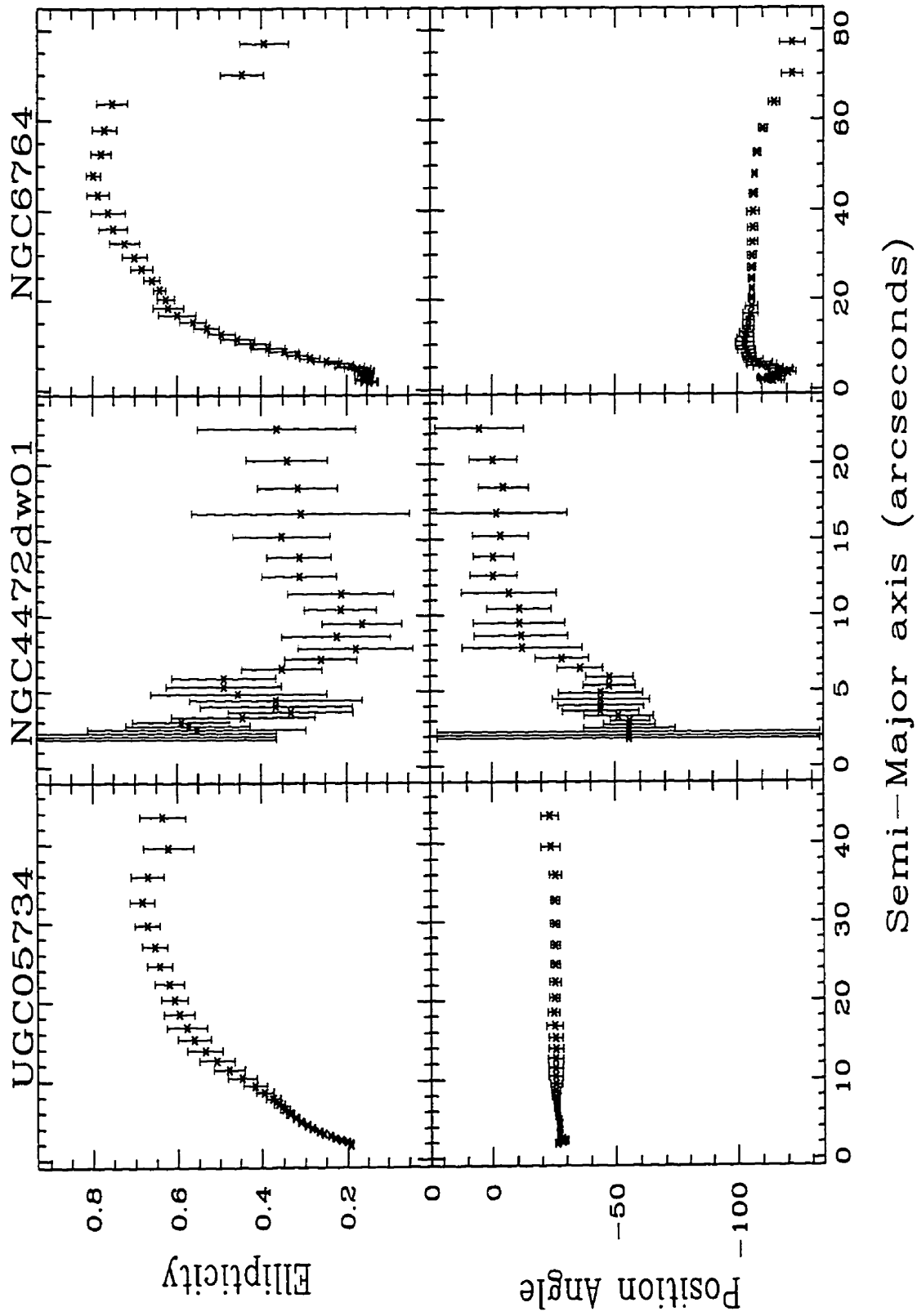


Figure B.20: Ellipticity and position angles of three galaxies

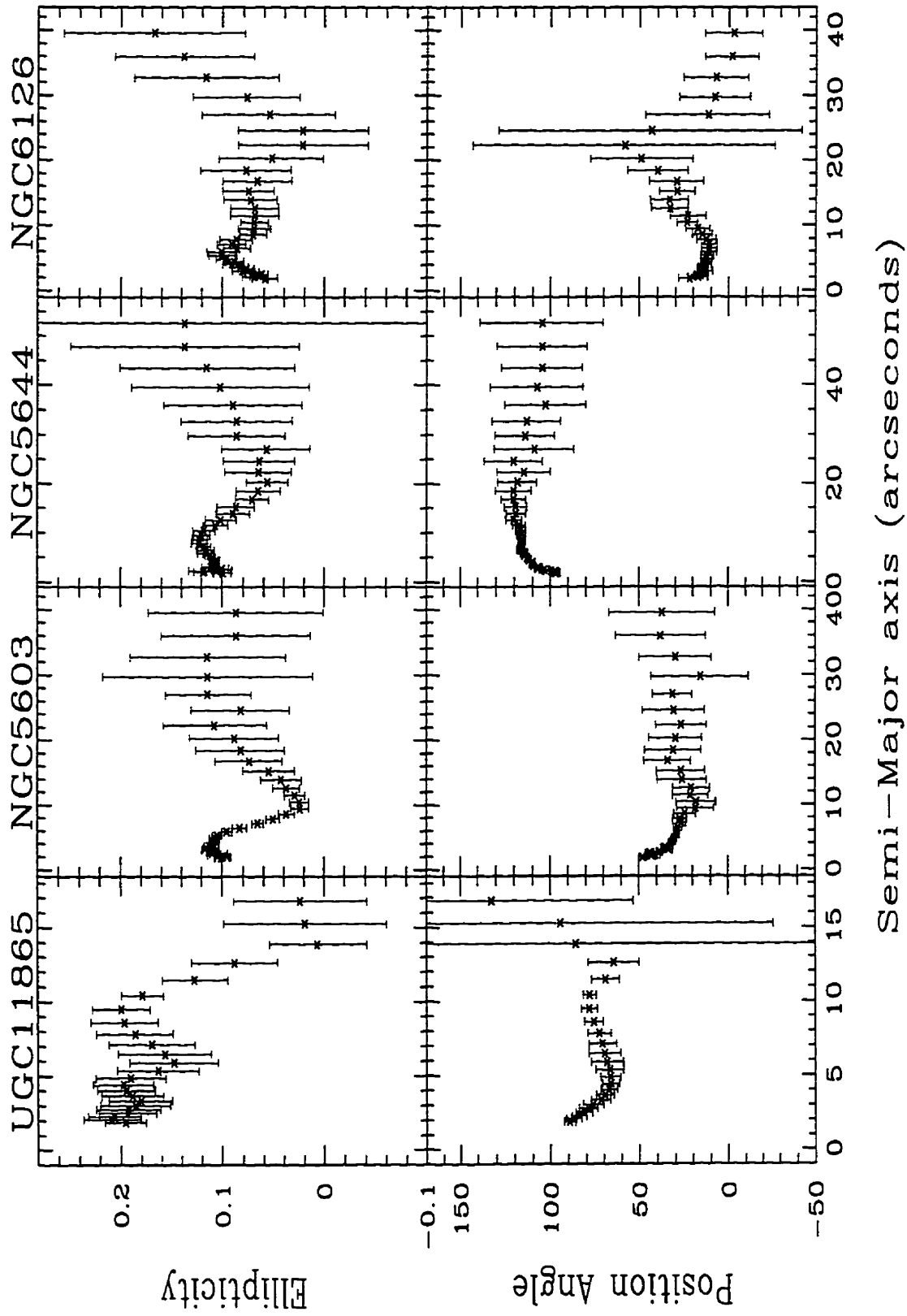


Figure B.21: Ellipticity and position angles of four galaxies